Time Resolved Crystallographic Studies

Stefanie Schiffers

A thesis submitted for the degree of Doctor of Philosophy

University of Bath

Department of Chemistry

April 2010

Table of Contents

Acknowledgements

Firstly I would like to thank my supervisor Paul Raithby for a continued support and encouragement over the last years. His consistent interest in my work and the provision of ideas and discussions were really helpful. Additionally he provided me with a lot of opportunities during my PhD.

I also want to thank all members of the Raithby-group, both past and present, for a pleasant working atmosphere and who helped enormously, especially during long beam time hours at various synchrotrons. Special thanks to Simon Brayshaw, Paul Raithby and André Mueller for reading this report and finding the hundreds of small errors.

The station scientists Dr. John Warren, Dr. Simon Teat and Dr. Dave Allen at Daresbury, ALS and Diamond synchrotrons, respectively, have provided an excellent service and helped throughout a large number of experiments. They also encouraged new ideas and investigations through long hours of experiments.

I would like to thank Dr. Tim Easun and Dr. Mike George in Nottingham for their low temperature Raman spectroscopy on the nickel complexes, as well as Simon Cotton for the crystals.

I would like to express my gratitude to the sponsors of this work which was funded by the EPSRC.

Finally, thanks to my friends and family who have supported me throughout my PhD and made my stay in the UK very pleasant and worthwhile.

Abstract

X-ray crystallography is an important analytical method for the characterisation of materials in the solid state. During the last decade, it has become important as a tool in the new field of photocrystallography. This combines both crystallography and photochemistry and is used to monitor the formation of light-induced metastable and transient species, so that structural information can be obtained during the change of a material. This is an important area of research as solid state chemistry can display new phenomena and reveal properties that are not possible in solution.

Chapter 1 of this thesis commences with a brief introduction to the different methods used to achieve and measure the excitation within crystalline compounds, while Chapter 2 contains an introduction into diffraction methods.

In Chapters 3-5 new photocrystallographic studies were performed on two series of compounds. The first one consists of a systematic study on metal complexes with different pyridylethylene ligands. The focus was to align complexes in the solid state so that they can undergo photo induced cycloaddition reactions. These solid state reactions are important as they present "green synthetic chemistry". The second study involves the photoinduced linkage isomerisation of $[Ni(L)_2(NO_2)_2]$ complexes. Structural characterisation shows that the NO_2 ligands change their coordination mode when irradiated with light of different wavelengths. Conditions for the metastable isomerisation were optimised by altering temperature and wavelengths.

In Chapters 6 and 7 a systematic study of structural changes in a series of lanthanide complexes and their use as triboluminescence materials, is described. The proposed mechanism of triboluminescence for these complexes is discussed.

To summarise, in this thesis, systematic investigations have been carried out in different aspects of crystallography using appropriate series of compounds. The nature of and the conditions required for the change to occur within the solid state have been established.

Abbreviations

Abbreviation	Definition	Abbreviation	Definition
A	acceptor	h	hour
A	ampere	hal	halogen
a	a axis	Hz	HERTZ
ALS	Advanced Light Source	*hkl*	MILLER indices
a.u.	arbitrary unit	HOMO	highest occupied molecular orbital
b	b axis	*I*	body centred
C	CELSIUS	I	intensity
C	centred	I_c	ionic
c	c axis	I_{hkl}	intensity of reflection *hkl*
CCD	change coupled detector	IR	infrared
CCDC	Cambridge Crystallographic Data Centre	K	KELVIN
$CDCl_3$	deuterated chloroform	k_b	BOLTZMANN constant
cm	centimetre	L	litre
CN	coordination number	LED	light emitting diode
xD	x dimension	LUMO	lowest unoccupied molecular orbital
D	donor	M	metal
d	distance	M_m	monomer
d	days	mcd	millicandela
d	doubled	Me	methyl
d^x	d-orbital	MeOH	methanol
D_c	calculated density	mer	meridonal
D_m	dimer	min	minute
DCM	dichloromethane	mg	milligrams
DLS	Diamond Light Source	ml	milliliter
DMSO	dimethylsulfoxide	mm	millimetre
E	*cis*-isomer	mmol	millimol
e^-	electron	MOF	metal organic framework
ES	excited state	ms	millisecond
ESI	electrospray ionisation mass spectroscopy	MS	metastable state
EtOH	ethanol	MS	mass spectrometry
F	face centred	nm	nanometre
f	atomic scattering factor	NMR	nuclear magnetic resonance
F_{hkl}	structure factor for	ns	nanosecond

	reflection *hkl*		
fac	facial	OTf	triflate
FT	fourier transformation	P	polymer
g	gram	p	para
GS	ground state	*P*	primitive
h	PLANCK's constant	p^x	p-orbital
pm	picometre	W	watt
R	R-factor	wR_2	weighted R-factor
R_{int}	internal R-factor	Z	*trans*-isomer
RMS	root mean square	Å	ÅNGSTROEM
RT	room temperature	°	degree
S_x	singlet state	%	percentage
s	second	α	alpha
s	singlet	β	beta
SRS	Synchrotron Radiation Source	γ	gamma
T	temperature	δ	delta
T_{min}	minimal absorption correction	ε	phase
T_{max}	maximal absorption correction	η	eta
T_x	tripled state	θ	theta
terpy	terpyridine	λ	wavelength
thf	tetrahydrofuran	μ	absorption coefficient
TLC	thin layer chromatography	μs	microsecond
UV	ultra violet	ν	nu
V	volume	π	pi
V	volt	ρ	density
vis	visible light	σ	sigma
vol.	volume	τ	lifetime

List of Figures

Chapter 1

Chapter 2

Chapter 3

Chapter 4

Chapter 5

Chapter 6

Chapter 7

Chapter 8

List of Tables

Chapter 2

Chapter 3

Chapter 4

Chapter 5

Chapter 6

Chapter 7

Chapter 8

1. Photochemistry

The study of changes in chemical systems actuated by irradiation is termed photochemistry. The studied compounds can undergo a conformation or configuration change or react under irradiation. The energy, which is needed for the change to occur, is supplied in form of photons from the electromagnetic radiation. This phenomenon is found in a wide variety of systems in nature and technology, for example in photography, solar cells or photosynthesis in plants.

Chemical reactions proceed generally through a transition state, which means that energy is necessary to excite reacting molecules to a higher energy state. This energy is normally supplied by thermal stimulation. In photochemistry light is used to provide the energy which result in molecular rearrangements or bond cleavage in the molecule through the excitation process. Commonly the electrons are redistributed from the HOMO (highest occupied molecular orbital) to the LUMO (lowest unoccupied molecular orbital). The JABLONSKI diagram (Fig. 1.1) illustrates the electronic states of a molecule and the transitions between them. Following excitation, decay proceeds either through emission (fluorescence or phosphorescence), internal conversion or intersystem crossing. Intersystem crossing is needed for phosphorescence to occur, as the transition responsible for it is forbidden. Intersystem crossing converts the total electronic and vibrational energy into another state (e.g. S to T). Phosphorescence has a longer lifetime, again because of spin conversion from T_1 to S_0. Fluorescence on the other hand occurs as a result of decay from a singlet excited state by emission of a photon (S_1 to S_0). This process is spin allowed and has therefore a short lifetime. Internal conversion is the transition of an electron from a higher to a lower electronic state (within S_0), this process is non-radiative.

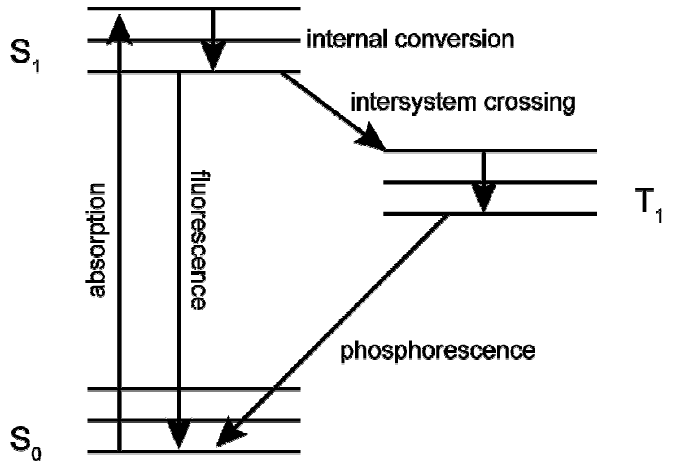

Figure 1.1: JABLONSKI diagram.

The electronically excited state is not thermodynamically stable and can decay either by the kinetic processes of luminescence, vibrational decay or via photochemical transformation. The following chapters focus on the last possibility, which involves atomic displacements, isomerisation or solid state chemical reactions.

1.1. Photocrystallography

X-ray diffraction is generally used for the identification of time-averaged solid state structures. A complete data collection takes between minutes and days, even though the X-ray scattering process for an individual photon occurs on the time scale of ~10^{-18} s. Photoreactions with a timescale down to picoseconds are therefore not straightforward to investigate. To overcome this problem a combination of spectroscopic and crystallographic techniques are used for measuring excited states and transition state reactions. Irradiation of the sample on the diffractometer induces a redistribution of the electrons at the molecular level which can lead to atomic movement or in extreme cases to isomerisation or to a chemical reaction. This photochemical change can be either reversible or irreversible; an example for an irreversible change is a cycloaddition reaction (Fig. 1.2).

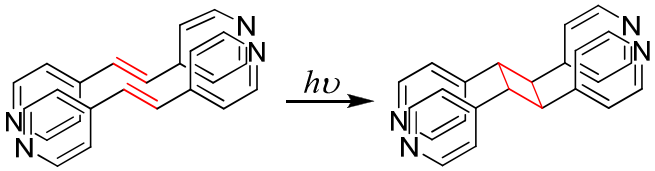

Figure 1.2: Photodimerisation of di-(4-pyridyl)-ethylene.

An example of a reversible change is the linkage isomerism observed in the coordination complex shown in Figure 1.3, where the SO_2 ligand changes conformation from η^1-S bound to η^1-O bound.

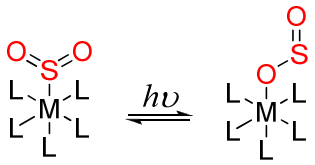

Figure 1.3: Excited state of a SO_2-metal-complex.

In a reversible case, it is necessary to differentiate between metastable and unstable states. A species is metastable if it exists without change as long as no external stimulation is applied even though that it is thermodynamically unstable with respect to another state (Fig. 1.4).

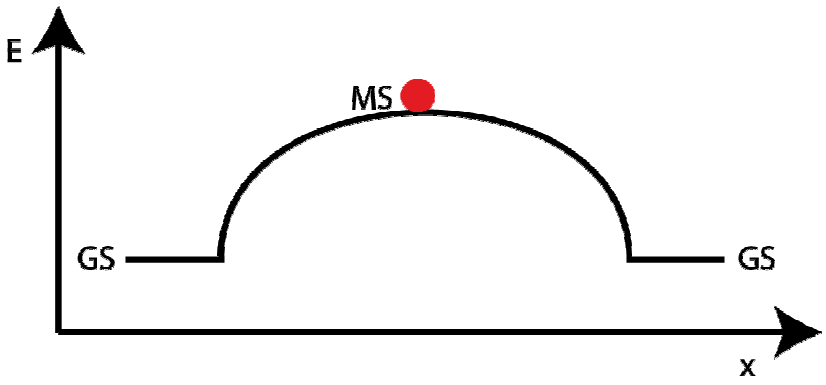

Figure 1.4: Schematic picture of a metastable state. MS relative to energies of GS.

To determine the structures of molecules in meta- or unstable states the experimental setup for the X-ray diffraction experiment has to be modified [1, 2],

depending on the lifetime τ of the photo-induced new state. Three different methods are used, which are known as steady-state methods (τ_0 > min), pseudo-steady-state methods (ms to min) and stroboscopic methods (ps to ms).

For materials with long lived or irreversible structural changes, steady-state methods are used; the experimental conditions are shown in Figure 1.5. The first step is to determine the ground state structure (GS) afterwards the crystal is optically-pumped for a period of time (depending on the light source and the sample) with a light source. This is followed by removal of the light source and a second data set containing the excited state (ES) is measured. If this data set contains both structures (ground state and excited state), the assigned structure is then refined using a disorder model. If the structure is metastable, it might be trapped under the experimental conditions after the excitation, which is consistent with their long lifetimes. Trapping is often achieved by maintaining the complex at low temperature.

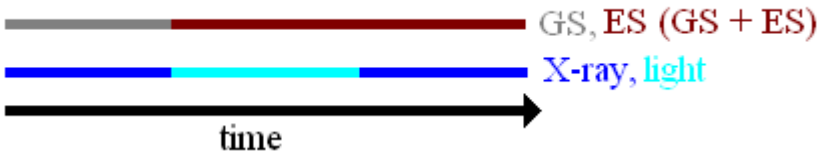

Figure 1.5: Experimental conditions for a steady-state experiment.

A pseudo-steady-state experiment (Fig. 1.6) will also start with a ground state measurement, followed by a measurement during the optical pumping. The sample remains in its pseudo-excited state for the duration of the experiment provided that the light remains cycling at the necessary pulse rate (Fig. 1.6a). This can cause problems, if the light source heats up the sample; to avoid this problem both structures can be measured at the same time. This means that each frame is measured twice, first a 'light-on' measurement, followed by a 'light-off' measurement (Fig. 1.6b) after the excitation has decayed. For this type of experiment a timing mechanism is set up between the diffractometer X-ray pulse and the laser.

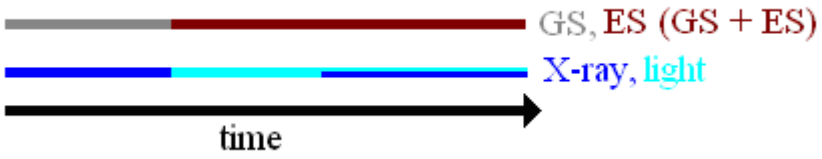

a

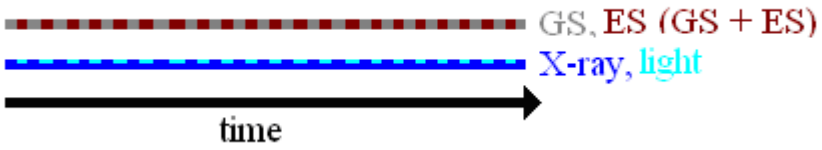

b

Figure 1.6: Experimental conditions for a pseudo-steady-state experiment.

Stroboscopic pump-probe methods (Fig. 1.7) are utilised for samples with excited state lifetimes of around πs-ms (pump-probe). This procedure utilises a pulsed laser and a mechanical chopper; the length of the pulse depends on the photoactive lifetime of the sample. The chopper and the pulsed laser are synchronised, so that both X-rays and optical pulses occur at the same time. The excited state structure is measured during the "on" period, where light and X-rays are on, whereas it returns to the ground state structure between the "on" times. The data are only recorded during the "on" time. For species with shorter lifetimes (ps to μs) the time structure of the synchrotron beam can be used instead of the mechanical chopper, which is then electronically synchronised.

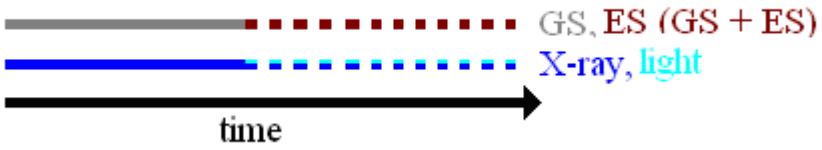

Figure 1.7: Experimental conditions for a stroboscopic pump-probe experiment [3, 4].

1.1.1. Examples for the Steady-state Method

Steady-state photo-induced processes may be placed in two categories: mostly irreversible structural changes and metastable reversible structural changes. The first type includes chemical reactions such as polymerisations, addition and cyclisation reactions and isomerisation reactions. The second type includes photo induced linkage isomerism and spin-crossover systems.

1.1.1.1. Irreversible Structural Changes within Crystals

The following section looks at the variety of reactions that belong to the group of mostly irreversible structural changes which occur in the solid state. Solid state reactions are topologically controlled; this means that they are controlled by the molecular packing within the crystal structure of the reactants. This concept was first proposed by SCHMIDT and co-workers, who analysed the role of lattice geometry to extend the understanding of solid state chemistry [5, 6, 7, 8]. His results suggested that:

a) Reactivity differs between reactions in solution and in the solid state
b) Chemical behaviour may be different for closely related chemicals
c) Different polymorphs display different chemical behaviour

1.1.1.1.1. [2+2] Cycloaddition Reactions

R. B. WOODWARD and R. HOFFMANN first used the term 'pericyclic reactions'; in organic chemistry this means that the reaction occurs in a concerted manner [9]. A cyclic transition state is involved during the reaction. Pericyclic reactions include among others DIELS-ALDER reactions, sigmatropic reactions, 1,3-dipolar cycloaddition and [2+2] cycloaddition reactions.

In order for a reaction to occur, the highest occupied molecular orbital (HOMO) and the lowest unoccupied molecular orbital (LUMO) must have the same symmetry. This is true for DIELS-ALDER reactions, which therefore proceed thermally, whereas [2+2] cycloaddition and [4+4] cycloaddition reactions can only occur photochemically, as the photochemical excitation has to promote an electron from the ground state HOMO into the ground state LUMO to provide the correct symmetry for the reaction to proceed.

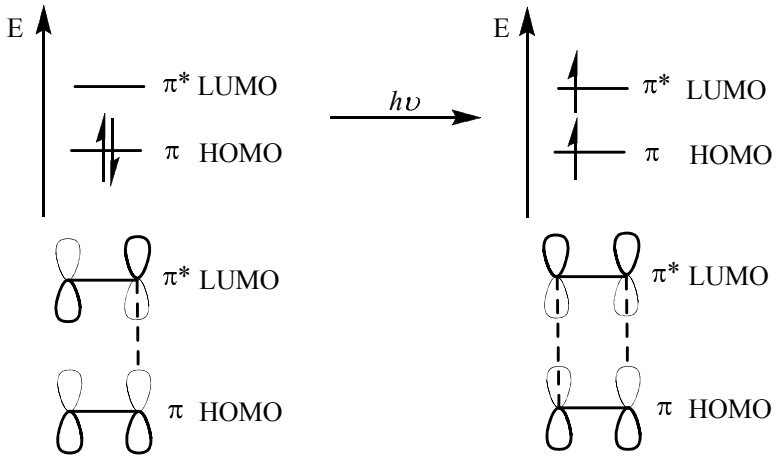

Figure 1.8: HOMO-LUMO-excitation with light for a [2+2] cycloaddition reaction.

Figure 1.8 shows the molecular orbital diagram corresponding to the double bond of an alkene. In the ground state only one binding interaction is possible**,** photochemical excitation produces two binding interactions, and a butane ring is built.

As described before, the molecular movement in the solid state is restricted; for this reason it is not possible to carry out solid state reactions in all crystals. It follows that for each reaction type there should exist an upper limit for the distances between the reacting centres beyond which reaction can no longer occur. Furthermore, bimolecular reactions are expected to take place between nearest neighbours, which in turn suggests that the molecular structure of the product might be a function of the geometric relation in the crystal lattice of reactant molecules [5, 6, 7, 8].

The upper limit for a [2+2] cycloaddition reaction for example is that the distance between the parallel double bonds should be below 4.2 Å [6]. However, these conclusions do not hold for all reactions, although this first hypothesis is a good starting point.

One exception for these rules is for example 7-chlorocoumarin, which has two pairs of double bonds, which have close separations (4.12 Å to 4.45 Å) (Fig. 1.9). Despite the closer distance and a necessary substantial movement due to the fact that no π-π-stacking is found [10], the reaction occurs between the bonds which are further apart (4.45 Å). The reason for this is the poor overlap of *p*-orbitals between the nearer bonds.

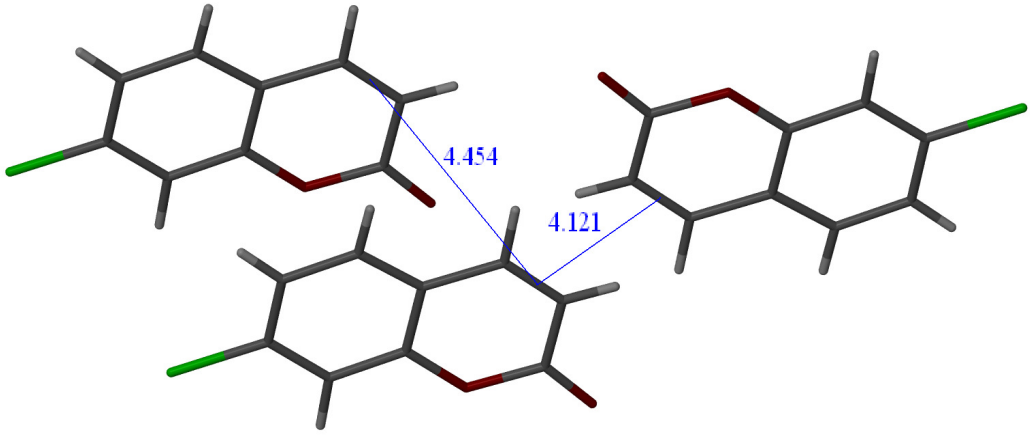

Figure 1.9: Crystal packing of 7-chlorocoumarin.

7-methoxycoumarin also undergoes a cycloaddition reaction in high yield. Here the distance between the double bonds is sufficient with 3.83 Å, but the bonds are rotated by 65° (Fig. 1.10). This reaction occurs due to the flexibility of 7-methoxycoumarin. The Ultra Violet (UV) irradiation provides enough energy for the required rotation of the bond to the correct orientation [10].

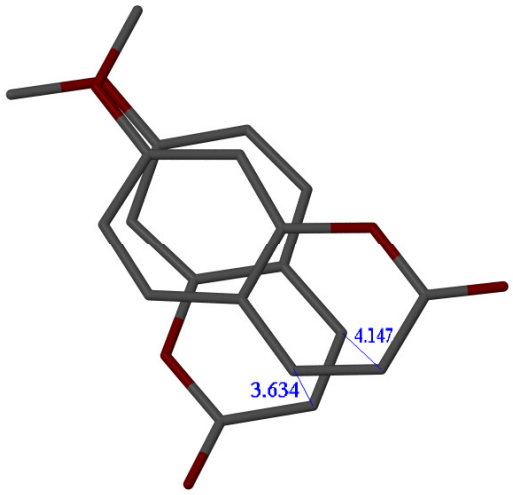

Figure 1.10: Rotation around the double bonds of 7-methoxycoumarin.

Even if all the criteria are met, a reaction does not always occur, as other factors in the crystal structure can prevent it. This is known for many different hydroxyl-coumarins, in which the hydrogen bonding presumably prevents the conformational changes necessary for a reaction to occur [10].

Obviously, solid state [2+2] cycloaddition reactions which produce only one reaction product is a 'green chemistry' approach, as no purification of the product is required. Unfortunately the practical applications of solid state [2+2] cycloadditions are limited by the fact that it is difficult to achieve the required orientation of the double bonds in the crystal structure. The factors which control the building of crystal structures are far from fully understood and small changes in a series of related molecules can change the structures totally. Achieving the correct orientation is often a matter of trial and error. To overcome this problem a number of methods have been developed including steering agents, host cavities and templates.

Atoms or functional groups, which are covalently attached to the molecule, can act as a steering agent and bring the molecules into a specific orientation inside a crystal structure. Known steering agents are acetoxy, chlorine and thiocyanate[10, 11].

This is shown in the following examples: Coumarin itself cannot undergo a [2+2] cycloaddition in the solid state as the double bonds in the monomers are too far

apart. However, when coumarin is substituted with an acetoxy group as in the case of 7-acetoxycoumarin a reaction occurs. This is due to C-H····O hydrogen bonds between the molecules, which help to align the double bonds in the correct orientation at a suitable distance [10]. In aromatic compounds chlorine is likewise an effective steering agent; the reason for this is the chlorine-chlorine interaction between the molecules with distances of around 3.8 - 4.0 Å [10].

The second method involves host-guest-interactions, for example an inclusion complex with the host compound regulates the packing and hence the orientation of the guest molecule. *β*-Cyclodextrin is a cyclic oligomer of *D*-glucose units, which acts as a host system for coumarin molecules (Fig. 1.11). A [2+2] cycloaddition occurs after a rearrangement has happened in the solid state, with a yield of 64 %. In this case 67 % is the maximum reaction yield possible, because of the 2:3 ratio of host and guest [12]; meaning that the reaction nearly goes to completion, as is the case for most solid state reactions.

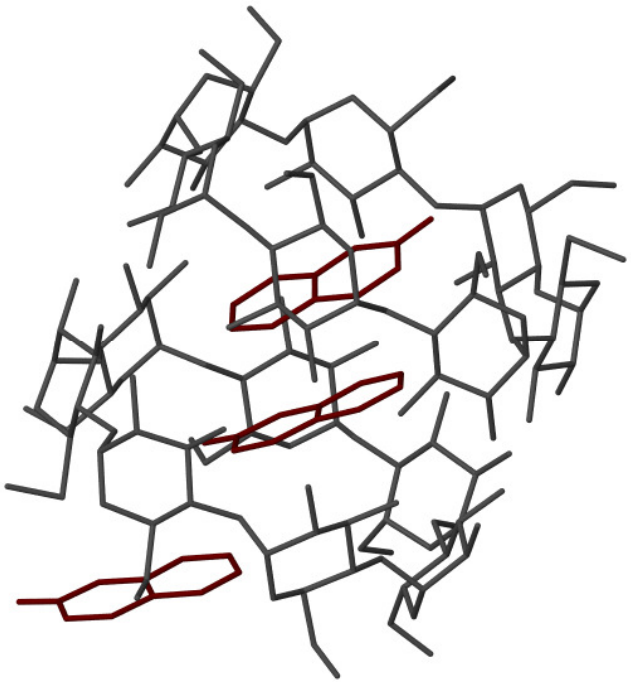

Figure 1.11: 2:3 Host (gray) - guest (red) reaction nano-tube.

Templates, as the third method, control the crystal structure by organising two molecules using self-assembly methods such as H- or halogen-bonding. This approach provides a greater degree of flexibility than steering agents and host cavities. The template can be used to bond to a variety of photoactive compounds and accommodate molecules of different sizes and shapes. This enables the solid state reactivity to be separated from the overall crystal structure.

An example is the use of resorcinol by MACGILLIVRAY and co-workers as a linear template to orientate (pyridyl)ethylene derivates for [2+2] cycloaddition reactions (Fig. 1.12) through hydrogen bonding. The template and the π-π-stacking between the aromatic rings cause the two double bonds to pack at a closer distance (3.6 – 3.9 Å) and a large channel supramolecular structure is built up after irradiation with UV-light [13].

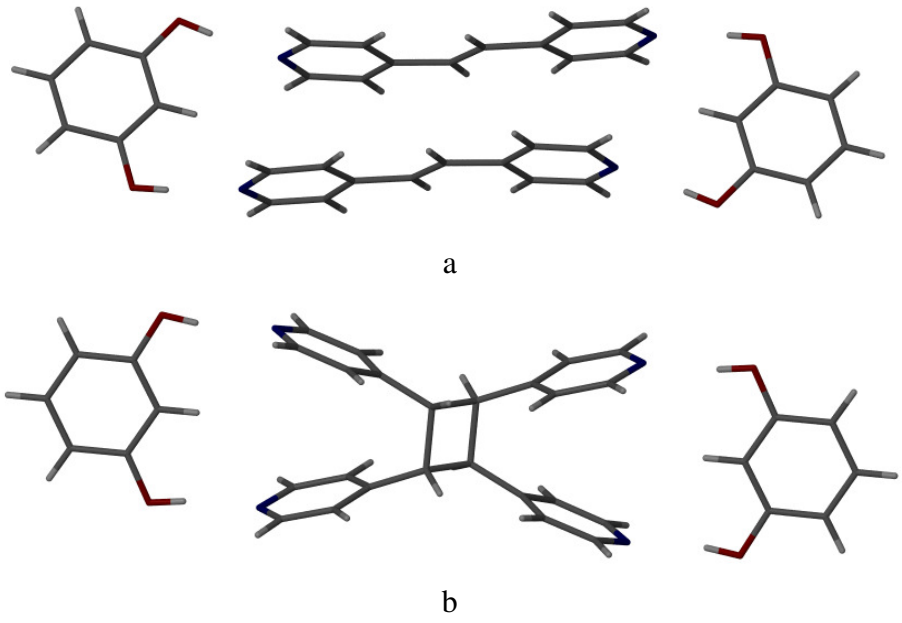

Figure 1.12: Resorcinol as a template which directs the reaction a) before and b) after irradiation in a single crystal to single crystal (scsc) transformation.

Following from this result MACGILLIVRAY *et al.* constructed many different co-crystals, which provide a route to reactive solids [13, 14, 15]. They have changed templates and ethylene derivates to get a whole range of different structures that can

undergo photodimerisation. One of these is a conjugated triene, which can dimerise in a solid state template-controlled synthesis as shown in Figure 1.13 [13].

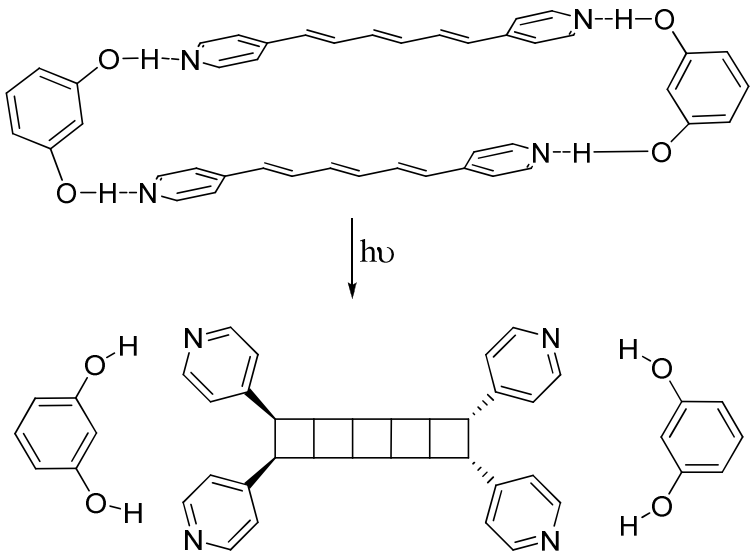

Figure 1.13: Conjugated triene dimerisation.

Besides bifunctional templates such as resorcinol, tri- or multifunctional templates can be used to organise olefins as well. Tricarballylic acid is an example of a trifunctional template. This template is building a polymeric structure as shown in Figure 1.14 [16] which then undergoes a reaction after irradiation.

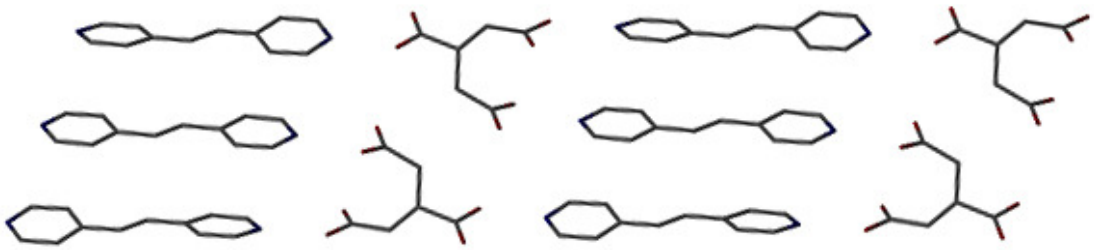

a

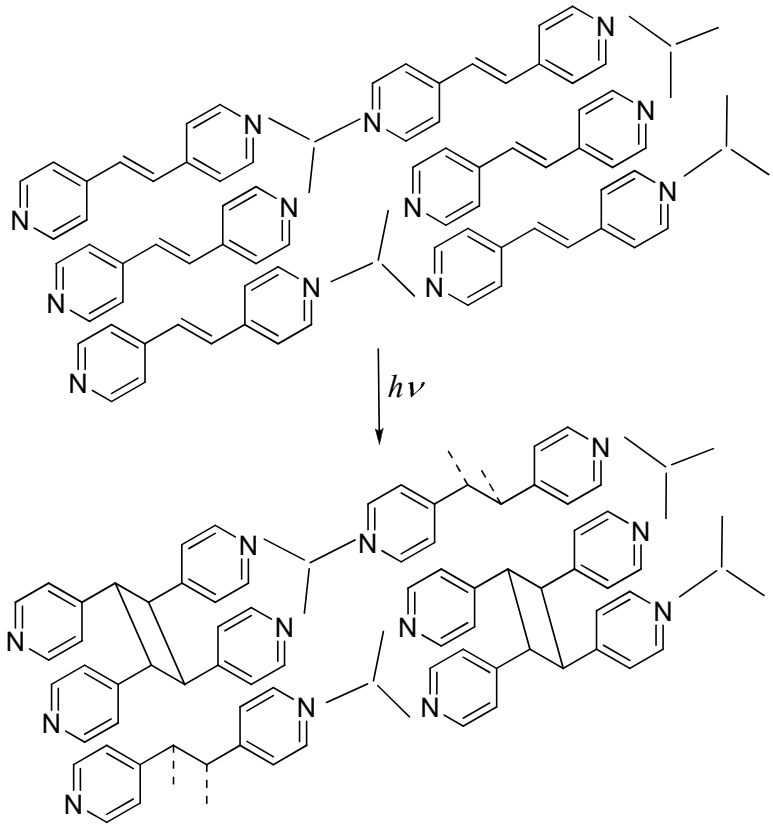

b

Figure 1.14: Trifunctional template structure a) crystal structure before irradiation with H-atoms removed in the structures for clarity b) reaction scheme.

In a similar manner to organic templates, transition metals can help arrange the alkenes in the crystal packing. The coordination to the metal arranges the organic ligands, that are the potential reactants. Silver, for example, can be used to direct [2+2] cycloaddition reaction via Ag···Ag argentophilic forces. This principle has been used to organise *trans*-1-(4-pyridyl)-2-(phenyl)ethylene so that it undergoes a [2+2]

cycloaddition reaction in the described complex (Fig. 1.15). A large movement (1.16 Å) of the silver ion is found as well [17] as a result of the channel produced. Other cases are, for example, Zn-complexes [18, 19, 20, 21] or Pb-complexes [22, 23] which can undergo [2+2] cycloaddition reactions in the solid state.

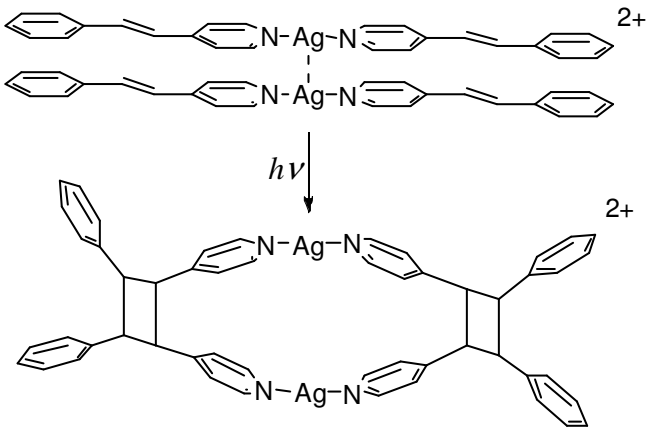

Figure 1.15: Silver complex in which the argentophilic forces direct the photoreaction.

All these examples show ways to organise alkenes so that SCHMIDTs criteria are met and a [2+2] cycloaddition reaction is likely to occur. While steering agents and host cavities are useful for specific types of molecules they cannot be used generally. This is where transition metal and supramolecular templates offer a better solution as they can be applied to a variety of different molecules and situations. Nevertheless, many structures are known, which appear to fulfil the necessary criteria to undergo a reaction, but are unreactive in the solid state under the reaction conditions employed.

1.1.1.1.2. Other Cyclisation Reactions

Pericyclic reactions other than [2+2] cycloaddition reactions are known in the solid state. There are not as well studied, but, for example, [4+4]

cycloaddition [24, 25, 26] and DIELS-ALDER reactions [27] are known as well as other photocyclisation reactions; for example the YANG reaction [28].

The DIELS–ALDER reaction in solution was discovered in 1928 by OTTO DIELS and KURT ALDER and is a [4+2] cycloaddition reaction, as a six-membered ring is produced from a conjugated diene (4 e^-) and a dienophile (2 e^-). A typical DIELS-ALDER reaction involves the formation of one π-bond and two σ-bonds. If only the HOMO from the electron rich diene and the LUMO from the electron deficient dienophile are considered, it is shown that they have the correct symmetry for a reaction to occur (Fig. 1.16). Consequently, a DIELS-ALDER reaction will occur thermally.

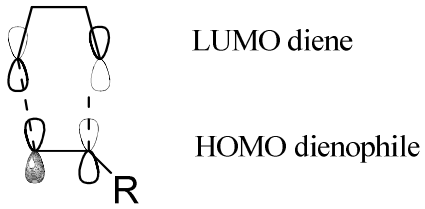

Figure 1.16: Orbital diagram of DIELS-ALDER reaction.

Solid state DIELS-ALDER reactions present a much bigger problem than [2+2] cycloaddition reactions. The reason for this is the fact that two mostly different reactants need to be co-crystallised with the right alignment to each other.

There are only a few examples of DIELS-ALDER reactions in the solid state. One of these is the reaction between anthracene and bis-(N-ethylimino)-1,4-dithiin by a thermal single phase transformation (Fig. 1.17) [27].

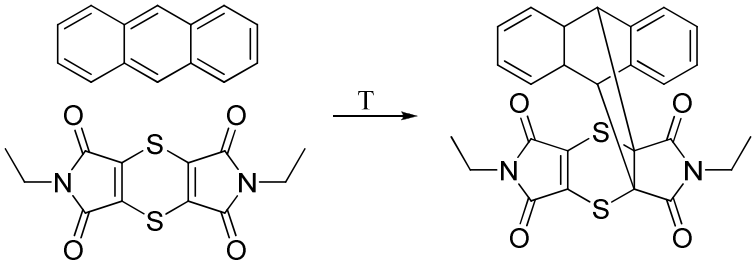

a

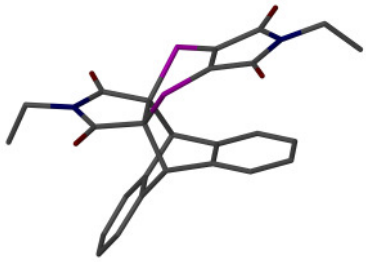

b

Figure 1.17: Solid state DIELS-ALDER reaction a) reaction scheme b) crystal structure of the product with H-atoms removed for clarity.

[4+4] cycloaddition reactions on the other hand are thermally forbidden as these involve 4n electrons. The first example of a [4+4] cycloaddition reaction in a single crystal between 9-methyl-anthracene molecules was reported by TUROWASKA-TYRK [24] in 2003. In a scsc-transformation, the reaction could only be monitored up to 28 % conversion as attempts to obtain higher conversions lead to crystal decomposition due to the large atomic movements which occur during the reaction (Fig. 1.18).

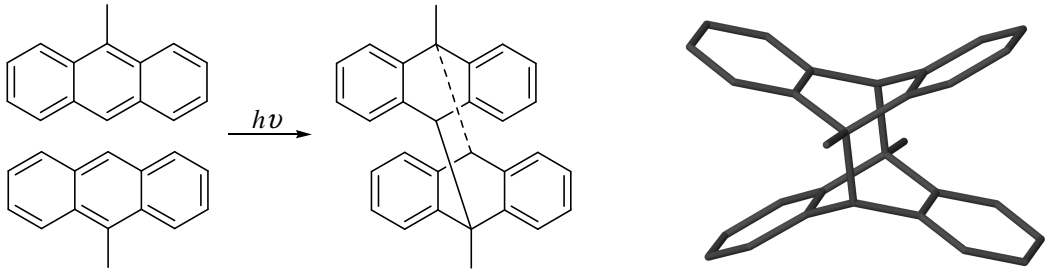

a b

Figure 1.18: Solid state [4+4]-cycloaddition reaction a) reaction scheme b) crystal structure of the dimer with H-atoms removed for clarity.

The YANG reaction is a ring closure reaction starting from a ketone and resulting in a cyclobutane ring, as shown below in Figure 1.19. In this specific solid state reaction the formation of the product is completed in a scsc-transformation [28].

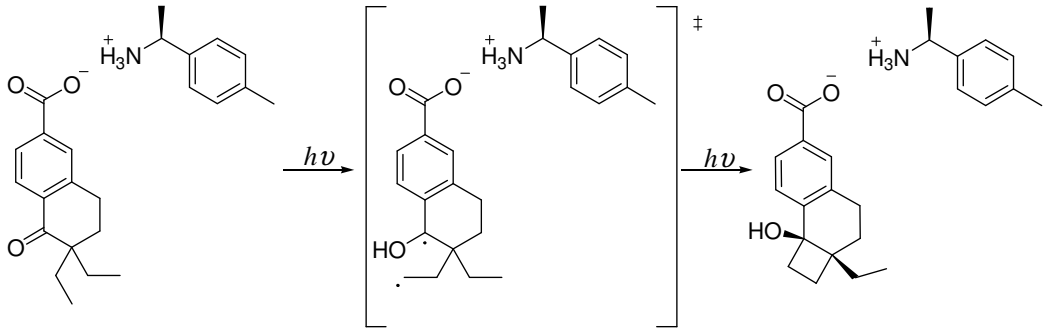

a

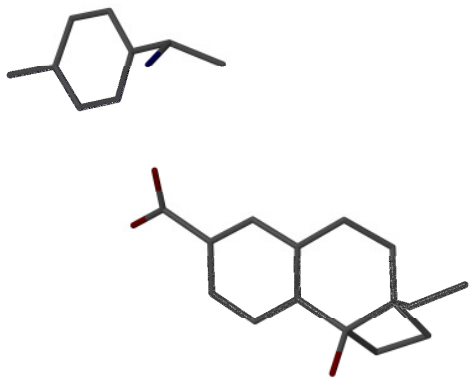

b

Figure 1.19: YANG reaction in the solid state a) proposed reaction scheme b) crystal structure of the cyclobutane product with H-atoms removed for clarity.

Another ring closing reaction is the intramolecular photocyclisation of diarylethylenes (Fig. 1.20). The pioneering researcher in that field is M. IRIE, who had published this example [29] (Fig. 1.20b) among many others [30]. During the reaction the crystal displays photochromism, defined as a photo-induced reversible transformation of a chemical species between two isomers which have different absorption spectra. Depending on the molecular structure these molecules change their colour upon irradiation with ultraviolet light from colourless to yellow, red, blue or green. These coloured molecules are in the closed-ring forms; they are thermally stable in the dark, but they convert to the open form upon irradiation with visible light. The cycling of the open to closed form and back can be repeated many times (>10^4 cycles) [29].

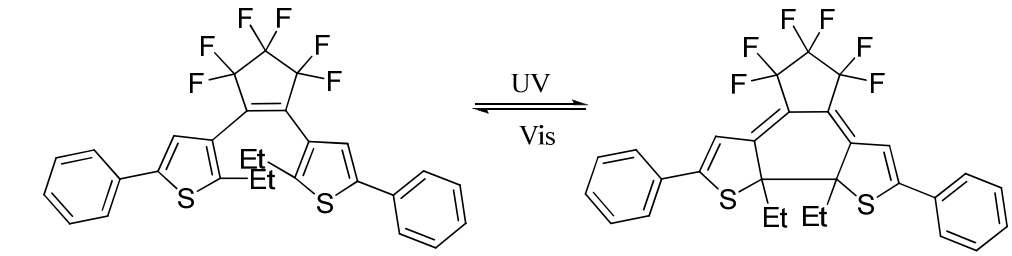

a

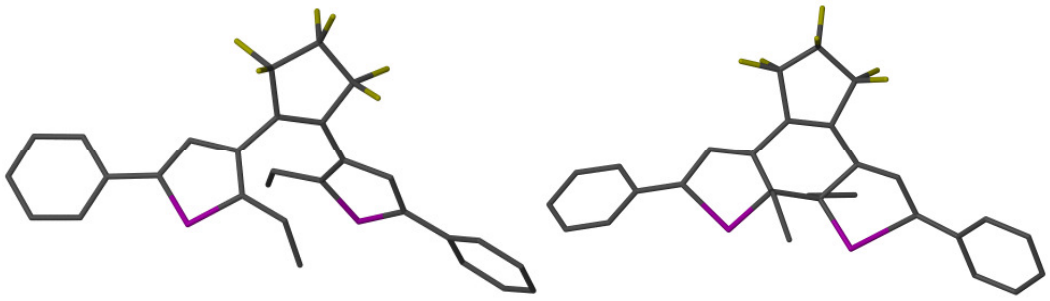

b

Figure 1.20: Ring closure reaction in the solid state a) reaction scheme b) crystal structure of the colourless open and blue closed form with H-atoms removed for clarity.

1.1.1.1.3. Isomerisation in the Solid State

Several isomerisation processes are known in the solid state, for example *E-Z*-isomerisation [31, 32, 33, 34], keto-enol-tautomerisation and linkage isomerism. The latter one is the most studied and examples are shown in Chapter 1.1.1.2.1..

Salicylideneaniline shows keto-enol-tautomerisation (Fig. 1.21) in the solid state, which was noticed because of a colour change after irradiation with UV light. The photocrystallographic study was undertaken with 730 nm light in form of a two-photon-excitation [35].

Two-photon-excitation is the simultaneous absorption of two photons in order to excite a molecule from one state to a higher energy state. The use of radiation with higher wavelengths minimises absorption of the light at the surface and allows deeper penetration of the radiation and therefore a more complete excitation of the crystal. Instead of using, for example, highly absorbed 300 nm radiation a light source of 600 nm is used. The problem is that two-photon absorption is many orders of magnitude less likely to occur than normal absorption, as two photons have to react with the crystal at exactly the same time, but on the other hand the crystal is less likely to decompose as not only the surface gets irradiated.

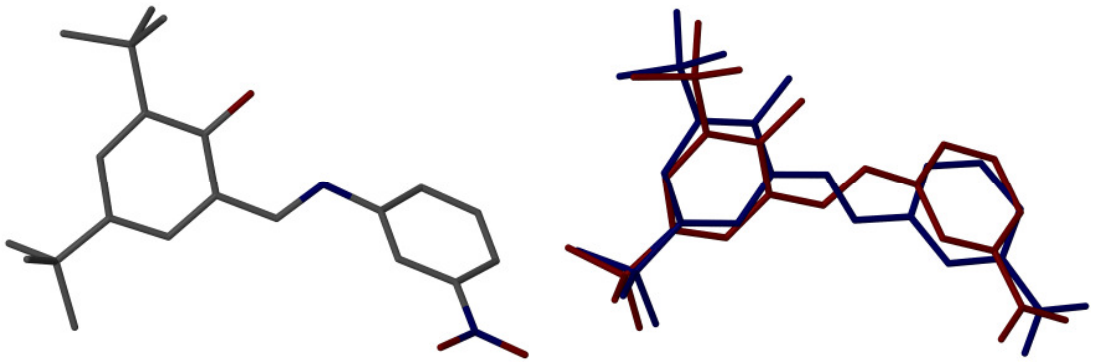

a b

Figure 1.21: Keto-enol-tautomerisation a) crystal structure before exposure with light b) after irradiation (blue = keto, red = enol) with H-atoms removed for clarity in both structures.

Because of the large atomic movements, which are necessary for an *E-Z*-isomerisation, these reactions are often performed in a host-guest framework [32, 36], which means that the guest molecules can move or rearrange without destroying the crystal lattice through the introduction of increased lattice strain. One interesting example is a co-crystal of 1,1,6,6-tetraphenyl-2,4-hexadiyne-1,6-diol and sorbic acid (Fig. 1.22), where, depending on the temperature, the isomerisation or the dimerisation is preferred. At 280 K, irradiation of the crystal with 325 nm light results in dimerisation, whereas at 90 K both processes take place to give a low product yield [33].

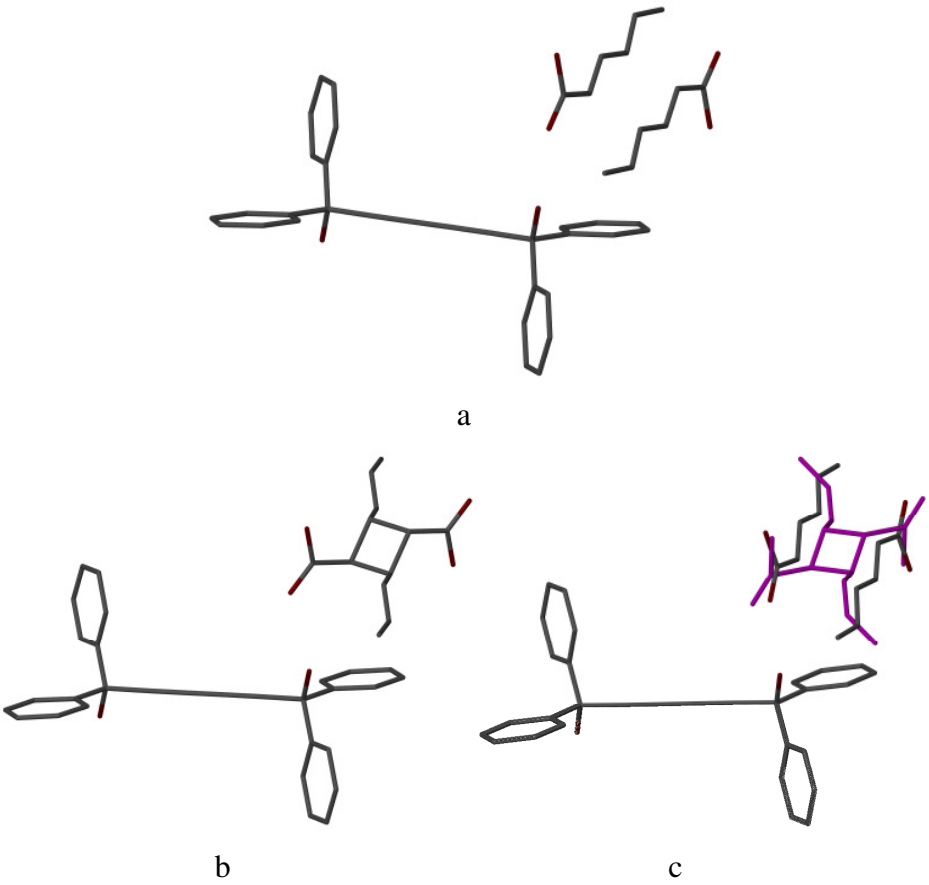

Figure 1.22: Competition between dimerisation and isomerisation a) crystal structure before exposure to light b) after exposure at 280 K c) after exposure at 90 K, with the dimer shown in violet for clarity with the isomerisation happening in the propylene chain. H-atoms removed for clarity in all structures.

1.1.1.2. Metastable Structures

These structures are thermodynamically unstable, but are trapped, in a particular temperature or pressure range, in a metastable state.

1.1.1.2.1. Linkage Isomerisation or 'THE SCHIZOPHRENICS OF COORDINATION CHEMISTRY' [36]

The definition of a linkage isomer is that the complex contains one or more ambidentate ligands. This means that the ligand can bind in more than one way to the metal centre. Today there are many different complexes with ambidentate ligands known, including NCS^- [38], NO [39], NO_2^- [37, 40], CN^- [41], NCO^- [38], SO_2 [42] and DMSO [43]. Such isomers can either be chemically synthesised [44], generated by light [2], high temperature [45] or electrochemically [46].

The concept of linkage isomers dates from JØRGENSEN's time [47], when he noted that two species could be isolated for $[Co(NH_3)_5(NO_2)]Cl_2$, one complex in which the NO_2 group is bound through nitrogen and the other when it is bound through oxygen. Since that time extensive additional studies have been carried out on linkage isomerism. Light induced linkage isomerism was first studied crystallographically in the early 1990s by T. WOIKE [48]. His group used neutron diffraction to study the structural changes in sodium nitroprusside (Fig. 1.23). The first X-ray experiment was carried out on the same compound by COPPENS *et al.*. In the experiment the crystal is cooled to a temperature below which the metastable linkage isomer exists and is then irradiated with light of a suitable wavelength to induce the isomerism [1]. In the case of the sodium nitroprusside two low temperature metastable states can be induced by using different wavelengths at different temperatures. In the lower temperature metastable state (MS2) the coordination of the nitrosyl changes from the η^1-N bound arrangement found in the ground state to the sideways η^2-N-O bonding mode as illustrated in Figure 1.23. The higher temperature metastable state (MS1)

involves a terminally bonded nitrosyl being coordinated through the oxygen atom, η^1-O.

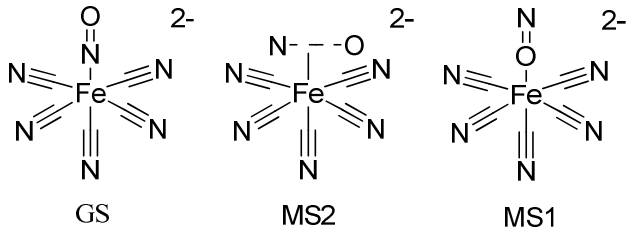

Figure 1.23: The ground and two photo-induced metastable states of nitroprusside.

These results were followed by a series of metastable state studies with complexes containing NO, SO_2 and NO_2.

As mentioned above the first NO_2 linkage isomer complex was recognised by ALFRED WERNER [49] on the *xantho* and *isoxantho* forms of the $[Co(NH_3)_5(NO_2)]Cl_2$ complex after JØRGENSEN had synthesised them [47].

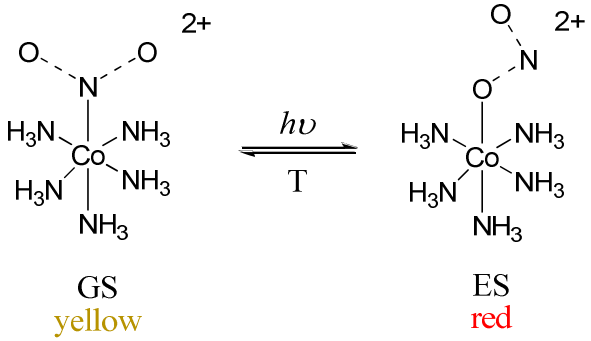

Figure 1.24: Linkage isomerism of $[(NH_3)_5Co(NO_2)]Cl_2$.

The *xantho* complex (yellow) corresponds to the more stable nitro isomer, whereas the *isoxantho* complex (red) corresponds to the nitrito isomer (Fig. 1.24). JØRGENSEN discovered that these nitrito isomers could be synthesised directly in solution or by irradiation of the other solid NO_2^- isomers. A low-temperature single-crystal diffraction study was also performed later on the nitro form of $[Co(NH_3)_5NO_2]Cl_2$ by OHBA [50]. The complex was irradiated using a xenon lamp and

an excited state with a population of 15 % of the nitrito compound could be achieved. GRENTHE and NORDIN showed that the nitrito cobalt complex is the kinetic product of the solution reaction [40]. Co^{III} forms more stable complexes with nitrogen than with oxygen donors, so that the nitrogen bound one would be the thermodynamic product.

The possible coordination modes for the nitrite group can be seen below in Figure 1.25. Only the structural types (e) and (f) have so far not been identified crystallographically. Recent results show that the most common coordination modes are a, b, c and d, but the bonding mode of the nitrite ion has been shown to be quite sensitive to changes in the steric requirements of other ligands in the coordination sphere. In all the complexes the nitrito isomers are thermodynamically unfavourable and are only formed under specific reaction conditions, such as high temperature [45], steric hindrance [51] or irradiation [44].

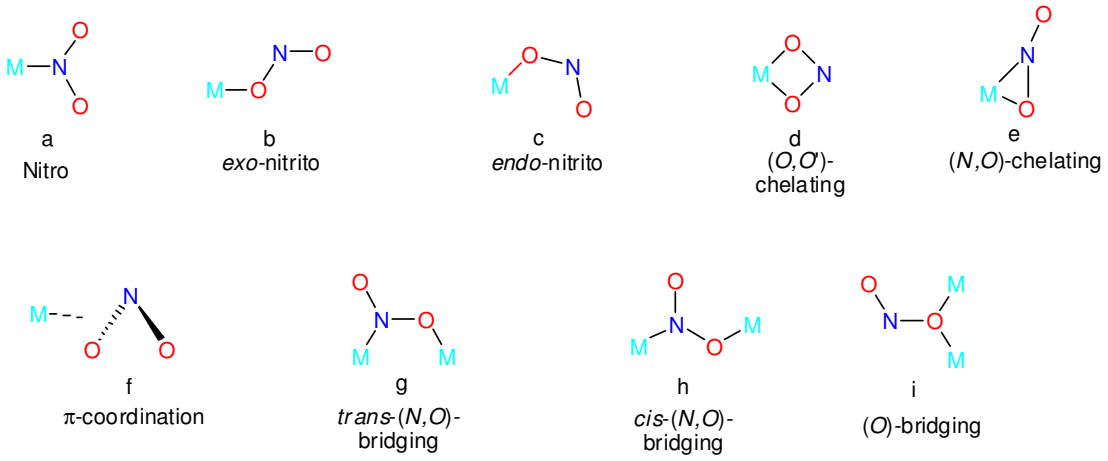

Figure 1.25: Coordination modes for the nitrite group [37].

The first linkage isomer, which undergoes a reversible 100 % excitation in a single crystal to single crystal manner under irradiation, was reported by RAITHBY *et al.* in 2009. [Ni(dppe)(η^1-ONO)Cl] (Fig. 1.26c) is formed upon irradiation with UV-LEDs, which were used as a cheaper light source than lasers [52]. Warming the η^1-O-bound species up to temperatures above 180 K, results in quantitative reversion to the η^1-N-bound complex. Further work on different complexes with nickel as the metal centre and other phosphorus ligands showed the same high conversion rates. These

results are very encouraging as it was believed for a long time that a high conversion is not possible without breakdown of the crystal. Obviously, high conversion rates are necessary for any material to have practical applications.

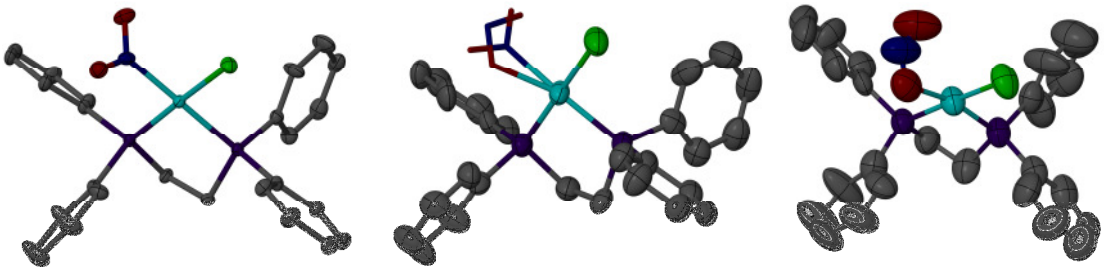

a b c

Figure 1.26: a) Ground state structure of [Ni(dppe)(η^1-ONO)Cl] b) both isomers after a short irradiation time c) 100 % converted structure with 50 % ellipsoids shown and H removed for clarity on all structures [52].

Since the 1980s, the nitrosyl group has been investigated through solution-based spectroscopy and by solid state techniques, including photocrystallography for its linkage isomerism properties, as it plays a part in many biological systems and has been recognised in physiological and pathological processes. As described above two metastable states can be achieved through photochemical excitation. The metastable complexes can interchange between excited states thermally or chemically.

After the first studies on sodium nitroprusside, the ground state and a light induced metastable state of [Ni(NO)(η^5-Cp*)] were determined by COPPENS using X-ray diffraction [53]. Cp* (pentamethyl cyclopentadienyl) was used as the similar complex with Cp (cyclopentadienyl) is a liquid at room temperature. The metastable state was achieved via irradiation of the crystal at 25 K for three hours using light with a wavelength of 458 nm. The observed metastable state was the η^2-NO isomer. The methyl groups are distorted away from the metal as a result of the displacement of the nitrosyl ligand (Fig. 1.27).

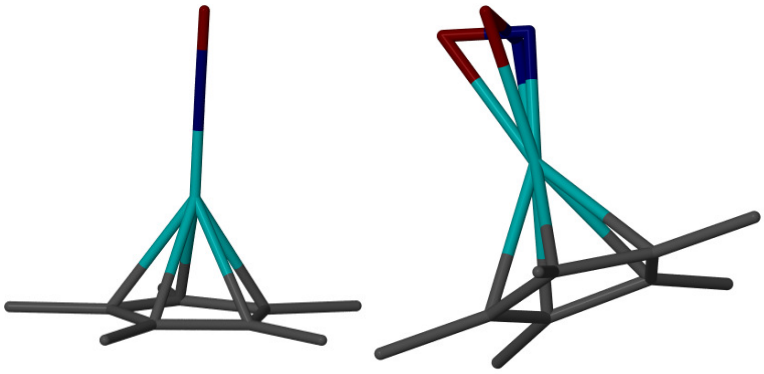

a b

Figure 1.27: [Ni(NO)(η^5-Cp*)] a) ground state structure b) metastable side-bond structure with H-atoms removed in both structures and GS removed in b for clarity.

Another ambidentate ligand is sulphur dioxide, which is a versatile ligand and can bond to a metal centre in a number of different ways (Fig. 1.28); which bonding mode is formed depends on the nature of the metal centre and the ligands in the complex. Upon irradiation only some of these bonding modes are seen.

The known metastable linkage isomers of SO_2 are similar to those of NO, as there is a MS1 and a MS2 state. In the MS1 state SO_2 is bonded to the metal through an oxygen atom (η^1-OSO) and in the MS2 state it is sideways bound to the metal (η^2-OS). Figure 1.28 shows the known and putative bonding modes of SO_2 [42]. Complexes with binding modes a, b, c and e have been structurally characterised, whereas d, f, g and h have not yet been observed.

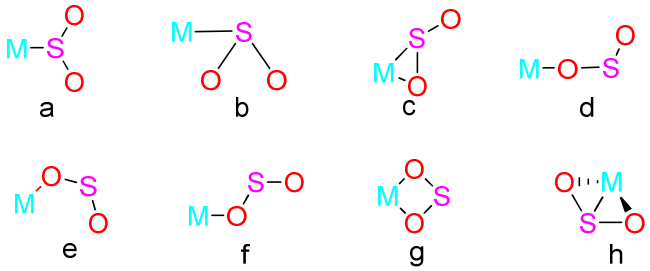

Figure 1.28: Bonding modes of SO_2.

In 1979 JOHNSON and DEW recognised the isomeric properties of SO_2 from low temperature IR spectra of *trans*-$[Ru(NH_3)_4(SO_2)Cl]Cl$ in solution [54]. COPPENS investigated this complex later with photocrystallographic methods, as well as the complex *trans*-$[Ru(NH_3)_4(H_2O)(SO_2)](C_6H_5SO_3)_2$. It was confirmed that on excitation, the sulphur dioxide rearranges from the η^1-S-bound conformation to an η^2-SO-side-bound isomer. This isomer was observed for both of the ruthenium complexes with the populations of the metastable state MS2 (Fig. 1.28c) refining to 10 % for *trans*-$[Ru(NH_3)_4(SO_2)Cl]Cl$ and 12 % for *trans*-$[Ru(NH_3)_4(H_2O)(SO_2)](C_6H_5SO_3)_2$ [41].

Following on from these results the linkage isomerism of the SO_2 group was further investigated. The following compounds were used: *trans*-$[Ru(NH_3)_4(H_2O)(SO_2)](tos)_2$ and *trans*-$[Ru(NH_3)_4(C_2O_2F_3)(SO_2)](C_2O_2F_3)*(CF_3COOH)$. These crystals darkened from orange to red upon irradiation with 488 nm light. In both samples the MS2 state was populated again, achieving higher populations than reported previously. The tosylate complex had a metastable state population of 20 %, whereas in the trifluoroacetate species up to 37 % excitation was observed [55].

In 2006, RAITHBY *et al.* determined a second metastable bonding mode of sulphur dioxide in $[Ru(NH_3)_4(H_2O)(SO_2)](tos)_2$. After irradiation of the crystal at 13 K for 75 min with a tungsten lamp 8 % of the MS2 component and 36 % of the novel MS1 (η^1-OSO) (Fig. 1.28e) component were found (Fig. 1.29) [56].

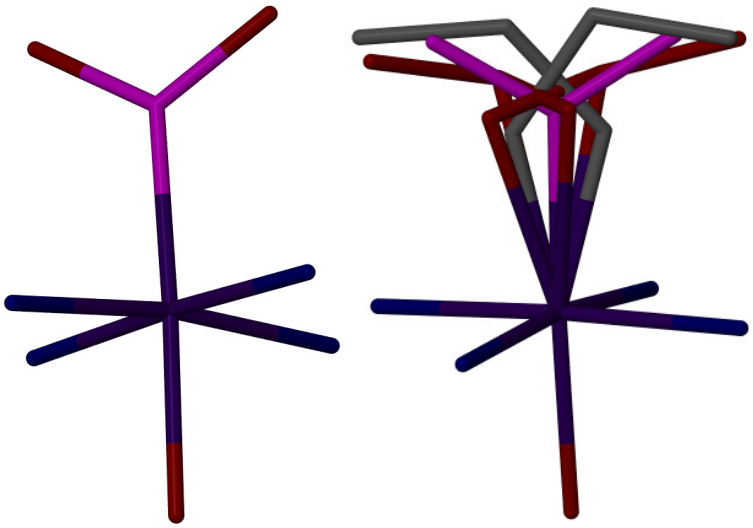

a b

Figure 1.29: $[Ru(NH_3)_4(H_2O)(SO_2)]$ a) ground state structure b) metastable and ground states with GS in pink, MS2 in red and MS1 in gray and with H-atoms removed in both structures for clarity.

Another ambidentate sulphur ligand is DMSO, which despite being larger in size than other ligands which show linkage isomerism, can also reorient itself in the solid state. This was observed for a single crystal of $[Ru^{II}(terpy)(bipy)(DMSO)](SO_3CF_3)_2$. Upon irradiation at 442 nm, a sample of the complex underwent a colour change from yellow to red with the initial colour returning after several minutes [43].

1.1.1.2.2. Spin-crossover

Octahedral metal complexes with d^4, d^5, d^6 and d^7 electronic configurations can adopt high spin and low spin configurations. Whether a high spin or low spin complex is formed depends on the oxidation state of the metal, which row of the periodic table it belongs to and what kind of ligands are involved. Figure 1.30 illustrates the low and high spin configurations possible for a d^5 metal complex.

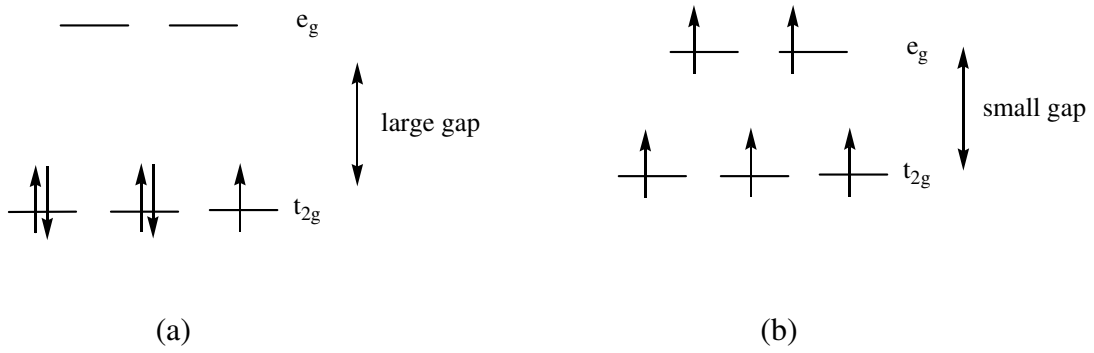

(a) (b)

Figure 1.30: a) Low and b) high spin configurations of a d^5 metal complex.

For structures, which have an energy gap between low and high spin state of approximately k_bT (k_b is the BOLTZMANN constant and T the temperature in Kelvin), it is possible to convert from one to the other by changing temperature, pressure and in some cases by applying light. If the spin-crossover system is excited by light it is called LIESST effect (light-induced excited spin state trapping). This metastable high spin state can have lifetimes of hours below a critical temperature T_{LIESST} [57, 58]. A system where it is possible to convert between the two spin-states is known as a spin-crossover system. Changing from low spin to high spin involves the transfer of an electron into a higher energy orbital (typically a M-L antibonding orbital), which makes bond lengths longer for high spin configurations than for low spin configurations. While this has no major implications in solution it does cause fundamental changes within the crystal lattice in the solid state. As well as the bond length changes there are also differences in magnetic and optical properties.

A typical example of a spin crossover system is $[Fe(phen)_2(NCS)_2]$ (Fig. 1.31), which changes with temperature at 176 K, pressure at room temperature and irradiation at low temperatures [59]. It converts from the high spin state at RT to a low spin state below 176 K, to form a new high spin state if irradiated at 30 K with light.

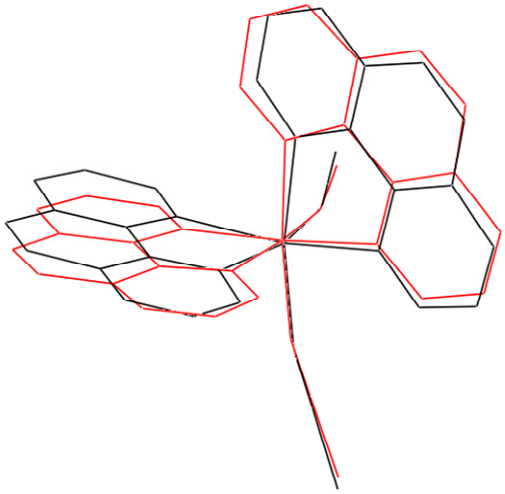

Figure 1.31: Both structures of $[Fe(phen)_2(NCS)_2]$ are measured at 30 K with H-atoms removed for clarity, with the low spin state in red and the irradiated (647 nm laser, 1 h) high spin configuration in black.

1.1.2. Non-steady State Methods

1.1.2.1. Bond Distance Change

In 2002 the groups of COPPENS [60] and OHASHI [61] both discovered independently a significant change in the Pt-Pt bond distance of $Pt_2(pop)_4^{4-}$ (Fig. 1.32) after irradiation with light. In the two independent experiments the shortening was 0.23 Å and 0.28 Å, respectively. The difference is explainable as they have used different counter ions in their experiments and altered experimental procedures. COPPENS used stroboscopic pump-probe, whereas OHASHI used pseudo-steady-state methods. This bond length change was the first direct measurement on an interatomic distance within an excited triplet state. Their estimation of the population of the excited state is only 2 % to 5 % and new methods have to be found to give higher populations of the excited state.

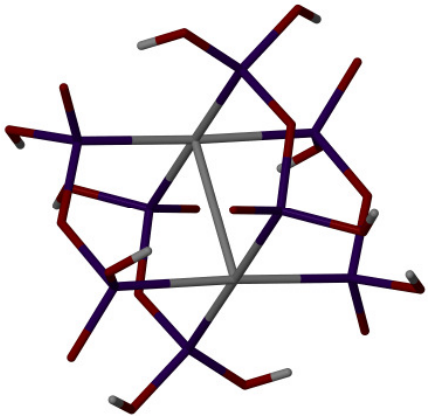

Figure 1.32: Ground state structure of $Pt_2(pop)_4^{4-}$ [61].

A second example is a Rh-Rh bond shortening in $[Rh_2(1,8\text{-diisocyano-}p\text{-menthane})_4]^{2+}$ upon excitation. The contraction of about 0.85 Å occurs on excitation with a neodymium vanadate laser. The short lived tripled state has a lifetime of 11.7 µs at 23 K [62].

It was also shown that Cu(I) complexes undergo a conformational flattening from tetrahedral to square planar [63]. Theoretically the flattening is of approximately 30º, but it is doubtful that large distortions are ever achieved in a crystalline environment. Nonetheless it was found that the two molecules within the structure are reacting differently upon excitation, this result provides evidence for the influence of the packing. Encouraging is that excitation levels of up to 10 % are found for this system, which is a significant increase to the 2 % described above. These results have also been co-observed by complementary EXAFS studies in solution.

1.1.2.2. Picosecond Powder Experiments

The group of S. TECHERT has reported a lot of work on excitation of powder samples. Their experimental setup follows a classical optical pump-probe scheme [64]. One example is the flattening of 4-(diisopropylamino)benzonitrile upon excitation.

The twist angle between the aromatic ring and the amino group decreased from 14° to 10° [65].

The same group have investigated the kinetics of the dimerisation of *p*-formyl-*trans*-cinnamic acid with powder experiments. The BRAGG diffraction pattern was used to interpret an initial distortion. This reorientation was proceeding within a few picoseconds (< 70 ps), whereas the [2+2] cycloaddition reaction took more then 30 min. Crystallinity is lost during the reaction and the product is amorphous [66].

1.2. Aims

X-ray crystallography is an important analytical method for the characterisation of molecules and array materials in the solid state. During the last decade, it has become more important as a fundamental tool in different fields of research such as photocrystallography. In this report single crystal and X-ray powder diffraction methods are used to analyse molecular and crystal structures of materials at different temperatures and under conditions of photoactivation. Photocrystallography is a developing technique, where every experiment involves new challenges and new ideas are formed and investigated. It is necessary to optimise the experimental conditions by varying the temperature, light source intensities and wavelengths. Some of the experiments need synchrotron radiation as the high intensity of radiation allows short data collection times and the use of smaller crystals. This decreases potential problems of absorbance of light on the surface of the crystals.

The aim of the work presented in this thesis has been to investigate the structure properties of crystalline materials under external non-ambient conditions. In these experiments crystalline materials have been irradiated with light or are exposed to a range of temperatures or pressure has been applied to them. Three different examples are investigated within this thesis. These include [2+2] cycloaddition reactions in the solid state of metal complexes, along side photo induced linkage isomerisation

studies on octahedral $[Ni(L)_2(NO_2)_2]$ complexes and a systematic studies on structural changes in a series of lanthanide complexes.

2. X-Ray Crystallography

The following section gives a brief overview of the basic principles of crystal X-ray diffraction. X-ray diffraction is a fundamental analytical technique used to determine the solid state structure of a crystalline material.

2.1. Introduction

2.1.1. BRAGG's Law

Crystalline materials have highly ordered periodic internal structures. This property, together with the fact that lattice sizes are typically in the order of ÅNGSTROEMS, means that they can act as a three dimensional diffraction grating for X-rays. X-rays were discovered by ROENTGEN in 1895 [67] and VON LAUE revealed their wavelength characteristics later in 1912 [68]. X-rays are defined as electromagnetic radiation with a wavelength between 0.01 nm and 10 nm, and they are usually produced by electronic processes. This radiation can be diffracted by electrons around the atom nuclei in crystals, if the wavelength of the incident light is comparable to the interatomic distances between the atoms within the crystal, which are approximately 100 pm (1 Å).

The first diffraction photograph was taken by FRIEDRICH and KNIPPING. WILLIAM L. BRAGG subsequently solved the first crystal structure of NaCl in 1913 [69], after his son LAWRENCE BRAGG discovered the equation now known as BRAGG'S law (Eqn. 2.1 and Fig. 2.1) [70]. He identified the diffraction spots as reflections of the X-ray beam from the parallel planes in the crystal. Each plane is characterised by MILLER indices (*hkl*) [71] and planes are separated by the distance *d*. In order for constructive interference, which is necessary for a diffraction peak, the path

difference (o + p) must equal an integral value of the wavelength λ.

$$n \cdot \lambda = 2d \sin\theta \tag{2.1}$$

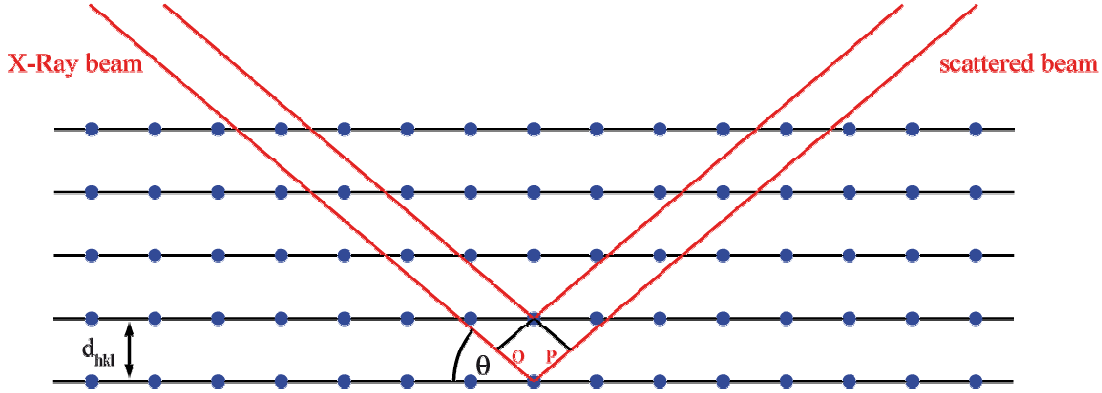

Figure 2.1: BRAGG reflections from a set of planes with spacing d_{hkl}.

This equation allows simple conceptualisation, but it is important to note two significant deficiencies: firstly reflection from a plane is an incorrect concept, as the X-rays are diffracted by the electrons around the nuclei; and secondly the equation cannot provide any information about the intensity of the reflected beam.

2.1.2. Atomic Scattering Factors

The interactions between X-rays and electrons are not isotropic, which is shown by the atomic scattering factor *f*. It differs depending on the element and the scattering angle. The magnitude of the scattering is dependant on the angle of incidence of the incident beam, it is largest at $\theta = 0°$ as all the electrons are in phase. The scattering factor value is identical to the atomic number for neutral atoms, as the scattering power increases with the number of electrons. The atomic scattering factors of some elements are illustrated in Figure 2.2 [68].

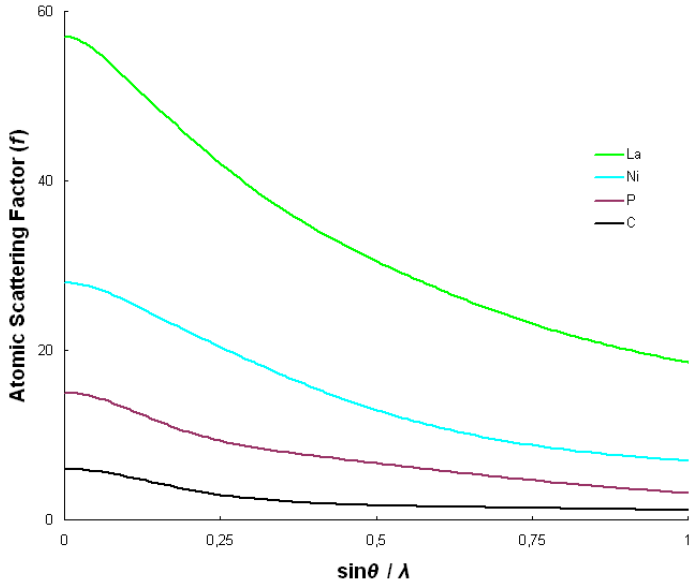

Figure 2.2: Atomic scattering factor.

2.1.3. Unit Cells and BRAVAIS Lattices [72]

The smallest repeating unit in a three dimensional crystal lattice is the unit cell, which when replicated by translation alone shows the full crystal structure. The conventional choice of unit cell is made by choosing a convenient shape, which presents the full symmetry of the lattice. This convention causes the axial lengths to be the shortest possible ones and the interaxial angles to be as near as possible to 90°. The unit cell parameters are the three vector lengths of the unit cell (*a*, *b, c)* and the angles (α, β, γ) as shown in Figure 2.3.

The unit cell can often be broken down into an even smaller unit known as the "asymmetric unit" from which the entire structure can be obtained by the application of symmetry operations, such as an inversion centre or a rotation axis. The unit cell contains at least one asymmetric unit.

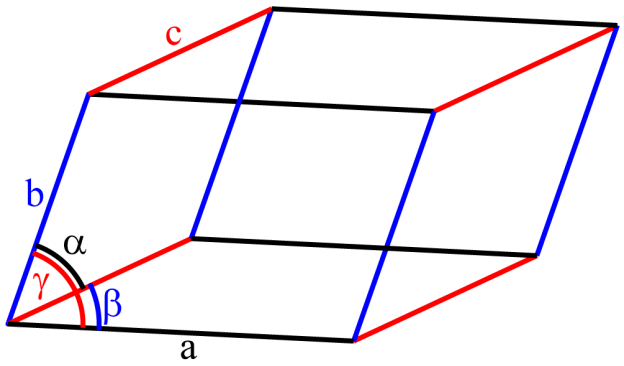

Figure 2.3: The unit cell.

There are four different basic lattice types possible: primitive (*P*), body centred (*I*), all face centred (*F*) and centred (*C*) (Fig. 2.4).

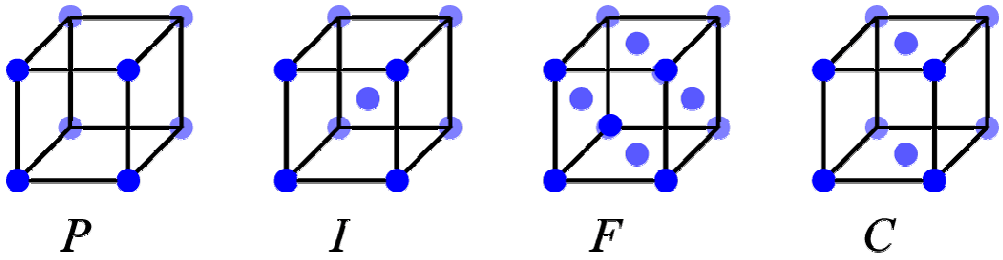

Figure 2.4: The four basic lattice types.

The different unit cell shapes are known as the seven crystal systems (triclinic, monoclinic, orthorhombic, tetragonal, hexagonal, trigonal and cubic). The crystal type depends on the side lengths and the angles, with the minimum symmetry for triclinic ($a \neq b \neq c$; $\alpha \neq \beta \neq \gamma \neq 90°$) and with the highest symmetry for cubic. The combination of the seven crystal systems and the four basic lattice types gives rise to 14 different crystal lattices in 3-dimensional space, these are the BRAVAIS lattices. All the possible 14 BRAVAIS lattices are defined in Table 2.1.

Table 2.1: BRAVAIS lattice

Crystal system	Axes	Angles	Lattice types
Triclinic	$a \neq b \neq c$	$\alpha \neq \beta \neq \gamma \neq 90°$	*P*
Monoclinic	$a \neq b \neq c$	$\alpha = \gamma = 90°, \beta \neq 90°$	*P, C*
Orthorhombic	$a \neq b \neq c$	$\alpha = \beta = \gamma = 90°$	*P, C, I, F*
Tetragonal	$a = b \neq c$	$\alpha = \beta = \gamma = 90°$	*P, I*
Hexagonal	$a = b \neq c$	$a = \beta = 90°, \gamma = 120°$	*P*
Trigonal (Rhombohedral)	$a = b = c$	$\alpha = \beta = \gamma \neq 90°$	*P*
Cubic	$a = b = c$	$\alpha = \beta = \gamma = 90°$	*P, I, F*

2.1.4. Space Groups [73]

As distinct from molecular symmetry, only six types of symmetry operators (Fig. 2.5) are possible within crystals; these operators are divided into non-translational (rotations, inversions, reflections and rotary inversions) and translational symmetry elements (screw axes and glide planes). The latter ones cause systematic absences in the diffraction pattern, as does lattice centring (see Chapter 2.1.5.).

A rotation means that all properties of the space remain the same after a rotation of $2\pi/n$ about an axis has occurred. A rotation is possible with n equals 1, 2, 3, 4 or 6, whereby $n = 1$ is trivial with a rotation around $2\pi = 360°$ which always implies that the crystal stays the same. Values for n of 2, 3, 4 and 6 result in rotations of 180°, 120°, 90° and 60° respectively. All rotations are defined to occur anticlockwise. An inversion proceeds around the centre point and a reflection produces a mirror image. Space groups which do not have an inversion centre are non-centrosymmetric and because of that chiral molecules (not as a racemate) can only adopt these space groups, but not every molecule in a non-centrosymmetric space group has to be chiral. Nonetheless most structures are in centrosymmetric space groups. A rotary inversion is the combination of a rotation and a following inversion on the end point of the rotation. A rotation is combined with a translation along the rotational axis in a screw operation. The notation for a screw operator is n_i, whereby i/n is the translation distance. For example a 3_1 screw axis is a rotation of 120° followed by a translation

of 1/3 of the total unit cell. In a glide plane a reflection is combined with the translation.

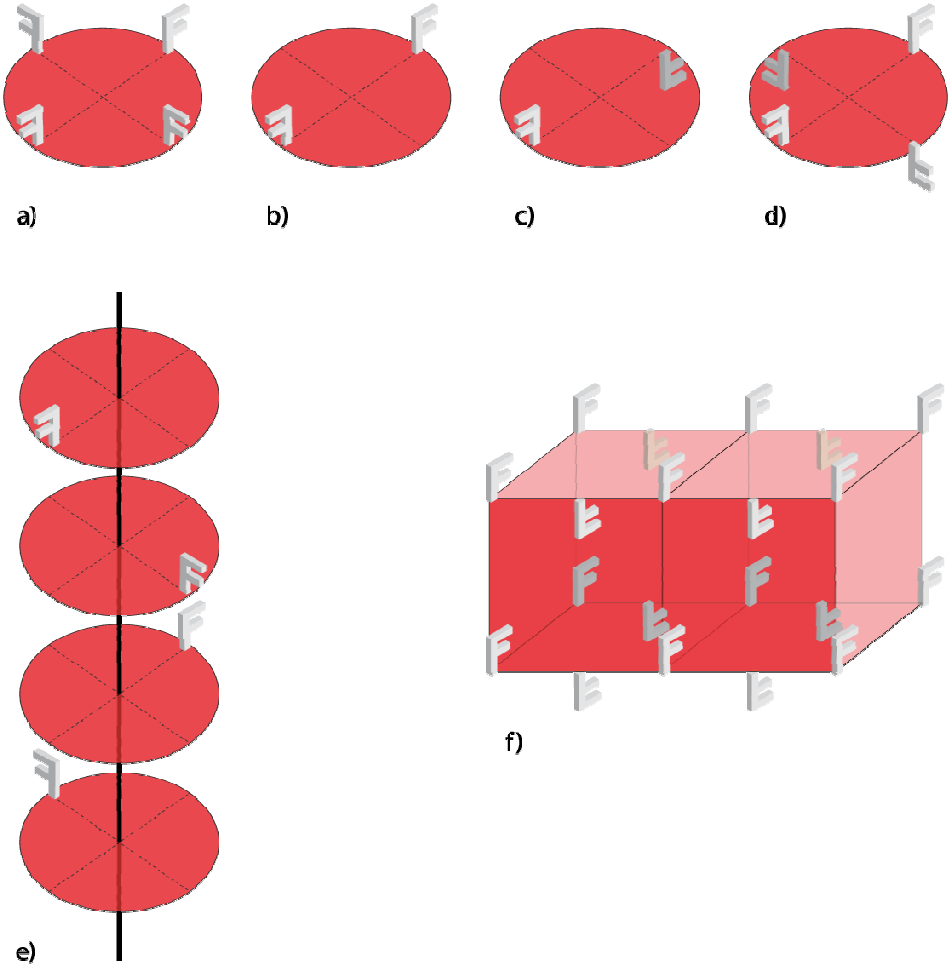

Figure 2.5: Six symmetry elements possible within crystals a) rotation b) reflection c) inversion d) rotary inversion e) screw axis f) glide plane. **F** equals an asymmetric object.

The combination of the symmetry elements and the BRAVAIS lattices generate 230 different crystallographic space groups. Space group diagrams, as in the International Tables for Crystallography, Vol. A [74], describe the location of symmetry elements in the unit cell.

2.1.5. Absences and Intensity Distribution [75]

The interference of the scattered waves results in different intensities for each reflection, whereby any reflection may have zero intensity, but for a reflection to have a theoretically zero intensity it must be systematically absent. This follows as a result of lattice centring and / or translational symmetry elements. The former ones affect the whole dataset and are called general absences (Tab. 2.2), while the latter ones only affect subsets of the reflections (Tab. 2.3).

Table 2.2: General absences

Lattice type		Affected reflection	Reflection occurs
Primitive lattice	*P*	*hkl*	-
Body-centred lattice	*I*	*hkl*	$h + k + l$ = even
Centred lattice	*A*	*hkl*	$k + l$ = even
	B	*hkl*	$h + l$ = even
	C	*hkl*	$h + k$ = even
Face-centred lattice	*F*	*hkl*	$k + l$ = even, $h + l$ = even, $h + k$ = even

Table 2.3: Systematic absences

Symmetry element		Affected reflection	Reflection occurs
2_1, 4_2, 6_3 along	*a*	*h00*	h = even
3_1, 3_2, 6_2, 6_4 along	*c*	*00l*	l = 3 n
4_1, 4_3 along	*a*	*h00*	$h = 4\ n$
6_1, 6_5 along	*c*	*00l*	l = 6 n
a glide perpendicular to	*b*	*h0l*	h = even
c glide perpendicular to	*b*	*h0l*	l = even
n glide perpendicular to	*b*	*h0l*	$h+ l$ = even
d glide perpendicular to	*b*	*h0l*	$h+ l$ = 4 n

Similar relationships for glides perpendicular to *a* or *c* instead of *b* (described in Tab. 2.3) occur as well.

Systematic absences can be used to determine the space group of a crystal. However, an unique identification is not always possible; particular for higher symmetry BRAVAIS lattices, such as tetragonal or cubic. In these circumstances,

statistical tests can help to distinguish between centro and non-centrosymmetric space groups; as even non-translational symmetry elements affect the intensity distribution to a certain extent. Only the inversion centre is routinely used for these statistical tests as the whole dataset is affected. If no crystallographic inversion is present, the data are acentric with no variation of their mean value. In a centrosymmetric structure an inversion centre is present and the normalised intensities demonstrate more variation (Fig. 2.6).

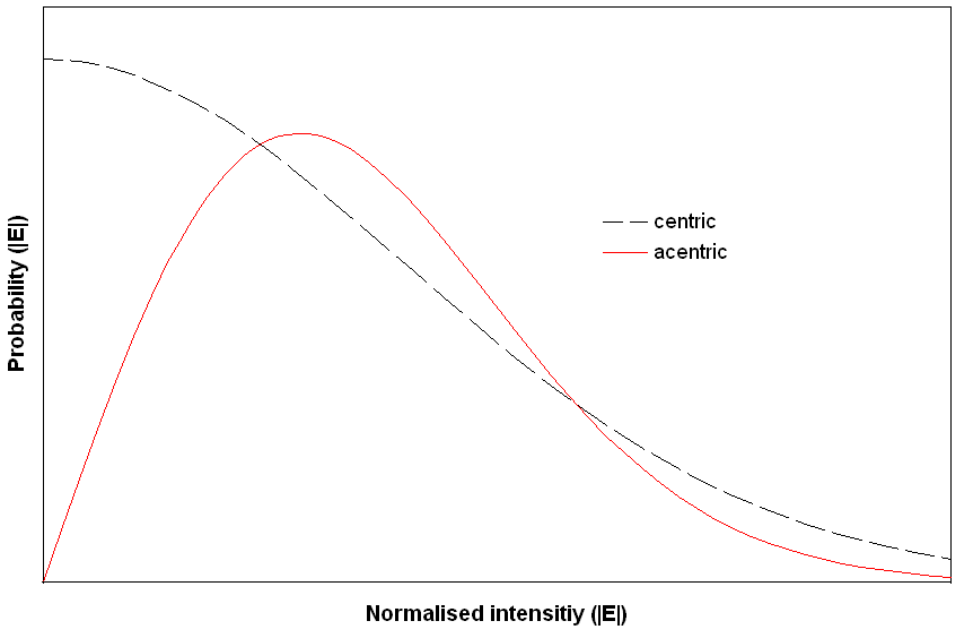

Figure 2.6: Distribution of intensities for model acentric and centric data.

2.2. Single Crystal X-ray Diffraction Experiments

The first step, after growing crystals, is to choose a single crystal. This crystal is then mounted on a fibre, which is put on a goniometer head and the goniometer head is placed on a diffractometer. The crystal is then centred relative to the X-ray beam. The cell constants and the BRAVAIS lattice will then be determined by indexing the first few frames (10-20). The measuring range is chosen and the data set collected.

The processing of the data includes background subtraction, integration and scaling of the frames (Lorentz polarisation and absorption corrections [76]).

The first step of the structure determination is to examine the space group. This is achieved by an analysis of geometric parameters and systematically absent reflections. The next step is the structure solution, typically by PATTERSON or direct methods.

2.2.1. Structure Solution [77]

Each reflection in the diffraction pattern can be described by a structure factor F_{hkl}, which relates to the atomic coordinates of the structure by the following equation:

$$F_{hkl} = \sum_{j=1}^{N} f_j exp\left[2\pi i\left(hx_j + ky_j + lz_j\right)\right] \tag{2.2}$$

Here f_j is the atomic scattering factor for one specific atom j, this atom has the fractional coordinates $x_j y_j z_j$ and the indices for a particular refection are hkl.

During the X-ray experiment, the intensity I of the diffracted beam from each set of MILLER planes is measured; this value is proportional to the square of the structure factor (Eqn. 2.3).

$$I_{hkl} \propto (F_{hkl})^2 \tag{2.3}$$

The absolute value can be determined, but not the phase ε. To produce an electron density [ρ(xyz)] map, both intensity and phase must be known. This is the crystallographic phase problem. The relationship between the electron density at a point xyz and the structure factor is given by:

$$\rho(xyz) = \frac{1}{V}\sum_{hkl}|F_{hkl}|\exp[2\pi i(hx + ky + lz) - \varepsilon] \qquad (2.4)$$

Crystal structures are solved by the use of trial phases for the structure factors. There are two main methods: The PATTERSON method and direct methods.

The PATTERSON method was developed by A. L. PATTERSON (1934)[78] and relies on the presence of at least one heavy atom within the structure. For this reason, it is also called the heavy-atom method. A map is computed on F^2 which eliminates the phase and results in a vector map showing all the interatomic distances in the structure. Since the peak sizes are proportional to the atomic number, those relating the heavy atoms dominate the map. It is then possible to obtain the heavy atom coordinates by analysing the relationships between the highest peaks in the map.

Direct methods[79] may be used when no heavy atoms are present or all atoms have similar scattering power. Direct method routines are used to calculate the mathematical probabilities for the phase values from relationships between some intense reflections in the data set. This is possible as the intensities are not wholly independent of one another and are linked through the electron density of the structure. Constraints may be applied to ensure the electron density is chemically reasonable, which results in constraints on the structure factors. As the amplitudes of the structure factors are known from the experimental results the constraints can be used to restrict the possible values for the phases and hence allow solution of the structure.

1. The electron density map must always be positive.
2. The discrete atomic nature, following from that the atomic shape is removed and the produced normalised structure factors *E* are used.
3. The atoms are distributed randomly throughout the unit cell.
4. The atoms have approximately equal scattering power.

2.2.2. Refinement

Structure models obtained from the structure solution are often incomplete; to complete them a FOURIER recycling and a refinement is performed. During this process the phasing is improved and all parameters are adjusted to get the best fit to the model. It is usually carried out by least squares analysis of $F(\text{obs})_{hkl}$ versus $F(\text{calc})_{hkl}$ or $F^2(\text{obs})_{hkl}$ versus $F^2(\text{calc})_{hkl}$. After all non-hydrogen atoms are found, the H-atoms can be put in idealised positions, where they are allowed to ride on the heavier atom to which they are bound or they can be located in the electron density map. Due to their low scattering power, hydrogen atoms are often difficult to locate, particularly in heavy-atom structures, and in these cases idealised hydrogen placement is usually necessary. At the end of the refinement the degree to which the final model fits the data is normally assessed using an *R*-factor (R_1), as described in Equation 2.5 and a weighted *R*-factor *wR*, as described in Equation 2.6. For small molecule structures the *R*-factor is typically in the range of 2 - 7 %, whereby a smaller value indicates a better structure solution. It is necessary that the refinement converges at the end, meaning a stable positioning of all atoms within the structure [74].

$$R_1 = \frac{\sum || F_{obs} | - | F_{calc} ||}{\sum | F_{obs} |} \tag{2.5}$$

$$wR = \left(\frac{\sum w(|F_{obs}| - |F_{calc}|)^2}{\sum \left(w|F_{obs}|\right)^2} \right)^{1/2} \tag{2.6}$$

F_{obs} equals the observed and F_{calc} the calculated structure factors *F* respectively.

The last step is to check the structure and to validate the model, according to chemical sense. Crystallographic results are commonly saved in the form of a cif file.

2.2.3. Single Crystal Setup

Figure 2.7 illustrates a standard set-up for a single crystal experiment. X-rays are generated by firing electrons onto a metal target (anode). The produced radiation is called Bremsstrahlung, as the electrons get deaccelerated by the metal. For the determination of metal-organic compounds, a molybdenum anode is usually used ($\lambda = 0.71073$ Å), and for light atom structures a copper anode may be used ($\lambda = 1.54184$ Å). The X-rays produced have variable wavelength, which are then monochromated and collimated into a parallel beam. The focused beam is centred onto the crystal, which is mounted upon a glass fibre on the goniometer head. The goniometer head is designed to be able to rotate during the data collection enabling the collection of nearly all possible reflections. The crystal can be cooled by nitrogen or helium gas through the cryostream. Data collection at low temperature provides two important advantages: crystal decomposition caused by the X-ray beam or other external effects as well as thermal motion of the atoms within the crystal lattice is reduced, giving higher quality data. The beam, which is not diffracted by the crystal lattice, is blocked with the backstop, whereas the diffracted portion of the beam gets recorded by the detector.

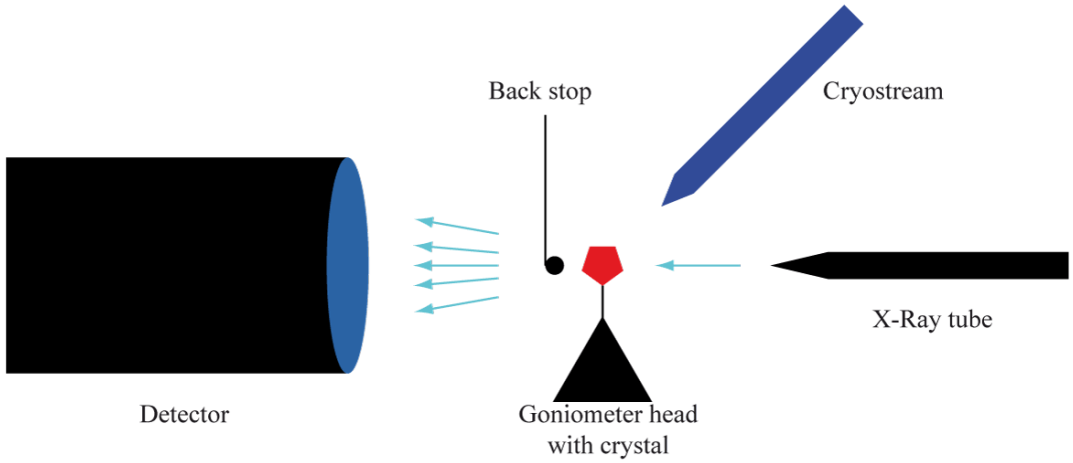

Figure 2.7: Schematic illustration for a single crystal experimental set-up.

2.3. Powder Diffraction[69]

The information which is recorded during a powder or single crystal experiment is the same, although single crystal data is the preferred experiment to obtain accurate structure data. This is due to the fact that data in powder experiments is condensed into one dimension, which is a convolution of the data for all three dimensions, whereas a single crystal is measured in three dimensions. The powder sample contains multiple crystals in random orientation, which result in peak overlap.

X-ray powder diffraction is a powerful tool for obtaining information about the composition of a bulk material. In addition to identification of materials, it can be used for both qualitative and quantitative sample analysis. It is possible to have a quick structure check, to verify the purity of the sample or to establish which polymorph it contains. However, amorphous products or impurities of less than 5 % cannot be detected readily. It is also a rapid technique for the analysis of unit cell parameters as a function of temperature and / or pressure.

A crushed crystalline powder typically contains a large number of randomly oriented microcrystallites. Each of the crystallites gives its own diffraction pattern and thus instead of obtaining discrete diffraction spots the diffraction is spread out into rings (Fig. 2.8).

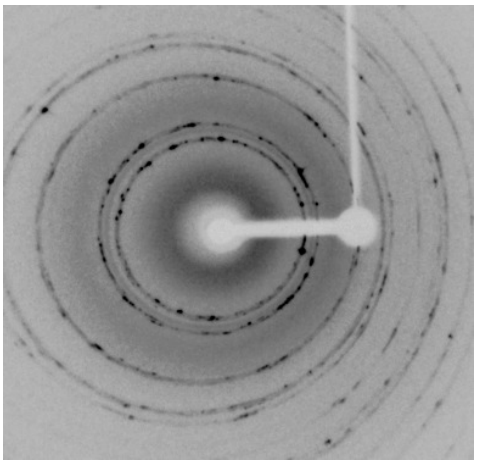

Figure 2.8: X-ray powder diffraction pattern for LiCl semi-crystals.

The data are normally presented in a plot of intensity against diffraction angle 2θ. The 2D pattern of a single crystal experiment is reduced to a 1D one (Fig. 2.9).

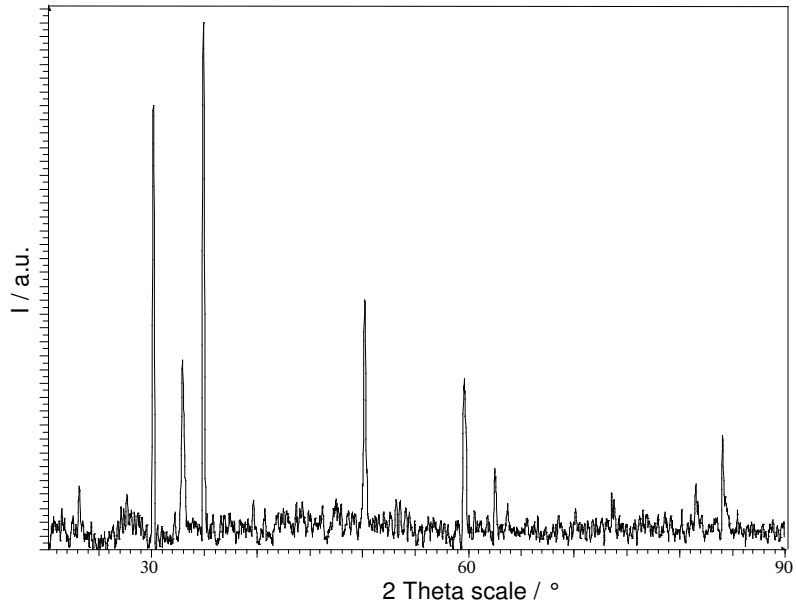

Figure 2.9: Powder diffraction pattern of LiCl.

The difficulty in powder diffraction is the indexation. This means that the correct *hkl* index for each reflection has to be found. This is possible for simple compounds in high symmetry cells, although it is extremely difficult for more complex structures. This is because of additional lines and the overlap of reflections. Developments of new methods (RIETVELD methods and others) make it possible to solve and refine structures from powder diffraction data. Most X-ray powder diffraction experiments are carried out using copper radiation, which has a longer wavelength than molybdenum (which is usually used for single crystal measurements as mentioned earlier). As a result the diffraction pattern is expanded and the peak overlap is reduced. The intensity is increased as well, as higher voltage can be used for X-ray tubes with Cu targets.

2.4. Synchrotron [80,81, 82]

A synchrotron (Fig. 2.10) is a particle accelerator, which produces very intense radiation with a wide range of wavelengths. This specific accelerator has the form of a ring which allows the electrons to travel in complete circles. The ring is called storage ring and is under high vacuum. To prepare the electrons for the storage ring, charged particles are injected into the linear accelerator from where they get into the booster. In there, their energy is increased, before the accelerated electron beam is injected into the storage ring. The electrons travel around the storage ring at nearly the speed of light. The particles circulate with the help of a magnetic field, which accelerates charged particles inwards. As a consequence of the constant change in direction, the electrons lose energy in form of electromagnetic radiation (so-called Bremsstrahlung) at each magnet. At relativistic velocities these photons are emitted in a narrow cone in the forward direction, where they are captured by station beamlines. The loss of energy has to be replenished by delivering electromagnetic radiation in the straight sections between the bending magnets, as the beam of orbiting electrons would otherwise collapse. The limiting beam energy is reached when the energy lost to the lateral acceleration is equal to the energy added at each cycle maintaining the beam in a circular path.

The generated radiation ranges from IR to hard X-rays, the latter are needed for diffraction experiments. Additional magnetic components (wigglers) are used to extend the energy range and increase the intensity. Wigglers deflect the beam through a straight section of the storage ring; send it around a curve before returning it back to the original path. The extra emission has a shorter wavelength and is used for diffraction experiments. Synchrotron radiation is highly polarised in the plane of the storage ring, which means that the diffractometer is positioned vertically (instead of horizontally as in a laboratory one). Due to the nature of the rotating electron beam, the X-rays do not form a continuous wave as they leave the synchrotron; instead the X-rays are emitted in a pulsed beam with a frequency given by the setup of the synchrotron. This is important for some photocrystallographic experiments which

were discussed previously.

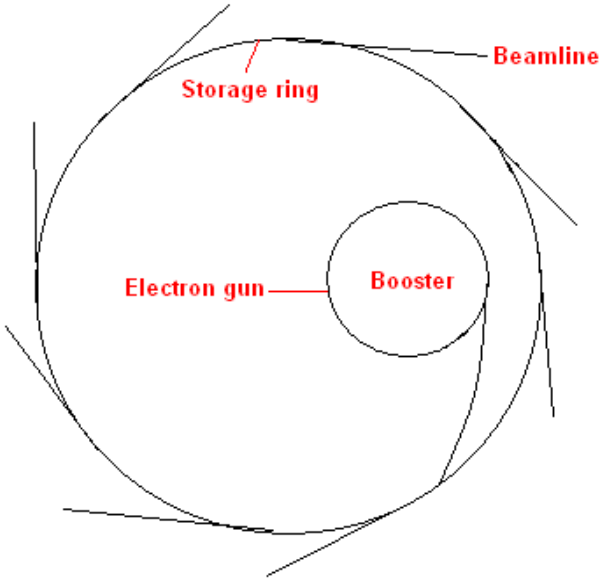

Figure 2.10: Synchrotron.

First generation synchrotron sources were high energy physics accelerators, where the synchrotron radiation was a by-product. ROENTGEN diffractometers were built next to the synchrotrons in a parasitic manner. Second generation synchrotrons were constructed specifically to provide synchrotron X-rays for research. Today's third generation synchrotrons provide higher brightness X-ray beams (about 10,000 times higher as was produced by earlier dedicated synchrotrons) [83].

3. [2+2]-Cycloaddition Reactions

3.1. Introduction

As described in Chapter 1, the group of MACGILLIVRAY used templates or silver to orientate (pyridyl)ethylene derivates for [2+2] cycloaddition reactions [13, 17]. The correct orientation of the atoms is achieved through the template, π-π-stacking or the silver-silver interactions. In order to develop the research area and produce a wider range of systems capable of undergoing solid state [2+2] cycloaddition reactions, the same type of ligands were used, but they were aligned in metal complexes with the help of the thiocyanate steering agent. Other experiments were performed in attempt to crystallise complexes with other halides. For these experiments, a series of metal-complexes were crystallised by alcohol / water layer-separation diffusion at room temperature. This method was used as it facilitates the slow growth of suitable single crystals [84].

3.2. Ligands

The five ligands in Figure 3.1 were synthesised and tested for their propensity to form crystalline complexes:

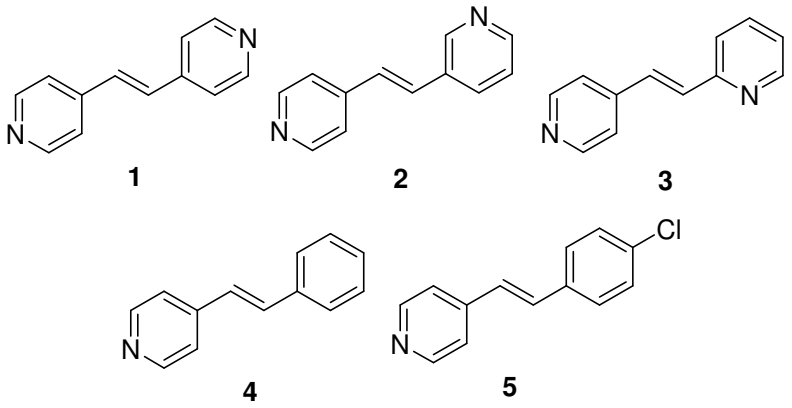

Figure 3.1: Tested ligands.

These ligands were used, as they all have at least one nitrogen atom in 4-position, which can act as a donor atom for the formation of a metal complex. The reactivity to form the appropriate complexes $[M^{II}(NCS)_2(L)_2(sol)_2]$ with some of these ligands (L = **1**, **3**, **4**) is well known from literature [11, 85, 86].

3.3. $[M^{II}(hal)_2(L)_2(H_2O)_2]$ - complexes

Attempts were made to crystallise cobalt, manganese and iron salts with thiocyanate and the ligands **1**, **2**, **3**, **4** and **5**. Additionally, the different halides (Cl^-, Br^-, I^-) were used in combination with **1** or **3**. Despite numerous attempts only seven complexes of the form $[M^{II}(hal)_2(L)_2(H_2O)_2]$ (shown in Table 3.1), could be crystallised and characterised by X-ray crystallography.

Table 3.1: $[M^{II}(hal)_2(L)_2(H_2O)_2]$ complexes

Name	Metal	Anion	Ligand
1a	Co	NCS	**1**
1b	Mn	NCS	**1**
1c	Fe[87]	NCS	**1**
3a	Co	NCS	**3**
3b	Mn[85]	NCS	**3**
3c	Fe[11]	NCS	**3**
3d	Mn	Br	**3**

3.3.1. Structures

The complexes with the molecular formula of $[M^{II}(hal)_2(L)_2(H_2O)_2]$ are not isostructural, but they all show a similar packing motif. This motif involves π-π-stacking (3.4 - 4.2 Å) between the pyridyl rings and aligns the double bonds in a way that dimerisation is achievable.

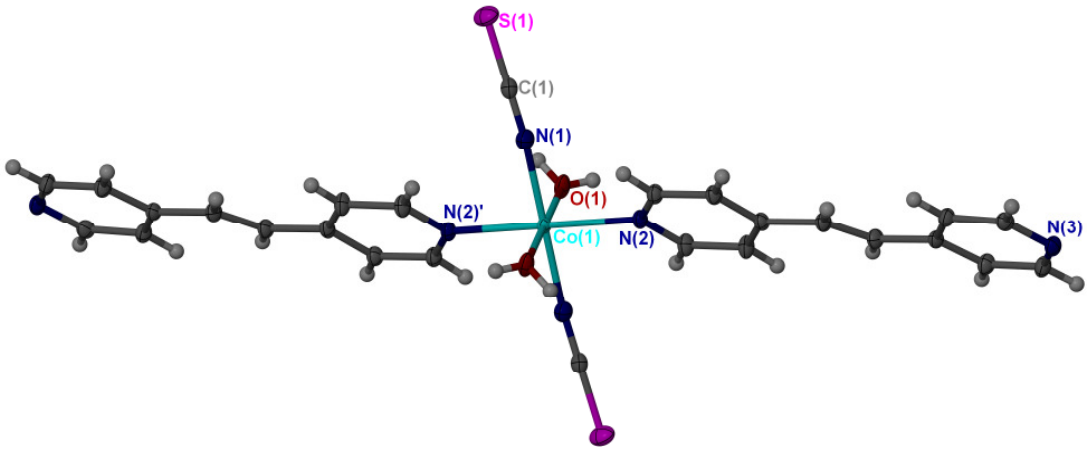

Figure 3.2: Structure of **1a** with 50 % ellipsoids shown.

Figure 3.2 shows the structure of **1a**, with the cobalt ion sitting in a distorted octahedral environment with the pairs of similar ligands being *trans* to each other. The complex crystallises in the space group *P*-1 with half the molecule in the asymmetric unit and therefore the cobalt is sitting on a centre of symmetry. N2 is related to N2' by the symmetry operation *-x, -y, -z+1*. The two pyridine rings of the ligand are coplanar and the thiocyanate ligands are coordinated to the metal in a bent orientation with a Co-C-N angle of 162.5(1) °. The crystal packing involves hydrogen bonds between the coordinated water and non-coordinated nitrogen and sulphur atoms. All four hydrogen bonds are to different ligands, as the molecules are forming a stacking motif, shown in Figure 3.3. One other feature is the π-π-stacking between the pyridyl rings, displayed through the midpoints of the double bonds, which is 3.67 Å.

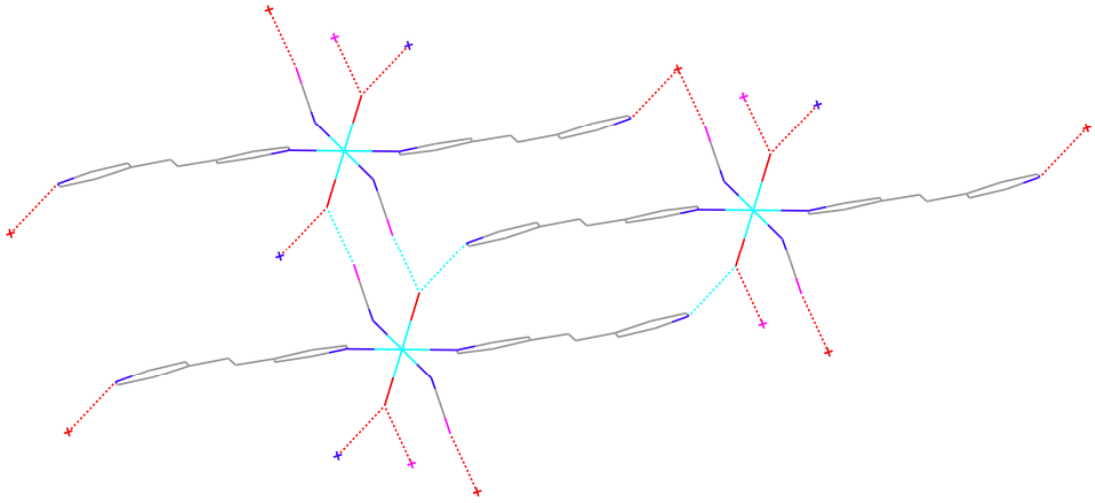

Figure 3.3: Hydrogen bonding in the complex of **1a**.

The cobalt structure of **1a** is isostructural with the iron structure **1c**, as the unit cell and the 3D motif of the structure are very similar (Tab. 3.4). Despite the fact that the structure of the iron complex was reported in *P*1 (FESVEF[87]), the comparison of the single crystal data of the cobalt and the iron structures gives a nice overlay, with a RMS of 0.076 Å for an overlay of all the atoms (Fig. 3.4). Following from this, the iron structure was redetermined; the result was the expected structure in *P*-1. The midpoint distance between the double bonds is very similar with 3.83 Å in both structures.

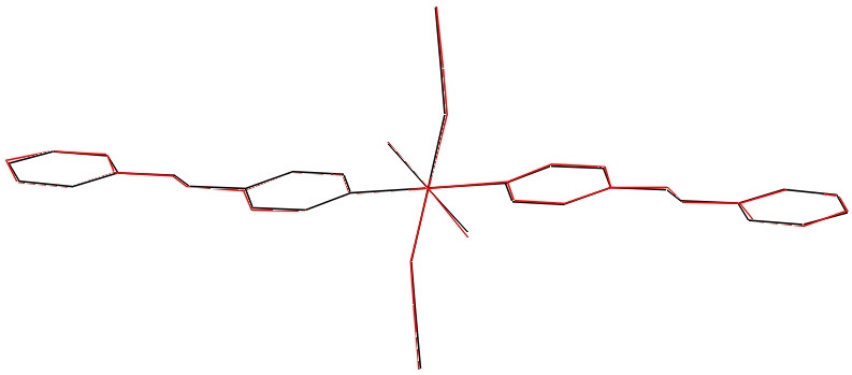

Figure 3.4: Overlay of the cobalt (black) and iron (red) complex.

The structure of **1b** is again isostructural to the other two structures with ligand **1** and therefore a [2+2] cycloaddition reaction should also be possible. The midpoint

distance between the double bonds is 3.67 Å. The hydrogen bonding parameters for the three complexes are shown in Table 3.2.

Table 3.2: Hydrogen bonds within the $[M(NCS)_2(\mathbf{1})_2(H_2O)_2]$ complexes

Compound	DHA	DH / Å	HA / Å	DA / Å	Angle / °
1a	O1-H1A-N3	0.76(3)	1.98(3)	2.7150(15)	163(3)
	O1-H1B-S1	0.75(3)	2.41(2)	3.2743(11)	169(2)
1b	O1-H1A-N3	0.79(2)	1.93(2)	2.7007(16)	163(2)
	O1-H1B-S1	0.72(2)	2.57(2)	3.2728(14)	170(2)
1c	O1-H1A-N3	0.81(3)	1.93(3)	2.7194(14)	165(2)
	O1-H1B-S1	0.76(2)	2.55(2)	3.2864(11)	165(2)

The structure of **3b** has a whole molecule in the asymmetric unit (Fig. 3.5) in contrast to those of ligand **1**. While this work was in progress, the structure was reported by HILL and BRICEÑO [85]. Again the crystal belongs to the space group *P*-1. Similar to the other structures the pairs of similar ligands are *trans* to each other and the pyridine rings are coplanar, and one of the ethylene bridges is disordered (65:35). The distance between the two ethylene bridges is 3.90 Å, which makes a [2+2] cycloaddition reaction possible and means that π-π-stacking exists as the ligands are parallel to each other. As noted above, the structure has been reported and the authors have shown the dimerisation possibility as well [85]. A second packing force might be the hydrogen bond between sulphur and coordinated water (Fig. 3.6). **3c** crystallises isostructurally to the manganese complex with a midpoint distance between the double bonds of 3.85 Å.

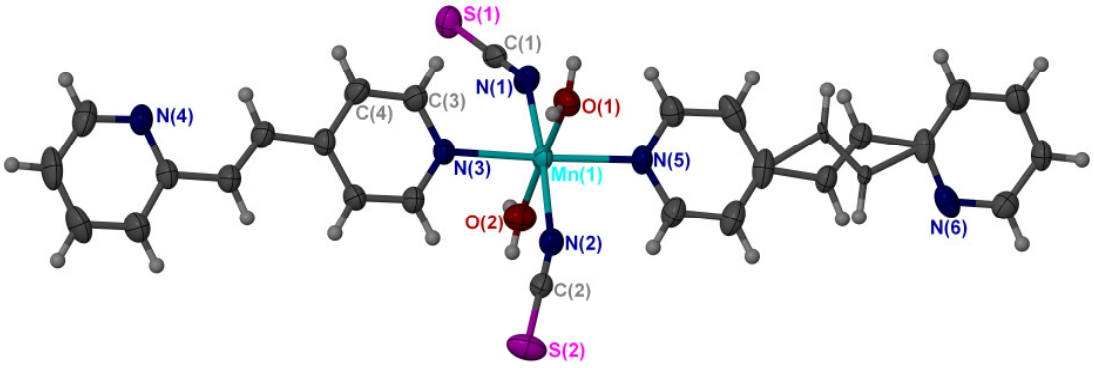

Figure 3.5: **3b** with 50 % ellipsoids shown.

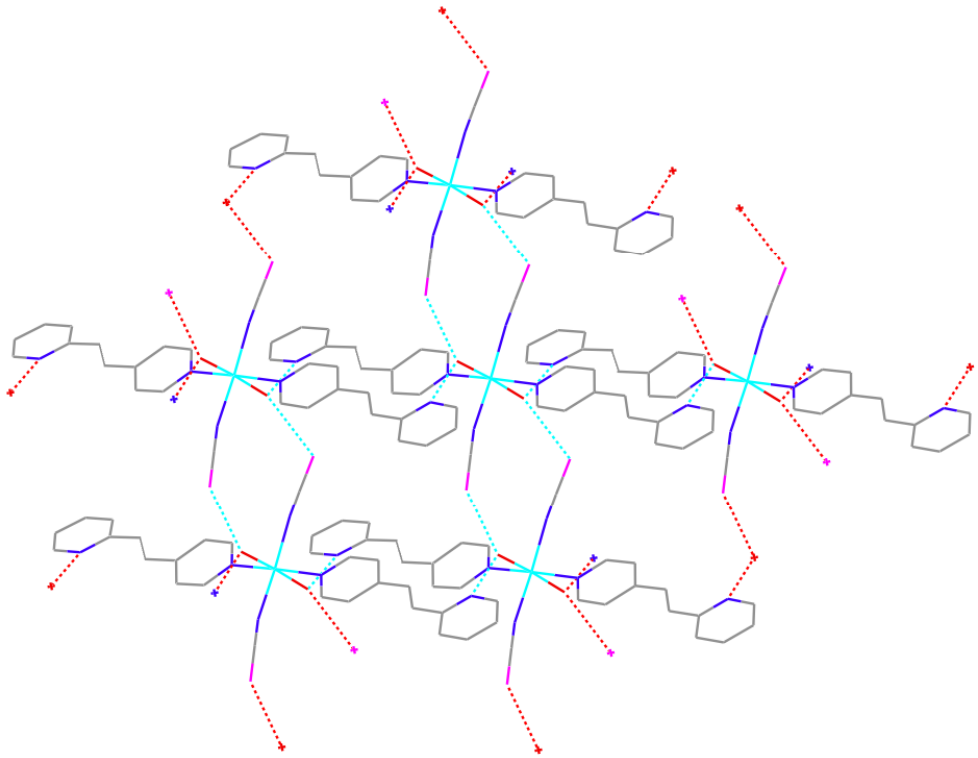

Figure 3.6: Hydrogen bonding in the complex **3b** with hydrogens and disorder removed for clarity.

The structure of **3a** is shown in Figure 3.7, the molecule again crystallises in the triclinic space group *P*-1. N2 is related by N2' through the symmetry operation *-x+1, -y, -z*. Just as in the other complexes all the pairs of ligands are *trans* to each other and the pyridine rings are coplanar. A [2+2] cycloaddition reaction is again possible, as the two pyridine rings are separated by 3.97 Å. Significant packing forces

within the structure include π-π-stacking between the rings and hydrogen bonding from the coordinated water to sulphur and nitrogen (N3) (Fig. 3.8). This results in a 3D network, which is a shifted version of the **1a** complex along the axis through the molecule.

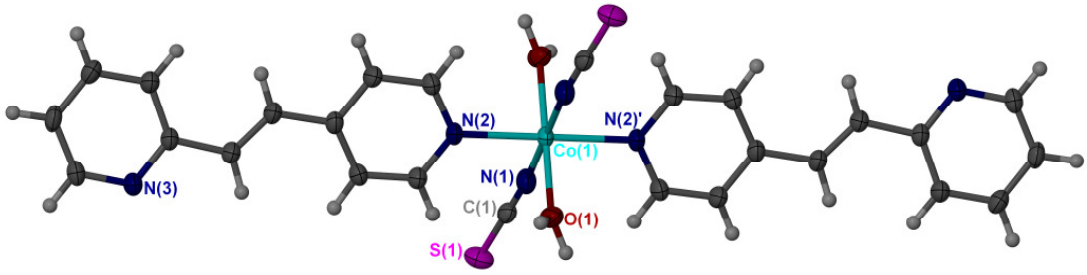

Figure 3.7: **3a** with 50 % ellipsoids shown.

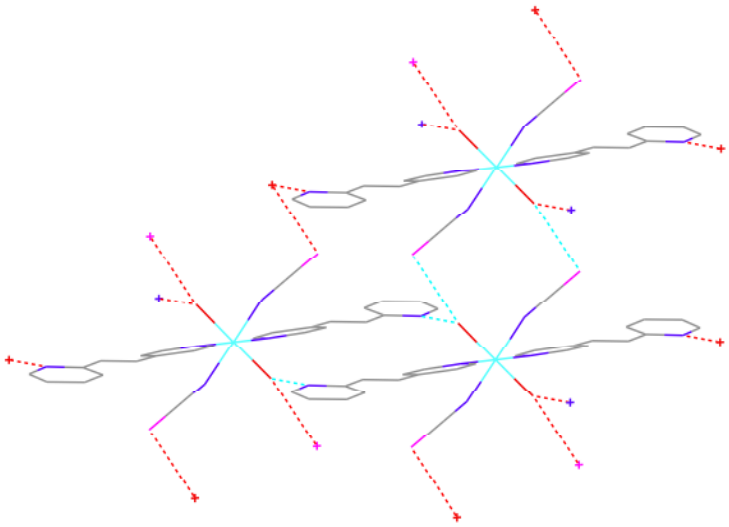

Figure 3.8: Packing of **3a** with hydrogens removed for clarity.

Changing from ligand **1** to **3** does not change the structure of the individual $[M(NCS)_2(L)_2(H_2O)_2]$ units, but does result in a change in crystal packing and unit cell. The difference between the three structural motifs is easily shown in Figure 3.3, 3.5 and 3.8; in the structures with **1** the hydrogen bonds form a 3D network, as well as for the complex **3a**, whereas a 2D chain occurs in the structures of **3b** and **3c**. The π-π-stacking on the other hand is very similar in all structures.

The last crystal structure in this series is slightly different as the coordinating anion is bromide rather than thiocyanate. Of the bromide species, only the manganese complex with **3** gave crystals of the desired quality $[M(hal)_2(L)_2(H_2O)_2]$ suitable for diffraction studies. Figure 3.9 shows the structure of **3d**, which crystallises in *P*-1 with half a molecule in the asymmetric unit. All the pairs of ligands are again *trans* to each other and the two disordered pyridylethylene ligands (70:30) are coplanar with an intermolecular distance of 3.69 Å. N1 is related to N1' by the symmetry operation *-x+1, -y, -z+1*. In addition to π-π-stacking, one hydrogen bond between nitrogen (N2) and coordinated water forms the 2D structure (Fig. 3.10). All the hydrogen bonding details are displayed in Table 3.3.

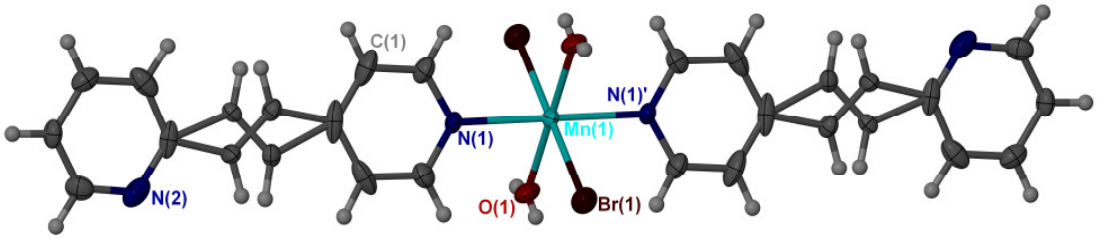

Figure 3.9: Structure of **3d** with 50 % ellipsoids shown.

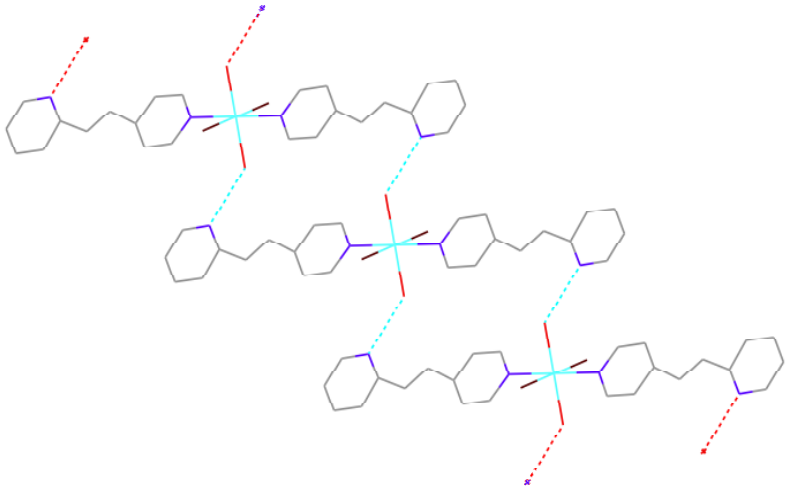

Figure 3.10: 3D structure of **3d** with hydrogen atoms removed for clarity.

Table 3.3: Hydrogen bonds within the $[M(hal)_2(\mathbf{3})_2(H_2O)_2]$ complexes

Compound	DHA	DH / Å	HA / Å	DA / Å	Angle / °
3a	O1-H1A-S1	0.88(3)	2.37(3)	3.2128(15)	160(2)
	O1-H1B-N3	0.91(3)	1.88(3)	2.796(2)	177(3)
3b	O1-H1A-S2	0.89(3)	2.33(3)	3.204(2)	172(2)
	O1-H1B-N6	0.82(3)	1.91(3)	2.731(3)	175(3)
	O2-H2A-N4	0.90(3)	1.87(3)	2.762(3)	171(3)
	O2-H2B-S1	0.77(3)	2.49(3)	3.201(2)	153(3)
3c	O1-H1A-N6	0.86(9)	1.96(9)	2.806(15)	170(8)
	O1-H1B-S3	0.74(7)	2.50(7)	3.225(10)	164(7)
	O2-H2A-S4	0.82(7)	2.46(7)	3.259(14)	168(6)
	O2-H2B-N4	0.84(8)	1.97(8)	2.796(14)	167(7)
3d	O1-H1A-N2	0.54(6)	2.32(6)	2.854(8)	173(8)
	O1-H1B-Br1	0.54(6)	2.87(6)	3.398(7)	163(8)

In Table 3.4 unit cell data from all seven complexes are shown, divided into the four different structural motifs. As the structures are measured at different temperatures, a direct comparison of the volumes is not possible.

Table 3.4: Comparison of crystal structures (from top to bottom: compound name, space group, *a, b, c* in Å, *α, β, γ* in °, V in $Å^3$ and T in K)

3a	**1a**	**1b**	**1c**	**3b**	**3c**	**3d**
P-1	*P*-1	*P*-1	*P*-1	*P*-1	*P*-1	*P*-1
7.3810(2)	6.7773(4)	6.7953(4)	6.7995(3)	7.8810(2)	7.7658(3)	6.9030(3)
9.7990(4)	9.8853(5)	9.9406(6)	9.9224(3)	10.2360(3)	10.2633(3)	9.0560(4)
10.2270(3)	10.6298(6)	10.6603(7)	10.6360(5)	17.5590(6)	17.5454(5)	10.2360(4)
91.685(2)	89.393(1)	84.224(1)	89.761(3)	76.404(2)	77.832(3)	73.406(2)
99.040(2)	80.926(1)	81.485(1)	81.277(4)	80.996(2)	82.124(3)	77.005(2)
111.784(2)	70.930(1)	70.452(1)	70.852(4)	79.406(1)	79.198(3)	77.005(3)
675.22(4)	664.01(6)	670.10(7)	669.24(5)	1343.77(7)	1335.83(8)	588.63(4)
150	120	150	100	150	150	150

3.3.2. [2+2] Cycloaddition Reaction

3.3.2.1. Single Crystal Experiment

Once the crystal structures of the seven compounds had been fully determined the crystals were placed under a UV lamp for a short period of time. The irradiated sample was again placed on the diffractometer and a second data set measured. Unfortunately, all the crystals of the complexes described above decomposed under irradiation, preventing a second measurement of the crystal structure after irradiation. Figure 3.11 shows a sample of **3a** before and after irradiation with broadband UV light.

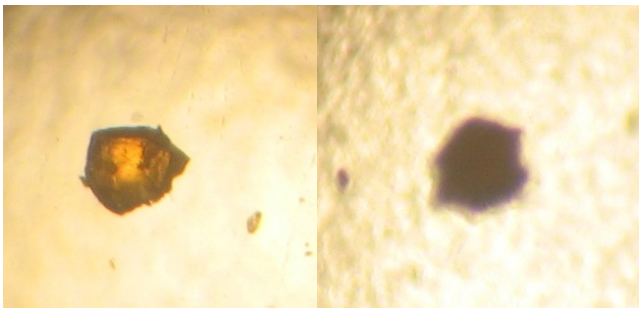

Figure 3.11: Decomposition of the crystal **3a** after irradiation with UV light.

In an attempt to prevent the decomposition, different wavelengths and light sources were tried (Tab. 3.5). Different wavelengths were tested between UV and red light. No reaction occurs upon irradiation with the TLC lamp, the red laser or the UV LEDs, whereas both broadband UV and the 600 nm LEDs decomposed the crystals. The red laser and the 600 nm LEDs were used to try two-photon excitation on this system. Two-photon excitation is known to prevent decomposition[35] in similar systems. The reduced decomposition is due to a slower conversion rate. This rate is lower as the possibility of two photons exciting one molecule at the same time is the square root of the light intensity smaller than a one photon excitation. Therefore the light intensity or the experiment time has to be increased. On the other hand this gives the crystal time to relax between the occurrences of excitation and the reduced strain

decreases the likelihood of the decomposition. The light source was placed at a distance of 1 cm above the single crystal. The red laser did not excite the complexes, whereas the 600 nm LEDs did. Unfortunately the crystal still decomposed, but it took 2.5 days for this instead of a few minutes to hours under UV light.

Table 3.5: Tested wavelengths and irradiation sources and results of irradiation

Red	Yellow	UV	UV	UV	UV	UV	UV
663 nm	600 nm	400 nm	361 nm	351 nm	365 nm	254 nm	broadband
laser	LED	LED	LED	LED	TLC lamp	TLC lamp	lamp
x	decompose	x	x	x	x	x	decompose

3.3.2.2. High Temperature Single Crystal Test

Irradiation at higher temperatures was attempted to test if this would allow a photo-activation reaction to take place in a single crystal transformation. This experiment was performed as the unit cell would increase in volume at higher temperature and therefore more flexibility within the crystal could increase the chance of a reaction occurring through a single crystal to single crystal transformation. After measuring the crystal **3b** at a temperature of 250 K, the temperature was first increased to 373 K, which led to the decomposition of the crystal. The experiment was possible at a temperature of 323 K, which is low enough for the crystal to diffract. Nonetheless, crystal decomposition occurs after exposure to UV light, despite the higher flexibility within the crystal.

3.3.2.3. Powder Experiments

As the single crystal cycloaddition experiments did not work, a parallel series of experiments were run on powder samples. A powder pattern was first calculated from the single crystal structure for these experiments and was compared to the data from the following test. The comparison of the calculated and measured pattern is necessary, as sometimes a crystal structure changes under grinding. For the powder experiment a powder sample was prepared, measured and the background was corrected. After the data collection the sample was irradiated in a capillary with UV light. As the capillary is made from glass, which absorbs a large amount of UV light, the irradiation of the powder inside the capillary was performed for longer than for the pure powder. The irradiated sample was then measured again and the two powder patterns are compared to see if any diffraction peaks are changing. If no change was observed, the sample was irradiated again for a longer time and another diffraction pattern was collected.

The powder pattern of the **3a** is consistent with the calculated powder pattern from the single crystal data. As shown in Figure 3.12 this powder pattern changes after irradiation. A data set was collected over time and is displayed in Figure 3.13. Most peaks lose intensity with time, but two new peaks appear as well (at values of 2-theta of 12° and 15°). The powder lost overall crystallinity, which is in agreement with the observed single crystal decomposition.

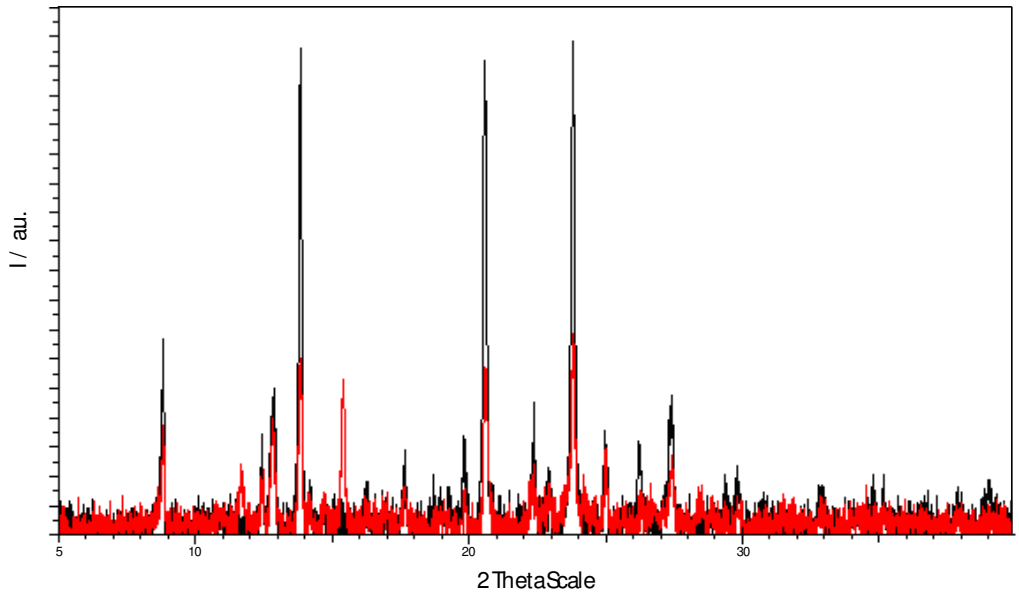

Figure 3.12: Powder pattern of **3a**; before (black) and after (red) irradiation.

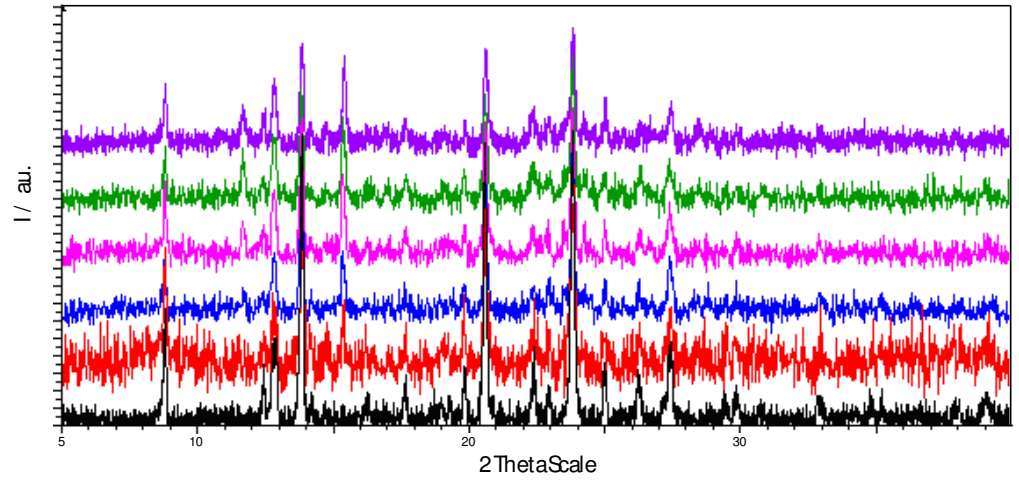

Figure 3.13: Change of powder pattern of **3a** over irradiation time; 0 h in black, 29 h in red, 2 d in blue, 3 d in pink, 4 d in green and 5 d in violet, curves offset for clarity.

The powder pattern of the complex **1a** is consistent with the simulated data from the single crystal. Again loss of crystallinity over irradiation time is observed, which is accompanied by an extreme change of the powder pattern (Fig. 3.14).

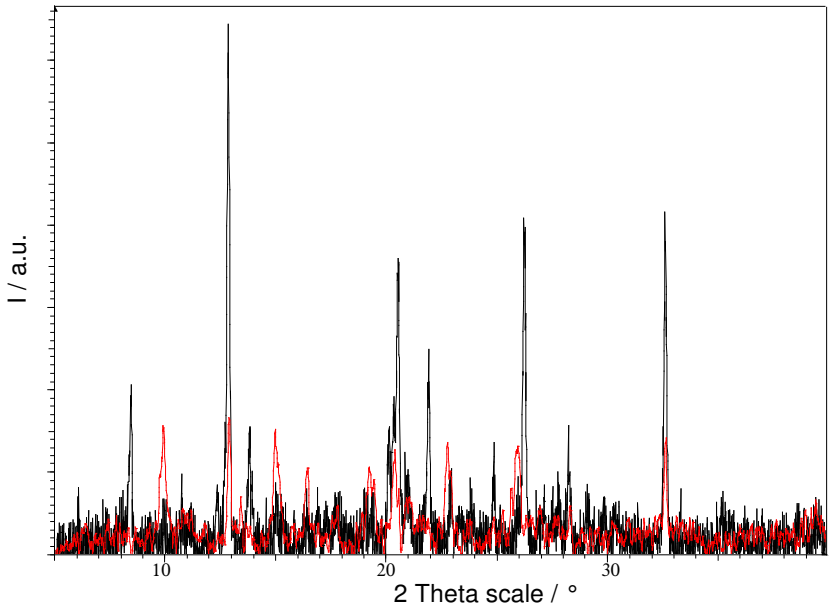

Figure 3.14: Powder pattern of **1a**; before (black) and after (red) irradiation.

The powder pattern of the **3b** is again consistent with the calculated powder pattern. In contrast with the cobalt structures the sample loses less of its crystallinity, and the changes in peak positions are less obvious. Nonetheless two new peaks grow in at the 2-theta values of 15° and 16° and some intensity changes are observed (Fig. 3.15).

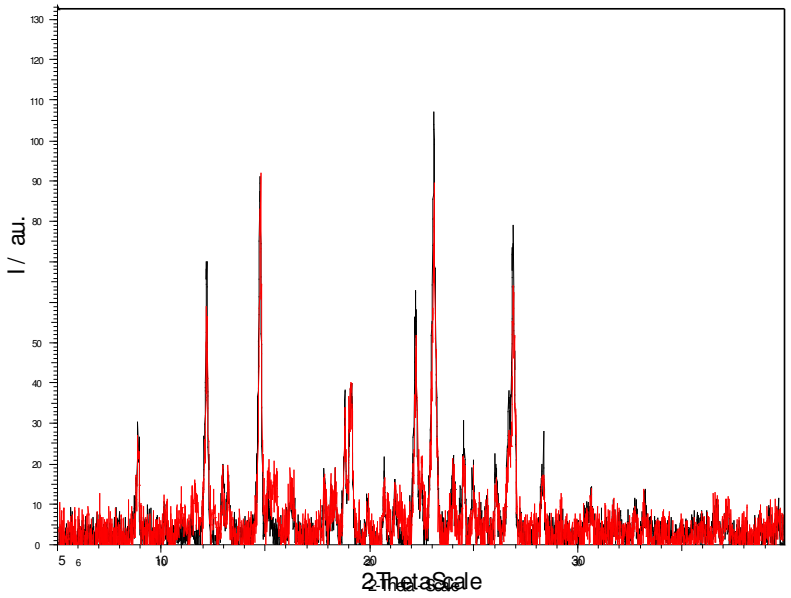

Figure 3.15: Powder pattern of **3b**; before (black) and after (red) irradiation [88].

A loss in crystallinity is also observed for the irradiated powder of **1b**, along with two new peaks, which were found at values of 2-theta of 14° and 15° (Fig. 3.16). The calculated single crystal powder pattern is again consistent with the measured data.

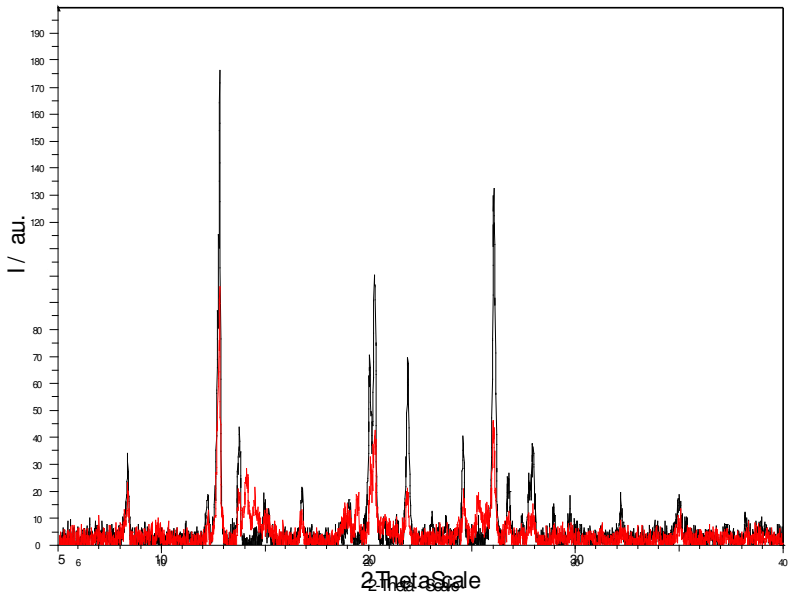

Figure 3.16: Powder pattern of **1b**; before (black) and after (red) irradiation.

In contrast to the cobalt and manganese thiocyanate complexes, no change of the powder pattern was found for the iron complexes. The irradiation time was increased from 7 d to 14 d, but no difference was observed (Fig. 3.17). Given that **1a**, **1b** and **1c** as well as **3b** and **3c** have similar structures, it was surprising that no reaction occurs for the iron structures. Especially as these single crystals decompose in the same way as described for the other complexes. The powder sample was therefore remeasured, but instead of filling a capillary with the powder sample, a glass fibre was used and the powder was placed on the outside. To keep the powder in place the fibre was first dipped into grease. Unfortunately this method decreases the quality of the powder pattern even further, so that the poor quality of the original pattern is accompanied by an increased background.

Nonetheless it is obvious that the sample of **3c** loses crystallinity after irradiation of only one day. A new peak appears with a value of 2-theta of 30°, whereas most other peaks disappear (15°, 20°, 22°, 23°, 27°) (Fig. 3.18). Both powder patterns (in the capillary and on glass) are very similar to the calculated powder pattern of the single crystal.

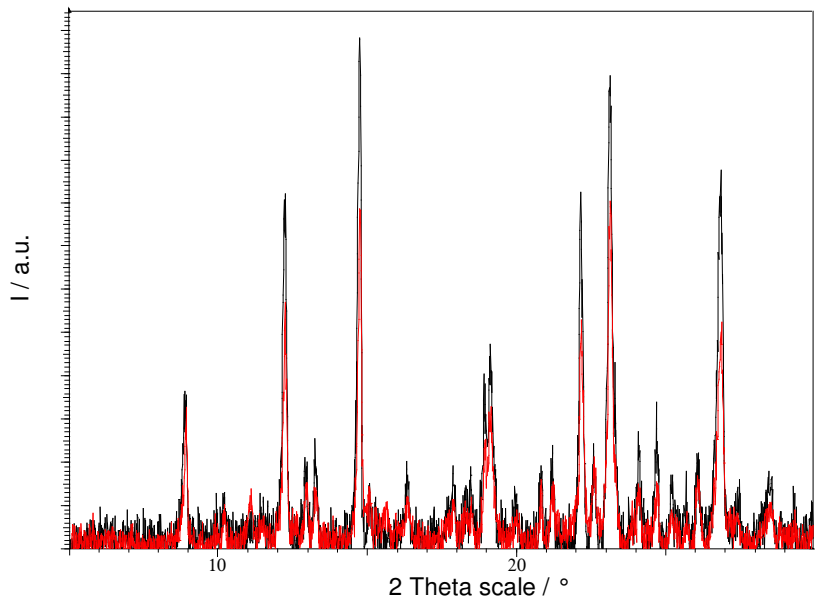

Figure 3.17: Powder pattern of **3c** within a capillary; before (black) and after (red) 14 d of irradiation.

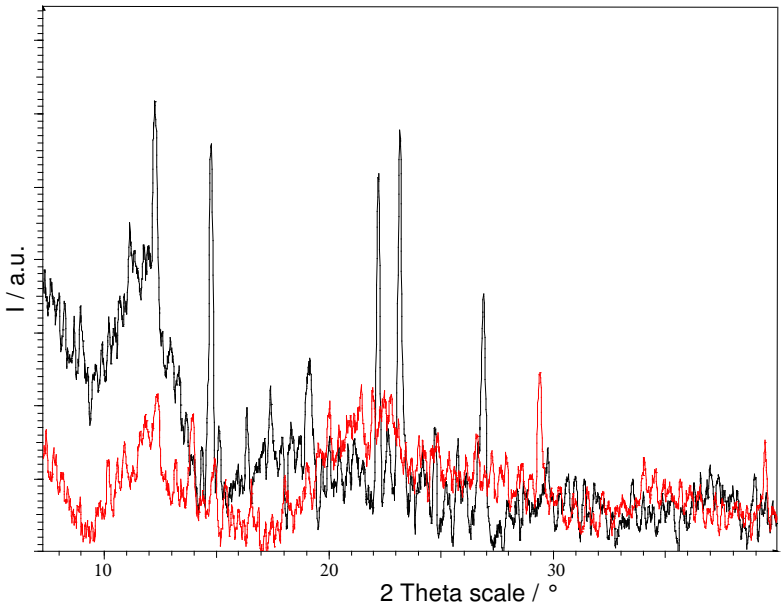

Figure 3.18: Smoothed powder pattern of **3c** on a glass fibre; before (black) and after (red) irradiation.

The calculated and measured powder patterns for **1c** are again in reasonable agreement, but the powder pattern change of **1c** on glass is not totally conclusive. A new weak peak appears at 23°, but the high signal to noise ratio makes it almost indistinguishable (Fig. 3.19). As the same peak is found via remeasuring the same powder after one, three and five days, the intensity change is regarded as a real difference.

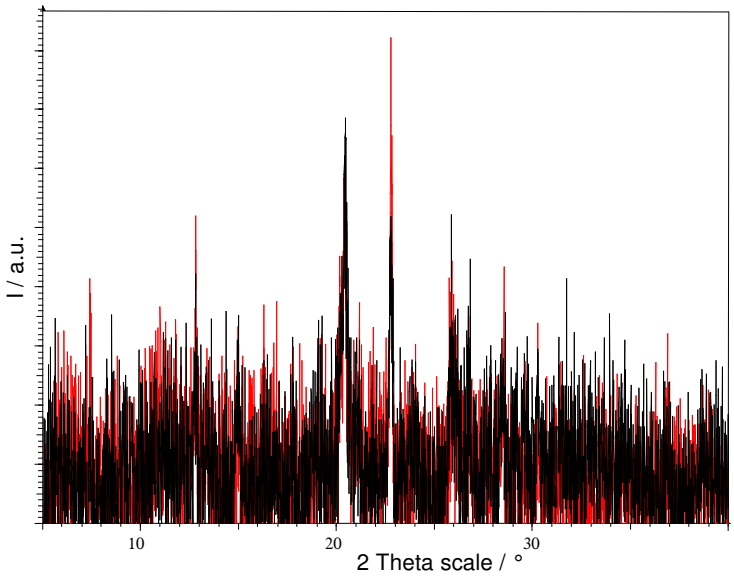

Figure 3.19: Powder pattern of **1c** on a glass fibre; before (black) and after (red) irradiation for 5 d.

As the $[Mn(Br)_2(\mathbf{3})_2(H_2O)_2]$ complex was only crystallised in a late stage of the project, the powder sample was measured on glass instead of inside a capillary. Nonetheless it is easily observed that the pattern changes quite significantly after irradiation of 1 d (Fig. 3.20). The crystallinity is not reduced through the change. The comparison to the predicted powder pattern is in good agreement.

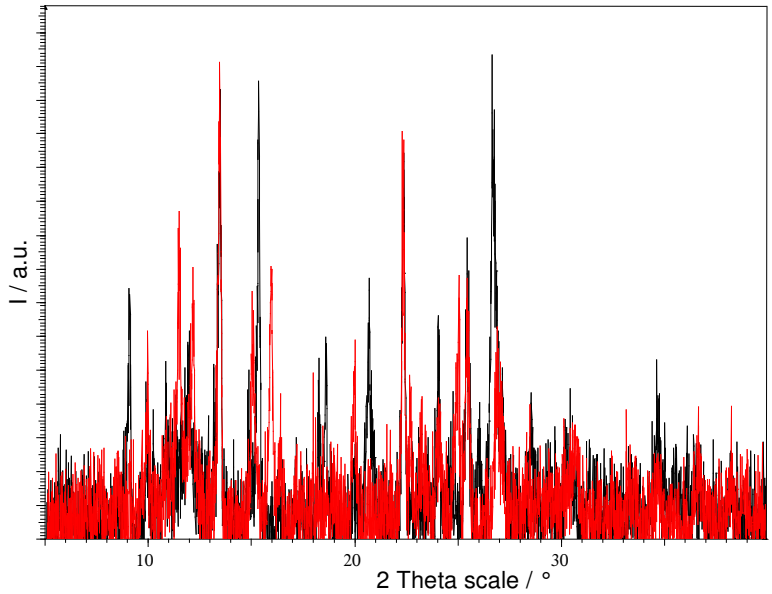

Figure 3.20: Powder pattern of **3d** on a glass fibre; before (black) and after (red) irradiation.

The conclusion from the powder diffraction experiments is that all the powdered complexes change under irradiation, and that they take different amounts of time and that the powder patterns after irradiation are not consistent within an isostructural series. This might be due to the fact that different amounts of ligand are converted to the dimer and that the dimers can form within different stacked complexes. For example, it is possible that only one side of the complex dimerises, which can change the pattern massively, especially in the structures with an inversion centre.

3.3.2.4. UV-vis Experiments

To assist with the interpretation of the powder diffraction data solution UV-vis experiments were performed in MeOH. Solutions of the powders of $M(NCS)_2(\mathbf{3})_2(H_2O)_2]$ (M = Co, Mn, Fe) before and after irradiation were prepared at concentration of 0.008 g/L. All UV-vis measurements were performed at these concentrations at room temperature. As shown in Figure 3.21 the three measurements

of the samples before irradiation (solid lines) show a broad ligand based peak at 304 nm with a shoulder at 270 nm. After irradiation (dashed lines) all three samples exhibit reduction in intensity of the broad peak at 304 nm combined with an apparent splitting of the second peak.

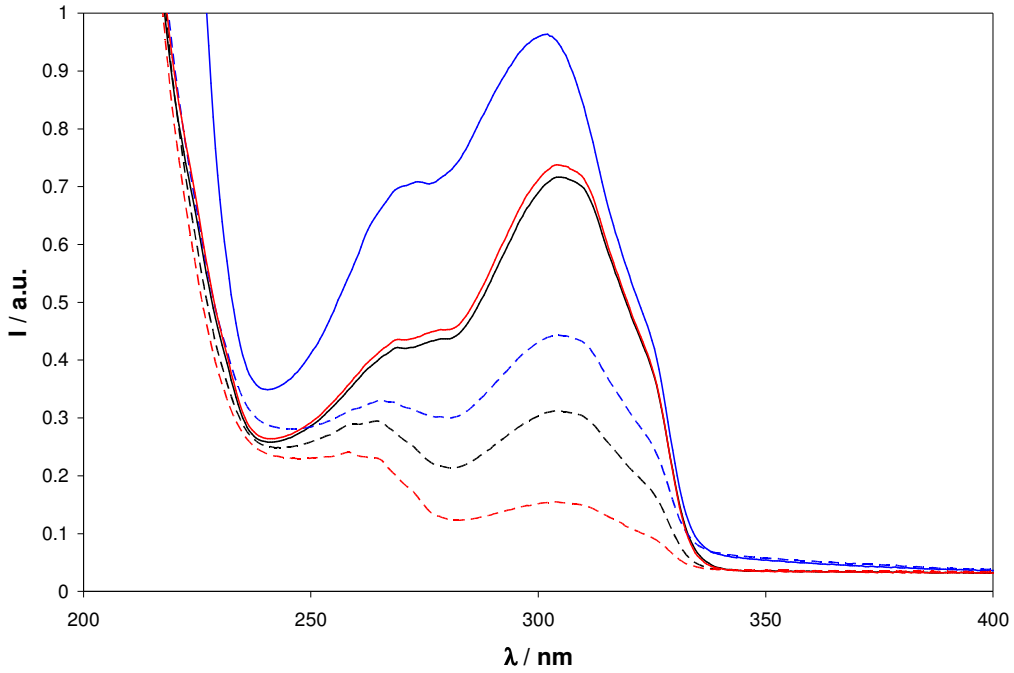

Figure 3.21: UV-vis spectra in MeOH before (solid line) and after (dashed line) irradiation of the complexes $M(NCS)_2(\mathbf{3})_2(H_2O)_2]$; **3a** in black, **3b** in red, **3c** in blue.

Following from the solution experiment, solid state UV-vis experiments were tried. The measurements were performed on powdered materials stuck to sticky tape with the same UV-vis spectrometer. The intensity of the powder spectrum is lower than the intensity in solution, nevertheless as shown in Figure 3.22 it is possible to see the same shift from approx. 310 nm to 265 nm and it is possible to follow the dimerisation over time on the same sample.

Following the dimerisation of a **3b** powder, monitored by UV-vis proves that most of the reaction takes place within the first hour and that no change is observed after more than 150 min.

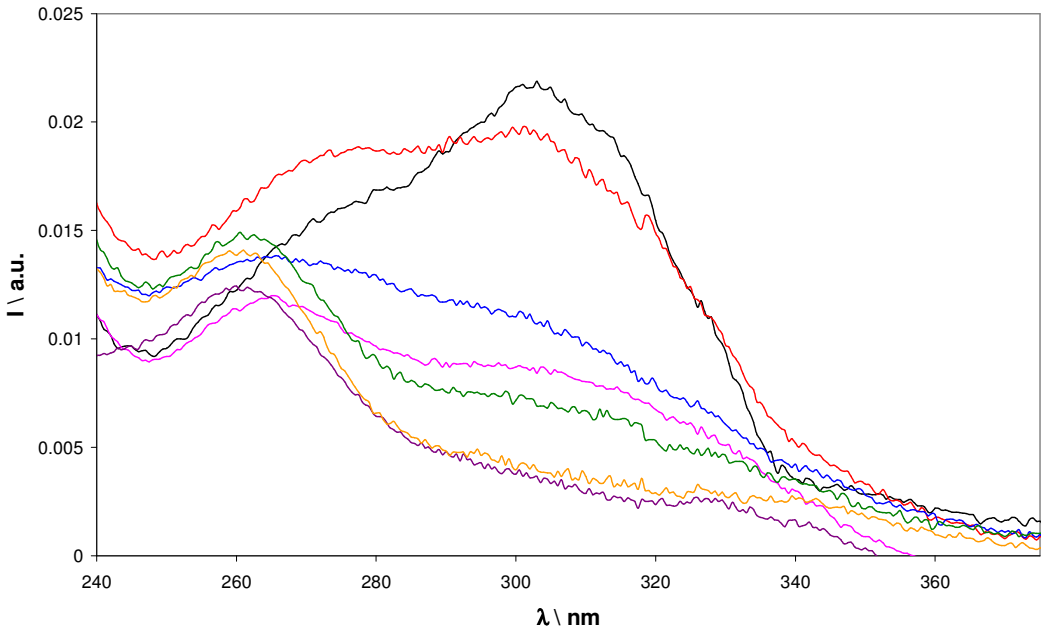

Figure 3.22: Solid state UV-vis spectra during irradiation of the complex **3b**; 0 h in black, 30 min in red, 60 min in blue, 90 min in pink, 120 min in green, 150 min in violet, 210 min yellow.

Figure 3.23 shows the UV-vis spectra of the seven metal complexes before (solid line) and after irradiation (dashed line). It is easy to see that all complexes change through irradiation, as similar shifts of the peaks are observed. Even though the non-irradiated complex of **1b** (violet solid line) has a very weak UV-vis spectra, not showing any major peak, it is possible to follow the change, as the spectrum of the irradiated powder has a stronger absorption at 260 nm.

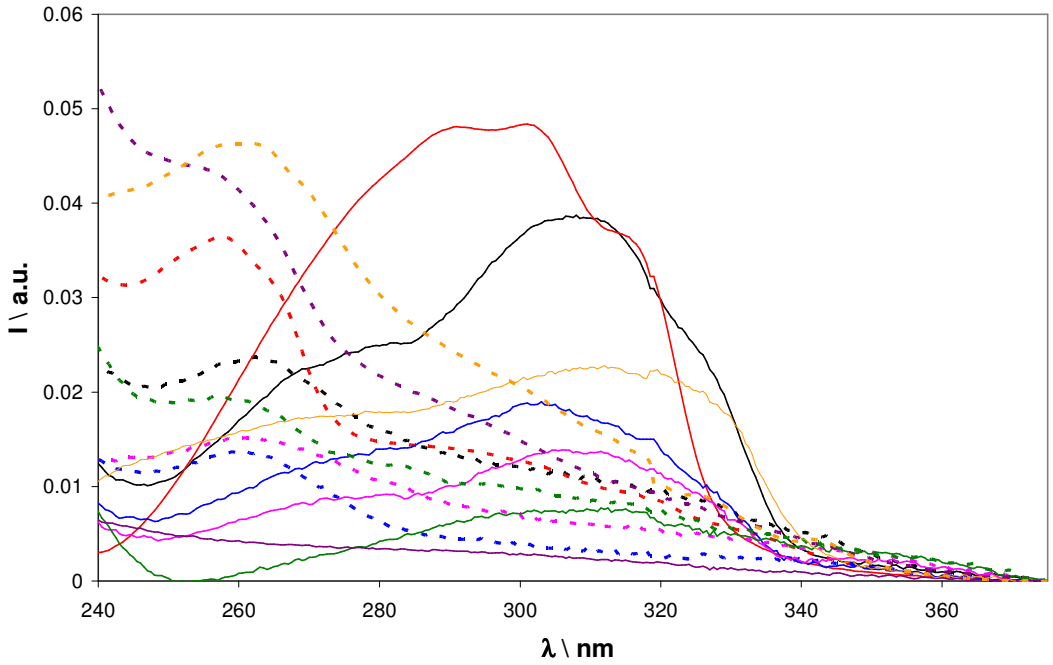

Figure 3.23: Solid state UV-vis spectra before (solid line) and after (dashed line) irradiation of the complex $M(hal)_2(L)_2(H_2O)_2]$; **1a** in green, **1b** in violet, **1c** in red, **3a** in pink, **3b** in blue, **3c** in black, **3d** in yellow.

3.3.2.5. Recrystallisation

The irradiated sample of **1a** was used for a recrystallisation experiment. As the complexes dissociate upon dissolution, as shown by mass spectrometry, a recrystallisation is only possible after an extraction of the organic ligand. The complex was dissolved in DCM and after extraction with water the organic phase was separated and the solvent was allowed to slowly evaporate. Only very thin needles were formed, but despite this problem it was possible to collect a X-ray single crystal data set, which solved (Fig. 3.24), as expected, to give the known crystal structure of the dimer **6** [90].

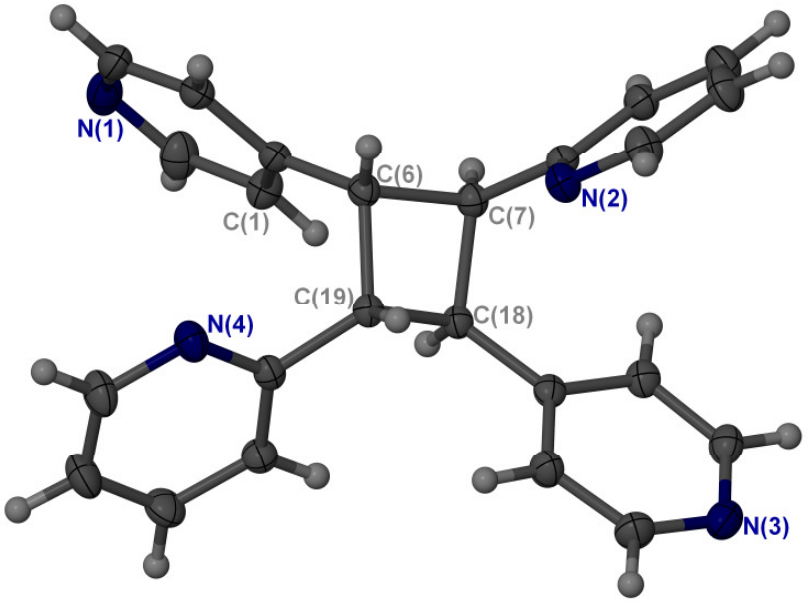

Figure 3.24: Dimer **6** after recrystallisation with 50 % ellipsoids shown.

3.3.2.6. IR Spectrometry

IR measurements were tested as a different technique for monitoring structural changes as well through this project. It was shown that a change of the band at around 1640 cm^{-1} occurs, as known from literature [89], but the intensity difference was too small compared to the differences between two measurements on our IR machine. Even so the procedure might be interesting for other crystalline materials, displaying more intense C=C bands.

3.4. Conclusion

It can be concluded from the measured data using different techniques that a [2+2] cycloaddition reaction takes place within the solid state. Unfortunately the goal of finding a single crystal to single crystal transformation was not achieved. Nonetheless it is shown that series of similar crystals with similar crystal packing motifs react in the same way. With the help of different analytical techniques a solid state reaction can be followed over time and quick and easy experiments, such as powder diffraction or UV-vis measurements can show if a reaction occurs.

3.5. Summary of the Crystal Data

Table 3.6: Summary of crystal data for $[Mn(NCS)_2(L)_2(H_2O)_2]$

Compound	**1b**	**3b**
Empirical formula	C13 H12 Mn0.5 N3 O1 S1	C26 H24 Mn N6 O2 S2
Formula weight	285.79	571.57
T/K	100	150
Wavelength / Å	0.69420	0.71073
Crystal system	*P*-1	*P*-1
Space group	triclinic	triclinic
a/Å	6.7953(4)	7.8810(2)
b/Å	9.9406(6)	10.2360(3)
c/Å	10.6603(7)	17.5590(6)
α/°	84.224(1)	76.404(2)
β/°	81.485(1)	80.996(2)
γ/°	70.452(1)	79.406(1)
V/Å^3	670.10(7)	1343.77(7)
Size/mm	0.03, 0.02, 0.02	0.4, 0.4, 0.3
Z	2	2
D_c/g cm^{-3}	1.416	1.413
μ/mm^{-1}	0.684	0.682
$2\theta_{max}$	59.44	60.96
Reflections collected	7556	20665
Independent reflections, R_{int}	3947, 0.0180	7182, 0.0487
Reflections obs. (> 2σ)	3556	5094
T_{min}/T_{max}	0.806	0.940
Final R_1, wR_2 [I>2σ(I)]	0.0334, 0.0898	0.0462, 0.1139
Final R_1, wR_2 (all data)	0.0369, 0.0927	0.0798, 0.1336

Table 3.7: Summary of crystal data for $[Co(NCS)_2(L)_2(H_2O)_2]$

Compound	**1a**	**3a**
Empirical formula	C26 H24 Co N6 O2 S2	C26 H24 Co N6 O2 S2
Formula weight	575.56	575.56
T/K	120	150
Wavelength / Å	0.69430	0.71073
Crystal system	*P*-1	*P*-1
Space group	triclinic	triclinic
a/Å	6.7773(4)	7.3810(2)
b/Å	9.8853(5)	9.7990(4)
c/Å	10.6298(6)	10.2270(3)
α/°	89.393(1)	91.685(2)
β/°	80.926(1)	99.040(2)
γ/°	70.930(1)	111.784(2)
V/Å^3	664.01(6)	675.22(4)
Size/mm	0.05, 0.03, 0.03	0.4, 0.4, 0.4
Z	1	1
D_c/g cm^{-3}	1.439	1.415
μ/mm^{-1}	0.839	0.825
$2\theta_{max}$	59.44	61.02
Reflections collected	7014	10607
Independent reflections, R_{int}	3768, 0.0177	3583, 0.0316
Reflections obs. (> 2σ)	3458	3199
T_{min}/T_{max}	0.980	0.960
Final R_1, wR_2 [I>2σ(I)]	0.0319, 0.0996	0.0412, 0.1107
Final R_1, wR_2 (all data)	0.0351, 0.1018	0.0471, 0.1154

Table 3.8: Summary of crystal data for $[Fe(NCS)_2(L)_2(H_2O)_2]$

Compound	**1c**	**3c**
Empirical formula	C13 H12 Fe0.50 N3 O S	C26 H24 Fe N6 O2 S2
Formula weight	286.24	572.48
T/K	150	150
Wavelength / Å	0.71073	0.71073
Crystal system	*P*-1	*P*-1
Space group	triclinic	triclinic
a/Å	6.7995(3)	7.7658(3)
b/Å	9.9224(3)	10.2633(3)
c/Å	10.6360(5)	17.5454(5)
α/°	89.761(3)	77.832(3)
β/°	81.277(4)	82.124(3)
γ/°	70.852(4)	79.198(3)
V/Å^3	669.24(5)	1335.83(8)
Size/mm	0.1707, 0.1206, 0.0755	0.2014, 0.1383, 0.0587
Z	2	2
D_c/g cm^{-3}	1.420	1.423
μ/mm^{-1}	0.755	0.756
$2\theta_{max}$	65.68	60.80
Reflections collected	8072	13937
Independent reflections, R_{int}	4425, 0.0277	6886, 0.0444
Reflections obs. (> 2σ)	3004	3511
T_{min}/T_{max}	0.812	0.995
Final R_1, wR_2 [I>2σ(I)]	0.0332, 0.0697	0.0446, 0.0737
Final R_1, wR_2 (all data)	0.0569, 0.0727	0.1052, 0.0819

Table 3.9: Summary of crystal data for **6** and $[Mn(Br)_2(\mathbf{3})_2(H_2O)_2]$

Compound	**6**	**3d**
Empirical formula	C24 H20 N4	C12 H12 Br Mn0.5 N2
Formula weight	364.44	307.62
T/K	150	150
Wavelength / Å	0.68890	0.71073
Crystal system	*P*2/*n*	*P*-1
Space group	monoclinic	triclinic
a/Å	16.123(3)	6.9030(3)
b/Å	5.670(1)	9.0560(4)
c/Å	21.544(4)	10.2360(4)
α/°	90	73.406(2)
β/°	103.667(2)	77.005(2)
γ/°	90	77.005(3)
V/Å^3	1913(7)	588.63(4)
Size/mm	0.06, 0.02, 0.02	0.4, 0.2, 0.2
Z	4	2
D_c/g cm^{-3}	1.265	1.736
μ/mm^{-1}	0.077	3.985
$2\theta_{max}$	67.44	60.68
Reflections collected	24689	9716
Independent reflections, R_{int}	5842, 0.0522	3150, 0.0690
Reflections obs. (> 2σ)	4076	2348
T_{min}/T_{max}	0.856	0.594
Final R_1, wR_2 [I>2σ(I)]	0.0466, 0.1087	0.0666, 0.1696
Final R_1, wR_2 (all data)	0.0760, 0.1225	0.0974, 0.1886

4. Crystals of Other Complexes with Ligand 1-5

During the desired synthesis of the complexes in Chapter 3, a lot of different other crystals were synthesised. This chapter describes the wide variety of complexes including the five ligands, which were introduced in Chapter 3. During the project different kind of crystal systems were found, some of them crystallise out with different amount of solvent and ligand. As described before during the synthesis of the **1a** cobalt complex different nitrate and thiocyanate complexes with Co(II) were synthesised. Additionally, metal salts, ligands and halides were reacted together and the found crystallised complexes are described within this chapter. At the end of the chapter some co-crystals of organic templates and the ligands are described. On the crystals, where a [2+2] cycloaddition reaction might be possible, some analytical characterisation (UV-vis spectroscopy or powder diffraction) are performed.

4.1. Cobalt structures of 1

During the synthesis of **1a** a lot of different complexes crystallised out. The first reactions were performed using $Co(NO_3)_2$ as the Co(II) source; this led to four crystals with nitrate instead of thiocyanate as counter ions. Changing the salt to cobalt chloride resulted in complexes with thiocyanate as counter ion, but five different complexes were found, of which one was the target crystal structure of **1a**.

A systematic study was undertaken, in an attempt to perturb the chemical equilibrium of this crystallisation to give a specific product. To achieve this, reagent concentrations were varied and seeding experiments were tried. For the latter one of these experiments, some of the crystals grown in the original attempt to get **1a**, were reused as seeding agents, as well as crystals of the other $[M(NCS)_2(\mathbf{1})_2(H_2O)_2]$ complexes. For varying the concentration three sets of crystallisations were carried out: The original 1:1 ratio of cobalt salt and ligand, a 2:1 and a 1:2 ratio. Nonetheless

all the seeding and concentration experiments resulted in the synthesis of the network structure **1d**. As all these syntheses were performed during the summer period, it was concluded that the concentration might not be the primary factor of this crystal growth. Redoing the experiment during the winter again resulted in a combination of different compounds, not being related to the concentrations used. Following from that result a temperature study was performed. The crystallisations were kept at different temperatures (277 K, 293 K 303 K and 323 K), but it was found that in all 20 test tubes the same crystal product crystallised out **1d**. The driving force for the single crystal growth was not found and might be a combination of different laboratory conditions and / or the solvent purity and temperature.

4.1.1. Nitrate Structures

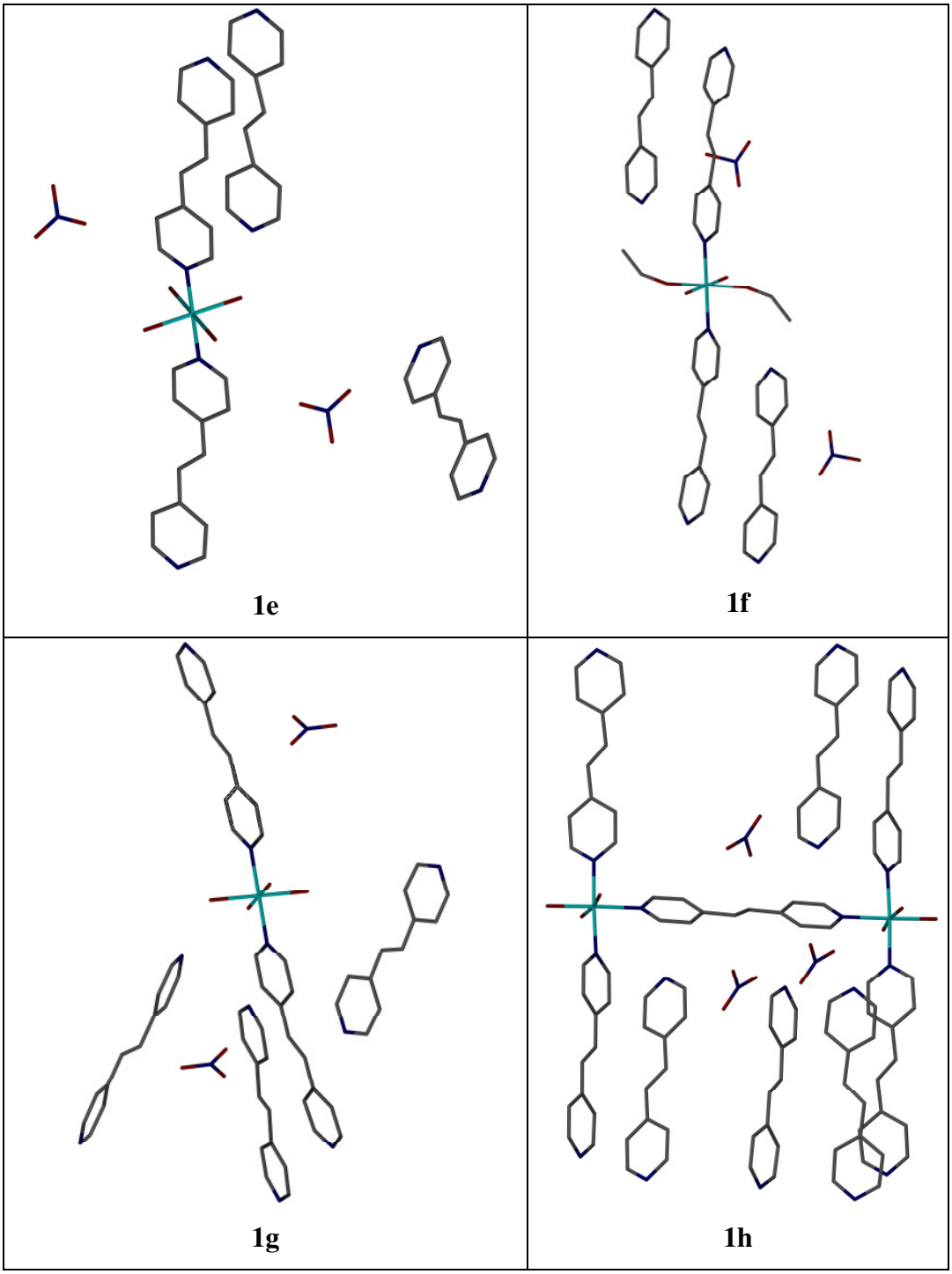

Figure 4.1: Comparison of the four different crystal cobalt structures with nitrate as counter ion. All the solvent, disorder and hydrogens are removed for clarity.

The first three structures (**1e**, **1f**, **1g**) in Figure 4.1 are cobalt complexes of the following overall structure: $[Co(\mathbf{1})_2(sol)_4]^{2+}$. The cobalt centre is octahedral, surrounded by ligands, with all the ligands being *trans* to each other. Complex **1h** on the other hand is a dimeric structure with $[Co_2(\mathbf{1})_5(H_2O)_6]^{4+}$, again with both cobalt centres in an octahedral environment.

The difference between the first three structures is the amount of solvent and free ligand within the unit cell. The second example **1f** has a mixture of ethanol and water in the structure with both ethanol and water bound to the metal centre. The structures of **1e**, **1g** and **1h** crystallise in the triclinic space group *P*-1, whereas **1f** crystallises in the monoclinic space group $P2_1/c$.

In **1e** the cobalt ion sits on a crystallographic centre of symmetry and is coordinated to four oxygen atoms from water solvate molecules and two nitrogen atoms from the ligand. In this structure, the two halves of the molecules are related by the symmetry operation *-x+2, -y+1, -z*. This structure is highly disordered, with both of the free ligands having two components, as well as the nitro group and most water molecules being only partially occupied, resulting in a high R_1 value (0.083), even though the main molecule refines nicely with sensible displacement parameters. The 3D packing consists of an extended hydrogen bond network, occurring between the hydrogens on the solvent molecules and the lone pairs on the nitrogen and oxygen atoms from the ligand and the solvent, as shown in Figure 4.2. Additionally, π-π-stacking interactions are found between adjacent aromatic rings in the cobalt complex and the free ligand **1**, which falls within the criteria for a [2+2] cycloaddition reaction to occur. The midpoint distances of the interactions are 3.6 Å and 4.0 Å respectively. However, solid state UV-vis measurements and powder diffraction experiments suggest that no cycloaddition does occur (Fig. 4.3).

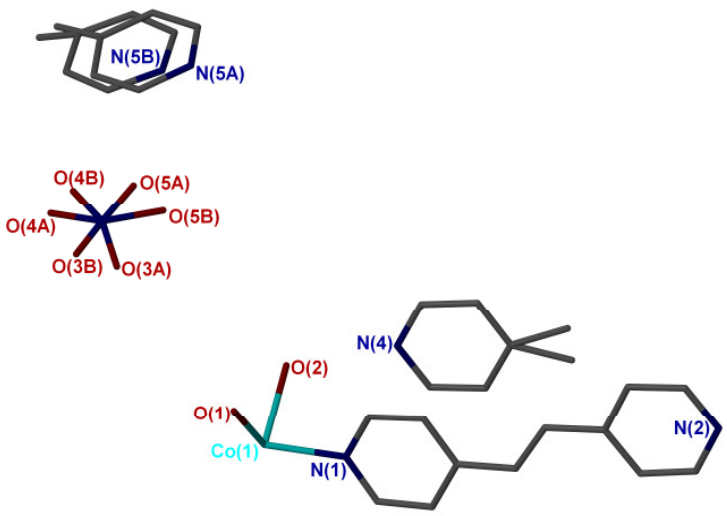

a

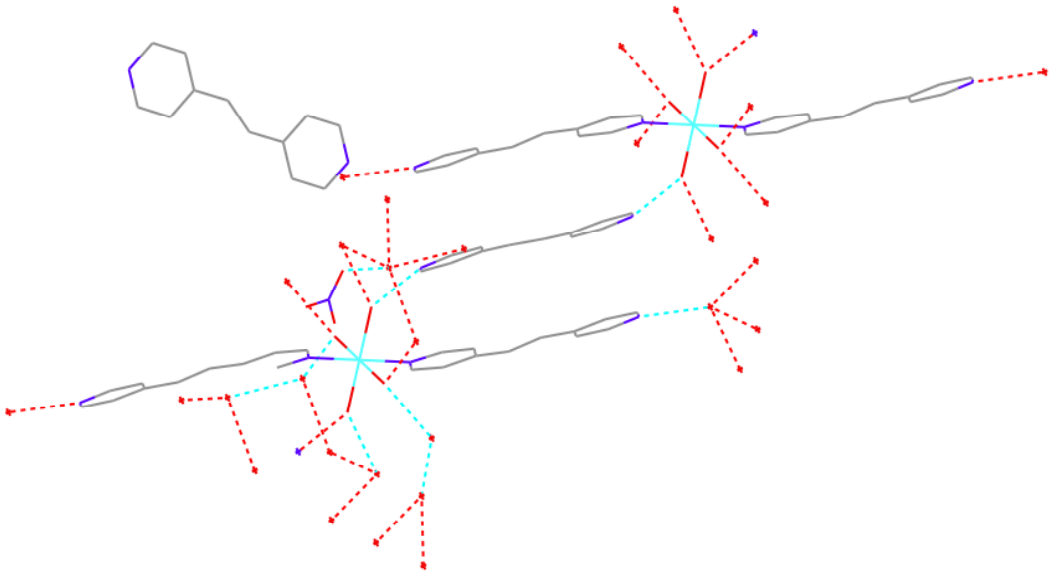

b

Figure 4.2: a) Asymmetric unit of structure **1e** b) and hydrogen bonding with all four coordinated water molecules (O1, O2, O1', O2') form hydrogen bonding to the non coordinated nitrogens of the ligand and to the unbounded water.

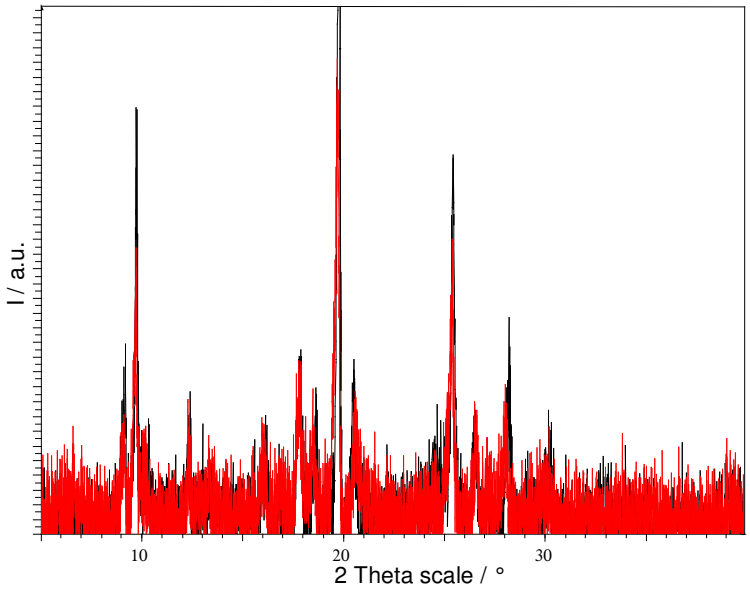

Figure 4.3: Powder pattern of **1e** before (black) and after irradiation (red).

The crystal structure of **1f** consists of discrete $[Co(H_2O)_2(\mathbf{1})_2(EtOH)_2]^{2+}$ cations together with nitrate anions, a free ligand **1** and water and ethanol solvent molecules. In **1f** the cobalt ion, which sits on a crystallographic centre of symmetry, has a distorted octahedral geometry, being coordinated to four oxygen atoms (water and ethanol) and two nitrogen atoms (**1**), with all the ligands being *trans* to each other. Hereby the two halves of the molecule are related to each other by the symmetry operation *-x+1, -y+1, -z*. Hydrogen bonding and π-π-stacking interactions are the intermolecular interactions observed within the crystal packing. A 1D layer is formed through hydrogen bonding from water molecules to the lone pairs of nitrogens in the ligand (Fig. 4.4). Additionally there are π-π-stacking interactions between adjacent aromatic rings in the cobalt complex and a free ligand and to another complex. The two midpoint distances between the double bonds are 3.7 Å and 3.8 Å respective. Even though the geometry of the molecules suggests a [2+2] cycloaddition reaction should be possible, the UV-vis spectrum implies that no reaction takes place within the powdered crystals.

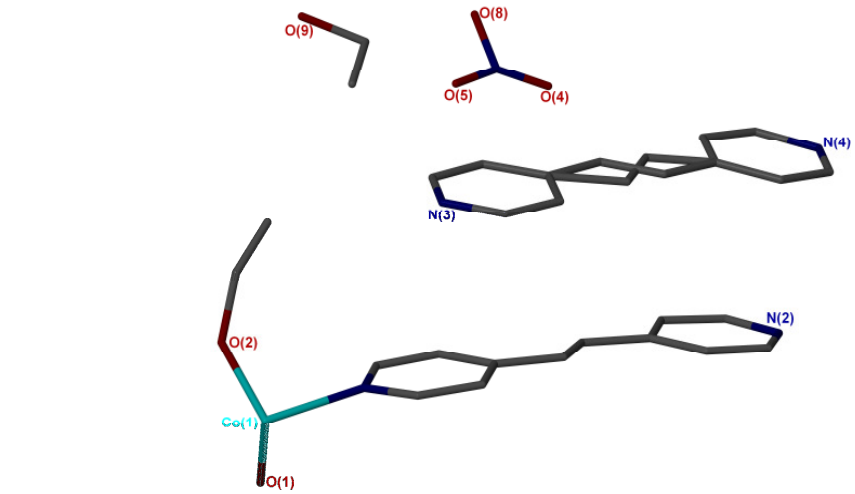

a

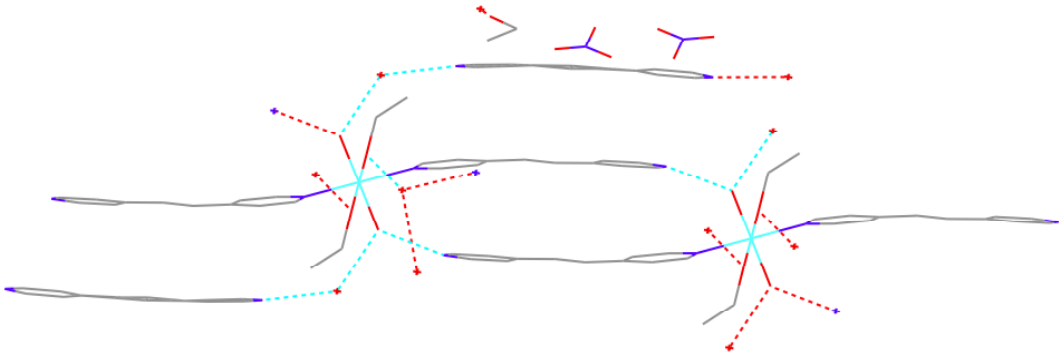

b

Figure 4.4: a) Asymmetric unit of structure **1f** b) and hydrogen bonding forming a layered structure between the complexes; the two coordinated water molecules (O1 and O1') coordinate to free solvent and nitrogen (N2) of the coordinated ligand molecule, whereby the coordinated ethanol oxygen (O2) is part of the extended hydrogen bonding between the solvent and the unbounded ligand (N3 and N4).

The crystal structure of **1g** consists of discrete $[Co(H_2O)_4(\mathbf{1})_2]^{2+}$ cations together with two non bonded nitrate anions, three non bonded ligands and four water molecules. The cobalt ion sits on a crystallographic centre of symmetry as in the other two structures before; with one half of the molecule being related to the other half by the symmetry operation *-x+1, -y+1, -z*. The molecular structure of the complex is identical to **1e**, but the packing of the crystal structure is different. There are π-π-stacking interactions between adjacent aromatic rings of two cobalt complexes

(3.8 Å). Additionally there are hydrogen bonds forcing the ligands to be parallel as shown in Figure 4.5. Additionally, one of the free ligands also has π-π-stacking interactions with the coordinated ligand, but is slightly twisted from co-planarity (ca. 10º).

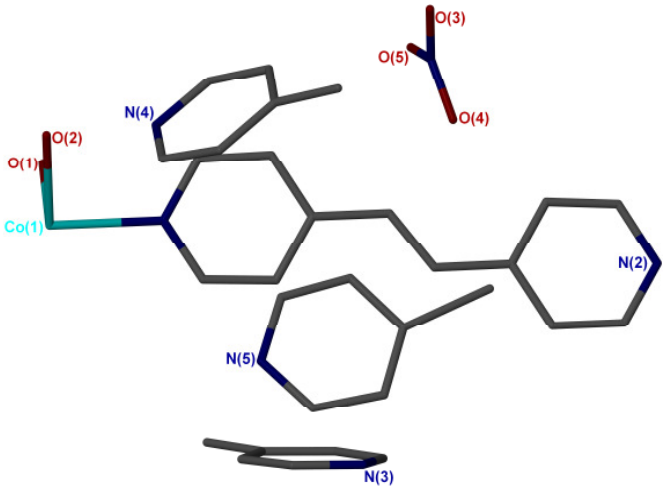

a

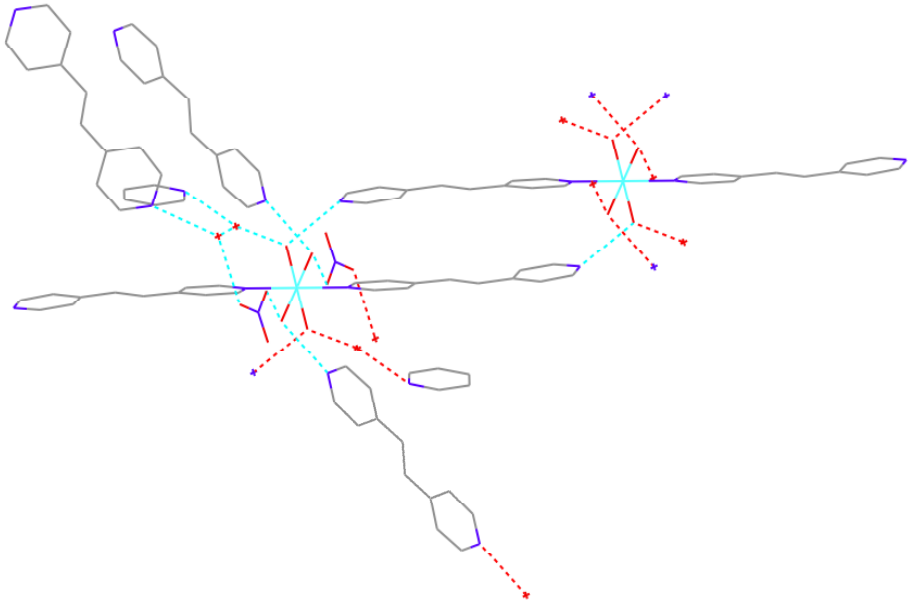

b

Figure 4.5: a) Asymmetric unit of **1g** b) and hydrogen bonding; the coordinated water molecule (O1) forms a hydrogen bond to the non coordinated nitrogen (N2) of the coordinated ligand and the water molecule (O7), whereby the second coordinated water (O2) interact with water (O3) and N4 of the free ligand.

The last of the four nitrate structures is different, as a dimer is formed. Two metal centres are bound by a ligand and additionally each cobalt ion is bound to two ligands, which are *trans* to each other, and three water molecules. The inversion centre is in the middle of the ligand between the two cobalt ions; therefore Co1 is related to Co1' by the symmetry operation *-x, -y+1, -z*. Four unbound ligands are found within the unit cell, one of which is appropriately placed to undergo a [2+2] cycloaddition reaction with the dimer. The distance between the midpoints of the ethylene bridges is 3.7 Å and the pyridyl rings are parallel to each other. Through hydrogen bonding a ladder like structure is formed. The cobalt ions and the ligand between them form the sides of the ladder, whereas the ligands form the steps between them (Fig. 4.6).

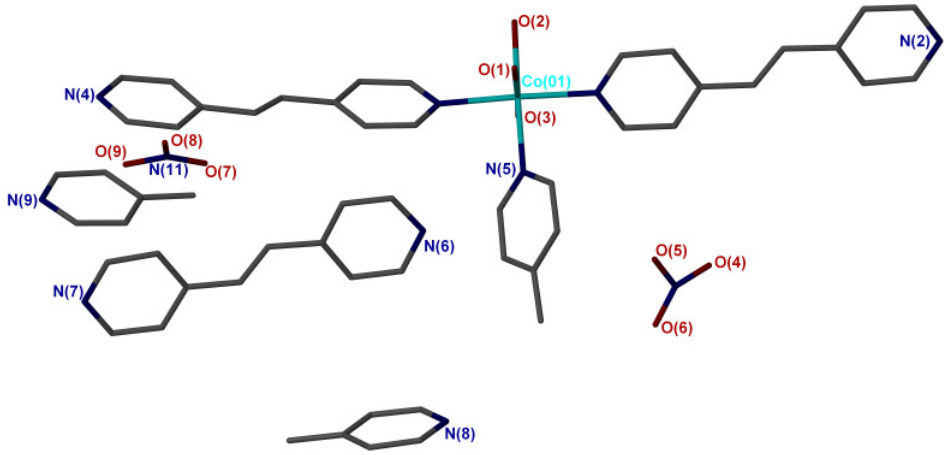

a

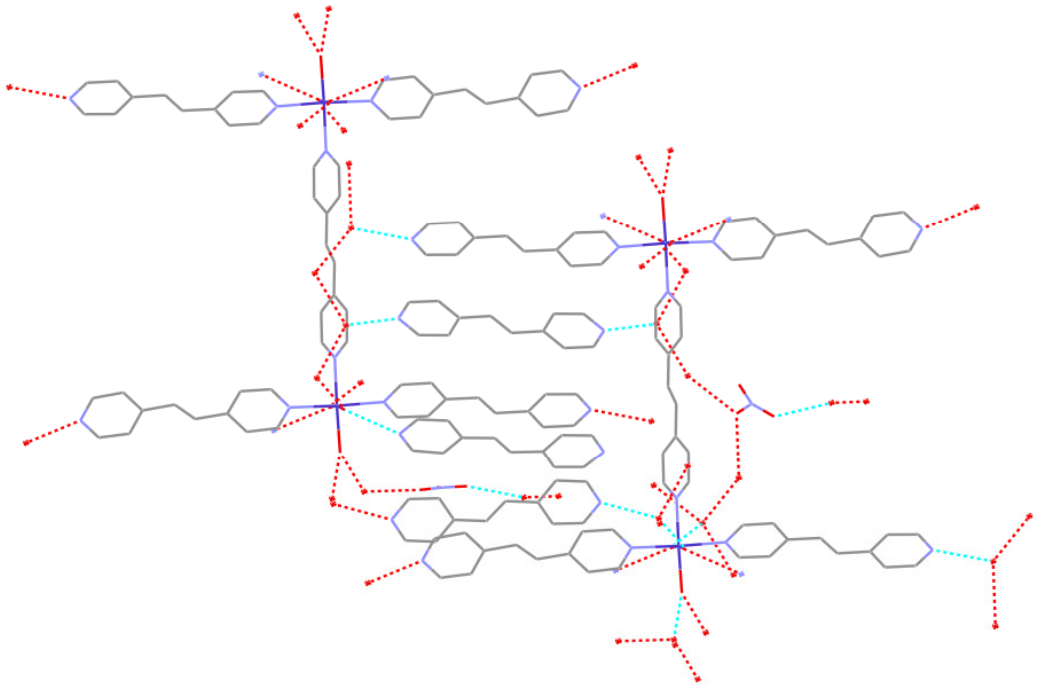

b

Figure 4.6: a) Asymmetric unit of structure **1h** b) and hydrogen bonding; bounded water O2 interacts to two free water molecules, whereby the other two bounded water molecules (O1 and O3) both interact to one water molecule and one nitrogen of the ligand (N4 and N7).

All four structures have an extended hydrogen bond network resulting from the high amount of unbounded molecules. These varieties of solvent molecules, ligands and the unbounded nitrate anions make it difficult to redo the crystals. Following

from this only two of the complexes were tested for a [2+2] cycloaddition reaction within the solid state. Neither showed any reactivity to UV light through UV-vis solid state measurements. The hydrogen bonds are found in Table 4.1.

Table 4.1: Hydrogen bonds within the cobalt nitrate complexes

Compound	DHA	DH / Å	HA / Å	DA / Å	Angle / °
1e	O2-H2B-N4	0.88	1.86	2.705(6)	161.6
	O2-H2A-O3	1.06	1.83	2.802(6)	149.7
	O1-H1A-O8	1.02	1.99	2.694(6)	123.7
	O1-H1B-O7A	0.98	1.72	2.694(7)	170.8
1f	O2-H2A-O6	0.83	1.93	2.726(7)	160
	O1-H1A-N2	0.84	1.90	2.739(5)	175
	O7-H7A-O9	0.84	2.57	3.181(17)	130
	O7-H7B-N3	0.84	1.97	2.790(8)	167
	O1-H1B-O7	0.84	1.90	2.730(6)	166
1g	O1-H1B-N2	0.87	1.89	2.745(3)	170
	O2-H2B-N4	0.80	2.04	2.829(3)	172
	O2-H2A-O3	0.84	1.94	2.774(3)	170
	O7-H7A-O6	0.87	1.91	2.775(3)	177
	O6-H6A-N3	0.86	2.05	2.857(3)	156
	O6-H6B-O4	0.86	2.00	2.852(3)	171
	O7-H7B-N5	0.82	1.99	2.791(3)	168
	O1-H1A-O7	0.87	1.76	2.628(3)	172
1h	O10-H10A-O7	0.91	1.89	2.710(4)	149
	O2-H2B-O15	0.90	1.86	2.753(3)	171
	O1-H1B-O12	0.90	1.90	2.779(3)	167
	O2-H2A-O15	0.90	1.96	2.845(3)	167
	O1-H1A-N4	0.90	1.86	2.750(3)	174
	O15-H15B-O9	0.91	1.86	2.734(4)	159
	O12-H12B-O6	0.89	2.33	3.135(7)	149
	O15-H15A-O16	0.90	2.06	2.828(3)	142

	O13-H13A-O10	0.90	2.07	2.779(3)	135
	O12-H12A-O14	0.90	1.80	2.693(4)	169
	O14-H14B-O5	0.90	2.14	2.947(5)	149
	O14-H14A-N2	0.90	1.91	2.777(3)	162
	O13-H13B-O4	0.91	2.09	2.819(5)	137
	O10-H10A-O7	0.91	1.89	2.710(4)	149
	O3-H3B-N7	0.90	1.88	2.769(3)	171
	O3-H3A-O16	0.90	1.94	2.810(3)	165
	O16-H16A-N9	0.92	1.91	2.826(4)	175
	O12-H12B-N10	0.89	2.60	3.490(4)	176

4.1.2. Thiocyanate Structures

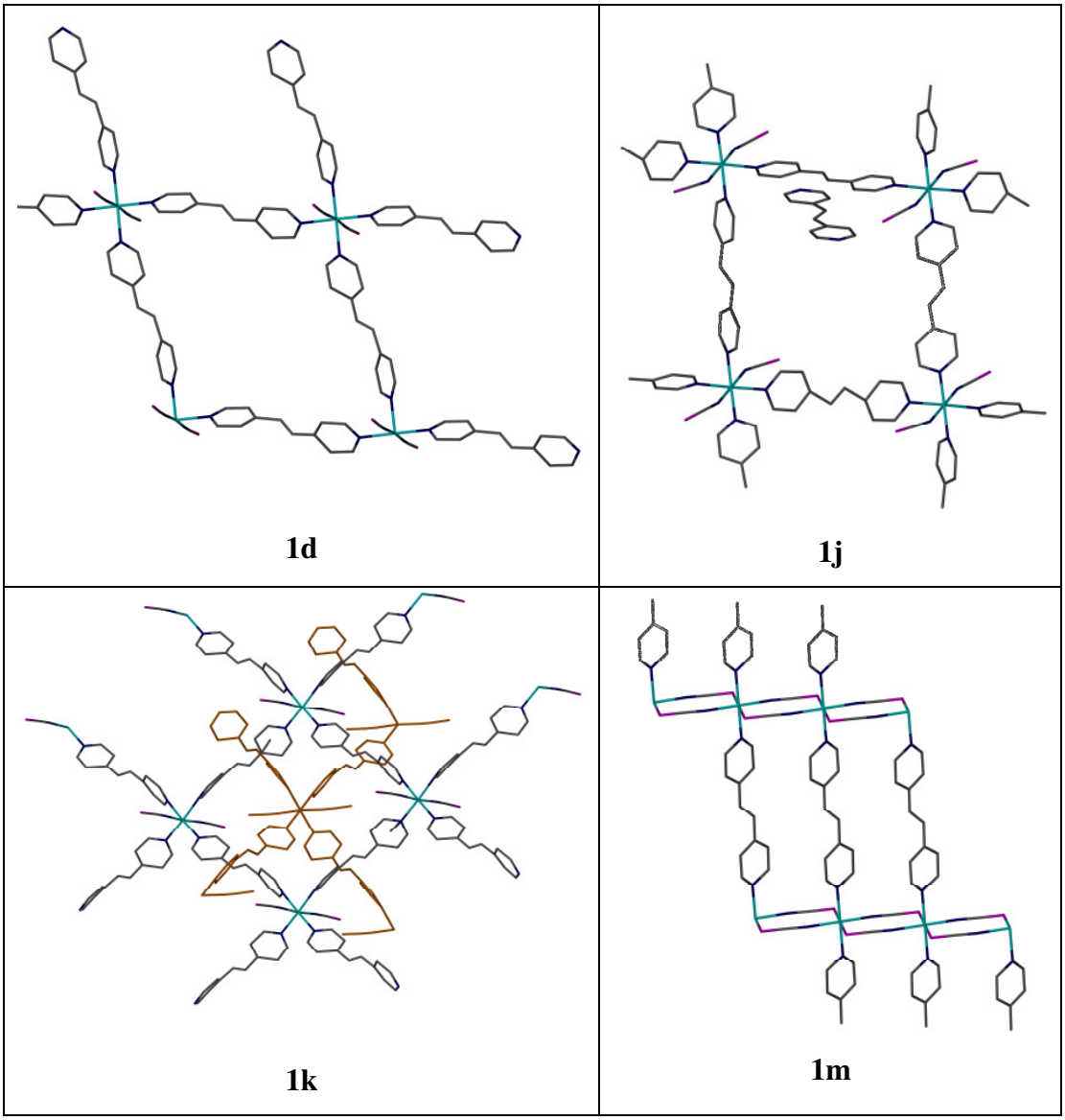

Figure 4.7: Comparison of the four different crystal structures with thiocyanate as counter ion. Hydrogens, solvents and disorder are removed for clarity.

The four structures shown in Figure 4.7 were found in the attempt to prepare crystals of **1a**, and they have the common feature that they formed 2D network structures. Three of the structures **1d**, **1j** and **1k** form the same building unit, a square, in which the ligand is bound to two metal centres. Every cobalt ion is bound to four ligands and two thiocyanate groups, which are *trans* to each other. The

difference between the structures is that in **1d** only solvent molecules are in the pores, whereas unbound ligand and solvents are found in **1j** and in **1k** a second network interpenetrates the first one. All structures display disorder within the ligand and the thiocyanate is disordered as well in structure **1j**.

The two dimensional network material **1d** crystallises in the tetragonal space group *I*-4. The cobalt ion sits on a 2 fold rotation axis. Therefore N1 is related to N1' by the symmetry operation *-x+1, -y, z*. The asymmetric unit contains $Co_{0.5}(NCS)(\mathbf{1})$, with the pyridyl rings of the ligands being disordered (Fig. 4.8) each with ca. 50 % occupancy, and a non-coordinated methanol. The four solvent positions are all not fully occupied, but have approximately two methanol molecules per asymmetric unit (Fig. 4.9).

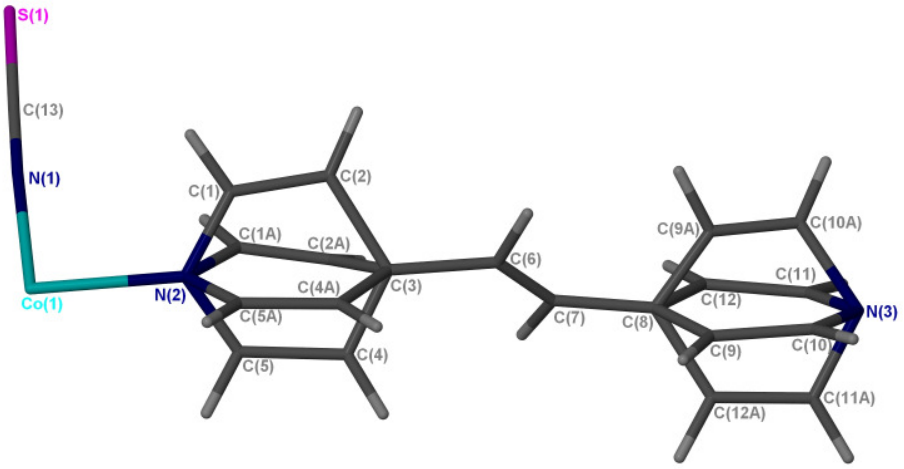

Figure 4.8: Asymmetric unit of **1d**, displaying the disorder over the ligand with the four partially occupied methanol molecules removed for clarity.

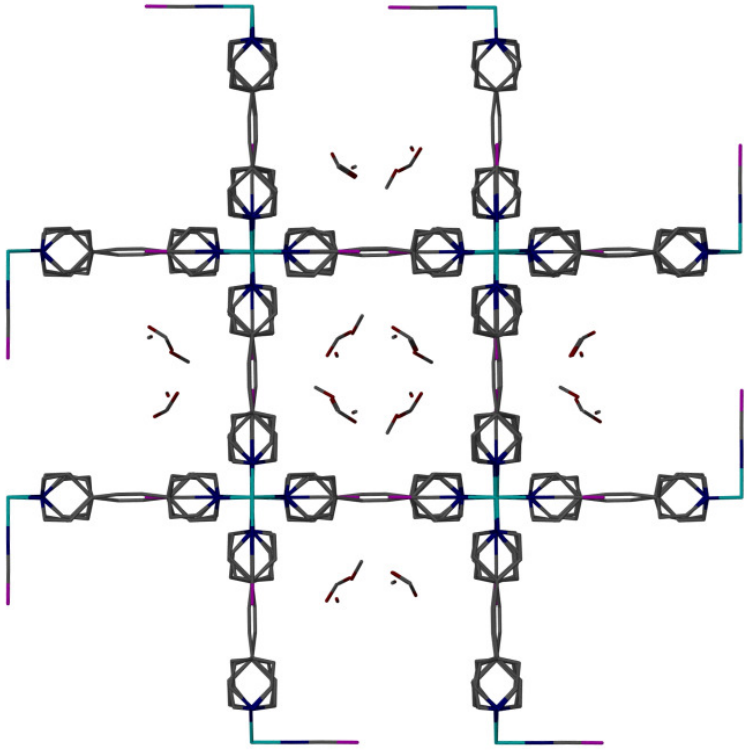

Figure 4.9: Packing of **1d** with the disorder and the solvent shown, but hydrogens removed for clarity.

The network material **1j** on the other hand crystallises in the triclinic space group *P*-1. The network is formed in the same way as in **1d** with the inversion centre being situated in the middle of the ligand. N6 is therefore related to N6' by the symmetry operation *-x+2, -y+1, -z+1*. The asymmetric unit contains $Co(NCS)_2(\mathbf{1})_2$, half a ligand and two water molecules. One of the four bridges between the pyridyl rings is disordered (Fig. 4.10) with a ratio of ca. 60:40, as well as the bridge in the free ligand and the two thiocyanates. There are hydrogen bonds between the sulphurs of the thiocyanate and the water molecule O2, between O1 and N7 and O1 and O2. The free ligand is not situated appropriately for a [2+2] cycloaddition reaction, as the free ligand is orthogonal to the bound one.

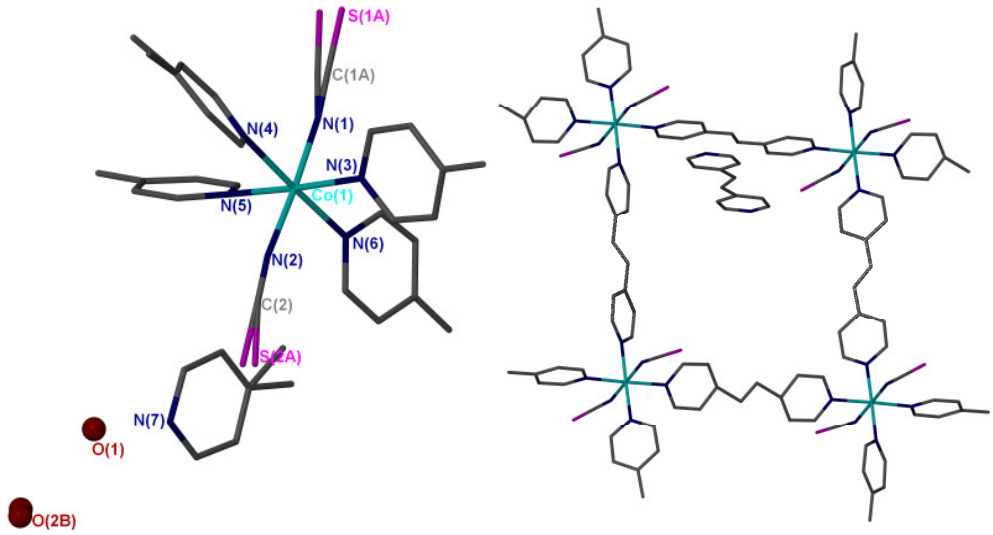

a b

Figure 4.10: a) Asymmetric unit of **1j**, displaying the disorder, b) packing of **1j** without disorder or solvent shown. Hydrogens are removed for clarity in both pictures.

The network material **1k** crystallises in the orthorhombic space group *Fdd*2 and has the form of an interpenetrating spiral staircase. The environment of the cobalt ion is the same as for the last two structures, but because of a twist between the ligands the four cobalt ions are not in a plane. The asymmetric unit is again $Co(NCS)_2(\mathbf{1})_2$ and one water molecule. In one of the two ligands the ethylene bridge is disordered. There is no hydrogen bonding found between the water molecules. Figure 4.11 displays the spiral staircase of the network in green with the interpenetration going diagonally through the other network (black).

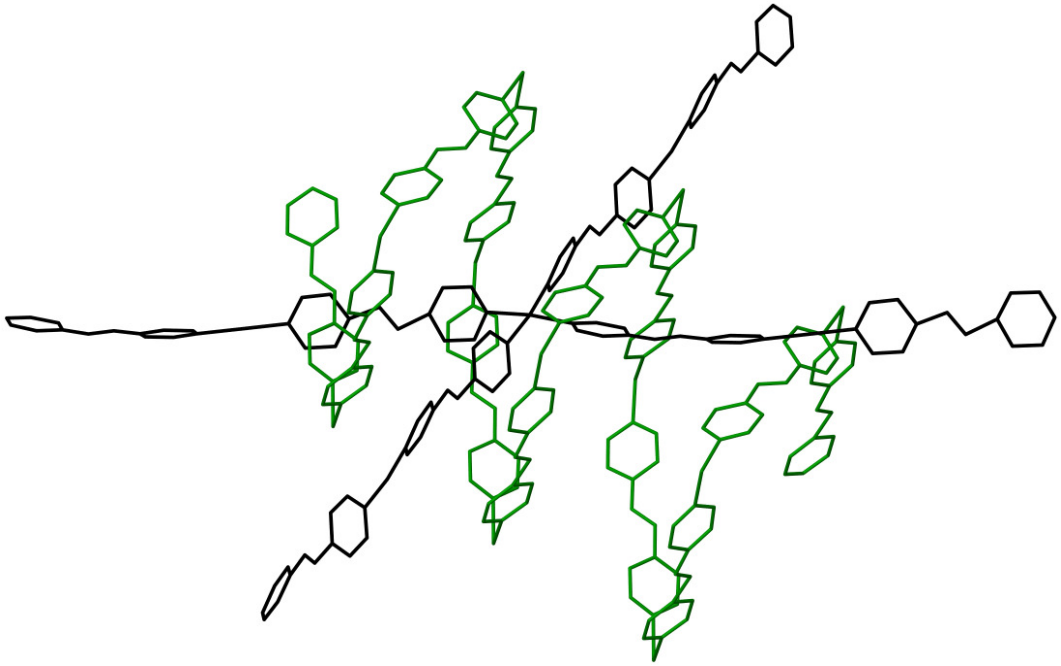

Figure 4.11: Scheme of the spiral staircase in green with the interpenetration in black.

The bonding mode of these three structures is not uncommon for cobalt thiocyanate complexes. There are two more structures known in the literature with the same building unit. They are also built from squares as shown for **1d**, **1j** and **1k**. One of the structures crystallises in *P*4/*ncc* with no disorder being present (REVQAK) [90], whereas the other structure displays disorder within the ligand and crystallises in *Ibam* (XACYAB) [91].

The network material **1m** on the other hand is different as cobalt is bound to four thiocyanate groups of which two are bound through the nitrogen and through the two sulphurs. To complete the octahedron around the cobalt ion, it is bound to two ligands as well. The space group is again triclinic *P*-1, with the cobalt sitting on the centre of symmetry, following from that the asymmetric unit is only $Co_{0.5}(\mathbf{1})_{0.5}(NCS)$. The nitrogen of the thiocyanate N1 is related to N1' by the symmetry operation *-x, -y+1, -z+1*. The ligand is disordered in a ratio of 50:50 and bound to two cobalt ions (Fig. 4.12), giving an extended 2D network.

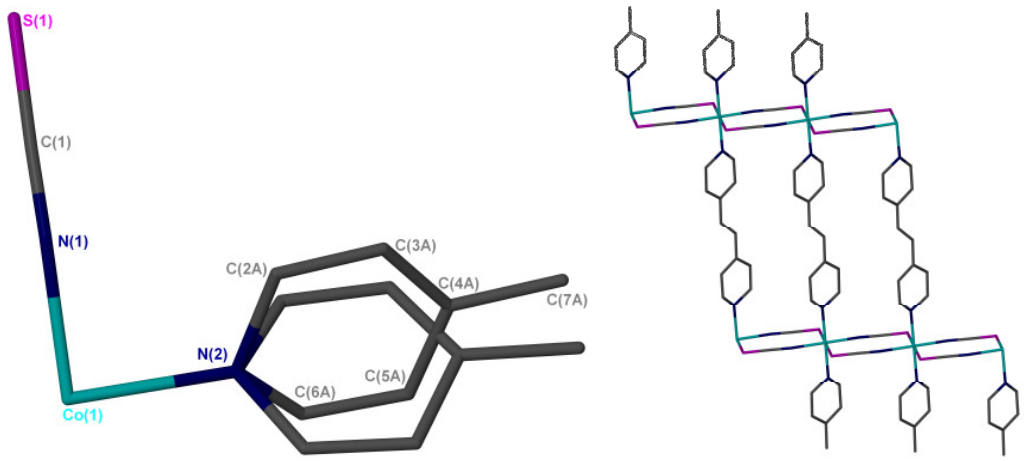

a b

Figure 4.12: a) Asymmetric unit of the network **1m** and b) packing of **1m**, with hydrogens removed in both structures and the disorder removed in b.

Bonding to both nitrogen and sulphur of the thiocyanate group is an uncommon structural feature for cobalt complexes; there are only five structures found within the CSD [92], from which three are very similar to the one described here, as they also form a network. These complexes contain the ligands nicotinic acid [93], pyridine [94] or picoline [95], with all four ligands having the same pyridine unit. The difference between the structures from the literature and the network structure **1m** is that the pyridylethylene binds to two cobalt centres forming a 2D network.

None of the four structures are suitable for a [2+2] cycloaddition reaction in the solid state, which is easy to see for the structures of **1d**, **1j** and **1m** as all the ligands are build into the network. The free ligand in network **1k** on the other hand goes through the pores and is therefore orthogonal to the bonded ligands. The hydrogen bonds for the four structures are given in Table 4.2.

Table 4.2: Hydrogen bonds within the cobalt thiocyanate complexes

Compound	DHA	DH / Å	HA / Å	DA / Å	Angle / °
1d	O2-H2B-O3	0.84	2.42	3.05(4)	132.3
1j	O1-H1A-O2B	1.06	1.83	2.871(6)	167
	O1-H1A-O2A	1.06	1.84	2.828(6)	154
	O1-H1B-N7	0.85	2.17	2.857(5)	138
	O2A-H2B-O1	1.00	1.88	2.828(6)	158
	O2B-H2D-O1	0.92	1.96	2.871(6)	168

MOFs are known to show interesting gas exchange reactions, whereby solvent can be removed from the network and replaced by other solvent molecules or by gas molecules or the pores are left empty [96]. Therefore attempts were made to remove the solvent by evacuating the frameworks **1d** and **1j**. Unfortunately they collapse, if they were left under vacuum for desolvation. Following from that the crystals loses diffraction power.

4.2. Other Metal Complexes with Thiocyanate

In addition to the cobalt complexes which were found with ligand **1**, two more thiocyanate structures were found within this project. The first is an iron structure **1n** similar to the previously described cobalt MOFs, whereas the second one can be compared to the $[Mn(NCS)_2(L)_2(H_2O)_2]$ complexes from Chapter 3.

A comparable structure to the cobalt metal organic frameworks is the following iron structure **1n**. The metal organic framework crystallised in the tetragonal space group *P4/ncc.* The network is an interpenetrating framework with methanol and water within the pores (Fig. 4.14). The iron centre is surrounded by four ligands in a plane and two thiocyanates. N1 is related to N1', N'' and N''' by the symmetry operations *-x+1.5, -y+0.5, z; y+0.5, x-0.5, -z+0.5, -y+1* and *-x+1, -z+0.5*. The asymmetric unit contains $Fe_{0.25}(NCS)_1(\mathbf{1})_{0.5}$, one methanol and one water (Fig. 4.13). Only one

hydrogen bond is found between the water molecules (Tab. 4.3). This structure is comparable to $Fe(NCS)_2(\mathbf{1})_2$ (FESVIJ) [87], which shows a similar network in terms of the 2D sheets, but with a free ligand and methanol within the pores.

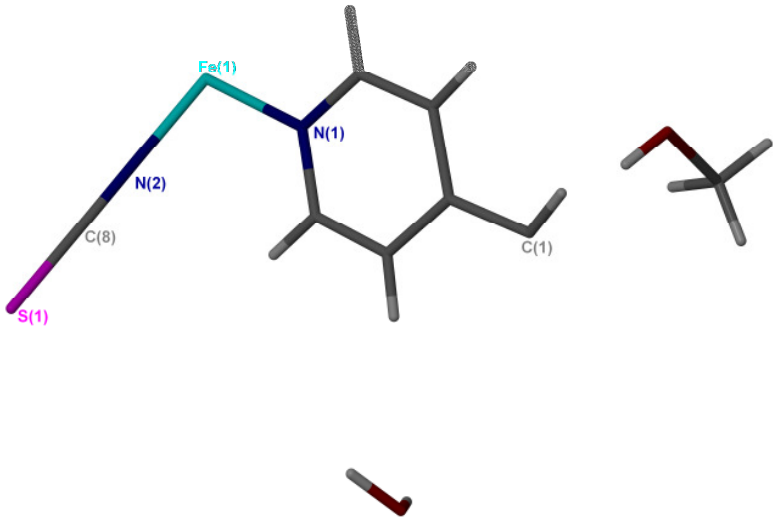

Figure 4.13: Asymmetric unit of the network **1n**.

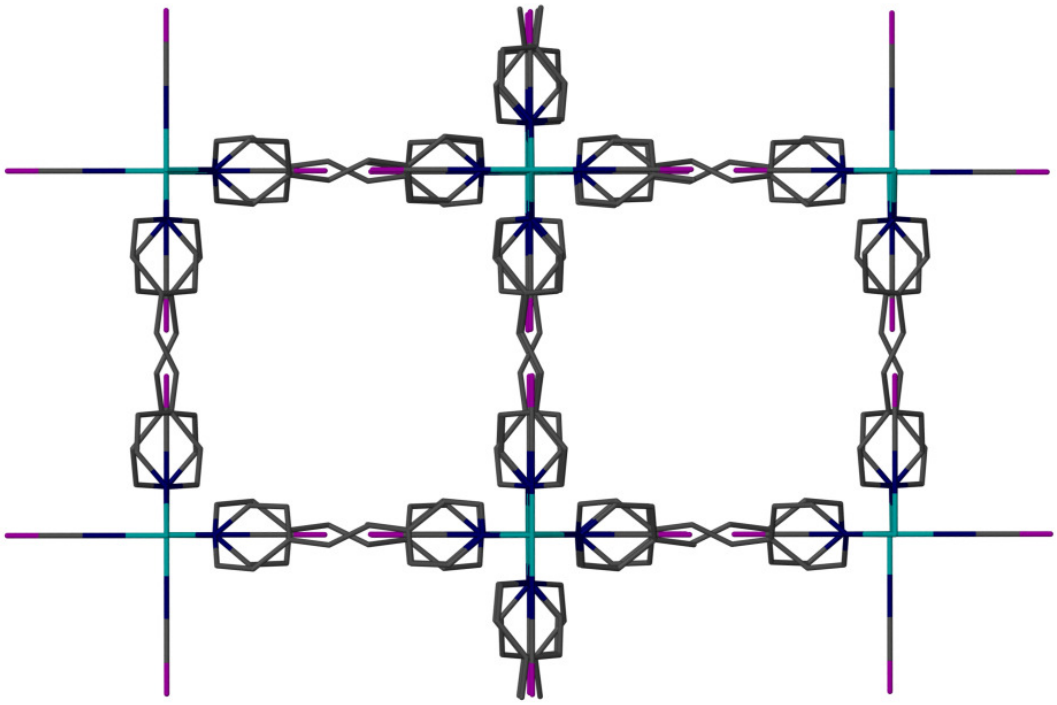

Figure 4.14: Porous iron network **1n** with solvent and hydrogens removed for clarity.

The complex of $Mn(NCS)_2(\mathbf{5})_2(H_2O)_2$ **5a** (Fig. 4.15) crystallises with methanol and ligand **5** in the monoclinic space group $P2_1/c$. The complex itself has the same features as the desired complexes, but because of the additional two ligand molecules within the unit cell a [2+2] cycloaddition reaction is impossible. The manganese ion is sitting in a distorted octahedral environment with all the ligands being *trans* to each other. The complex crystallises with half the molecule in the asymmetric unit and therefore the manganese is sitting on a centre of symmetry and N1 is related to N1' by the symmetry operation *-x, -y, -z*. The complete model with the hydrogen bonding is shown in Figure 4.16. The hydrogen bonding in the crystal structure involves the bound water molecules and two methanol molecules. Additionally there is hydrogen bonding between the methanol (O2) and the nitrogen of the free ligand (N3) (Tab. 4.3).

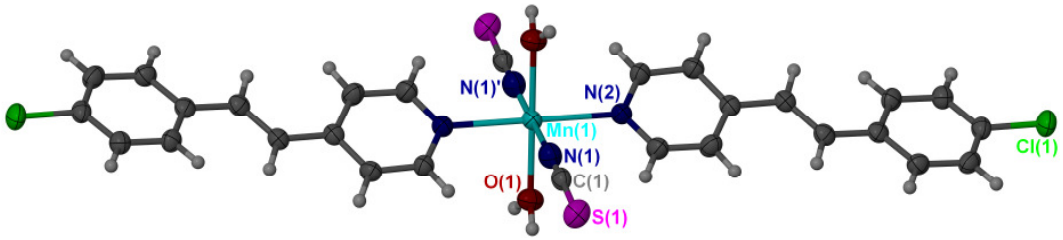

Figure 4.15: Modeled structure of the complex **5a** with 50 % ellipsoids shown and free ligands and methanol hidden.

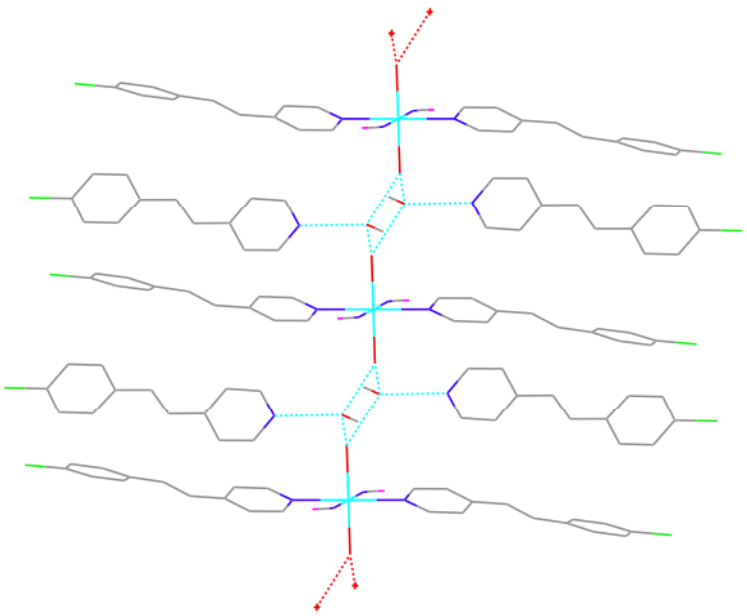

Figure 4.16: Hydrogen bonding and the whole structural model of **5a**.

Table 4.3: Hydrogen bonds within the metal thiocyanate complexes

Compound	DHA	DH / Å	HA / Å	DA / Å	Angle / °
1n	O1-H1A-O1	0.89	1.63	2.513 (12)	174
5a	O1-H1A-O2	0.85	1.91	2.747(2)	169
	O1-H1B-O2	0.88	1.86	2.733(2)	170
	O2-H2A-N3	0.97	1.71	2.676(2)	170

4.3. Metal Complexes with Other Halides

A number of other bromide and iodide structures with cobalt or manganese were also crystallised. Except for one structure with ligand **2**, all the other structures are with **1**. Four of these structures are cobalt structures, of which two are with iodide and two with bromide.

The complex of $[Co(\mathbf{2})_2(H_2O)_4]^{2+}$ **2a** with Br^- as the counterion (Fig. 4.17) crystallises with water and unbound **2** in the orthorhombic space group *Pccn*. The

complex is comparable to the cobalt structures with nitrate, as four water and two ligand molecules are bound to the octahedrally coordinated cobalt ion, which sits on a crystallographic centre of symmetry. The complex crystallises with half the molecule in the asymmetric unit and the bromides on special positions, each position accommodating half a bromide. Additionally one unbound ligand is found per asymmetric unit.

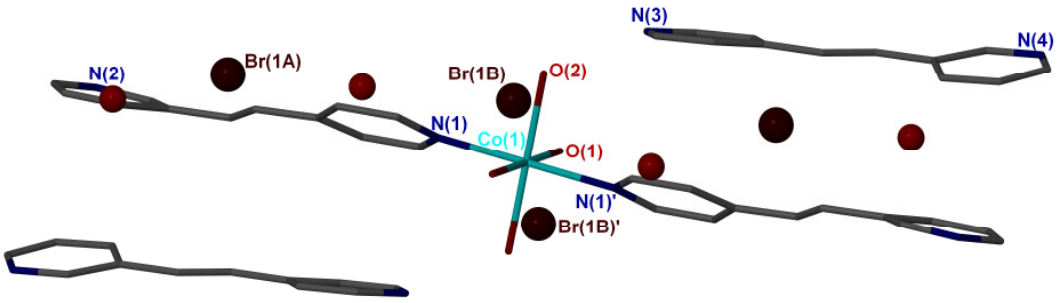

Figure 4.17: Structure of **2a** with hydrogens removed for clarity.

The extended structure which displays the hydrogen bonding is shown in Figure 4.18. The Br1B ion and N2 of the bound ligand align two complexes next to each other in one dimension through hydrogen bonding with the water molecules (O1) (Fig. 4.18a). Additionally, the hydrogen bonds between O2 and the free ligand (N3, N4) form the second dimension within the hydrogen bonding network (Fig. 4.18b). This network and π-π-stacking between the bound and unbound ligands would make a [2+2] cycloaddition reaction possible, as the two ligands are separated by 3.7 Å.

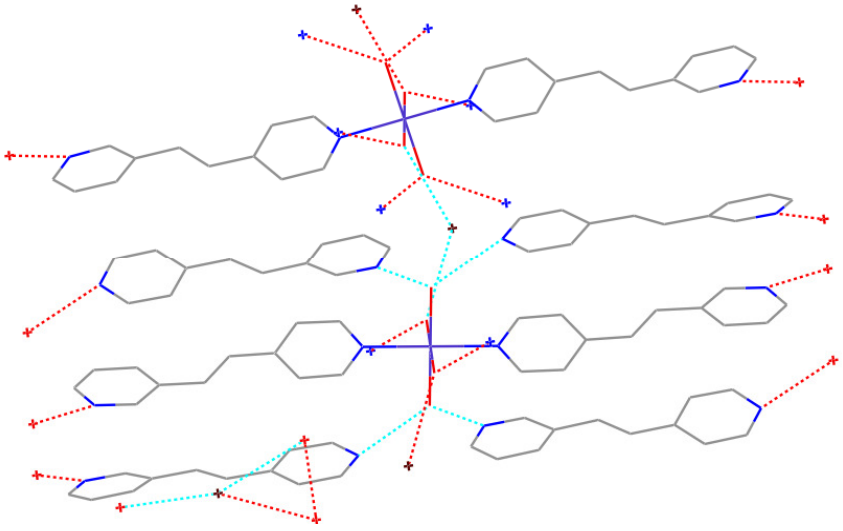

a

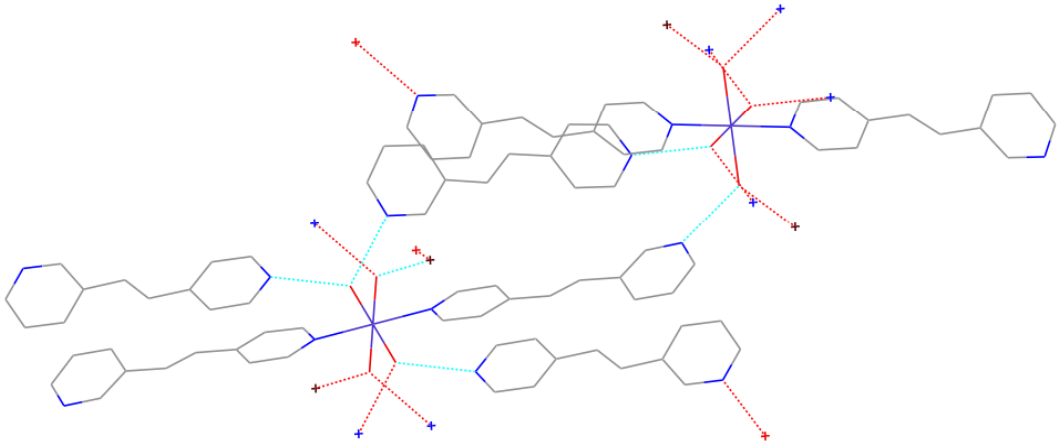

b

Figure 4.18: Hydrogen bonding within **2a** with hydrogens removed for clarity.

Cobalt salts crystallise with bromide and **1** to give $[Co(\mathbf{1})_3(H_2O)_2]^{2+}$ **1o** (Fig. 4.19), which forms a one dimensional chain. This structure crystallises in the triclinic space group *P*-1 with the cobalt sitting on a centre of inversion. The cobalt ion is again octahedrally coordinated with equivalent ligands being *trans* to each other. N1 is related to N1' by the symmetry operation *-x+1, -y, -z+1*. In addition to the complex and the two bromide ions, water and unbound **1** are found within the unit cell. Two of the unbounded ligands could potentially undergo a [2+2] cycloaddition reaction, as their double bonds are only separated by 3.7 Å. A possible reaction could also occur between the bound ligand and one of the unbound ones, which are 3.6 Å

apart and a third reaction might take place between two bound ligands (3.9 Å). To follow these possibilities up, a single crystal was irradiated with the UV lamp, but it decomposed during the irradiation. Afterwards UV-vis solid state measurements (Fig. 4.20) were performed on a powdered sample. The UV-vis spectra suggest that a reaction occurs, as the broad band around 300 nm decreases and a new band appears around 260 nm. As the transformation could not be followed by single crystal X-ray diffraction it has not been possible to confirm whether a [2+2] cycloaddition reaction has occurred. However, within the structure several pairs of molecules are aligned for the reaction to occur, it would also be possible that more than one of them takes place.

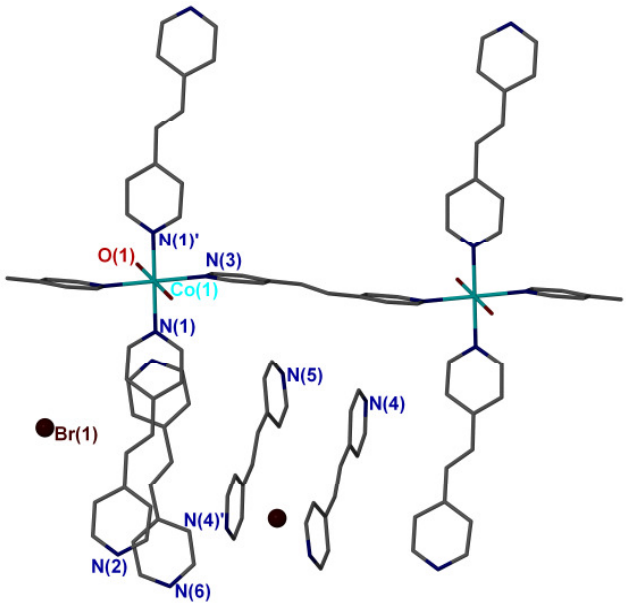

Figure 4.19: Structural model of **1o** with bromide. Hydrogens are removed for clarity.

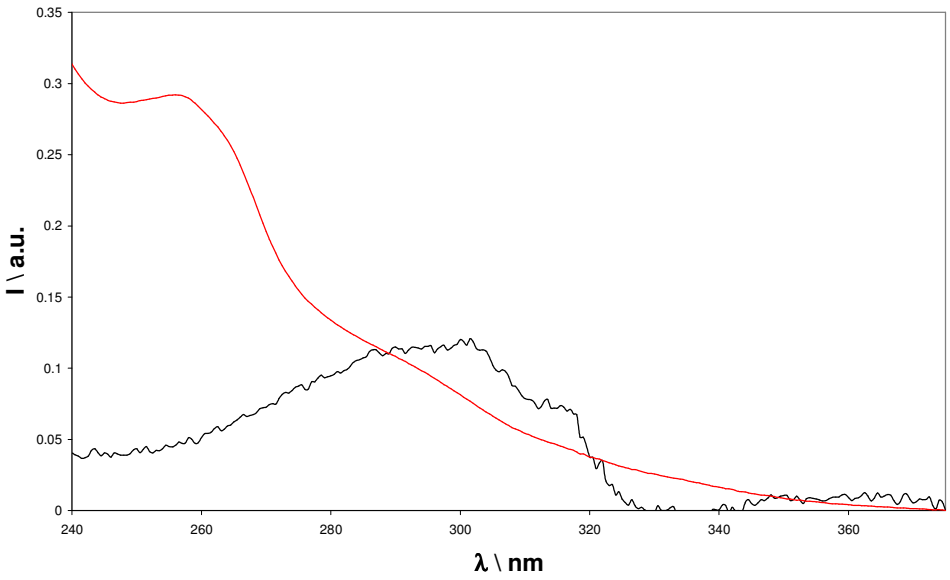

Figure 4.20: UV-vis spectra of **1o** before (black) and after (red) irradiation.

The hydrogen bonding of this complex is displayed in Figure 4.21. It is obvious that the different chains are stacked above each other through hydrogen bonding of the water molecules to the nitrogen (N2) of the ligand. This forms a two dimensional sheet structure. Additionally there is an extended hydrogen network, involving six membered rings of water molecules, which are additionally bound to the bromides and the unbound ligand molecules, which are stacked above each other through this network.

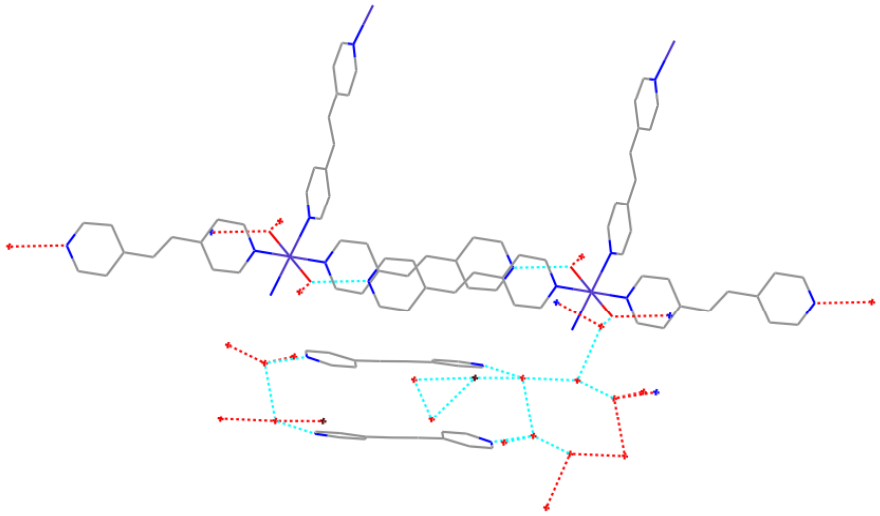

Figure 4.21: Hydrogen bonding model for **1o**, with hydrogens removed for clarity.

Switching the counter ion from bromide to iodide gives $[Co(H_2O)_2(MeOH)_2(\mathbf{1})_2]^{2+}$ **1p**, which crystallises in the monoclinic space group $P2_1$. The cobalt ion has octahedral geometry through the ligands, again with pairs of similar ligands *trans* to each other. The asymmetric unit contains $[Co(H_2O)_2(MeOH)_2(\mathbf{1})_2]^{2+}$, in addition to two non-complexed ligands, water and methanol molecules, as well as two iodine anions to balance the charge. The $[Co(H_2O)_2(MeOH)_2(\mathbf{1})_2]^{2+}$ units form a chain along the *a*-axis. One of the bridges between the pyridyl rings of an unbound ligand is disordered (Fig. 4.22) with a ratio of ca. 55:45. As displayed in Figure 4.23 there are hydrogen bonds between the coordinated and uncoordinated solvent molecules of the complex and the ligand of the adjacent complex, as well as to the unbound ligand through other water molecules. The iodine ions are not involved in any hydrogen bonding. The ligands of two different complexes are stacked appropriately for a [2+2] cycloaddition reaction, with an interplanar distance of 3.8 Å. A cyclisation reaction may also be possible between the free ligand and one ligand of the complex, as these are separated by 4.0 Å. However, after irradiation of a powdered sample no change was found within the UV-vis spectra, suggesting that no reaction occurs within the crystalline state.

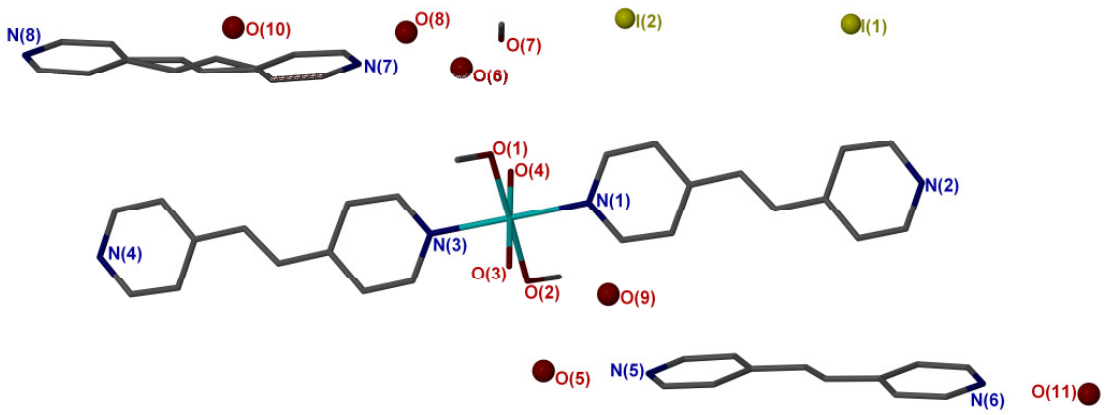

Figure 4.22: Structure of **1p** with iodine counter ions. The hydrogens are removed for clarity.

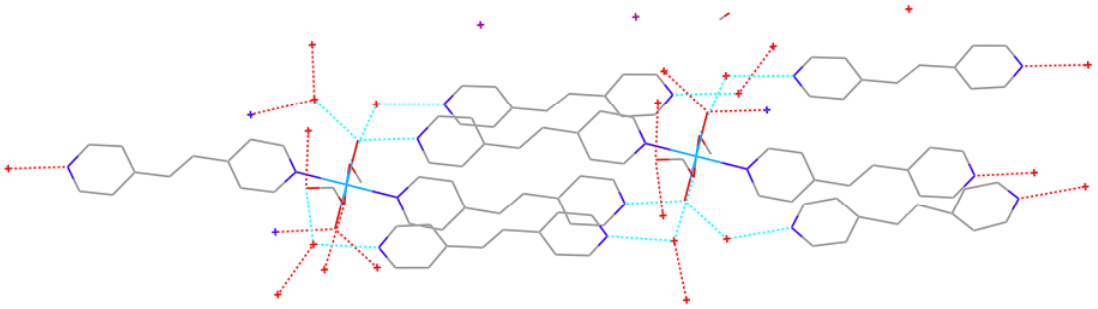

Figure 4.23: Display of the hydrogen network of **1p** with iodine counter anions. The hydrogens are removed for clarity.

Reaction of manganese salts with iodine salts and **1** gave the cationic chain structure $[Mn(\mathbf{1})_1(H_2O)_4]^{2+}$. In this structure **1q** the manganese centre is octahedrally coordinated by two ligands and four water molecules; the two ligands are *trans* to each other, forming the chain as both nitrogen atoms are bound to manganese (Fig. 4.24). The bounded ligand is disordered over the ethylene bridge in a ratio 75:25. Additionally three unbound ligands, water and two counter iodines are found within the unit cell. The manganese ion sits on an inversion centre as the structure crystallises in the triclinic space group *P*-1. N1 is related to N1' by the symmetry operation *-x, -y, -z+2*. The ligands are aligned through the hydrogen bond network in such a way that a [2+2] cycloaddition reaction might be possible (Fig. 4.25). The bound ligand is 3.9 Å away from the nearest unbound ligand, this ligand includes the nitrogens N2 and N3. The two unbounded ligands with N2 and N3 on the other hand

are too far apart to react. The iodine does not play a role within the network, as in the previously described iodine structure.

The possibility of a [2+2] cycloaddition reaction occuring in a solid state sample of this complex was tested using a series of UV-vis measurements. The spectra are shown in Figure 4.26, and the band at 295 nm disappears after irradiation with a UV lamp for 2.5 h. This change is consistent with the occurrence of a [2+2] cycloaddition reaction but the result is not conclusive.

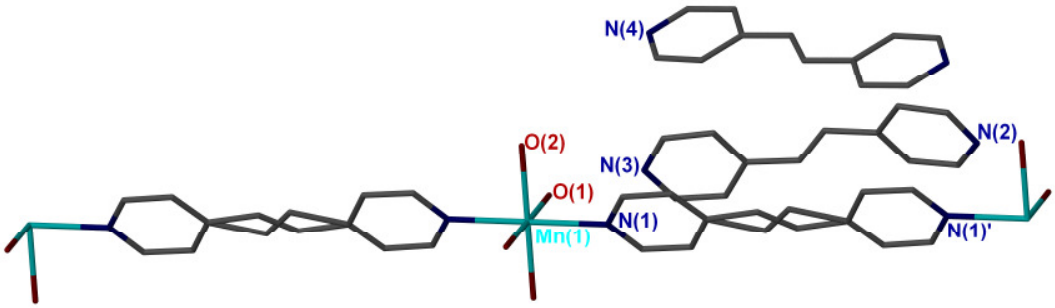

Figure 4.24: 1D-chain structure of **1q** with iodine and hydrogens removed for clarity.

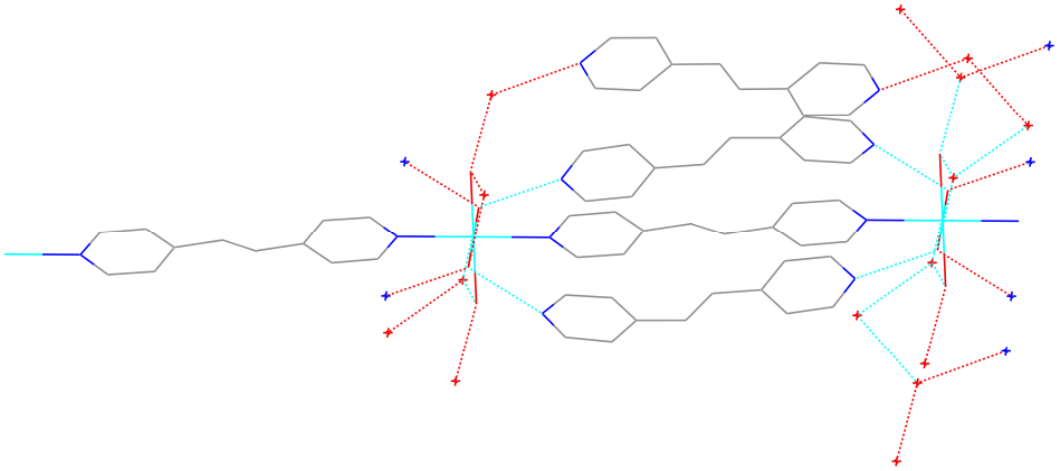

Figure 4.25: Aligning the ligands through hydrogen bonding in a ladder like structure within **1q**. The hydrogens are removed for clarity.

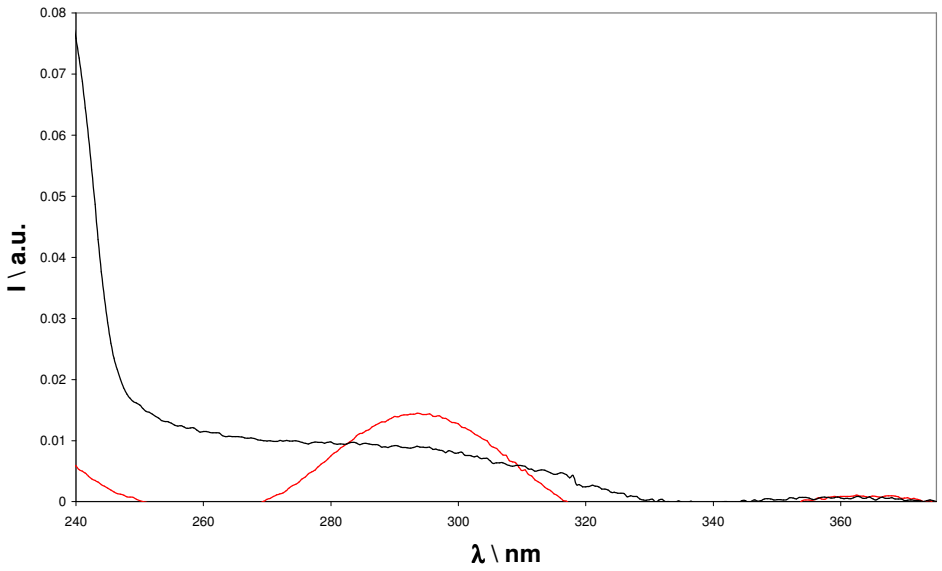

Figure 4.26: UV-vis spectra before (black) and after irradiation (red) of the complex **1q**.

Table 4.4: Hydrogen bonds within the metal halogen complexes

Compound	DHA	DH / Å	HA / Å	DA / Å	Angle / °
2a	O2-H2B-N3	0.85	1.94	2.783(8)	171
	O2-H2A-N4	0.84	1.94	2.764(8)	167
	O1-H1A-N2	0.86	1.93	2.782(9)	172
	O1-H1B-Br1B	0.86	2.54	3.320(6)	152
	O3-H3A-Br1B	0.86	2.72	3.440(13)	142
	O3-H3A-O3	0.86	2.03	2.62(2)	125
1o	O1-H1A-O2	0.76	1.91	2.662(2)	175
	O1-H1B-N2	0.80	1.93	2.730(2)	179
	O2-H2B-O4	0.85	1.93	2.778(3)	171
	O2-H2A-N6	0.86	2.00	2.842(2)	170
	O3-H3B-Br1	0.89	2.36	3.2451(18)	176
	O3-H3A-N4	0.87	1.94	2.804(3)	173
	O6-H6A-Br1	0.86	2.54	3.375(3)	164
	O6-H6B-O5	0.86	2.12	2.964(3)	169

	O5-H5B-O3	0.86	1.98	2.827(2)	169
	O4-H4B-O5	0.85	1.95	2.787(3)	168
	O4-H4A-O3	0.85	1.96	2.776(2)	161
	O5-H5A-N5	0.86	1.91	2.763(3)	172
1p	O4-H4A-O11	0.83	1.95	2.742(4)	158
	O7-H7A-I1	1.19	3.22	4.316(4)	153
	O11-H11A-I2	0.83	2.79	3.576(3)	161
	O6-H6B-N7	0.84	2.03	2.788(5)	150
	O11-H11B-N6	0.79	2.04	2.804(5)	163
	O8-H8A-O6	0.86	2.64	3.466(6)	162
	O9-H9A-O2	0.85	1.91	2.719(5)	159
	O9-H9B-O11	0.84	2.13	2.892(6)	150
	O10-H10A-I2	0.84	2.99	3.642(4)	136
	O10-H10B-I1	1.00	2.52	3.515(4)	171
	O5-H5B-N5	0.83	1.97	2.793(4)	172
	O4-H4B-N2	0.84	1.97	2.740(3)	154
	O1-H1A-O6	0.74	2.01	2.709(5)	160
	O5-H5A-I2	0.84	3.19	3.814(4)	133
	O3-H3A-N4	0.83	1.94	2.741(3)	160
	O3-H3B-O8	0.81	1.92	2.702(4)	163
	O2-H2A-O5	0.71	2.06	2.750(4)	163
1q	O5-H5A-O3	0.95	2.02	2.794(3)	137.1
	O1-H1A-N3	0.86	1.84	2.698(2)	175
	O1-H1B-N2	0.82	1.89	2.699(2)	168
	O2-H2A-O4	0.85	1.83	2.677(3)	176
	O2-H2B-O3	0.85	2.15	2.880(2)	145
	O3-H3A-I1	0.80	2.73	3.526(1)	176
	O3-H3B-O1	0.84	1.99	2.802(2)	163
	O4-H4A-N4	0.81	2.09	2.875(3)	164
	O4-H4B-O5	0.74	2.06	2.800(3)	171
	O5-H5B-I1	0.69	2.97	3.648(2)	168

The conclusion from the structures described within this chapter and Chapter 3 is that iron, cobalt and manganese prefer octahedral coordination geometry with the matching ligands being *trans* to each other. Additionally there is preferred coordination of water or alcohol molecules to the metal centres by comparison to nitrate or halide ligands, with only the structure of $[Mn(H_2O)_2(Br)_2(\mathbf{3})_2]$ **3d** being an exception. π-π-Stacking is a common feature of the complexes that contain these ligands. Surprisingly, the intention of preparing other ligands than **1** and **3** did not result in the same crystallisation properties for them. Therefore **1** and **3** form crystals of metal complexes more easily than **2**, **4** or **5**. Complexes with **1** often form chain structures or metal organic frameworks, following from the possibility of binding both nitrogens to two metal cations in a linear fashion.

4.4. Protonated Structures

A number of crystallisations were performed in an acidic environment, as a data search within the CCDC [92] showed many protonated structures with these ligands. Four different structures with tetrahedrally coordinated metals were found; the metal is always surrounded by chloride, which was picked up from the added HCl. The higher concentration of chloride compared to other anions within the solution moved the chemical equilibrium in this direction.

The first structure is an iron structure with **5** (**5b**) (Fig. 4.27), which crystallises in the orthorhombic space group $P2_12_12_1$. The asymmetric unit contains the anion $[Fe(III)Cl_4]^-$ and one protonated ligand **5**, which shows disorder of the whole molecule in a 9:1 ratio. Additionally, this structure displays a racemic twinning in a ratio of 7:3. No hydrogen bonding is found within the structure, but the ligands are aligned through π-π-stacking with a distance of ca. 3.7 Å, which is suitable for a [2+2] cycloaddition reaction in the solid state (Fig. 4.28). This reaction was followed by solid state UV-vis measurements. The spectra after the irradiation with UV light

does not show the distinct band at around 330 nm anymore and the data implies therefore that a solid state reaction takes place; this is shown in Figure 4.29.

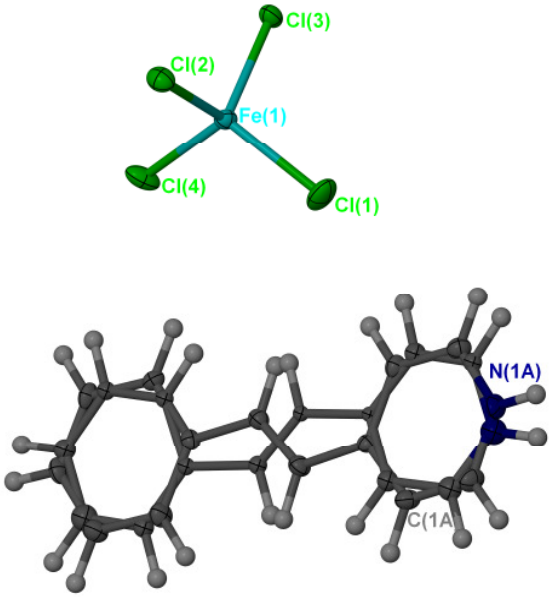

Figure 4.27: Display of the disordered structure of **5b** with 50 % ellipsoids shown.

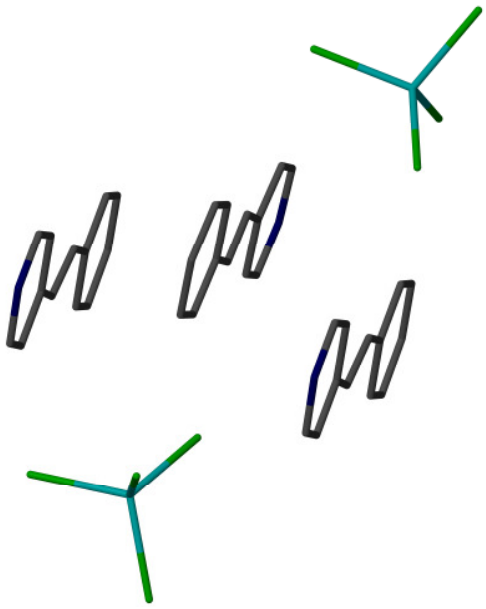

Figure 4.28: Stacking of the ligands in chains between the $[Fe(III)Cl_4]^-$ cluster. Hydrogens and disorder are removed for clarity.

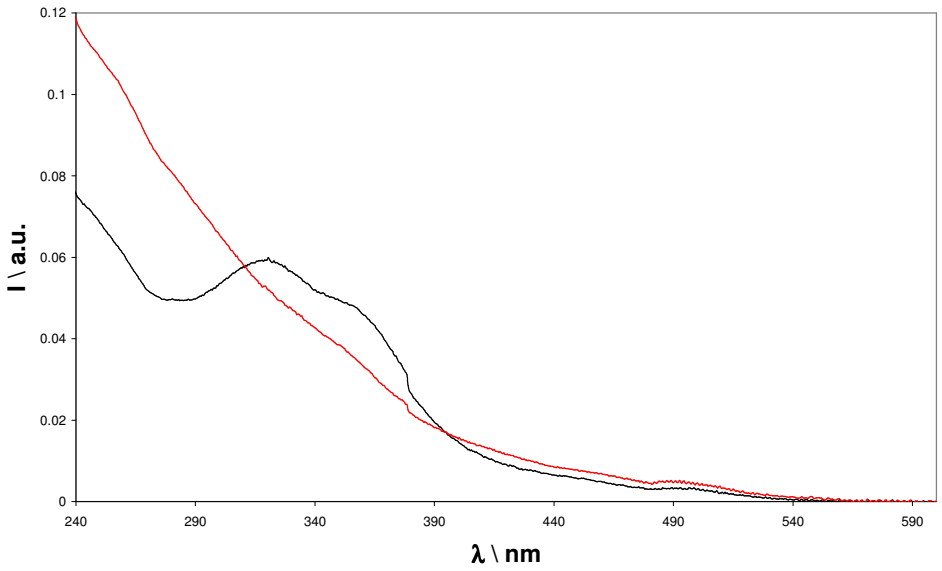

Figure 4.29: UV-vis specra of **5b** before (black) and after (red) irradiation of the crystals.

The other three structures all contain Co(II) anions, with only one of them being suitable for a solid state [2+2] cycloaddition reaction. They all have the same structural feature of one $[Co(II)Cl_4]^{2-}$ anion and one double protonated ligand.

The first cobalt structure is with **1** (**1r**); it crystallises in the monoclinic space group *C*2/*c*, with half a protonated **1** cation, half a water molecule and half a $CoCl_4^{2-}$ anion per asymmetric unit. Two halves of the ligand are related by the symmetry operation *-x, -y+1, -z* and two halves of the $CoCl_4^{2-}$ anion are related by

-x, y, -z+0.5. Hydrogen bonding is found between the water molecule and the anion, as well as between the protonated nitrogen of the ligand and the lone pairs of the oxygen (Fig. 4.30, Tab. 4.5).

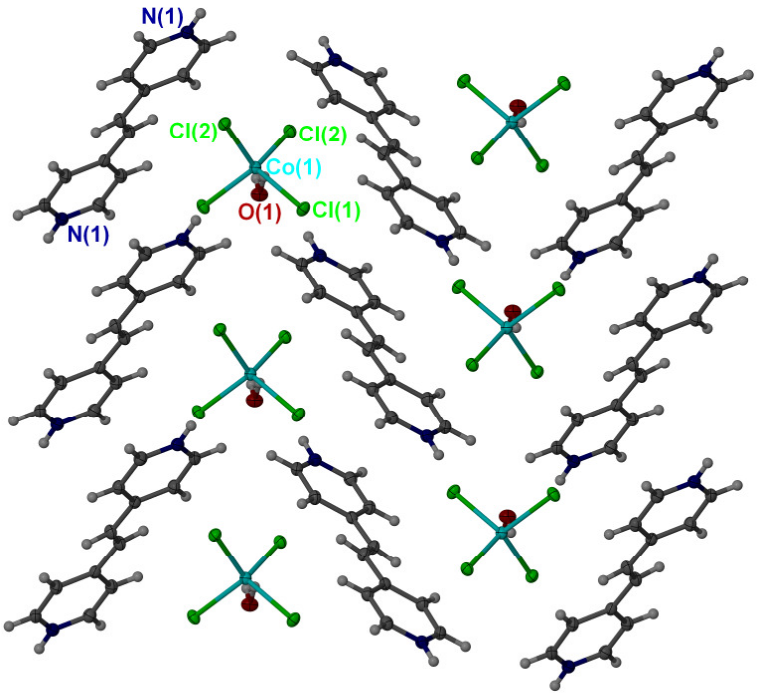

Figure 4.30: Packing of the crystal structure **1r** with 50 % ellipsoids shown.

The next structure also contains $[Co(II)Cl_4]^{2-}$ anions and protonated cations of **1** (**1s**), but in this case no water is found within the structure and a whole anion and cation is found per asymmetric unit. The structure crystallises in the monoclinic space group $P2_1/n$. The 3D structure is build from dimeric building blocks; each building block contains one asymmetric unit. The dimers are formed through hydrogen bonding between the protonated nitrogens and the chlorines of the anion, as seen in Figure 4.31.

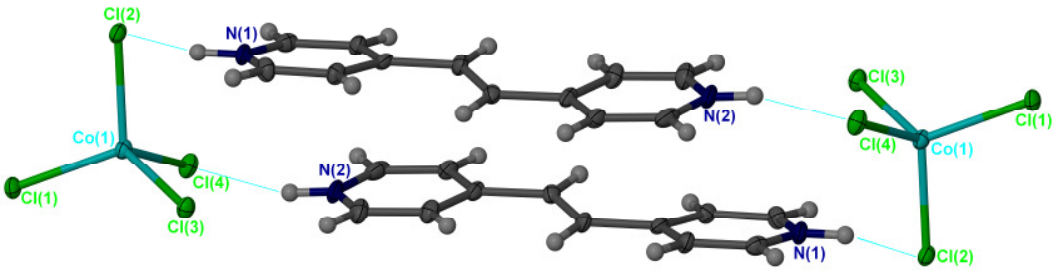

Figure 4.31: Dimer formed through hydrogen bonding with 50 % ellipsoids shown for the structure **1s**.

The last structure of this type is with **3** (**3e**) and it crystallises in the monoclinic space group $P2_1/c$, again with a whole $CoCl_4^{2-}$ anion and protonated **3** cation within the asymmetric unit. There is hydrogen bonding found between the protonated N2 and Cl2, as well as between the hydrogen on N1 and Cl3. The 3D structure is therefore build from ligand chains with the cobalt anion in rows between them (Fig. 4.32). This forms a ladder like pattern as shown in Figure 4.33.

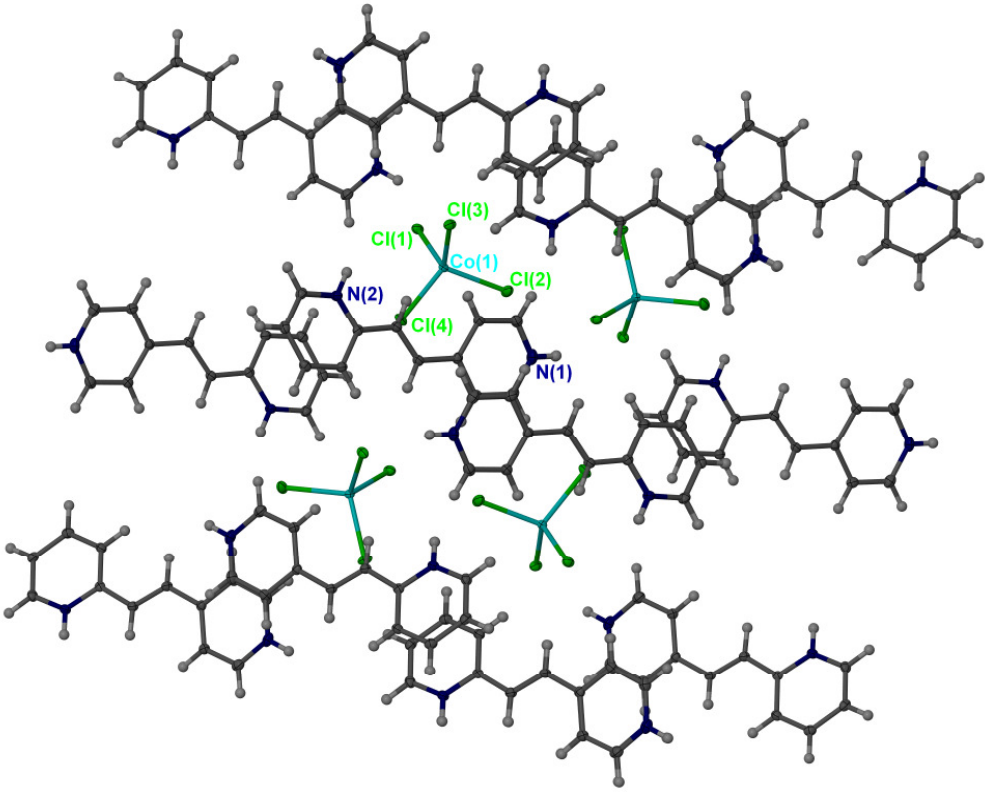

Figure 4.32: 3D structure of **3e**.

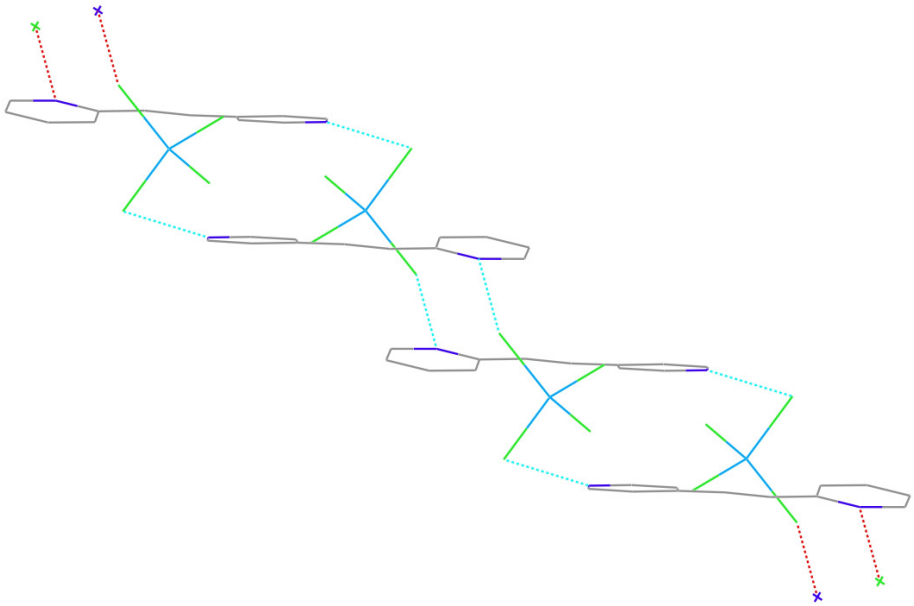

Figure 4.33: Hydrogen bonding in structure **3e** with hydrogens removed for clarity.

Table 4.5: Hydrogen bond table of the $[Co(II)(Cl)_4]^{2-}$ complexes

Compound	DHA	DH / Å	HA / Å	DA / Å	Angle / °
1r	N1-H1A-O1	0.88	2.06	2.787(1)	139.5
	O1-H1B-Cl2	0.95	2.21	3.132(1)	165.0
1s	N1-H1-Cl2	0.88	2.51	3.212(1)	137.8
	N2-H2-Cl4	0.88	2.29	3.111 (1)	156.2
3e	N1-H1A-Cl3	0.86	2.28	3.111(1)	160.9
	N2-H2A-Cl2	0.88	2.43	3.147(1)	139.5

4.5. Structures with Other Templates

Additional organic templates were also used in an attempt to align the ligands parallel to each other. Here *p*-benzoquinone **7** and resorcinol **8** are used, as both are known to align these kinds of pyridyl ligands in an appropriate manner [92].

The first structure is built from **7** and **1** in a 1:1 ratio. It crystallises in the monoclinic space group $P2_1/c$, with half a molecule of each component within the

asymmetric unit. Half the molecule of **7** is related by the symmetry operation *-x+1, -y, -z+1* and half the ligand is related to the other half by *-x, -y, -z*. There are short contacts of 2.7 Å between the oxygens of the template and the nitrogens of the ligand, forming a 1D chain (Fig. 4.34). These chains are packed parallel to each other, but the distance between the molecules is more than 6 Å, a [2+2]-cycloaddition reaction is therefore not possible.

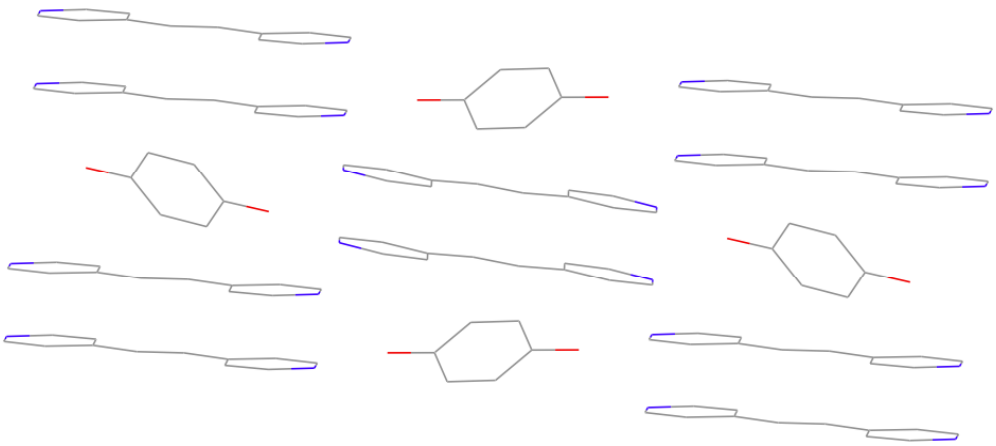

Figure 4.34: Chain structure of **7*1**.

A similar structure is formed between **7**, water and 1,2-bis(2-pyridyl)ethylene **9**, which crystallises in the monoclinic space group $P2_1/n$. Here half of the ligand **7** is related by the symmetry operation *-x, -y+1, -z+1*. The ratio between the three molecules is 1:2:2 and the crystal packing displays hydrogen bonding. Two water molecules and two ligand molecules form a ring as shown in Figure 4.35. Additional π-π-stacking (4 Å) between two ligands means a [2+2] cycloaddition reaction could possibly occur.

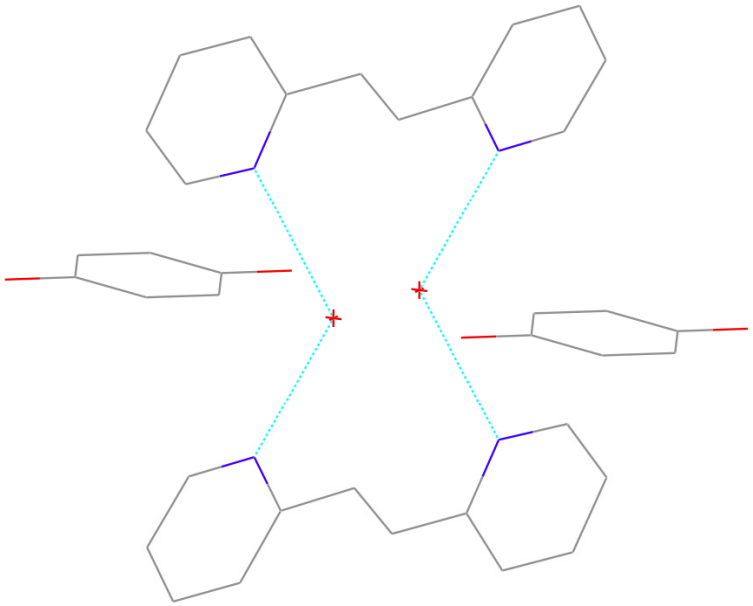

Figure 4.35: Hydrogen bonding between water and **9** in the structure with **7**.

A third structure is found between **7** and **4** in the ratio of 1:2. The molecules form a co-crystal in the space group $P2_1/c$. Half a molecule of **7** is related to the other half by the symmetry operation *-x, -y+1, -z+1* and by *–x+1, -y, -z+1*. One of the ligands within the structure shows disorder within the ethylene bridge of ca. 60:40. A [2+2] cycloaddition reaction is not possible as the ligands are separated by nearly 6 Å (Fig. 4.36). Short contacts (O-N = 2.7 Å) are found between the oxygen of the **7** and the nitrogen of the ligand. These short contacts between two negative polarised atoms are not unusual for **7**. Two other structures are found in a database search: BNQBRP (O-Br = 3.284 Å) [97] and GAPWEZ (O-I = 3.357 Å) [98].

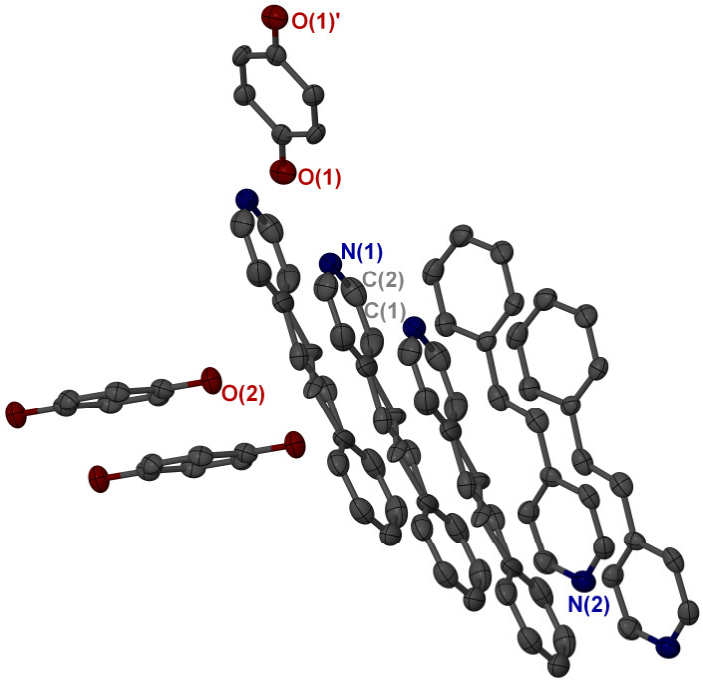

Figure 4.36: 3D packing of **4** and **7** with hydrogens removed for clarity.

The structure of the co-crystal of **8** and **5** crystallises in the triclinic space group *P*-1 in a 1:2 ratio. Both ligands show a very small amount of disorder within the double bond (below 6 %). The crystal packing displays hydrogen bonding and chlorine-chlorine-interactions. Two ligands are aligned parallel to each other through hydrogen bonding of the two hydroxyl groups of resorcinol and the lone pairs on the ligand nitrogen atoms. The distance between the two double bonds is 3.7 Å and therefore a [2+2] cycloaddition reaction could possibly occur. Two ligand molecules are additionally in a contact through halogen-halogen-interactions. The distance between the chlorines is 3.8 Å (Fig. 4.37). Even though that the structure is very similar to the ones from MACGILLIVRAY [13], which undergo a single crystal to single crystal transformation, the crystal of **8*5** decomposes under irradiation. The decomposition and the UV-vis data in Figure 4.38 suggest that a reaction takes place between the two molecules.

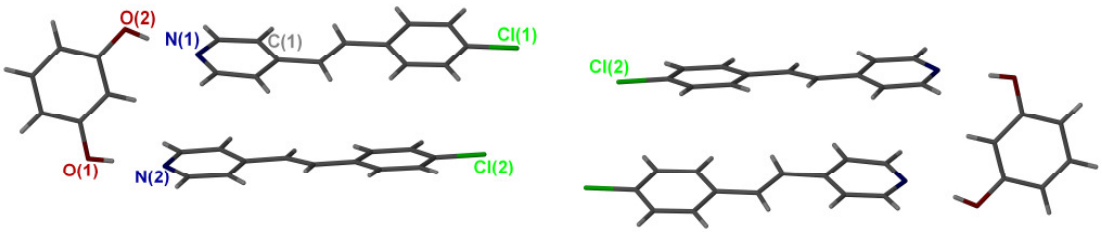

Figure 4.37: Hydrogen bonding between **8** and **5** and halogen-halogen-interactions.

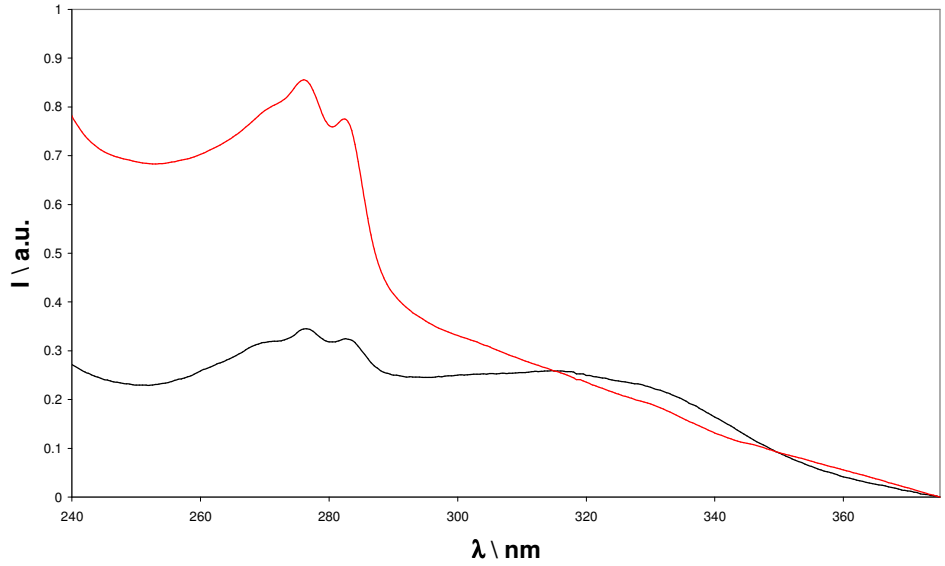

Figure 4.38: Solid state UV-vis spectra of **8** and **5** crystals before (black) and after irradiation (red).

8 also forms a co-crystal with **4**, which crystallises in the monoclinic space group $P2_1/c$ with one molecule each within the asymmetric unit. The nitrogen of the ligand N1 is related to N1' by the symmetry operation *-x+2, y-0.5, -z+0.5*. The packing is again dominated by hydrogen bonding. One resorcinol forms three hydrogen bonds, two as a donor of which one goes to a ligand molecule and one to oxygen in a different resorcinol (Tab. 4.6). This results in a ladder-like 2D network leaving the aromatic rings perpendicular to each other as shown in Figure 4.39. This and the displacement of the ligands away from each other make a reaction in the solid state impossible.

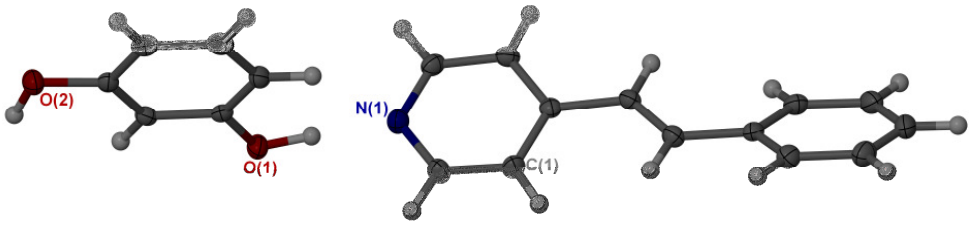

a

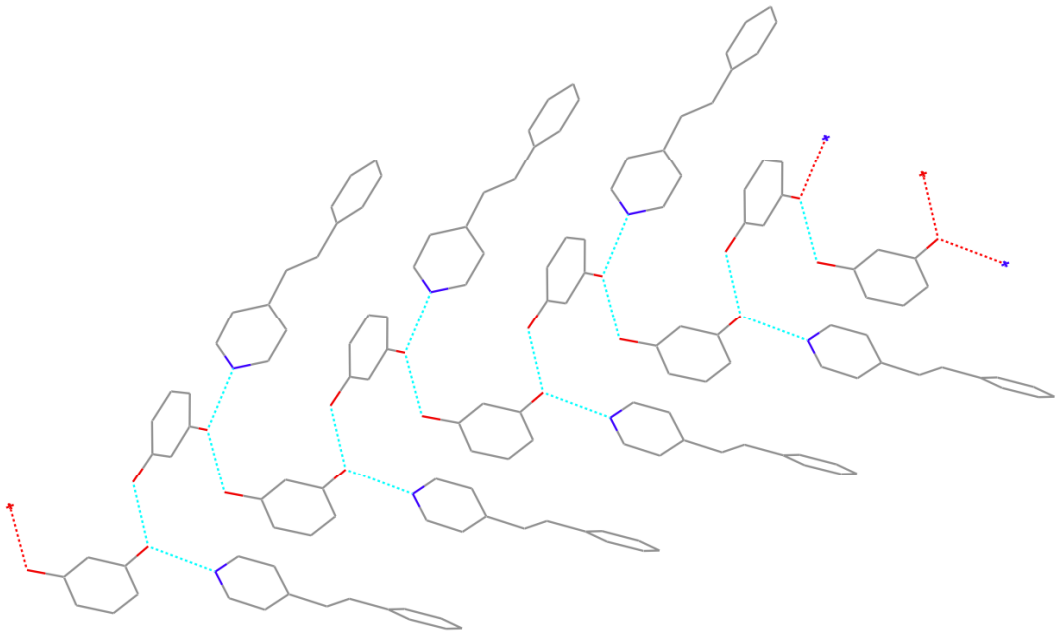

b

Figure 4.39: a) Asymmetric unit b) and ladder like structure of **8** and **4**.

Table 4.6: Hydrogen bond table of the resorcinol structures with ligand

Compound	DHA	DH / Å	HA / Å	DA / Å	Angle / °
8*4	O2-H2A-O1	0.97	1.72	2.686(1)	172
	O1-H1A-N1	1.01	1.61	2.622(1)	178
8*5	O2-H2A-N1	0.84	1.90	2.733(1)	175
	O1-H1A-N2	0.84	1.84	2.678(1)	173

4.6. Conclusion

Within this chapter it was shown that cobalt salts with ligand **1** display a variety of possibilities to crystallise out from methanol-water solutions. Additionally, the found complexes of manganese, iron and cobalt cations with ligands **1**-**5** and halides or pseudo-halides were described and characterised within this chapter. It was shown that complexes **1o** and **1q** might undergo a solid state reaction, as well as the protonated structure **5b** and the co-crystallised structure **8*5**.

4.7. Summary of Crystal Data

Table 4.7: Summary of crystal data for cobalt nitrate structures **1e** and **1f**

Compound	**1e**	**1f**
Empirical formula	C24 H33.34 Co0.5 N5 O8.9	C28 H38 Co0.50 N5 O8
Formula weight	564.42	602.10
T/K	150	150
Wavelength / Å	0.71073	0.71073
Crystal system	*P*-1	$P2_1/c$
Space group	triclinic	monoclinic
a/Å	10.2950(3)	14.6840(5)
b/Å	10.8260(3)	11.2510(4)
c/Å	15.3110(6)	16.8430(6)
α/°	72.217(1)	90
β/°	75.843(1)	97.266(2)
γ/°	62.977(1)	90
V/Å^3	1436.22(8)	2760.28(17)
Size/mm	0.60, 0.60, 0.50	0.20, 0.20, 0.10
Z	2	4
D_c/g cm^{-3}	1.305	1.449
μ/mm^{-1}	0.375	0.393
$2\theta_{max}$	60.40	59.68
Reflections collected	15721	35156
Independent reflections, R_{int}	6500, 0.0486	7146, 0.0921
Reflections obs. (> 2σ)	3630	4202
T_{min}/T_{max}	0.965	0.962
Final R_1, wR_2 [I>2σ(I)]	0.1013, 0.2962	0.0977, 0.2552
Final R_1, wR_2 (all data)	0.1737, 0.3432	0.1604, 0.2988

Table 4.8: Summary of crystal data for cobalt nitrate structures **1g** and **1h**

Compound	**1g**	**1h**
Empirical formula	C30 H33 Co0.50 N6 O7	C54 H55 Co N11 O16
Formula weight	619.09	1173.02
T/K	100	150
Wavelength / Å	0.69420	0.69420
Crystal system	*P*-1	*P*-1
Space group	triclinic	triclinic
a/Å	11.1280(12)	10.4394(11)
b/Å	11.6230(13)	16.7798(17)
c/Å	12.3856(14)	18.3950(19)
α/º	79.526(1)	67.416(1)
β/°	73.940(1)	85.511(1)
γ/°	79.280(1)	76.935(1)
V/Å^3	1498.1(3)	2898.0(5)
Size/mm	0.04, 0.04, 0.04	0.04, 0.04, 0.04
Z	2	2
D_c/g cm^{-3}	1.372	1.344
μ/mm^{-1}	0.363	0.373
$2\theta_{max}$	59.70	59.44
Reflections collected	17374	32632
Independent reflections, R_{int}	8880, 0.0520	16996, 0.0266
Reflections obs. (> 2σ)	6133	11973
T_{min}/T_{max}	0.742	0.800
Final R_1, wR_2 [I>2σ(I)]	0.0669, 0.1355	0.0639, 0.1814
Final R_1, wR_2 (all data)	0.0972, 0.1535	0.0917, 0.2033

Table 4.9: Summary of crystal data for cobalt thiocyanate structures **1d** and **1j**

Compound	**1d**	**1j**
Empirical formula	C15 H18 Co0.50 N3 O2 S	C32 H29 Co N7 O2 S2
Formula weight	333.85	666.67
T/K	150	120
Wavelength / Å	0.69430	0.69430
Crystal system	*I*-4	*P*-1
Space group	tetragonal	triclinic
a/Å	15.879(3)	8.7485(9)
b/Å	15.879(3)	11.2911(12)
c/Å	15.249(3)	17.7185(18)
α/º	90	100.857(1)
β/°	90	102.236(1)
γ/°	90	96.268(1)
V/Å^3	3845.0(11)	1659.5(3)
Size/mm	0.06, 0.03, 0.03	0.05, 0.03, 0.03
Z	8	2
D_c/g cm^{-3}	1.153	1.334
μ/mm^{-1}	0.592	0.682
$2\theta_{max}$	59.56	59.56
Reflections collected	21889	18488
Independent reflections, R_{int}	5873, 0.0725	9688, 0.0341
Reflections obs. (> 2σ)	3383	7281
T_{min}/T_{max}	0.983	0.987
Final R_1, wR_2 [I>2σ(I)]	0.0857, 0.2421	0.0545, 0.1410
Final R_1, wR_2 (all data)	0.1398, 0.2884	0.0759, 0.1514
Flack parameter	0.56(6)	

Table 4.10: Summary of crystal data for cobalt thiocyanate structures **1k** and **1m**

Compound	**1k**	**1m**
Empirical formula	C26 H22 Co N6 O S2	C14 H10 Co N4 S2
Formula weight	557.55	357.31
T/K	150	120
Wavelength / Å	0.69390	0.69430
Crystal system	*Fdd*2	*P*-1
Space group	orthorhombic	triclinic
a/Å	25.622(10)	5.661(4)
b/Å	45.272(16)	8.308(6)
c/Å	9.878(4)	8.853(7)
α/º	90	106.099(10)
β/°	90	101.657(10)
γ/°	90	99.522(10)
V/Å^3	11459(7)	380.8(5)
Size/mm	0.03, 0.03, 0.02	0.08, 0.04, 0.04
Z	16	1
D_c/g cm^{-3}	1.293	1.558
μ/mm^{-1}	0.773	1.397
$2\theta_{max}$	48.26	59.66
Reflections collected	21053	7586
Independent reflections, R_{int}	4877, 0.0990	2258
Reflections obs. (> 2σ)	3781	1341
T_{min}/T_{max}	0.992	0.947
Final R_1, wR_2 [I>2σ(I)]	0.0857, 0.1985	0.0884, 0.2698
Final R_1, wR_2 (all data)	0.1097, 0.2117	0.1464, 0.2940
Flack parameter	0.18(4)	

Table 4.11: Summary of crystal data for other metal thiocyanate structures

Compound	**1n**	**5a**
Empirical formula	C7.5 H11 Fe0.25 N1.5 O2 S0.5	C28 H26 Cl2 Mn0.5 N3 O2 S
Formula weight	184.17	566.95
T/K	150	150
Wavelength / Å	0.6942	0.71073
Crystal system	tetragonal	monoclinic
Space group	*P*4/*ncc*	$P2_1/c$
a/Å	15.290(5)	12.0040(3)
b/Å	15.290(5)	7.8830(2)
c/Å	15.624(5)	29.7160(7)
α/º	90	90
β/°	90	100.138(2)
γ/°	90	90
V/Å^3	3653(2)	2768.05(12)
Size/mm	0.05, 0.04, 0.04	0.30, 0.20, 0.10
Z	16	4
D_c/g cm^{-3}	1.340	1.360
μ/mm^{-1}	0.581	0.558
$2\theta_{max}$	61.02	60.98
Reflections collected	38897	35990
Independent reflections, R_{int}	2794, 0.0777	7832, 0.0847
Reflections obs. (> 2σ)	1842	4692
T_{min}/T_{max}	0.741	0.821
Final R_1, wR_2 [I>2σ(I)]	0.0512, 0.1468	0.0465, 0.0946
Final R_1, wR_2 (all data)	0.0794, 0.1711	0.1051, 0.1128

Table 4.12: Summary of crystal data for other metal halide structures (**2a**, **1o**)

Compound	**2a**	**1o**
Empirical formula	C24 H25.7 Br Co0.5 N4 O2.8	C36 H42.74 Br Co0.5 N6 O6.38
Formula weight	524.82	770.88
T/K	120	150
Wavelength / Å	0.71073	0.71073
Crystal system	orthorhombic	triclinic
Space group	*Pccn*	*P*-1
a/Å	11.4267(5)	10.3810(2)
b/Å	15.9491(12)	12.6810(2)
c/Å	25.6692(17)	14.7490(2)
α/º	90	95.203(1)
β/°	90	90.449(1)
γ/°	90	106.651(1)
V/Å^3	4678.1(5)	1851.34(5)
Size/mm	0.20, 0.11, 0.07	0.60, 0.30, 0.10
Z	8	2
D_c/g cm^{-3}	1.490	1.383
μ/mm^{-1}	2.132	1.380
$2\theta_{max}$	52.74	61.16
Reflections collected	32824	34206
Independent reflections, R_{int}	4785, 0.1089	11212, 0.0362
Reflections obs. (> 2σ)	2762	9251
T_{min}/T_{max}	0.53505	0.936
Final R_1, wR_2 [I>2σ(I)]	0.0854, 0.1915	0.0482, 0.1285
Final R_1, wR_2 (all data)	0.1477, 0.2099	0.0619, 0.1375

Table 4.13: Summary of crystal data for other metal halide structures (**1p**, **1q**)

Compound	**1p**	**1q**
Empirical formula	C50.5 H65.5 Co I2 N8 O10.5	C24 H30 I Mn0.50 N4 O5
Formula weight	1265.35	608.89
T/K	150	150
Wavelength / Å	0.71073	0.71073
Crystal system	monoclinic	Triclinic
Space group	$P2_1$	P-1
a/Å	14.6789(2)	9.7760(2)
b/Å	11.7014(1)	10.9380(2)
c/Å	16.3721(3)	13.9590(2)
α/º	90	107.719(1)
β/°	98.563(2)	100.213(1)
γ/°	90	104.811(1)
V/Å^3	2780.78(7)	1320.79(4)
Size/mm	0.30, 0.20, 0.14	0.40, 0.40, 0.40
Z	2	2
D_c/g cm^{-3}	1.511	1.531
μ/mm^{-1}	1.481	1.480
$2\theta_{max}$	65.48	60.38
Reflections collected	28013	22334
Independent reflections, R_{int}	16967, 0.0231	7063, 0.0449
Reflections obs. (> 2σ)	13020	6488
T_{min}/T_{max}	0.80609	0.7692
Final R_1, wR_2 [I>2σ(I)]	0.0396, 0.0896	0.0293, 0.0706
Final R_1, wR_2 (all data)	0.0543, 0.0929	0.0348, 0.0756
Flack parameter	0.766(11)	

Table 4.14: Summary of crystal data for protonated structures **5b** and **1r**

Compound	**5b**	**1r**
Empirical formula	C13 H12 Cl4 Fe N	C12 H12 Cl4 Co N2
Formula weight	379.89	384.97
T/K	100	150
Wavelength / Å	0.71073	0.71073
Crystal system	orthorhombic	monoclinic
Space group	$P2_12_12_1$	$P2_1/c$
a/Å	6.5296(2)	7.7095(1)
b/Å	14.9893(3)	12.4822(2)
c/Å	15.9562(3)	15.9436(2)
α/º	90	90
β/°	90	102.218(2)
γ/°	90	90
V/Å^3	1561.70(6)	1499.52(4)
Size/mm	0.12, 0.10, 0.08	0.40, 0.30, 0.30
Z	4	4
D_c/g cm^{-3}	1.616	1.705
μ/mm^{-1}	1.634	1.842
$2\theta_{max}$	65.26	64.98
Reflections collected	17339	8481
Independent reflections, R_{int}	5329, 0.0199	4879, 0.0149
Reflections obs. (> 2σ)	5000	4092
T_{min}/T_{max}	0.782	0.916
Final R_1, wR_2 [I>2σ(I)]	0.0183, 0.0447	0.0226, 0.0542
Final R_1, wR_2 (all data)	0.0204, 0.0450	0.0296, 0.0554
Flack parameter	0.710(8)	

Table 4.15: Summary of crystal data for protonated structures **1s** and **3e**

Compound	**1s**	**3e**
Empirical formula	C12 H12 Cl4 Co N2	C6 H7 Cl2 Co0.5 N1 O0.5
Formula weight	384.97	201.49
T/K	100	150
Wavelength / Å	0.71073	0.71073
Crystal system	monoclinic	monoclinic
Space group	$P2_1/n$	$C2/c$
a/Å	7.8786(2)	7.6210(2)
b/Å	17.9063(4)	12.8745(3)
c/Å	11.3804(4)	16.3183(3)
α/º	90	90
β/°	107.421(3)	97.182(2)
γ/°	90	90
V/Å^3	1531.86(7)	1588.53(6)
Size/mm	0.20, 0.10, 0.05	0.31, 0.26, 0.17
Z	4	8
D_c/g cm^{-3}	1.669	1.685
μ/mm^{-1}	1.803	1.748
$2\theta_{max}$	65.22	65.62
Reflections collected	9875	7939
Independent reflections, R_{int}	5065, 0.0396	2698, 0.0195
Reflections obs. (> 2σ)	2820	2281
T_{min}/T_{max}	0.887	0.808
Final R_1, wR_2 [I>2σ(I)]	0.0322, 0.0486	0.0267, 0.0755
Final R_1, wR_2 (all data)	0.0773, 0.0517	0.0335, 0.0770

Table 4.16: Summary of crystal data for structures with **7** (**7*9** and **7*1**)

Compound	**7*9**	**7*1**
Empirical formula	C15 H14 N2 O2	C9 H7 N O
Formula weight	254.28	145.16
T/K	150	150
Wavelength / Å	0.71073	0.71073
Crystal system	monoclinic	monoclinic
Space group	$P2_1/n$	$P2_1/c$
a/Å	8.5650(3)	6.0040(3)
b/Å	19.1630(6)	17.2720(8)
c/Å	8.8990(3)	7.1210(4)
α/º	90	90
β/°	113.529(2)	92.521(2)
γ/°	90	90
V/Å^3	1339.17(8)	737.74(7)
Size/mm	0.40, 0.30, 0.30	0.30, 0.20, 0.20
Z	4	4
D_c/g cm^{-3}	1.261	1.307
μ/mm^{-1}	0.085	0.087
$2\theta_{max}$	60.32	59.66
Reflections collected	18877	4762
Independent reflections, R_{int}	3653, 0.0623	1893, 0.0315
Reflections obs. (> 2σ)	2446	1425
T_{min}/T_{max}	0.827	0.959
Final R_1, wR_2 [I>2σ(I)]	0.0530, 0.1282	0.0543, 0.1418
Final R_1, wR_2 (all data)	0.0909, 0.1485	0.0745, 0.1575

Table 4.17: Summary of crystal data for structure with **7** (**7*4**)

Compound	**7*4**
Empirical formula	C32 H26 N2 O2
Formula weight	470.55
T/K	150
Wavelength / Å	0.71073
Crystal system	monoclinic
Space group	$P2_1/c$
a/Å	18.409(3)
b/Å	5.8945(6)
c/Å	24.236(3)
α/°	90
β/°	105.974(13)
γ/°	90
V/Å^3	2528.4(5)
Size/mm	0.23, 0.18, 0.05
Z	4
D_c/g cm^{-3}	1.236
μ/mm^{-1}	0.077
$2\theta_{max}$	52,74
Reflections collected	11496
Independent reflections, R_{int}	5173, 0.0683
Reflections obs. (> 2σ)	1928
T_{min}/T_{max}	0.961
Final R_1, wR_2 [I>2σ(I)]	0.0472, 0.0743
Final R_1, wR_2 (all data)	0.1625, 0.091

Table 4.18: Summary of crystal data for structures with **8**

Compound	**8*5**	**8*4**
Empirical formula	C32 H26 Cl2 N2 O2	C19 H17 N O2
Formula weight	541.45	291.34
T/K	120	100
Wavelength / Å	0.71073	0.71073
Crystal system	triclinic	monoclinic
Space group	*P*-1	$P2_1/c$
a/Å	9.9237(5)	9.7367(2)
b/Å	10.1600(4)	7.9643(2)
c/Å	13.8231(6)	19.7146(5)
α/º	105.320(3)	90
β/°	98.283(4)	94.616(2)
γ/°	92.215(3)	90
V/Å^3	1325.86(10)	1523.83(6)
Size/mm	0.36, 0.19, 0.09	0.35, 0.27, 0.22
Z	2	4
D_c/g cm^{-3}	1.356	1.270
μ/mm^{-1}	0.278	0.082
$2\theta_{max}$	65.36	65.22
Reflections collected	25116	12619
Independent reflections, R_{int}	8879, 0.0265	5102, 0.0335
Reflections obs. (> 2σ)	5631	2960
T_{min}/T_{max}	0.957	0.98921
Final R_1, wR_2 [I>2σ(I)]	0.0403, 0.0966	0.0419, 0.0790
Final R_1, wR_2 (all data)	0.0699, 0.1028	0.0842, 0.0851

5. Linkage Isomerism in Nickel-Nitrite-Complexes

This chapter gives an overview about four nickel complexes and their behaviour under non-ambient conditions. This means specifically for our systems, irradiation with different light sources at low temperatures and complementary studies at high temperature. The experiments described in this section investigate the complexes of $[Ni(L)_2(NO_2)_2]$ where L = 1-(2-aminoethyl)piperidine (aep), 1-(2-aminoethyl)pyrolidine (aepy) and 1-(2-aminoethyl)morpholine (aem). As can be seen in Figure 5.1, it is possible to chemically synthesise $[Ni(aep)_2(NO_2)_2]$ in two forms (**10** and **11**). These are the nitro and the *exo*-nitrito complex structures, which were found by CHAUDHURI [44]. The initial experiment was therefore undertaken on the nitro-form, since it was known that an excitation of this complex was possible. The crystals of the two forms are easily distinguished by colour, as the nitro form is purple and nitrito isomer is blue. Following from these results the other two complexes were also investigated to examine how important small differences within the ligands are and to determine the activity of the complexes.

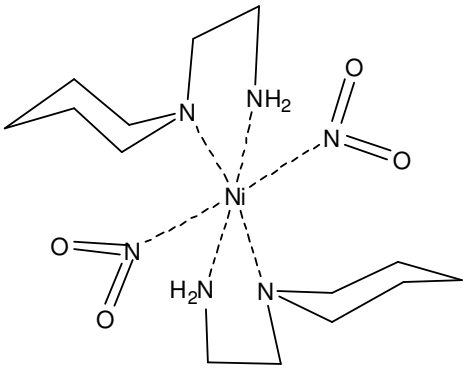

trans-bis[1-(2-aminoethyl)-piperidine]dinitronickel(II) **10**

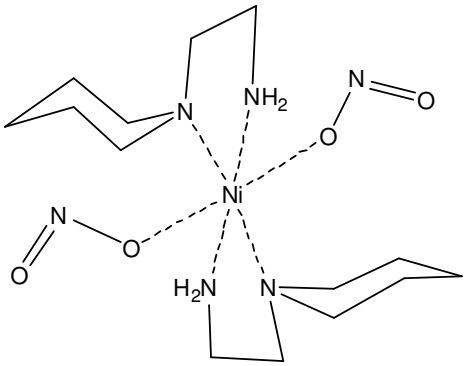

trans-bis[1-(2-aminoethyl)-piperidine]dinitritonickel(II) **11**

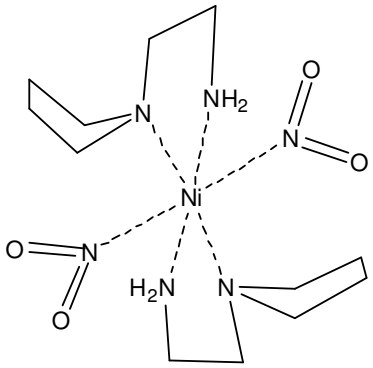

trans-bis[1-(2-amino-ethyl)-pyrolidine] dinitronickel(II) **12**

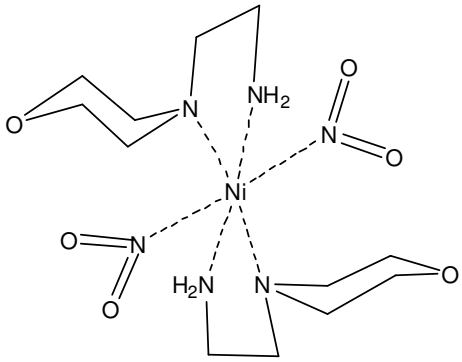

trans-bis[1-(2-aminoethyl)-morpholine]dinitronickel(II) **13**

Figure 5.1: Ni-complexes for linkage isomerism.

5.1. Photocrystallography

5.1.1. $[Ni(aep)_2(NO_2)_2]$ 10 and 11

As discussed above both isomers (nitro **10** and nitrito **11**) can be chemically synthesised [44]. **10** (Fig. 5.2) crystallises in the monoclinic space group $P2_1/c$, with half the molecule in the asymmetric unit. The nickel atom sits on an inversion centre and has octahedral coordination geometry. The four nitrogen atoms of the diamine part of

the ligands (N2, N3) and their centrosymmetrically related atoms are defined as the equatorial plane. The two nitro groups are *trans* to each other and η^1 coordinated to the metal centre, N1 is related to N1' by the symmetry operation *–x+1, -y, -z*. There is *ca.* 18 % disorder present involving the ethyl carbon atoms C1 and C2 and part of the piperidine ring, which was modelled with partial occupancies for each atom summed to unity. The crystal packing reveals two short contacts with donor-acceptor distances of 3.183(2) Å between N2···O1 and 2.909(2) Å between N2···O2, their NHO angles are 118° and 122° respectively.

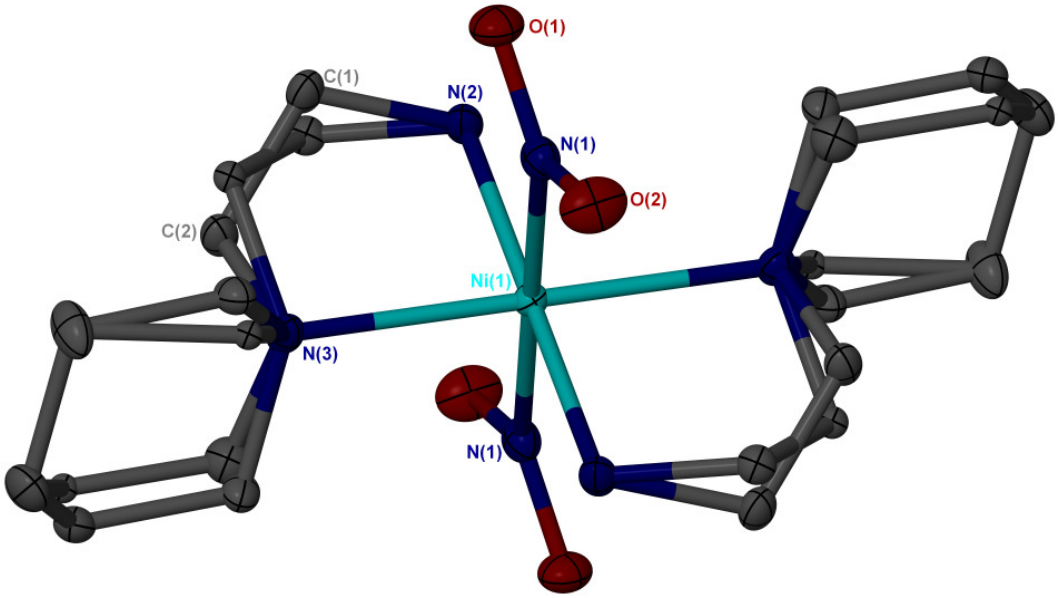

Figure 5.2: Ground state structure of **10** at 100 K with 50 % ellipsoids shown and hydrogens removed for clarity.

On the other hand, **11** has the molecular structure shown in Figure 5.3. The difference between the two structures is the coordinating atom of the nitrite to nickel. Instead of being bound through the nitrogen as in Figure 5.2, the nitrito form is bound η^1 through the oxygen and describes the *exo* conformation. The molecule crystallises in the orthorhombic space group *Pbca* without any disorder found within the ligand. The asymmetric unit is again half of the molecule with the nickel atom sitting on a crystallographic centre of symmetry, therefore O1 is related to O1' by the symmetry operation *–x+1, -y, -z+1*. The structure includes two short contacts as well; they are

situated between N2···O1 (3.388(3) Å, 146°) and N2···O2 (3.1031(14) Å, 116°).

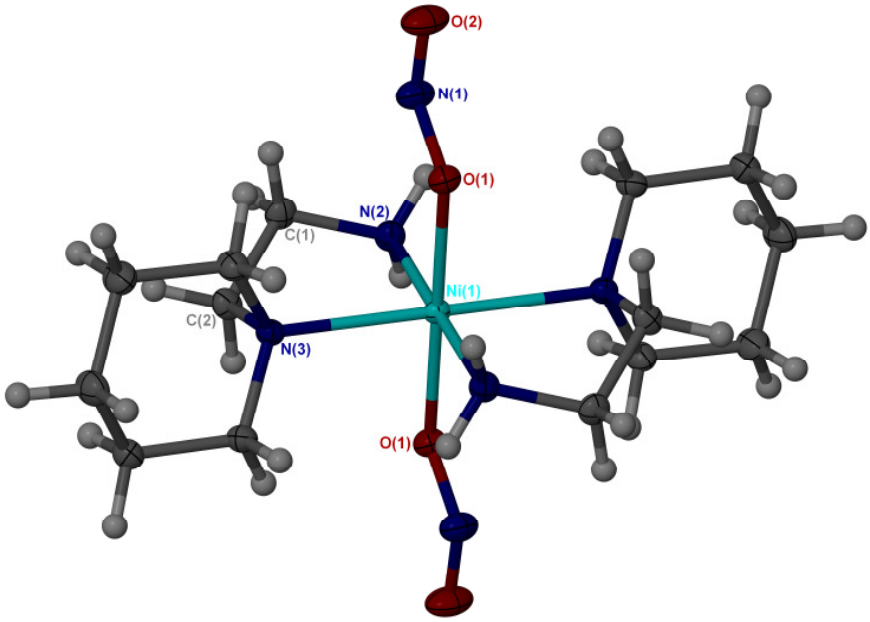

Figure 5.3: Ground state structure of **11** at 150 K with 50 % ellipsoids shown.

The crystal structure, which was obtained after irradiation of the nitro form **10*** at 90 K, is illustrated in Figure 5.4. The space group is maintained as $P2_1/c$, but the disorder around the aminoethylpiperidine ligand is increased up to 30 %, perhaps following from the need for more flexibility around the nitrite group, where now two different isomers are found. These are the nitro η^1-N-bound isomer as the main component (83 %) and the *endo* η^1-O-bound nitrito isomer with up to 17 %. Even though the *exo* form is thermodynamically more stable than the *endo* form, the latter needs less movement in the crystal (Fig. 5.5) and is therefore found here. The excitation was modelled as disorder and the percentages are calculated over the free variables. The peaks for N1A and O1A were easily identified in the electron density map. O2A on the other hand is to close to O2, so that it was necessary to duplicate O2 and let it refine freely. Only the main component for the disorder was refined anisotropically [99].

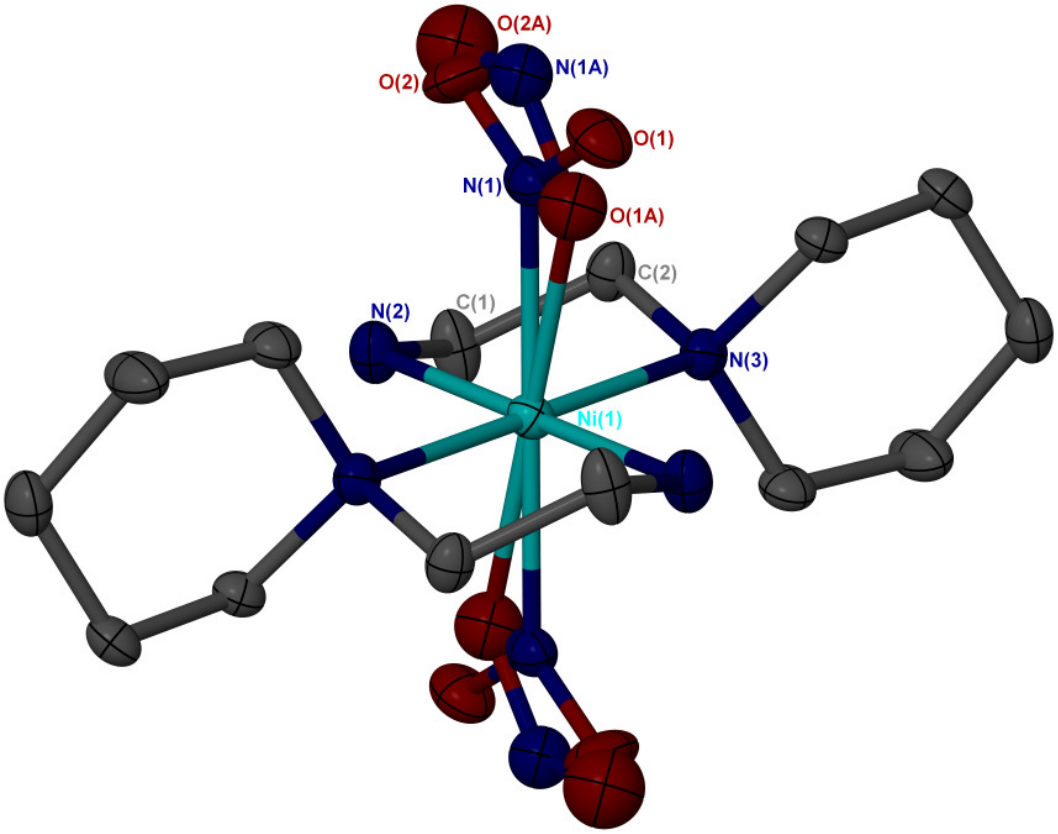

Figure 5.4: Excited state structure of **10*** at 90 K with 50 % ellipsoids shown and disorder and hydrogens removed for clarity.

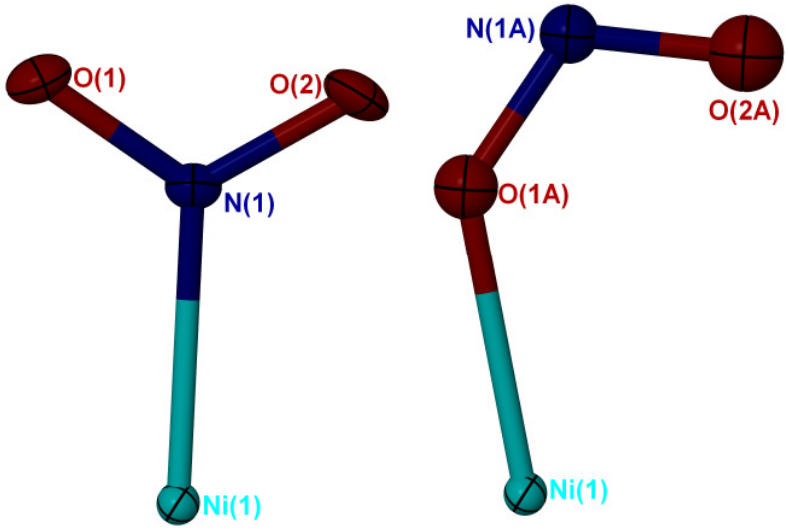

Figure 5.5: Close up of the separately displayed conformations in the excited structure of **10*** at 90 K with 30 % ellipsoids shown.

The changes which occur during irradiation are accompanied by an increase of the unit cell volume of approximately 26 Å^3, due to an increase in *a*, *b*, *c* and a decrease in *β*. In total, this corresponds to an increase of 2.9 vol. %. This increase is relatively large, suggesting that higher excitations could not be reached without inducing considerable crystal strain.

Table 5.1: Comparison of unit cell data for **10** and **10*** at 90 K

Structure	*a* (Å)	*b* (Å)	*c* (Å)	*α* (°)	*β* (°)	*γ* (°)	*V* (Å^3)
GS	9.629(5)	8.240(2)	11.804(2)	90	109.03(2)	90	885.4(5)
ES	9.672(4)	8.366(4)	11.903(5)	90	108.936(6)	90	911.1(7)
Δ	0.043	0.126	0.099	0	-0.077	0	25.7

The irradiated sample displays no decay of the second isomer at 90 K for at least 4 h, so that the presence of a metastable state at low temperature can easily be concluded. On the other hand this state is quenched in a few seconds at temperatures above 120 K as well as below 60 K.

The electron density difference is depicted in the Slant Plane Fourier Maps in Figure 5.6, which were generated using WinGX [100]. These maps are calculated through the nickel-nitro plane as the electron density in this plane gets reduced due to partial occupancy of the *endo*-NO_2 group, if there is any excitation present. After insertion of the ground state model and refining it against the excited state data, the electron density map confirms the observed movement of the electron density within the plane.

In the model, which includes both isomers, the *endo*-nitrito group does not lie completely in the plane of Ni1-N1-O1-O2, nonetheless it is still possible to see the excitation disappearing with temperature to a more even distribution of the residual electron density within the map. The maps are generated for all measured data between 115 K and 30 K. The data were collected using the following procedure: An excited sample was slowly warmed up or cooled down until the excitation was not observable anymore. During the experiment the sample was continuously irradiated. The warming up experiment was performed from 85 K to 120 K with a ramping time

of 5 K/h and the cooling down experiment was carried out between 100 K and 30 K with a cooling rate of 10 K/h. It is easily visible that there is an even distribution of electron density in pictures *a, j, k* and *l*. This suggest that a second process is occurring at temperatures below 60 K, which quenches the excitation, additionally higher temperatures extinguish the excitation as well, which is a known effect [52].

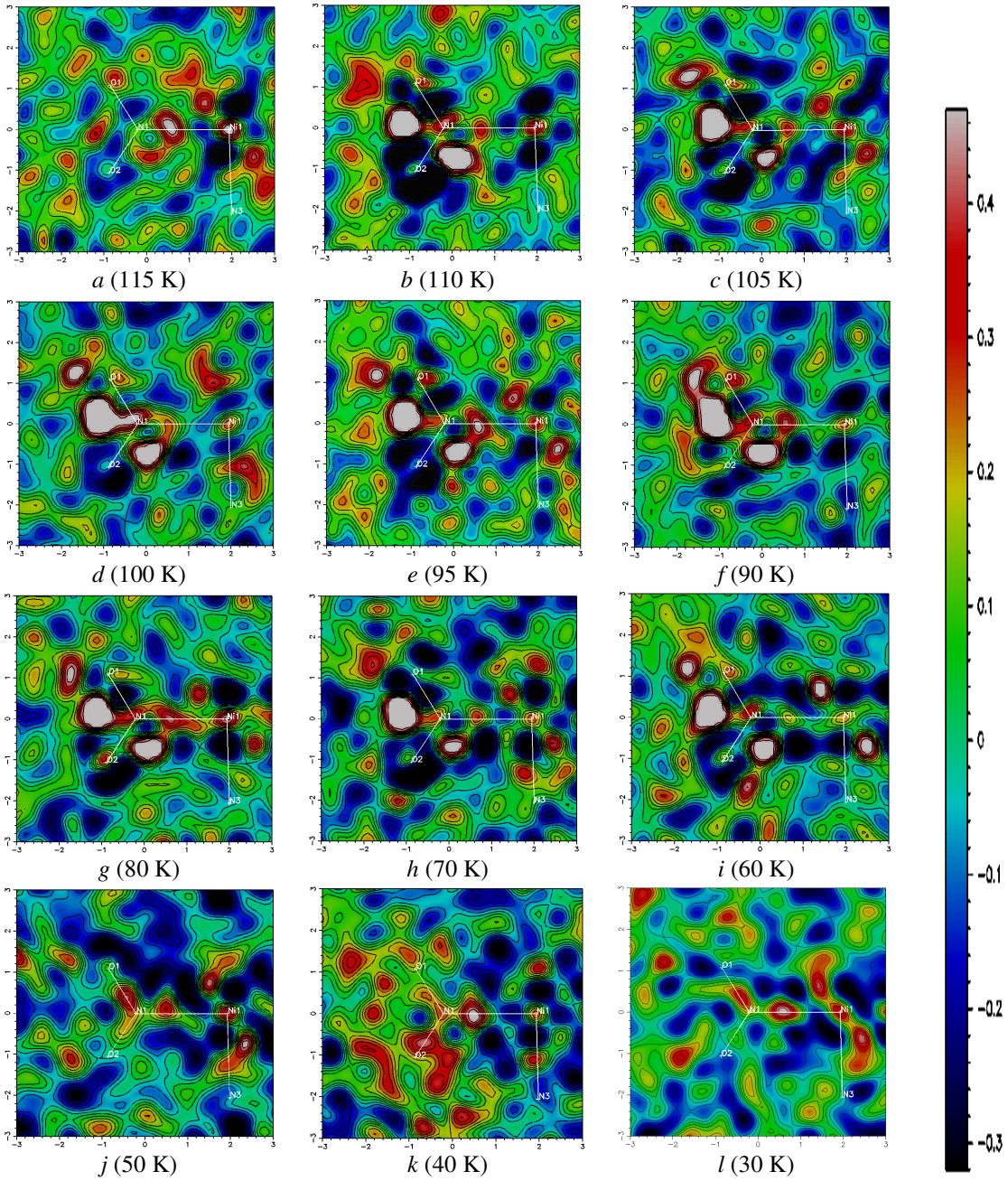

Figure 5.6: SLANT plane FOURIER maps of the disappearing of the excited state over a range of different temperatures.

Two more experiments have been carried out, in a similar way, to test the possibility of exciting a crystal at 60 K or at 110 K, but no changes were found, despite the fact that an excited state is stable at these temperatures [99]. This leads to the conclusion that the energy emitted by the light source at these temperatures is no longer high enough to excite the complex within the crystal environment.

Further measurements were taken to investigate the dependency of wavelength and excitation. For these a crystal was irradiated with different wavelengths at a temperature of 90 K or 100 K. It was possible to excite the crystal with 400 nm and 470 nm radiation, whereas no excitation was found after irradiation with 525 nm or white light. The excitation levels for UV or blue light are very similar, taking into account crystal size, power of light source and irradiation time.

All the excitation experiments described were performed using only a few crystals, with each crystal being used for more than one experiment. This is possible because of the reversibility of this process and because crystal decay due to irradiation damage was minimal.

Table 5.2: Dependency of wavelength and excitation for **10** at 90 K

Wavelength	400 nm	470 nm	525 nm	white
Estimated time	4 h	4 h	4 h	2 h
Excitation	13 %	16 %	0 %	0 %

5.1.2. $[Ni(aepy)_2(NO_2)_2]$ 12

12 crystallises in the monoclinic space group $P2_1/c$, again with half the molecule in the asymmetric unit and the nickel atom on the inversion centre. The molecule has octahedral coordination geometry; with the two η^1 coordinated nitro groups *trans* to each other, as can be seen in Figure 5.7. N1 is related to N1' by the symmetry operation *–x, -y, -z+1*. There are short contacts in the crystal packing between N2 and both nitro oxygens with donor-acceptor distances of 2.9603(16) Å to

O1 and 3.2266(15) Å to O2, their NHO angles are 120.7 ° and 130.1° respectively.

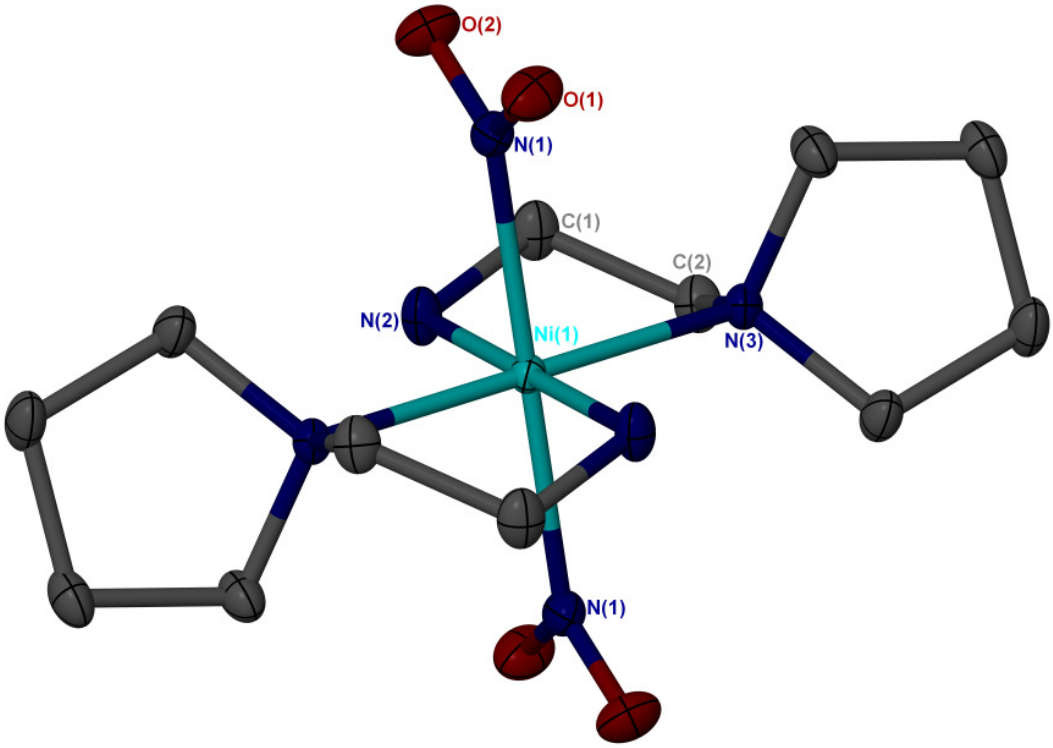

Figure 5.7: Ground state structure of **12** at 100 K with 50 % ellipsoids shown and with hydrogen atoms removed for clarity.

The excited state of this complex **12*** could be observed using the same conditions as for the previously described nickel species. Here two different metastable states were found which account for 35 % of the total structure. The major isomer is an η^1 coordinated *endo* nitrito species with 25 % occupancy, whereas the minor isomer has around 10 % in an *exo* η^1 coordinated state. The excitation was again modelled as disorder and the SUMP instruction was used to add the free variables up to unity. As in the pyridine structure an increase in disorder of the ethyl bridge was found, which increases from 0 % in the ground state to 35 % for the most excited structure. The model from the final refinement can be seen in Figure 5.8, with a close up of the nitrite group on the nickel atom in Figure 5.9 [99]. The increase in the disorder in the ethyl backbone is assumed to accompany the movements of the nitrite group and therefore reduce the strain into the crystal lattice.

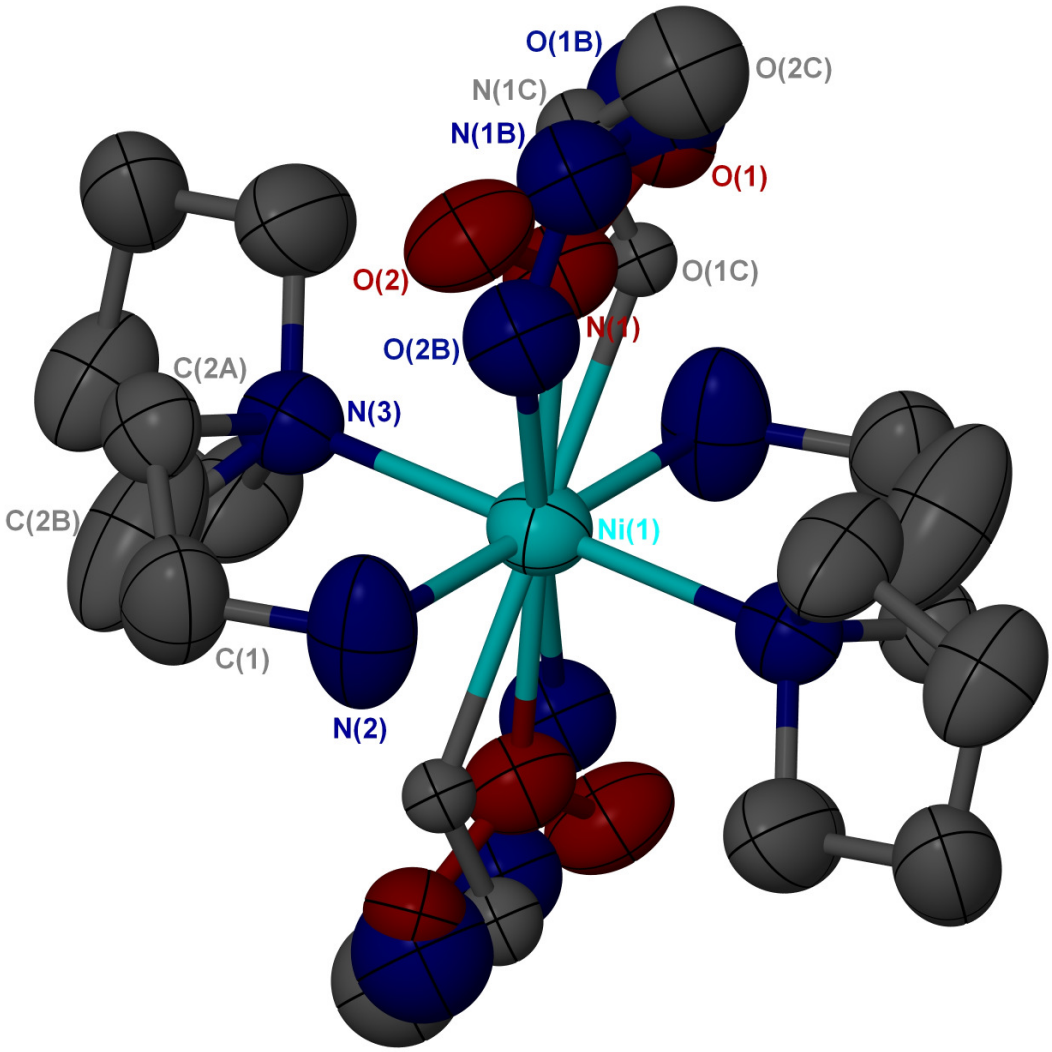

Figure 5.8: Excited state structure of **12*** at 100 K with 50 % ellipsoids shown and with hydrogens removed. The three isomers of the nitrite group are colour coded for clarity (nitro = red, *endo*-nitrito = blue, *exo*-nitrito = grey).

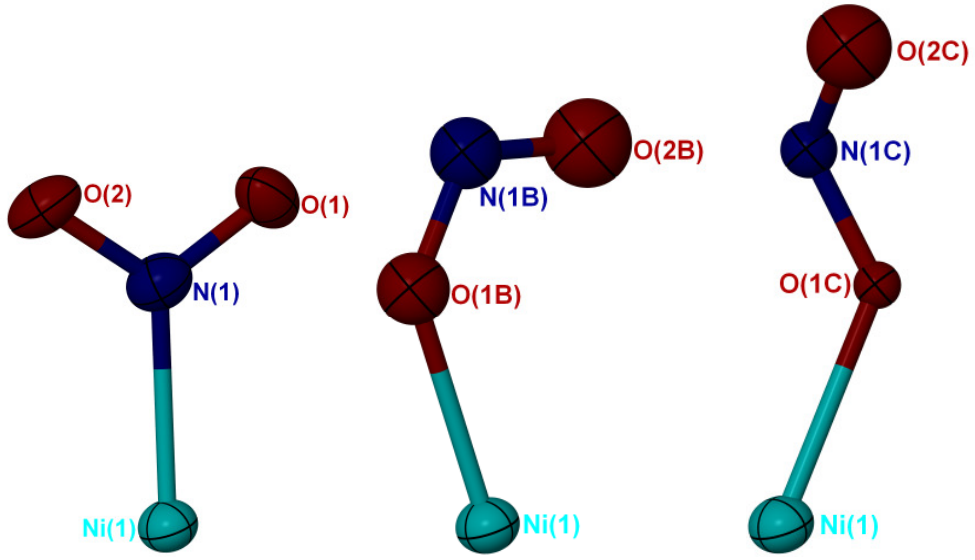

Figure 5.9: Close up of the three isomers of the nitrite group in the excited **12*** (η^1-NO_2, η^1-*endo*-ONO, η^1-*exo*-ONO) with 30 % ellipsoids shown.

The changes, which took place during irradiation, are followed by an increase of the unit cell volume of approximately 7 Å^3, due to an increase in *b*, *c* and a decrease in *a* and *β*. The increase of the unit cell volume is only 0.8 %. This smaller volume change compared to the **10** complex is in good agreement with the higher conversion; as a higher conversion is easier achieved if less movement is necessary.

Table 5.3: Comparison of unit cell data for **12** and **12*** at 100 K

Structure	*a* (Å)	*b* (Å)	*c* (Å)	*α* (°)	*β* (°)	*γ* (°)	*V* (Å^3)
GS	8.6169(5)	8.5490(5)	11.5680(7)	90	104.008(1)	90	826.83(8)
ES	8.349(2)	8.646(2)	11.836(3)	90	102.692(3)	90	833.5(3)
Δ	-0.268	0.097	0.268	0	-1.316	0	6.7

As with the previous compound the excitation does not decay with time at 100 K, and can be seen as a metastable state at this temperature. In contrast to the last sample **12*** does not convert back to the ground state at lower temperatures (down to 30 K), but is again quenched within a few seconds at temperatures above 120 K.

Crystals of **12** were tested with different light sources at a temperature of 90 K or 100 K. It was found that a different wavelength can decrease the excitation time

dramatically from 4 h with 400 nm to less than 1 h with 525 nm LEDs (Tab. 5.4). There is only a small difference in the final excitation level between the measurements at 400 nm, 470 nm and 525 nm, which might be accounted for by irradiation time or crystal size. The excitation with yellow light on the other hand was far slower and resulted in only 10 % excitation after 4 h. This experiment was stopped after 5 h as the excitation rate was too slow to reach a high level of excitation. These measurements suggest that the absorption is shifted to higher wavelength compared to the complex of **10**. Assumptions about the shape of the absorption curve can be made as well; suggesting the end of the absorption peak tail is near 600 nm, the half width about 525 nm and the highest absorption being near or between 470 nm and 400 nm. This conclusion can be drawn as it is known that highest conversion rates are found for the half width of the peak, with slower conversions for the irradiation in the tail or at the absorption maxima.

Table 5.4: Dependency of wavelength and excitation for **12**

Wavelength	400 nm	470 nm	525 nm	600 nm
Estimated time	4 h	3 h	1 h	4 h
Excitation	28 %	30 %	36 %	10 %

5.1.3. $[Ni(aem)_2(NO_2)_2]$ 13

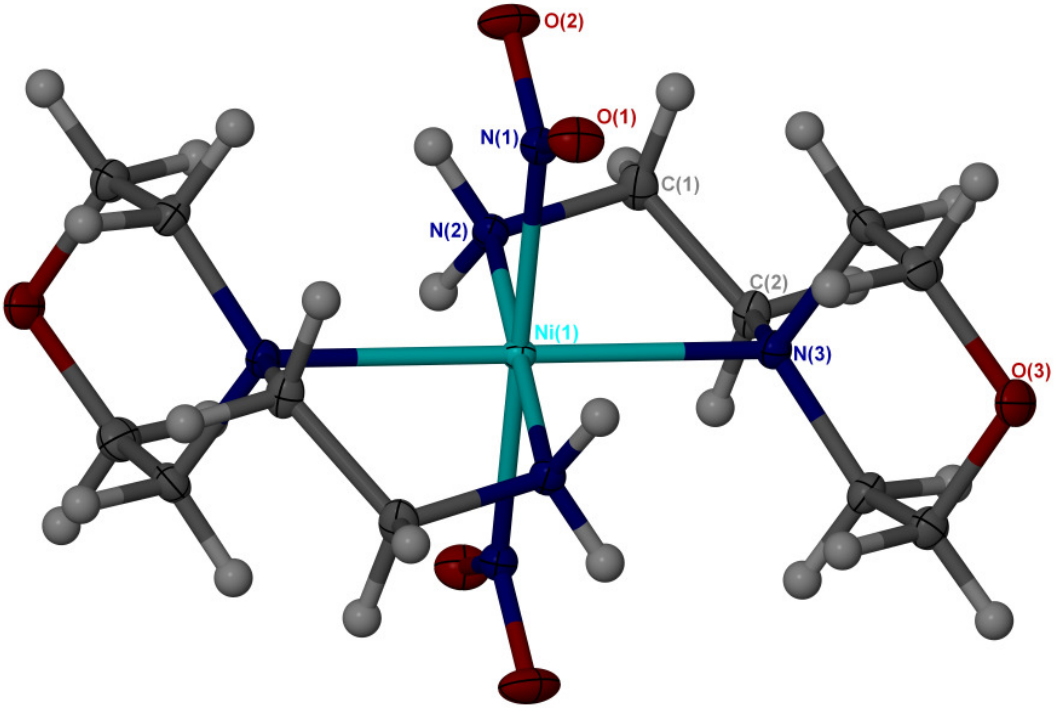

Figure 5.10: Ground state structure of **13** at 100 K with 50 % ellipsoids shown.

This complex crystallises in the triclinic space group *P*-1 (not *P*1 as reported previously [101], again with half the molecule as the asymmetric unit and the octahedral coordinated nickel atom on the crystallographic centre of symmetry (Fig. 5.10). As in both of the other complexes the nitrite groups are *trans* to each others and η^1-N-bound to the metal centre, with N1 related to N1' by the symmetry operation *–x+1, -y, -z+1*. This structure has intramolecular short contacts and intermolecular hydrogen bonds. The latter are between N2···H2B···O2 with a distance of 2.8943(18) Å and an angle of 111.9° and between N2···H2A···O3 with 3.128(2) Å and an angle of 147.1°, whereas the intramolecular contact is between N2···O1 with a distance of 2.985(2) Å and an angle of 119.6°. The intermolecular hydrogen bonds result in a sheet structure of the crystal packing as shown in Figure 5.11.

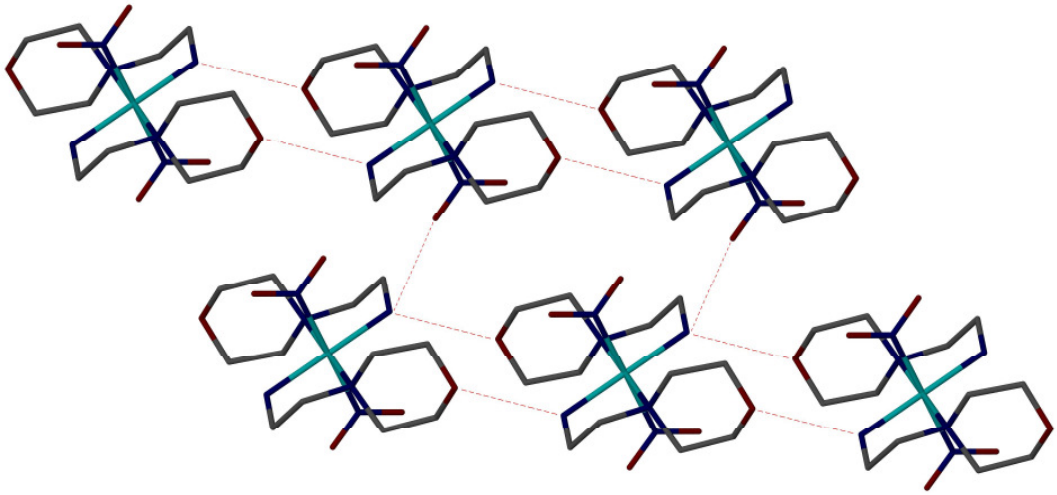

Figure 5.11: Packing of **13** with two different H-bonds shown and the hydrogens removed for clarity.

Table 5.5: Hydrogen bonds within the complex **13**

Compound	DHA	DH / Å	HA / Å	DA / Å	Angle / °
13	N2-H2A-O3	0.92	2.32	3.128(2)	147.1
	N2-H2B-O2	0.92	2.42	2.8943(18)	111.9

After irradiation with blue LEDs an excited state was found, in which 22 % of the nitro group changed into two *endo*-η^1-O coordinated nitrito isomers. The major isomer accounts for approximately 17 % and involves O1A-N1A-O2A. The overall structure stays in *P*-1 as found for the ground state (Fig. 5.12) [99]. A close up of the three forms of the nitrite ligand are displayed in Figure 5.13.

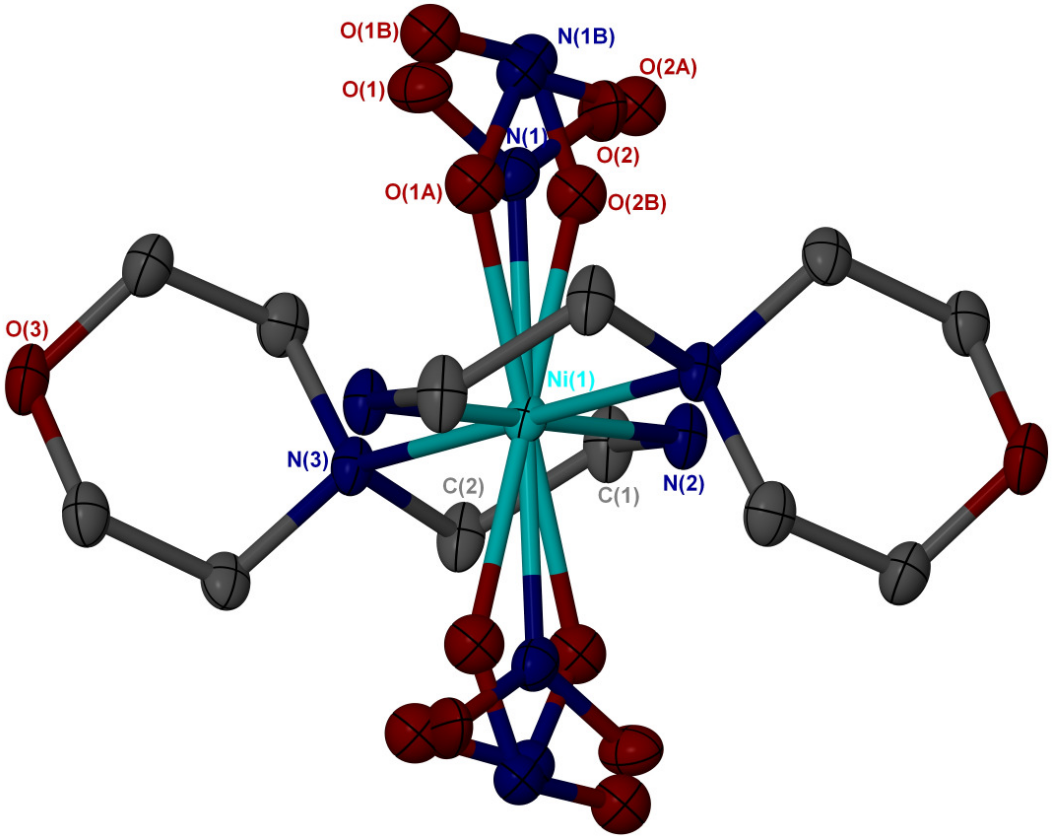

Figure 5.12: Excited state structure of **13*** at 100 K with 50 % ellipsoids shown and hydrogens removed for clarity.

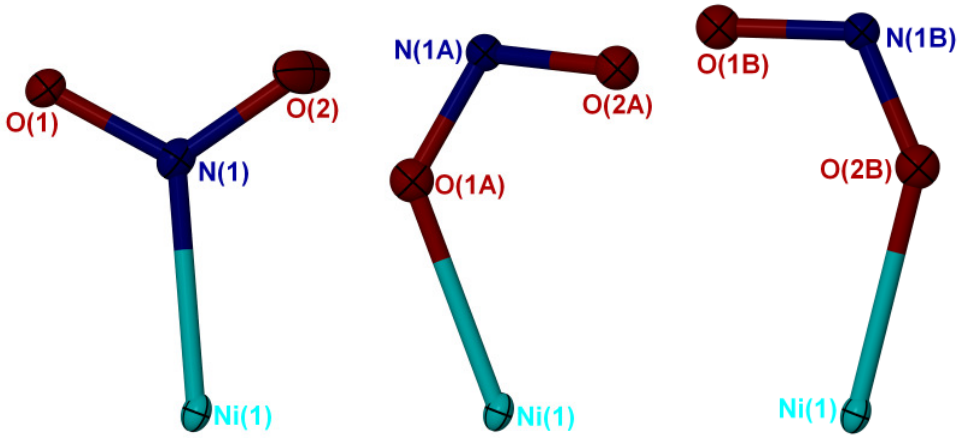

Figure 5.13: Close up of the separated nitrite group (η^1-NO_2, η^1-*endo*-ONO, η^1-*endo*-ONO) of the irradiated crystal **13*** at 100 K with 30 % ellipsoids shown.

The unit cell also increases upon irradiation as in the other two examples; again the change in volume is only 4 Å^3 or 0.9 % (Tab. 5.6).

Table 5.6: Comparison of unit cell data for **13** and **13*** at 100 K

Structure	*a* (Å)	*b* (Å)	*c* (Å)	*α* (°)	*β* (°)	*γ* (°)	*V* (Å^3)
GS	7.172(5)	7.988(5)	8.330(5)	94.306(5)	112.642(5)	100.496(5)	427.5(5)
ES	7.2136(13)	7.9994(14)	8.3000(14)	94.581(2)	111.364(2)	101.278(2)	431.39(13)
Δ	0.042	0.011	-0.030	0.275	-1.278	0.782	3.89

The excitation does not decay with time at 100 K, which means that this isomer is also metastable. It does not decay at lower temperatures (down to 30 K) either, but is quenched in a few seconds at temperatures of around 130 K.

Like the complex **10** this crystal can only be excited with blue or UV light after at least 3 h. Irradiation with green light did not result in any excitation in a comparable time scale (Tab. 5.7).

Table 5.7: Dependency of wavelength and excitation for **13**

Wavelength	400 nm	470 nm	525 nm
Estimated time	4 h	3 h	4 h
Excitation	20 %	22 %	0 %

5.2. Raman Spectroscopy

A series of low temperature solid-state Raman spectra were measured on these three complexes to confirm the single crystal X-ray diffraction results. The measurements were done in Nottingham in the group of M. GEORGE [99]. In each experiment, a large single-crystal was cooled to 100 K and the Raman spectrum was recorded. Subsequently the crystal was photolysed with UV LEDs and a second spectrum was measured. The crystal was then slowly warmed up, whereby further spectra were acquired every 10 K.

The nitro-η^1-NO_2 isomer has very distinctive Raman bands, in particularly the $\delta(NO_2)$ deformations at 800-900 cm^{-1} and the ν(N-O) stretches at 1350-1500 cm^{-1} [102]. Both bands are split for these complexes due to coupling between the two NO_2 groups. Unfortunately the ν(N-O) stretches are often overlapped with other Raman bands, making them less useful for assignment. As this is less problematic for the $\delta(NO_2)$ deformation band, the latter one was used to monitor changes during and after irradiation.

Two Raman spectra of **10** at 100 K are shown in Figure 5.14. The structure shown in black corresponds to the structure prior to irradiation and the spectrum shown in red was recorded after 4 h irradiation with UV LEDs. The intensity of the nitro isomer $\delta(NO_2)$ deformation band at 808 cm^{-1} decreases and new bands at 815 cm^{-1} and 803 cm^{-1} are formed, corresponding to the partial formation of the nitrito isomer. The intensity of the nitro-isomer band dropped to ca. 81 %, indicating that ca. 19 % of the complexes were excited; this result is comparable with the 16 % excitation measured by X-ray in the single crystal as shown above. It is possible that a higher percentage conversion is measured by Raman as only the molecules near the surface are measured, whereas the bulk conversion is measured by crystallographic experiments. This reveals one of the challenges: The penetration depths of the crystal depend on the light source. It is expected that more molecules on the surface get excited than in the middle of the crystal, as these 'see' a lower number of photons, which being absorbed as they pass through the crystal.

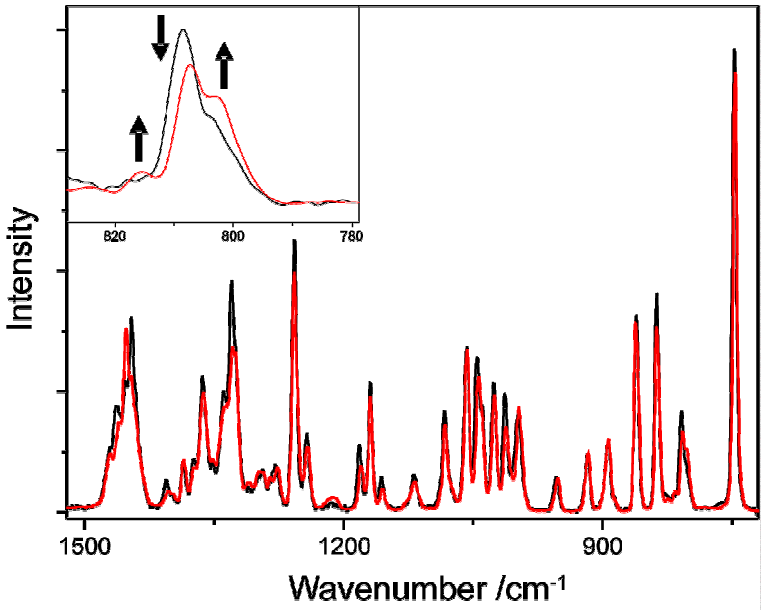

Figure 5.14: Solid state Raman spectra of a crystal of **10** at 100 K before (black) and after photolysis (red), with the inset showing the band at 810 cm^{-1}.

Figure 5.15 shows the Raman spectra recorded after photolysis of **10** as the temperature is progressively increased from 100 K to 110 K, 120 K and 130 K. As expected for the $\delta(NO_2)$ region the nitrito bands at 815 cm^{-1} and 803 cm^{-1} decrease again, whereas the nitro band at 808 cm^{-1} grows in intensity following the temperature increase. At a temperature of 120 K the spectrum is almost identical to the ground state spectrum shown above. At a temperature of 130 K the nitrito isomer bands have completely decayed, which agrees well with the observed decay temperature of 110 K recorded by crystallography.

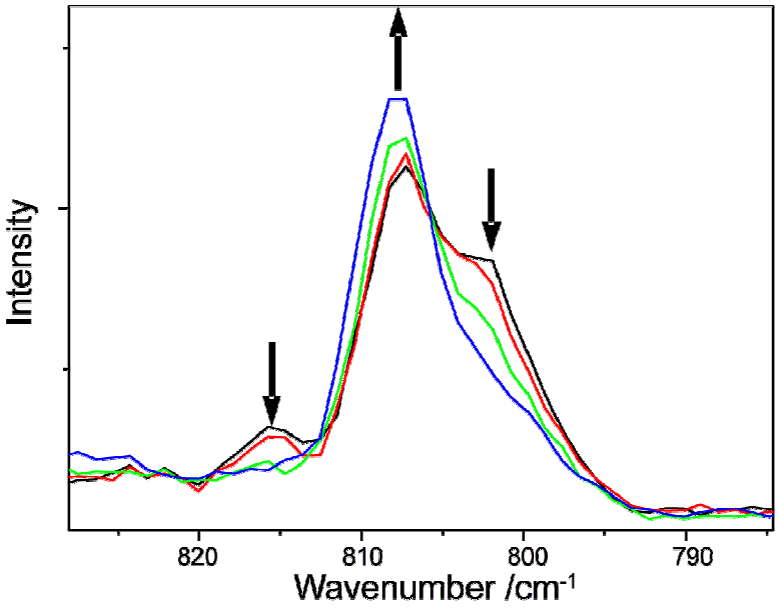

Figure 5.15: Solid state Raman spectra of a crystal of **10** displaying the band at 810 cm^{-1} after photolysis during warming up from 100 K (black) to 110 K (red), 120 K (green) and 130 K (blue).

Figure 5.16 shows the Raman spectrum of **12** at 100 K, which contains several overlapping bands in the $\delta(NO_2)$ region of the spectrum, consistent with significant coupling between the two NO_2 groups. Unlike the previously described experiment, this sample underwent photolysis during exposure with the 660 nm laser, used by the Raman spectrometer. The resulting spectrum, which is shown in Figure 5.16, was recorded after only 15 min irradiation with the laser operating at approximately 10 mW. This measurement displays a nice agreement with the crystallographic experiments, where it was possible to excite this complex, but none of the other two with higher wavelength. It appears that the $\delta(NO_2)$ deformation bands around 804 cm^{-1} decrease, whereby new bands establish at 798 cm^{-1} and 861 cm^{-1}. Other changes seem to appear in this region, but the data is not of sufficient quality to resolve these changes in detail. Due to the complex changes shown by X-ray crystallography, it can be suggested that these changes may be due to the presence of a mixture of different photo products. Additionally, because of the insufficient

spectral resolution of the data, this experiment cannot estimate the percentage conversion.

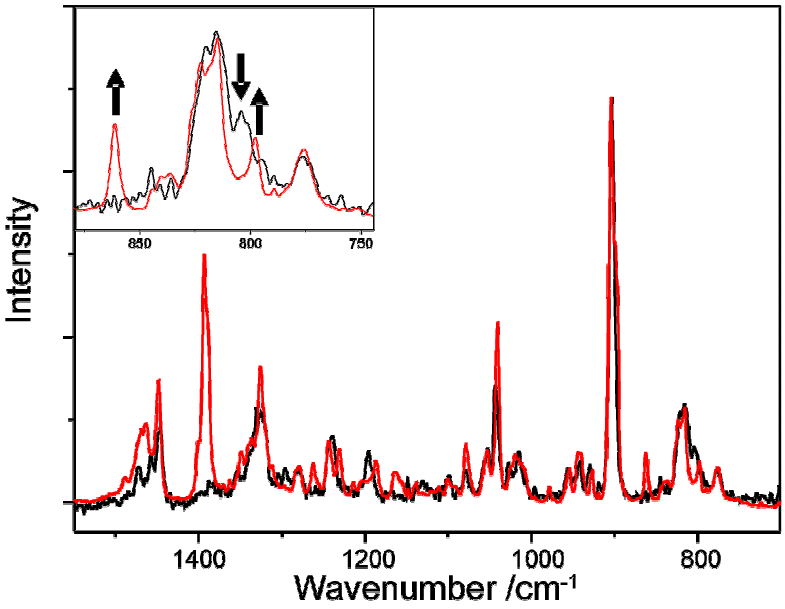

Figure 5.16: Solid state Raman spectra of a crystal of **12** at 100 K before (black) and after photolysis (red) by laser radiation (660 nm), with the inset showing the band at 810 cm^{-1}.

Warming the excited crystal of **12** results in the reformation of the ground state at temperatures above 130 K, again higher, but in reasonable agreement with the crystallographic measurement of 120 K.

The ground state Raman spectrum of **13** at 100 K is illustrated in Figure 5.17, along with the spectrum of the complex after irradiation for 1.5 h with UV LEDs. As described above for the **10** complex, the $\delta(NO_2)$ deformation band of the nitro isomer at 812 cm^{-1} decreases significantly in intensity and a new band at 821 cm^{-1} is formed. This corresponds to the formation of the nitrito isomer, which seems to go to completion by Raman spectroscopy. An explanation for the discrepancy of the full conversion compared to the 22 % measured by crystallographic methods might be the fundamental difference in the two experiments; one measuring the surface and one the bulk of the sample. The same warming up experiment as for **12** was performed on

the photolysed crystal resulting in the reformation of the ground state at temperatures above 130 K, in agreement with the crystallographic measurement of a decay temperature of 130 K.

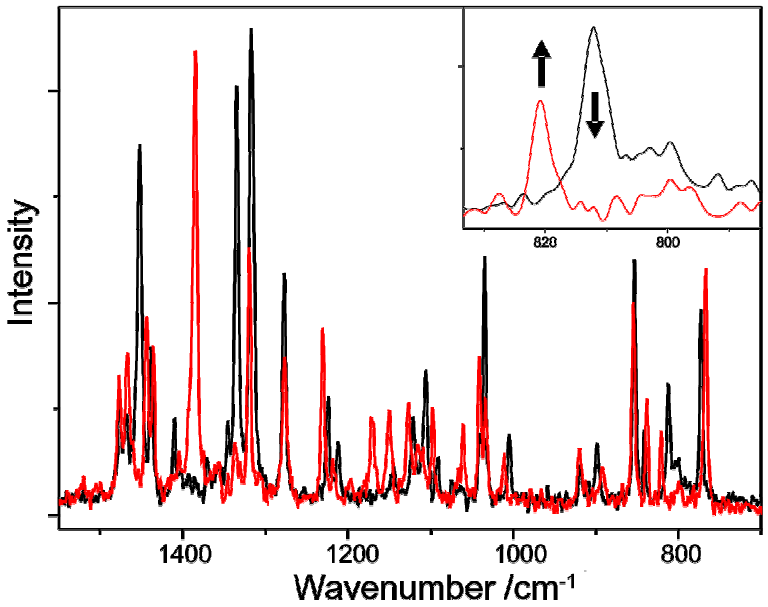

Figure 5.17: Solid state Raman spectra on a crystal of **13** at 100 K before (black) and after photolysis (red), with the inset showing the band at 810 cm^{-1}.

5.3. UV-vis Absorption Experiments

UV-vis experiments on the four compounds were measured in different solvents (DCM and MeOH). A saturated solution was used, as otherwise the spectra were only ligand based. Unfortunately the complexes decompose in most common solvents, such as MeOH. This is obvious from the colour of the solution, which changed from red or blue to green. The colour in DCM on the other hand does not change, but as shown in Figure 5.18 no difference in peak positions are found for the four complexes. The peak maxima are at 493 nm for **12** (pink line), 494 nm for **13** (red line), 497 nm for **11** (blue line) and 500 nm for **10** (black line). These small differences are insignificant and result from the fact that a mixture of isomers or one isomer for both forms of **10** has to exist in DCM. Unfortunately it was not possible to

see the shifted peak for **12** compared to the other two complexes, which are N-bound. This might be due to the fact that the experiment is performed in solution or it is possible that the maximum is shifted with temperature. Following from the solution measurements, solid state UV-vis experiments were also performed; however they were not sensitive enough to display any metal based excitation. Therefore no conclusion can be drawn, whether a temperature effect or a solvent effect is found here.

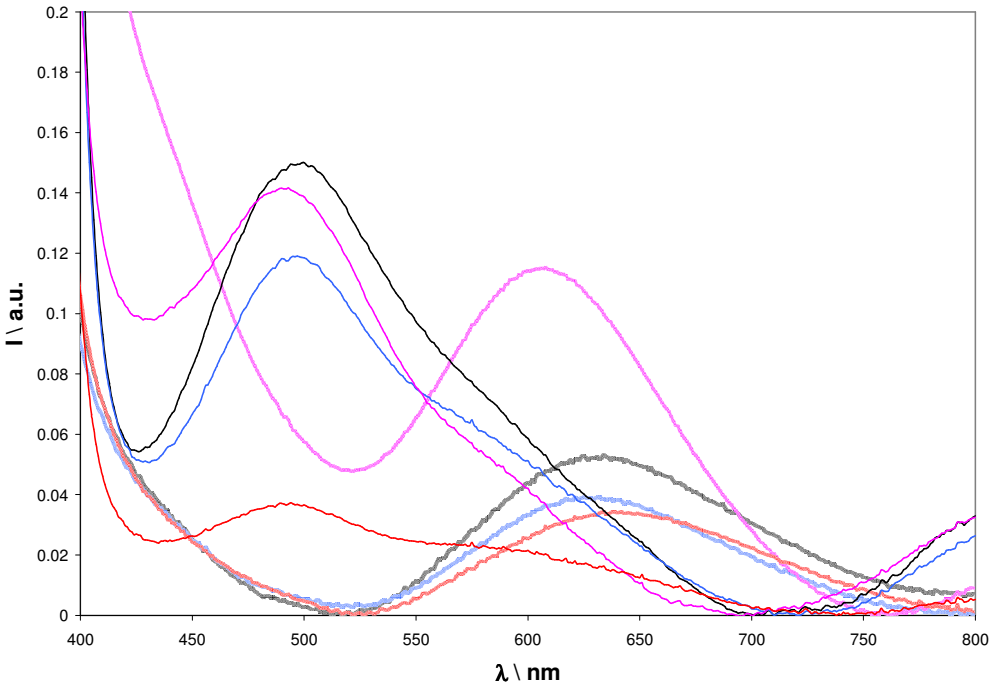

Figure 5.18: UV-vis measurements in DCM (solid line) and in MeOH (dashed line). **12** = pink, **13** = red, **11** = blue and **10** = black.

5.4. Temperature Experiments

Preliminary investigations of powdered samples of the nickel complexes at higher temperatures showed some colour changes. Powdered samples of all three $[Ni(L)_2(\eta^1\text{-}NO_2)_2]$ complexes, placed in a capillary, were heated on a hot plate to

different temperatures. **10** changed colour from pink to grey-blue at temperatures above 343 K (Fig. 5.19). This colour change was reversible and at lower temperatures the colour changes back to pink. Its melting point is 473 K, whereas **11** has a lower melting point of 458 K.

13 shows a colour change from pink to yellow at temperatures of 433 K, which is just below the melting point of the sample, which is at 458 K. This colour change is irreversible and might indicate that compound decomposition is occurring. **12** on the other hand shows no colour change below its melting point at 463 K.

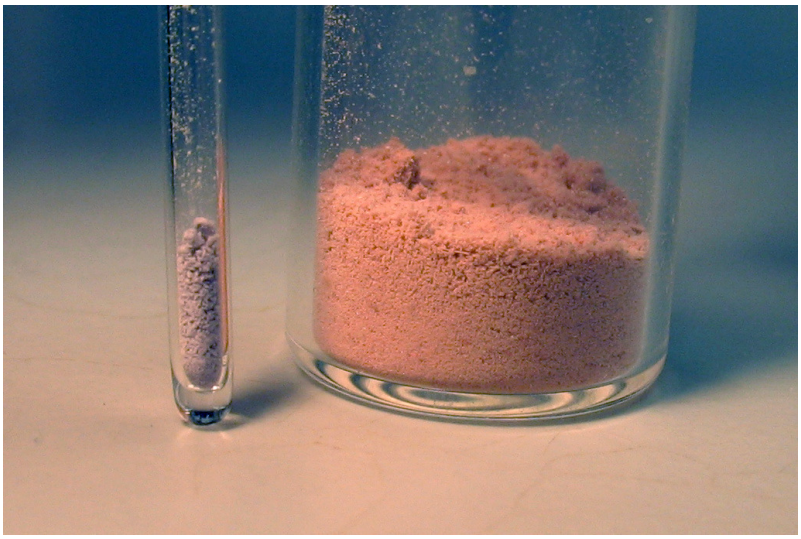

Figure 5.19: Powdered sample of **10** at temperature of 343 K (left) and at RT (right).

High temperature powder diffraction experiments gave different results for the four samples. The powder pattern of **10** does not change at temperatures below 373 K and at the next temperature step of 423 K the change is not reversible anymore and the change is accompanied by a loss of crystallinity (Fig. 5.20).

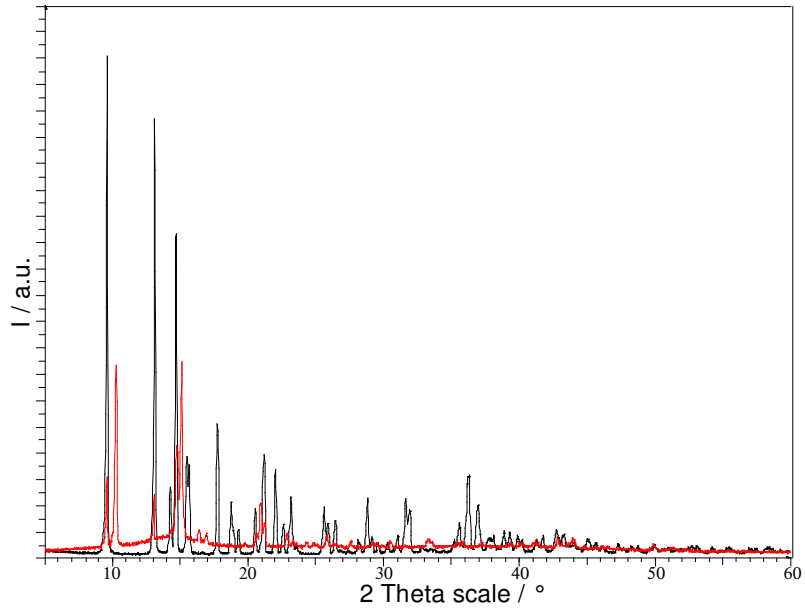

Figure 5.20: Powdered sample of **10** at temperature of 293 K (black) and at 423 K (red).

The powder pattern of **11** on the other hand is very variable, a change is visible after each temperature step of 20 K (Fig. 5.21). None of the patterns match the powder pattern of **10** or **11** and the changes were not reversible. This indicates a crystal change has occurred with grinding.

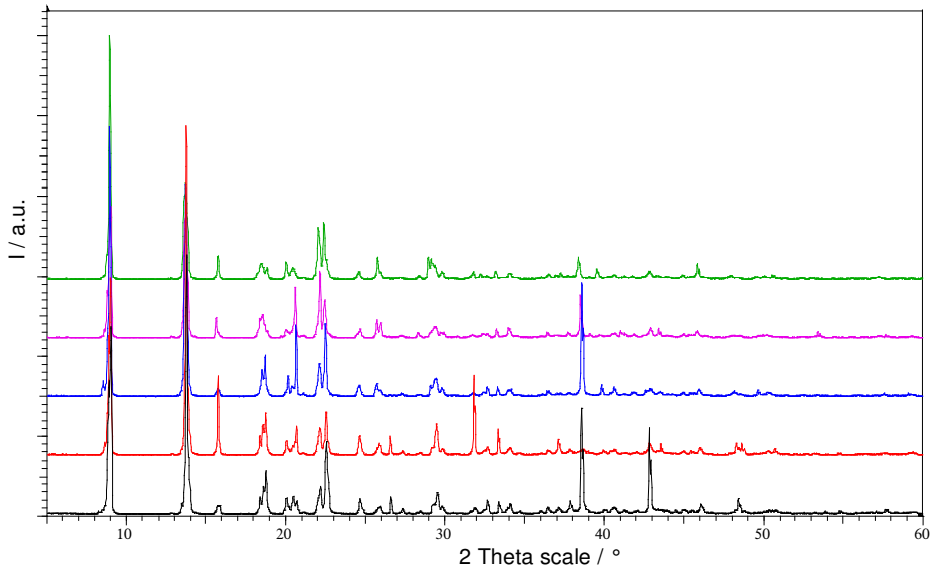

Figure 5.21: Powdered sample of **11** at temperature of 293 K (black), 313 K (red), 333 K (blue), 353 K (pink) and 373 K (green).

The same variability and nonreversibility was observed for **12** (Fig. 5.22). Nonetheless the powder pattern at 293 K is consistent with the calculated powder pattern from the single crystal. After the pattern at 373 K was measured a second powder pattern at 293 K was remeasured, which was different from the first one. As mentioned before the powder loses crystallinity at temperatures of 423 K (Fig. 5.22 violet).

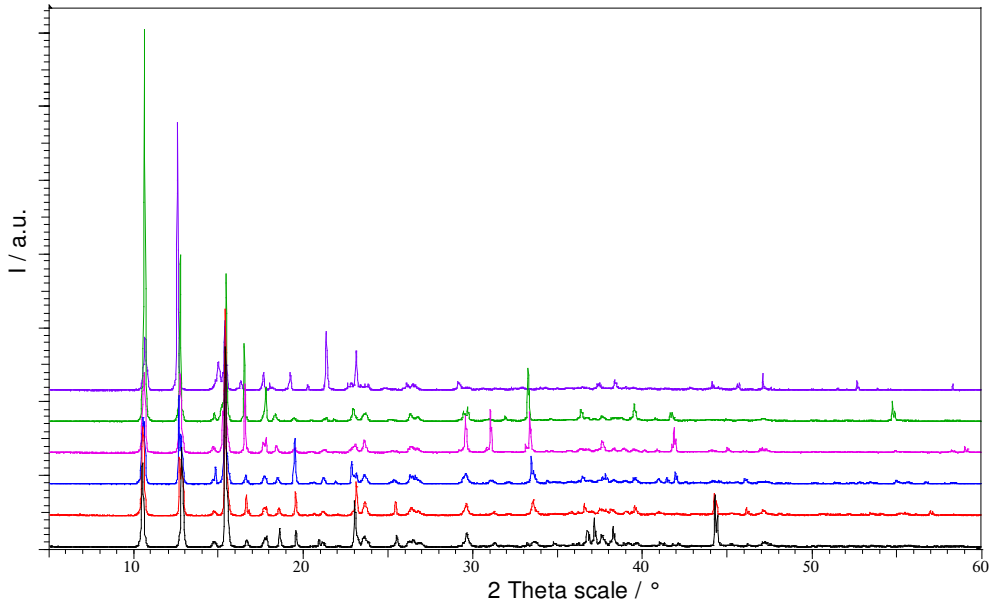

Figure 5.22: Powdered sample of **12** at temperature of 293 K (black), 313 K (red), 333 K (blue), 353 K (pink), 373 K (green) and 423 K (violet).

13 on the other hand shows a significant change of the pattern at 353 K, which is reversible (Fig. 5.23) and stable over a range of 40 K up to 393 K. A loss of crystallinity is again observed at a temperature of 423 K, as displayed in Figure 5.24.

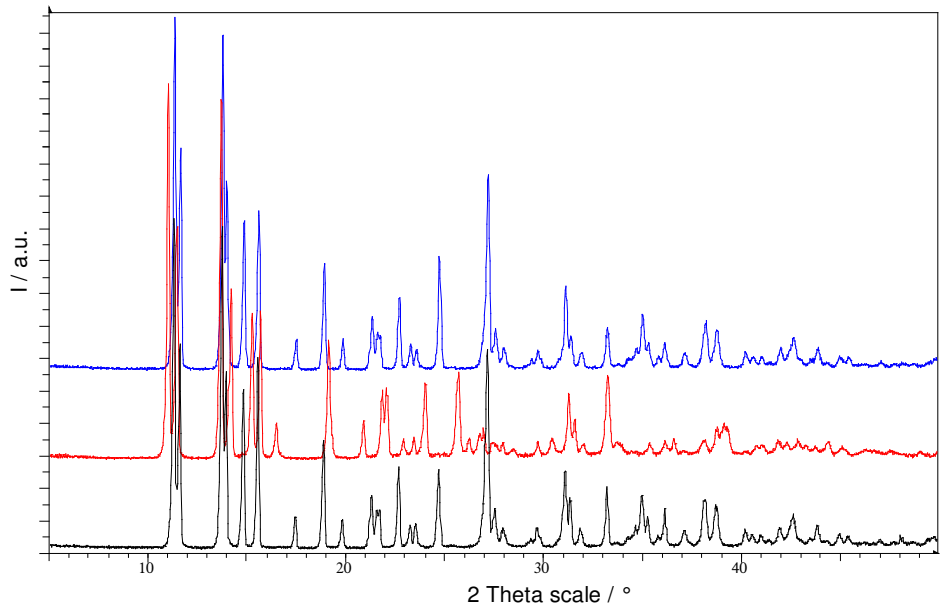

Figure 5.23: Powdered sample of **13** at temperature of 293 K (black), 313 K (red) and 293 K (blue) after heating and cooling.

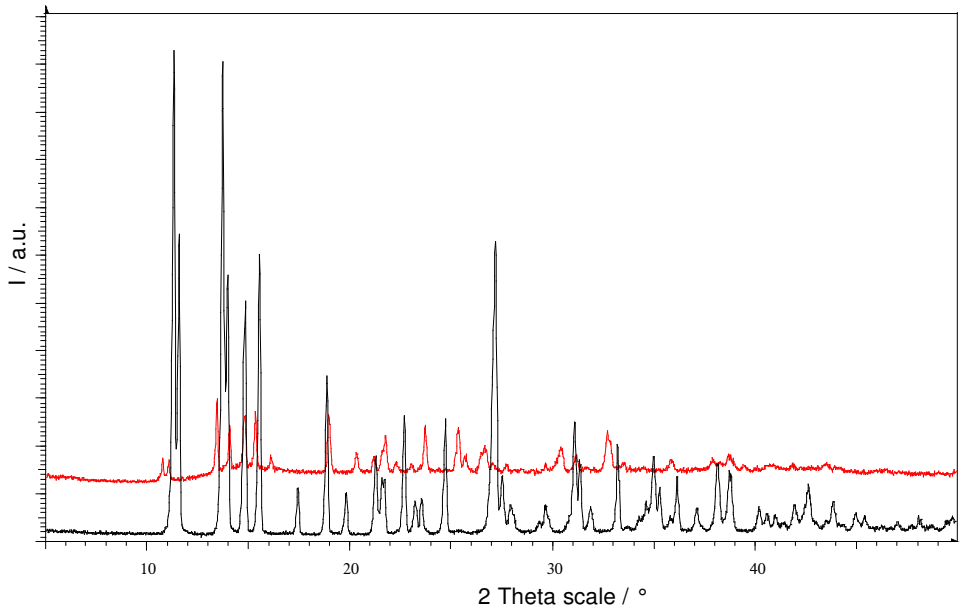

Figure 5.24: Powdered sample of **13** at temperature of 293 K (black) and 423 K (red).

Variable temperature experiments were also performed on the single crystals. **10** displays only an increase of the disorder within the ethyl chain of the chelating ligand from 18 % at 90 K (Fig. 5.2) to 35 % at a temperature of 373 K.

A single crystal of **11** at 373 K does not show any linkage isomerism, but a disorder within the ethyl chain of 15 % (Fig. 5.25) compared to no disorder at lower temperature. An increase in disorder is not uncommon for higher temperatures, following from raising thermal energy and a bigger unit cell. In this case the increase of the unit cell volume over the 223 K temperature increase was 69.7 Å^3, which means 3.8 % (Tab. 5.8). This greater static disorder is illustrated by the enlarged atomic displacement parameters compared to the ones in Figure 5.3.

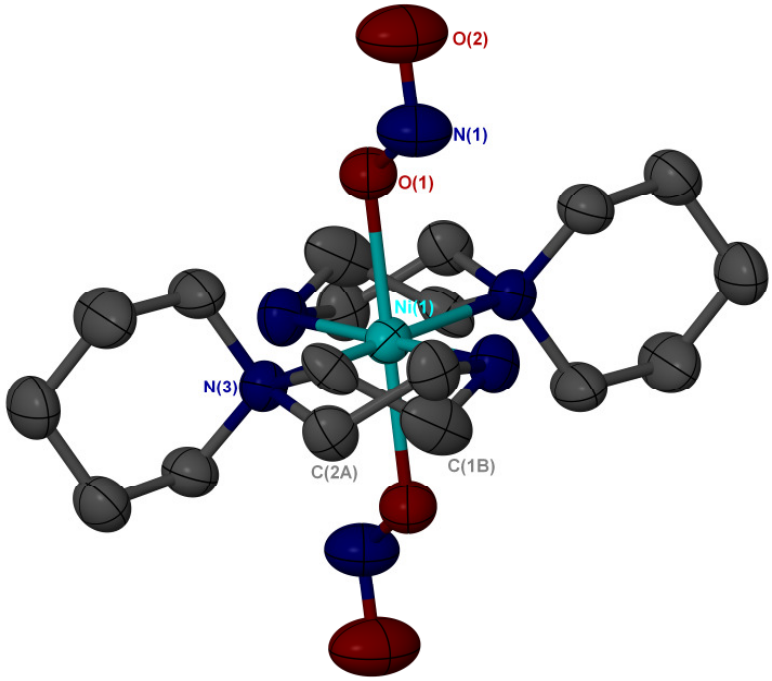

Figure 5.25: Single crystal structure of **11** at a temperature of 373 K with hydrogens removed for clarity and with 50 % ellipsoids shown.

Table 5.8: Comparison of unit cell data for **11** at 150 K and 373 K

Structure	*a* (Å)	*b* (Å)	*c* (Å)	*α* (°)	*β* (°)	*γ* (°)	*V* (Å^3)
150 K	9.42000(10)	9.6000(2)	19.8940(4)	90	90	90	1799.05(6)
373 K	9.6410(2)	9.7270(2)	19.9270(5)	90	90	90	1868.71(7)
Δ	0.221	0.1270	0.033	0	0	0	69.66

The variable temperature experiment on a single crystal of **13** showed an increase in the unit cell volume of 6.7 % (Tab. 5.9), corresponding to 28.8 Å^3. In this case no appearance of disorder was observed.

Table 5.9: Comparison of unit cell data for **13** at 100 K and 373 K

Structure	*a* (Å)	*b* (Å)	*c* (Å)	*α* (°)	*β* (°)	*γ* (°)	*V* (Å^3)
90 K	7.172(5)	7.988(5)	8.330(5)	94.306(5)	112.642(5)	100.496(5)	427.5(5)
373 K	7.149(13)	8.295(15)	8.440(15)	90.03(3)	111.18(2)	101.31(2)	456.3(14)
Δ	-0.023	0.307	0.110	-4.28	-1.46	0.814	28.8

As in the other experiments at higher temperature on single crystals, the crystal of **12** displays a change of the unit cell volume. It increases by 7.3 vol. %, which corresponds to 60.47 Å^3, this is due to an increase in the *b* and *c* axis, whereby *a* and *β* decrease slightly (Tab. 5.10). Additionally disorder builds up within the aminoethyl bridge of approx. 35 %.

Table 5.10: Comparison of unit cell data for **12** at 100 K and 373 K

Structure	*a* (Å)	*b* (Å)	*c* (Å)	*α* (°)	*β* (°)	*γ* (°)	*V* (Å^3)
90 K	8.6169(5)	8.5490(5)	11.5680(7)	90	104.0080(10)	90	826.83(8)
373 K	8.612(10)	8.745(10)	12.094(13)	90	103.059(12)	90	887.3(17)
Δ	-0.0049	0.196	0.526	0	-0.949	0	60.47

Calculations of the strain within the lattice [103, 104] by increasing temperature were performed on the four different complexes. The different strains along the unit cell axis are calculated through the differences between the unit cell dimensions of the structures. The calculation is performed between two structures (Δd), whereby the structure at the highest temperature is taken as the reference one (d). The graph in Figure 5.26 displays the calculations for **10**, and it is shown that the three slopes are very similar, especially the two from *b* and *c*. This shows that the change in cell dimensions with increasing temperature is relatively isotropic. The unit cell data used for this calculation comes from different single crystals; this indicates that the lattice parameters do not vary from crystal to crystal as is known for other complexes [104].

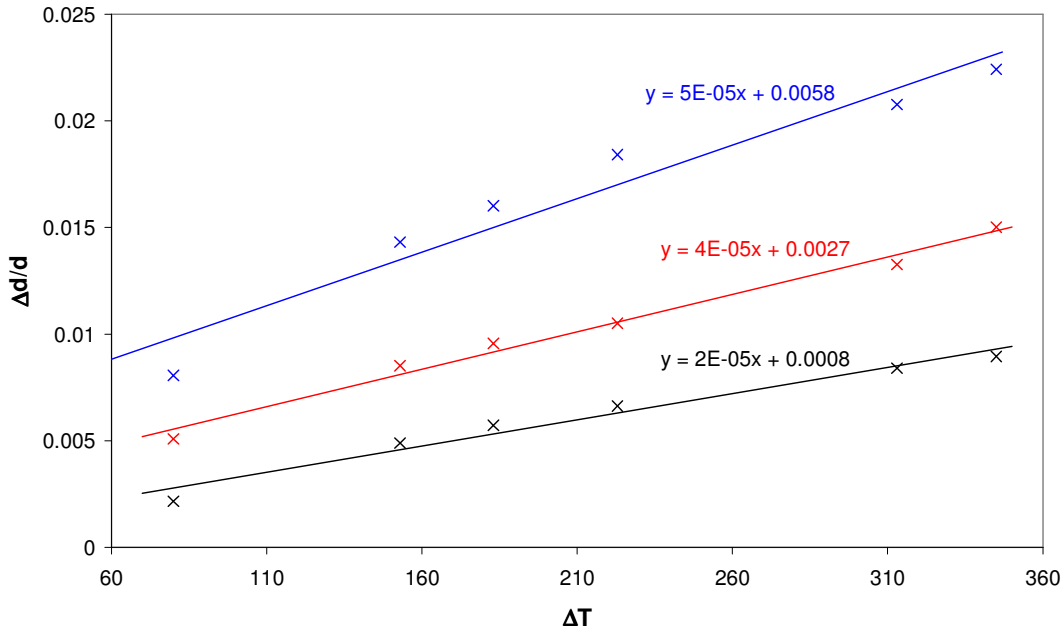

Figure 5.26: Different strains along the cell axis of **10**; *a* in black, *b* in blue and *c* in red.

Table 5.11: Comparison of unit cell data for **10** at different temperatures

T	*a* (Å)	*b* (Å)	*c* (Å)	*α* (°)	*β* (°)	*γ* (°)	*V* (Å^3)
28	9.627(1)	8.241(1)	11.802(1)	90	109.016(1)	90	885.2(2)
60	9.6323(8)	8.2549(7)	11.823(1)	90	109.029(1)	90	888.7(1)
150	9.629(5)	8.240(2)	11.804(2)	90	109.03(2)	90	885.4(5)
190	9.6496(8)	8.2747(7)	11.856(1)	90	109.056(1)	90	894.8(1)
220	9.6584(6)	8.2950(5)	11.8674(8)	90	109.040(1)	90	898.8(1)
293	9.6664(7)	8.3093(6)	11.8799(8)	90	109.045(1)	90	902.0(1)
373	9.693(1)	8.3620(9)	11.921(1)	90	108.961(1)	90	913.8(2)

The other three structures display a similar isotropic behaviour, also **12** has a very small increase of strain along *a*, as shown in Table 5.12, this could indicate no pressure increase along this axis. As the aminoethyl bridge is partially along this axis, this could indicate a reduction of strain through movement of the atoms. This is likely as an increase of 35 % in disorder over temperature is found. All the other strains have the same magnitude and are comparable to each other. It was not possible to perform the same comparison with the excited state data, as the low conversion rates do not give enough data points. However, the data suggest that the increase in

strain within the excited crystal is not linear. This is not surprising as higher conversions, especially just before the highest possible conversion if that is not 100 %, suggest higher crystal deformations.

Table 5.12: Strength upon the unit cell over temperature for $[Ni(L)_2(NO_2)_2]$ complexes

compound	strength for *a*	strength for *b*	strength for *c*
10	5^{-5}	2^{-5}	4^{-5}
11	5^{-5}	7^{-5}	4^{-5}
12	7^{-6}	5^{-5}	6^{-5}
13	2^{-5}	6^{-5}	3^{-5}

5.5. Conclusion

In conclusion single crystal X-ray photocrystallographic studies and Raman studies have shown that the metastable nitrito complexes **10***, **12*** and **13*** are generated under irradiation. The maximum excitation was found for **12*** with a maximum conversion level of 35 % at a temperature of 100 K. In the excited state all three complexes adopt an *endo*-conformation of the nitrito group, but there is also crystallographic evidence for the presence of an *exo*-nitrite isomer in the structure of **12***. This structure and the structure of **13*** remain metastable when the temperature is reduced to 30 K, whereas the excitation of **10*** is quenched below 60 K back to the ground state structure.

It was found that there are subtle differences in behaviour between these three closely related systems, when crystalline samples are irradiated with different light sources. Formation of linkage isomers within these three systems can be observed for radiation with a wavelength of 400 nm and 470 nm, nevertheless only **12** changes through irradiation with green (525 nm) or yellow (600 nm) LEDs. Even though the excitation takes different amounts of time to reach the maximum conversion, it seems that the maximum amount of excitation is approximately the same for all wavelengths. This is not proven for the irradiation of **12** with yellow light, as the

experiment would have been too time consuming, as excitation up to 10 % was only reached after 4 h.

One other result is that the ellipsoids in the excited states are bigger than in the ground state. This effect is expected as the excitation interferes with the order within the crystal. The slight movements of the ligands are not necessarily consistent across different unit cells and a greater spread of atomic positions occurs. Additionally found, is an increase within the mosaic spread of the structure resulting in smeared diffraction spots. As discussed above these changes are reversible, illustrated in comparable ellipsoids and spot shapes in a ground state structure before and after the excitation.

The high temperature experiments did not give conclusive results. All four single crystals do not change their conformation at a temperature of 373 K, although all of them, except **13**, display an increase of disorder within the bidentate ligand. This is explained, due to the higher movements of the atoms at higher temperature, which is also supported by the larger atomic displacement ellipsoids.

Nonetheless the high temperature powder experiments suggest that some changes within the material might occur. **10** displays a colour change at temperatures above 343 K and the high temperature powder patterns of **13** displays a reversible change of the pattern above 353 K. These two samples were considered to be interesting at higher temperature, but as the single crystal experiments were not successful other solid state analytical methods at higher temperature would be necessary to complete the high temperature experiments. Both samples of **11** and **12** demonstrate large non-reversible changes of their powder pattern and they are therefore inconclusive.

5.6. Summary of the Crystal Data

Table 5.13: Summary of crystal data for **10** and **10***

Compound	**10**	**10***
Empirical formula	$C_{14}H_{32}N_6NiO_4$	$C_{14}H_{32}N_6NiO_4$
Formula weight	407.17	407.17
T/K	90	90
Wavelength / Å	0.7749	0.7749
Crystal system	monoclinic	monoclinic
Space group	$P2_1/c$	$P2_1/c$
a/Å	9.629(5)	9.672(4)
b/Å	8.240(2)	8.366(4)
c/Å	11.804(2)	11.903(5)
α/º	90	90
β/°	109.03(2)	108.936(6)
γ/°	90	90
V/Å^3	885.4(5)	911.1(7)
Size/mm	0.10, 0.08, 0.08	0.10, 0.08, 0.08
Excitation/%	0	16
Z	2	2
D_c/g cm^{-3}	1.527	1.484
μ/mm^{-1}	1.129	1.097
$2\theta_{max}$	66.868	66.36
Reflections collected	8708	13361
Independent reflections, R_{int}	2609, 0.064	2778, 0.0649
Reflections obs. (> 2σ)	2277	2289
T_{min}/T_{max}	0.7673	0.8155
Final R_1, wR_2 [I>2σ(I)]	0.0434, 0.1150	0.0459, 0.1066
Final R_1, wR_2 (all data)	0.0481, 0.1178	0.0567, 0.1121

Table 5.14: Summary of crystal data for **11**

Compound	**11**
Empirical formula	$C_{14}H_{32}N_6NiO_4$
Formula weight	407.17
T/K	150
Wavelength / Å	0.71073
Crystal system	orthorhombic
Space group	*Pbca*
a/Å	9.4200(1)
b/Å	9.6000(2)
c/Å	19.8940(4)
α/°	90
β/°	90
γ/°	90
V/Å^3	1799.05(6)
Size/mm	0.3, 0.25, 0.2
Z	4
D_c/g cm^{-3}	1.503
μ/mm^{-1}	1.111
$2\theta_{max}$	60.98
Reflections collected	32058
Independent reflections, R_{int}	2746, 0.0456
Reflections obs. (> 2σ)	2261
T_{min}/T_{max}	0.4356
Final R_1, wR_2 [I>2σ(I)]	0.0285, 0.0697
Final R_1, wR_2 (all data)	0.0399, 0.0748

Table 5.15: Summary of crystal data for **12** and **12***

Compound	**12**	**12***
Empirical formula	$C_{12}H_{28}N_6NiO_4$	$C_{12}H_{28}N_6NiO_4$
Formula weight	379.11	379.11
T/K	100	100
Wavelength / Å	0.68960	0.7749
Crystal system	monoclinic	monoclinic
Space group	$P2_1/c$	$P2_1/c$
a/Å	8.6169(5)	8.349(2)
b/Å	8.5490(2)	8.646(2)
c/Å	11.5680(7)	11.836(3)
α/°	90	90
β/°	104.008(1)	102.692(3)
γ/°	90	90
V/Å^3	826.83(8)	833.5(3)
Size/mm	0.08, 0.05, 0.05	0.08, 0.05, 0.05
Excitation/%	0	35
Z	2	2
D_c/g cm^{-3}	1.523	1.511
μ/mm^{-1}	1.203	1.193
$2\theta_{max}$	59.04	60.82
Reflections collected	9220	9187
Independent reflections, R_{int}	2512, 0.0306	2505, 0.0396
Reflections obs. (> 2σ)	2247	1468
T_{min}/T_{max}	0.758026	0.7230
Final R_1, wR_2 [I>2σ(I)]	0.0285, 0.0729	0.0613, 0.1708
Final R_1, wR_2 (all data)	0.0320, 0.0756	0.1055, 0.1967

Table 5.16: Summary of crystal data for **13** and **13***

Compound	**13**	**13***
Empirical formula	$C_{12}H_{28}N_6NiO_6$	$C_{12}H_{28}N_6NiO_6$
Formula weight	411.11	411.11
T/K	100	100
Wavelength / Å	0.68960	0.68960
Crystal system	triclinic	triclinic
Space group	*P*-1	*P*-1
a/Å	7.172(5)	7.2136(13)
b/Å	7.988(5)	7.9994(14)
c/Å	8.330(5)	8.3000(14)
α/°	94.306(5)	94.581(2)
β/°	112.642(5)	111.364(2)
γ/°	100.496(5)	101.278(2)
V/Å^3	427.5(5)	431.39(13)
Size/mm	0.10, 0.08, 0.08	0.10, 0.08, 0.08
Excitation/%	0	22
Z	1	1
D_c/g cm^{-3}	1.597	1.582
μ/mm^{-1}	1.179	1.168
$2\theta_{max}$	59.00	59.12
Reflections collected	4890	4826
Independent reflections, R_{int}	2523, 0.0190	2533, 0.0185
Reflections obs. (> 2σ)	2437	2389
T_{min}/T_{max}	0.7551	0.7352
Final R_1, wR_2 [I>2σ(I)]	0.0278, 0.0722	0.0439, 0.1179
Final R_1, wR_2 (all data)	0.0288, 0.0732	0.0467, 0.1193

6. Triboluminescence of Lanthanide Complexes

A brief overview of the basic principles of luminescence, especially triboluminescence and sonoluminescence are given in this chapter together with the chemistry of some lanthanide complexes.

6.1. Introduction to Luminescence

Luminescence is the emission of light by a substance. It occurs after an appropriate material has absorbed energy (light, deformation, electronically, chemically) from a source and then, because excited states are unstable, the material undergoes another transition back to its ground state, and the absorbed energy is liberated in the form of light or heat. Luminescence efficiency depends on the degree of transformation of energy into light. Only a relatively small number of materials have sufficient luminescence efficiency to be of practical value. Examples for the use of luminescence involve the outputs from television or computer screens.

There are many different forms of luminescence depending on the method of excitation, including photoluminescence, cathodeluminescence, bioluminescence, triboluminescence and sonoluminescence. This project will focus on triboluminescence and sonoluminescence.

6.1.1. Triboluminescence

Triboluminescence occurs when crystalline materials are exposed to mechanical deformation. Light is then emitted from where the material is fractured and this is usually in the visible range. Although the existence of triboluminescence has been

known since at least 1605 (*The Advancement of Learning,* FRANCIS BACON), the mechanisms involved are still not well understood. Proposed mechanisms are able to explain the effects for a few materials, but there are always discrepancies to others and no consistent theory is available to date. According to literature estimates 50 % of all crystalline materials are triboluminescent, from which are 36 % inorganics, 19 % organics, 37 % aromatic compounds and 70 % alkaloids [105]. Crystals of nonluminescent compounds emit the spectrum produced through dinitrogen discharge as their triboluminescence; whereas crystals of luminescent materials display emission spectra characteristics of the material, occasionally combined with the dinitrogen discharge spectrum, when they triboluminesce [106].

6.1.1.1. History

After the first discovery of triboluminescence in household sucrose, much research focused on minerals and inorganic materials, as these were easily available. A list of triboluminescent materials can be found in GMELIN'S *Handbook of Chemistry* (1848). In the second half of the nineteenth century the research focused on organic compounds and by 1900, 400 to 500 different materials were known to show triboluminescence. During the 1950s the use of photomultipliers changed the available detection methods for new materials from the dark-adapted eye to scientific measurements.

Resulting from the new method, it was found that triboluminescence of a material is not independent of the way it is fractured, or for chiral molecules which enantiomer it is. This means that a crystal might be inactive along one axis, but is active along others, as well as that not both enantiomers have to be active. Other interesting factors are how the triboluminescence is affected by other external forces. It was found that some compounds lose their activation at higher temperatures; for example sucrose does not triboluminescence over 370 K. Even the change of the

surrounding atmosphere from air to other gases or solvents, can have an effect on triboluminescence and can increase or quench the triboluminescence [107].

Wint-O-Green lifesaver sweets show triboluminescence; in this case sucrose is the triboluminescent species, but the spectrum does not show the expected dinitrogen emission of sucrose, but instead the fluorescent spectra of the food additive methyl salicylate. This clearly demonstrates the possibility of shifting the wavelength of triboluminescence [108].

6.1.1.2. Brilliantly Triboluminescence Materials

The interest in triboluminescence did increase again as HURT found the first brilliantly triboluminescent materials [109]. This kind of luminescence has a higher intensity so that it is visible in broad daylight. Brilliant triboluminescence was found in a series of lanthanide complexes with chelating ligands. Triboluminescent materials with high intensities have much greater potential for use in practical applications.

One application, which has been suggested for these brilliantly triboluminescent materials, is the development of damage sensors. With decreasing amounts of fossil fuels, it has become necessary to reduce the weight of composites which are used, for example, in planes and cars. Metals are replaced by carbon fibres and resins, leaving one major drawback, the possibility to transfer an impact throughout the material. Even if the outside of these materials appears free of damage, there is a chance for invisible inner damage. Currently it is difficult and expensive to detect this kind of damage. Here is a possible application for triboluminescent materials, which would transform and emit light if damaged. This light could then been transferred with fibre optics to a detector, where it would be recorded and trigger an alarm. As the intensity is proportional to the impact, it would not only show if there is damage, but it would show the size of the damage as well.

As it is possible to tune the luminescence wavelength with the inclusion of dyes into the triboluminescent materials, different parts could show different emission to make an exact localisation easier. Nonetheless there are still some problems which need to be solved before these materials can be used in practice [110].

6.1.1.3. Mechanism of Triboluminescence

The mechanism can be separated into two different steps, excitation and emission. These specific mechanisms then vary between different compounds. For the excitation the varying factors named in the literature are the crystal system, disorder or forces in the structure, as well as impurities [111]. The emission mechanism on the other hand is based on empirical observations and is therefore easier to define. There are three different mechanisms to consider: emission on gas breakdown, photoluminescence because of gas discharge or luminescence from the metal centre. During the following paragraphs, these two steps are considered as totally separate. Although this is a major simplification, it is valid as interactions between excitation and emission cannot been studied with the current level of knowledge in this area.

The mechanism of excitation was hypothesised for many years as charge separation on each side of a fracture. Following from this fact, non-centrosymmetric crystals are very likely to show triboluminescence, whereas the occurrence of triboluminescence in centrosymmetric crystals produces a problem in this theory. Triboluminescence in many of these symmetric examples can be explained by impurities or disorder in the lattice, but there are other compounds with no obvious charge separation, which still show triboluminescence. Three of them were found by RHEINGOLD and are lanthanide complexes, which show brilliant triboluminescence (piperidinium-tetrakis-(benzoyl-acetonato)-europate, hexakis-(antipyrine)-terbium triiodide, hexa-aqua-terbium-chloride). It was suggested that weak polarisable interionic interactions might be responsible for the effect [112]. As there is no conclusive explanation yet for these materials this theory is still unproven. Nevertheless there are

good indications for the validity of the theory, as for example saccharin loses its ability for triboluminescence if it is highly purified [111]. This indicates that small defects might be enough to introduce a local discontinuity.

The mechanism of charge separation is probably based on the piezoelectric effect. An unstressed crystal has no dipole moment, whereas the electron density displaces under an external force. This produces a polarisation perpendicular to the vector of the straining force, as shown in Figure 6.1. The recombination of these charge carriers produces photons which are detectable as luminescence. This theory is strongly supported by the fact that crystals can have an axis where no triboluminescence is shown, even if the crystal in general is triboluminescent [105].

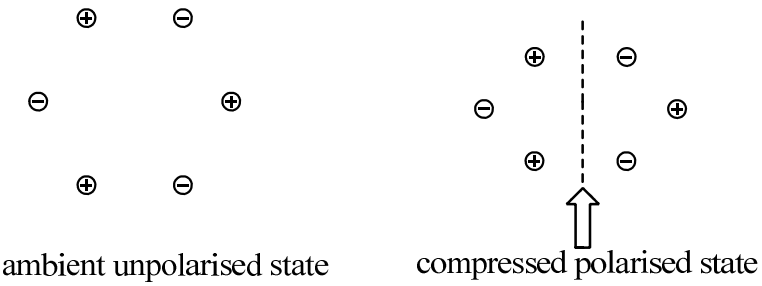

Figure 6.1: Schematic picture of the charge separation through an external force and the fracture along the dotted line after the compression.

Another factor affecting the excitation is the crystal structure. As mentioned above, aromatic compounds are more likely to show triboluminescence than other organic compounds; this is due to intermolecular forces in particular π-π-stacking arrangements. The importance of this interaction is obvious by comparison of different polymorphs, where the triboluminescence might depend on the polymorph [105].

As triboluminescent crystals show the spectrum of the surrounding gas [113], from phosphorescence [107] or fluorescence [109], these different spectra can help to distinguish between the emissions mechanisms. It is also possible that a combination of different spectra with different intensities [114] is observed for one material.

Most compounds shine with a white/blue colour. These spectra contain the bands of excited N_2 molecules. If the atmosphere is changed the spectra of these crystals change as well, it does for example increase in intensity under neon gas [107]. As a result of these spectra the following mechanism was proposed: The crystal fractures with charge separation occurring, which generates a potential difference. Upon discharge the N_2 molecules are excited by electron bombardment. Luminescent emission of molecular nitrogen then takes place. These materials lose their triboluminescence under liquids as their visible emission is only from the surrounding gas.

If the spectra indicate photoluminescence, but as before the compounds lose their emission under atmospheres where no gas discharge is possible, a second mechanism has been proposed. This mechanism is explained by inducing the photoluminescence through gas discharge. This means that the original gas discharge emission is self-absorbed by the crystal, which then produces the photoluminescence.

The third possible mechanism is of direct electron bombardment of the solid, which explains why this type of triboluminescence is not expected to be quenched under liquids [107]. This mechanism is named metal-centred luminescence, and it is most common for lanthanide complexes. Nevertheless it is known for other complexes, including complexes of manganese [115]. If the chromophores on a luminescent metal centre are excited, the energy is used to create an excited singlet state on the ligand. After an intersystem crossing, a triplet state is generated, which transfers the energy to the metal. This can than relax back into the ground state, resulting in luminescence. The emission is in the characteristic wavelength of the metal centre.

If the triboluminescent and the photoluminescent spectra are compared, a bathochromic shift is often found. It is suggested that self-absorption or fracture induced symmetry changes are responsible for this. Self-absorption occurs if the excitation and emission spectra of the solid show an overlap, as photoluminescence is

a surface effect, whereas triboluminescence is resulting from the bulk sample, so that the emitted light has to travel through the crystal [115].

All these mechanisms are interrelated and a compound might emit through more than one of the above to different degrees, as the combination of photoluminescence and a gas spectra is also possible [107]. While it is possible to predict which class of compounds follows which mechanism, it is impossible to predict which compound within this group will be triboluminescent.

6.2. Conclusion to Mechanism of Triboluminescence

The excitation mechanisms are as yet unproven, but the creation of an electric field seems to be a necessary condition. This can be achieved through missing symmetry, disorder or impurities.

The emission on the other hand can be separated into three different mechanisms:

a) The surrounding gas gets excited by electron bombardment, producing characteristic gas emission spectra. Changing the atmosphere produces different spectra. The emission is quenched under liquids.
b) The excited surrounding gas transfers the energy back to the compound, which then shows the specific photoluminescent spectra. As a gas is essential for this kind of excitation the emission is quenched under liquid as well.
c) The material gets directly excited through electron bombardment, producing a photoluminescence spectrum. This spectrum does not change under different atmospheres or liquids.

6.3. Introduction to Sonoluminescence

Sonoluminescence is luminescence of microscopic gas bubbles in a liquid under cavity formation. This occurs as micro sized bubbles form in a liquid, grow and finally collapse due to high-intensity ultrasound. Extreme conditions of high temperatures and high pressures are generated within the bubble. When it collapses, intense shock waves with velocities exceeding the speed of sound are initiated outwards from the imploded bubble [116].

In 1934, it was first found by FRENZEL and SCHULTES that these multi bubbles emit light of low intensity [116]. When the intense acoustic wave is passing through a liquid with gas bubbles, the latter are compressed to a degree such that the energy focusing at the time of the collapse leads to the emission of light. The spectrum of the emitted light tends to peak in the ultraviolet and depends strongly on the type of gas dissolved in the liquid. Small amounts of gases or other impurities can dramatically change the amount of light emission down to the total disappearance of it [116].

Even though a lot of research has been focused on sonoluminescence, the mechanism involved is still debatable. Two main theories govern the discussion, the theory of thermal excitation, and the theory of electric charge. According to the former, the luminescence is the result of thermal excitation which is achieved through collisions at high temperatures. On the other hand the electric theory explains the excitation processes as a result of an electron impact which leads to the electrical breakdown of the bubbles [117].

During the last decades research was firstly performed on solutions and slurries. For the former lanthanide salts were dissolved in water and processes related to photoluminescence in liquids were investigated. The characteristic luminescence of a series of lanthanide ions was observed against the background continuum of solvent emission during the sonication. It is assumed that for high-concentration, the ions can penetrate to the inside of the bubbles, which develop through sonication. The ions can then get involved in the internal processes within the bubble and the ions get excited.

The observed spectrum therefore depends on the photoluminescence of the metal used [118, 119]. If slurries or crystals of triboluminescent materials are sonicated, it was found that the emission is more intense than that from grinding. This was, for example, shown for sucrose where new emission lines were found, which might indicate that some reaction occurs in the solution [120, 121].

6.4. Introduction to Lanthanide Chemistry

The 14 elements following lanthanum in the periodic table are known as lanthanides. These are the elements from cerium to lutetium, which are also often called 'rare earth elements'. This is a misleading description as they are not necessary rare on earth, but initially it was difficult to extract them [122]. Another criterion for a lanthanide is a (partially) filled *f*-orbital; therefore lanthanum does not formally belong to the series, as it has no *f*-orbital electrons, nonetheless it is often included. The *f*-orbitals are filled along the series, if one proceeds from La to Lu. Scandium and yttrium are sometimes included in the lanthanide group as well, as they can show similar behaviour to the latter members of the group since they have a similar ionic radius, and have similar electronic configurations as lanthanum, as well as a chemistry which is dominated by the +3 oxidation state.

Historically lanthanides were found relatively late at the end of the 18th century and even then it was a mixture of more than one element: yttria. This misinterpretation was recognised 50 years later as cerium and lanthanum were extracted from yttria. The difficulty in separating these elements arises from their similarity [122]. Most of the lanthanide chemistry is dominated by the Ln^{3+} oxidation state, so that chemical separation generally failed. Even so, eventually, all naturally occurring lanthanides were found with the exception of promethium, which is radioactive. Promethium was eventually found as a decay product of Uranium 235 after the Second World War [122]. The separation of the lanthanides is nowadays achieved by solvent extraction; here the slight differences in solubility of the complexes are used [123].

The electronic structure of the lanthanide elements is [Xe] $4f^x\ 5d^0\ 6s^2$; although La, Gd and Lu have $5d^1$ instead of $5d^0$. This is due to the extra stability of empty, half or completely filled *f*-orbitals. La does not have any *f*-orbitals, whereas Gd gets its extra stability from the half filled *f*-shell and Lu from the fully filled *f*-shell.

As the *f*-orbitals are shielded by the 5*s* and 5*p* orbitals, they play little or no part in the bonding of the metal to ligands. The 4*f*-orbitals penetrate the 5*s* and 5*p*-orbitals, so that they are less shielded from the nucleus. The ionic radius decreases therefore from La to Lu, as the effective nuclear charge on the nucleus increases. This is called the 'lanthanide contraction' [123]. This effect however is not only found within the lanthanide series; in fact it is found across all periods, but it is most easily detectable in this series, as they typically all share the same oxidation state (III). This contraction is also seen in the analogy within the size between the 4*d* and 5*d* transition metals. Therefore 4*d* and 5*d* transition metals have a greater similarity than 3*d* and 4*d* transition metals.

The coordination chemistry of the lanthanides is mainly determined by the nature of the ligand. It is often constrained by the size of the ligands and of the steric interactions between them. It is therefore difficult to control the coordination number within the lanthanide series, as the metal ions are relatively large, and examples are known where the coordination number can range from 2 to 12 [123]. Most complexes have a coordination number which is bigger than six. A coordination number of 12 is only attainable using ligands with small 'bite angle' such as nitrate. Lanthanide complexes have an affinity for hard ligands, such as oxygen and fluorine [123].

There are several studies on the lanthanide contraction and the associated reduction in coordination number as the group is traversed. For $LnCl_3(thf)_x$ there are a range of different stoichiometries and structures reported. Different complexes were made with varied stoichiometries and / or reaction conditions, and a decrease of the coordination numbers from La to Lu was observed (Table 6.1) [124, 125].

Table 6.1: Structural change over the lanthanide series shown for $LnCl_3(thf)_x$

Ln	La	Ce	Pr	Nd	Sm	Eu	Gd	Tb	Dy	Ho	Er	Tm	Yb	Lu	Sc
CN	8	7	7	7 7	7	7	7 7 6	7 6	7 6	7 6	7 6	7 6	6 6	6	6
	P	P	P	P M_m	M_m	M_m	M_m I_c I_c	I_c I_c	I_c I_c	I_c I_c	I_c I_c	I_c I_c	D_m M_m	M_m	M_m

P = Polymer, M_m = Monomer, I_c = Ionic (cation / anion), D_m = Dimer

However, it is also possible that the coordination number does not change over the series. This is observed for the series of bipyridine complexes, $Ln(bipy)_2(NO_3)_3$ and the related 1,10-phenanthroline complexes $Ln(phen)_2(NO_3)_3$ (Ln = La, Pr, Nd, Eu, Lu), where all the complexes are 10 coordinate [124]. Nonetheless a reduction in coordination number is more common, as in the series of $Ln(terpy)(NO_3)_3 * x\ H_2O$ the earlier lanthanides (Ln = La - Gd) are ten coordinate being made up of salts containing $Ln(terpy)(NO_3)_2(H_2O)_3$ cations and the later elements (Ln = Y, Tb-Lu) are nine coordinate, containing $Ln(terpy)(NO_3)_2(H_2O)_2$ cations [126].

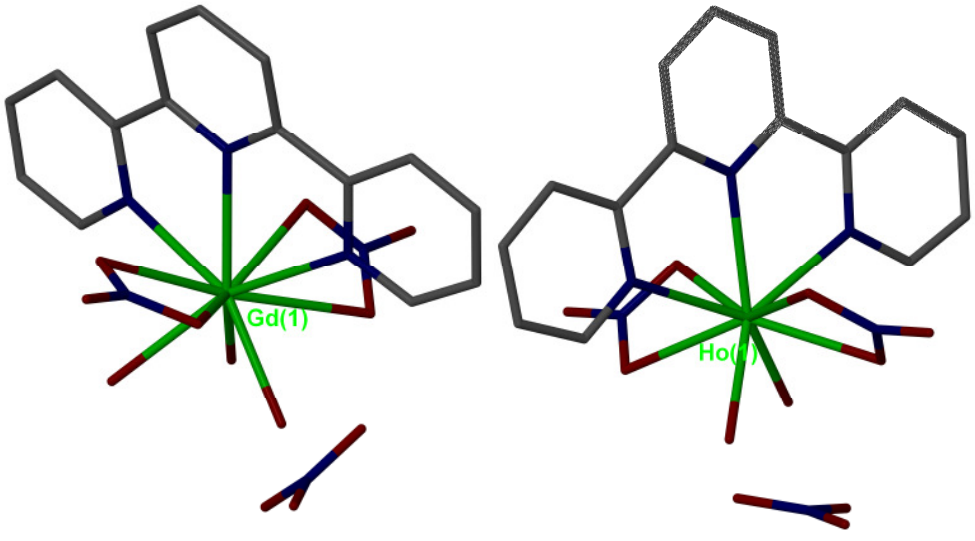

a b

Figure 6.2: Structures of a) $Gd(terpy)(NO_3)_2(H_2O)_3$ and b) $Ho(terpy)(NO_3)_2(H_2O)_2$ with hydrogens removed for clarity.

A big change in the coordination numbers is observed for the series of $Ln(CH_3COO)_3$. Here the numbers decrease from ten to seven [124, 127] (Table 6.2). The lanthanum complex (10 coordination) contains chelating and bridging acetates, the latter having one oxygen bound to two different lanthanum ions and the second oxygen only bound to one lanthanum. The nine coordinated structure of praseodymium involves only bridging acetates. All the structures with eight coordination involve only bridging acetates where only two oxygens per lanthanide ion are bound to two ions. All the structures with seven coordination involve only bridging acetates, where one oxygen per lanthanide ion is bound to two ions and in the Sc-complex all acetates are symmetrical.

Table 6.2: Example for a coordination number change shown on $Ln(CH_3COO)_3$

Ln	La-Nd	Pr-Nd	Sm-Er	Tm-Lu
CN	10	9	8	7

7. Triboluminescence Experiments

The interest in the structural correlations prompted the investigation of structural chemistry of several series of lanthanide complexes. One of these series is described within this chapter as some of these lanthanide complexes displayed strong triboluminescence under grinding.

*7.1. [Ln(Ph$_3$PO)$_x$(NCS)$_3$] - complexes (Ln*14 and Ln*15)*

7.1.1. Structures

Initially the complexes of [Ln(Ph$_3$PO)$_x$(NCS)$_3$] (x = 3 or 4) were prepared, following a similar metathetical route to that previously reported [128]. COUSIN and HART synthesised and characterised with IR spectroscopy the compounds [Ln(Ph$_3$PO)$_4$(NCS)$_3$] **Ln*14** (Ln = La-Sm, without Pm) and [Ln(Ph$_3$PO)$_3$(NCS)$_3$] **Ln*15** (Ln = Sm-Lu, Y). Additionally the 4:1 complexes of Eu, Gd and Tb were synthesised during this project. Following from the structure determination of all the compounds this series shows a decrease in the coordination number from seven to six, with a wide overlap in the middle of the sequence (Sm-Tb). The earlier lanthanides prefer the higher coordination number, whereas the latter ones have a smaller number of ligands, due to the lanthanide contraction. The only known structure of this series was [Nd(Ph$_3$PO)$_4$(NCS)$_3$], which was reported from KAUTZ [129], his structure is in extremely good agreement with ours. The average Nd-N distance being 2.502 Å compared to 2.503 Å and the average Nd-O distance being 2.371 Å instead of 2.375 Å, with the slight difference accounted for by a temperature difference of 10 K between the two structure determinations.

7.1.1.1. [Ln(Ph$_3$PO)$_4$(NCS)$_3$] Ln*14

The following complexes **Ln*14** (La-Tb) were isolated and structural identified, with all of them being isostructural. Here the structure of Pr(Ph$_3$PO)$_4$(NCS)$_3$ **Pr*14** (Fig. 7.1) is used to describe the geometry of the complexes. It displays a capped octahedral coordination geometry around Pr, with the thiocyanates along the capped axis of the octahedron. The first thought would be that this is due to the phosphine oxides being the bulkier ligands, but after measuring the structures of the 3:1 complexes this thought can be excluded. The complex crystallises in the monoclinic space group $P2_1/c$, with one molecule per asymmetric unit. Pr1 is related to Pr1' by the symmetry operation *x, -y+0.5, z-0.5*, to Pr1'' by *x-1, y, z* and to Pr1''' by *x, -y+1.5, z+0.5*. The average bond length for Pr-N and Pr-O is 2.523 Å and 2.389 Å respectively. Two of the Pr-N-C angles are nearly linear (170.7 ° and 172.0 °), whereas the third is slightly more bent (154.4 °), to avoid close contact to a phenyl ring of the neighbouring molecule. Nonetheless no obvious features are found in the crystal packing motif as no π-π-stacking of the phenyl rings or hydrogen bonds are found.

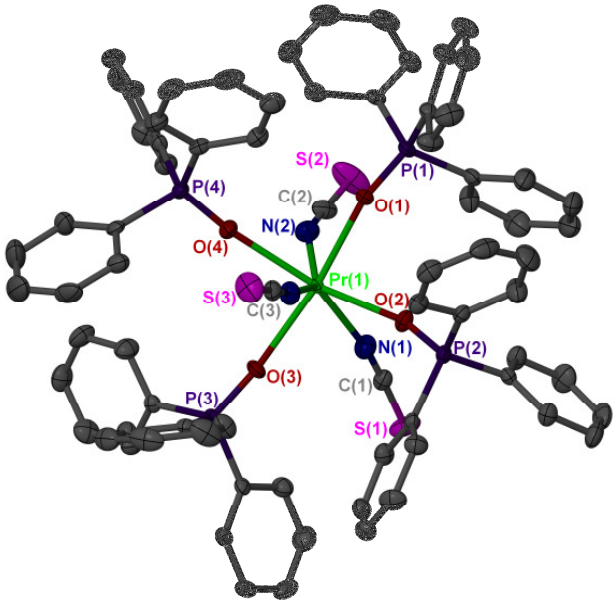

Figure 7.1: Structures of **Pr*14** with hydrogens removed for clarity.

On passing from **La*14** to **Tb*14**, the average Ln-O distance decreases from 2.429 Å to 2.307 Å, a decrease of 0.122 Å, whilst the average Ln-N distance decreases from 2.568 Å to 2.431 Å, a decrease of 0.137 Å. Both of these changes correspond closely to the change of ca. 0.11 Å predicted from crystal radii considerations [130].

The complexes of **Ln*14** have a similar structure to many other LnL_4X_3 systems. Examples are thf complexes with different halides ($[Yb(NCS)_3(thf)_4]$, $[EuCl_3(thf)_4]$ and $[GdCl_3(thf)_4]$ [125, 131], $[NdBr_3(thf)_4]$ [132] and $[PrI_3(thf)_4]$ [133]. In contrast to the $[Ln(NCS)_3(thf)_4]$, the $[Ln(Ph_3PO)_4(NCS)_3]$ complexes are monomeric, reflecting the increased steric bulk of Ph_3PO, related to thf. They share with the Pr complex the feature of one Pr-NCS linkage being noticeably more bent than the others (154.4 °, 170.7 ° and 172.0 °), as described for the La complex with angles of 153.4 °, 170.9 ° and 171.0 °. In the seven coordinate $[La((Me_2N)_3PO)_4(NCS)_3]$, the average La-O and La-N distances of 2.433 Å and 2.581 Å are closely comparable to the corresponding values of 2.429 Å and 2.568 Å in **La*14** [134]. The Nd-$OPPh_3$ distances in **Nd*14** (2.371 Å) are greater than those of $[Nd(Ph_3PO)_4(\eta^1\text{-OTf})(\eta^2\text{-OTf})]$ (2.323 Å), doubtless due to the small bite angle of the bidentate triflate permitting closer approach of the other ligands [135].

7.1.1.2. $[Ln(Ph_3PO)_3(NCS)_3]$ Ln*15

The 3:1 complexes are obtained for the later lanthanides (Ln = Y, Sm-Lu). These molecules have octahedral coordination, adopting the same structure as found for *fac*-$[Fe(Ph_3PO)_3(NCS)_3]$, a complex with a considerably smaller metal ion [136]. In contrast to the Fe structure both molecules in these structures have the same chirality. The complexes crystallise in the trigonal space group *R*3. The asymmetric unit contains one whole molecule and one third of a molecule, which is lying on a three fold axis (Fig. 7.2). N4 is therefore related to N4' by the symmetry operation *–x+y, -x+2, z* and to N4'' *by –y+2, x-y+2, z*. The two molecules have almost the

same geometry as shown in the description on the erbium structure **Er*15** in which the full molecule has average bond length of Er-N_{av}. 2.321 Å and Er-O_{av}. 2.213 Å, where the other ones are Er-N 2.312(4) Å, Er-O 2.221(2) Å. The N-C-Ln coordination is nearly linear, with values for the Er complex being 167.8 °, 174.2 ° and 175.4 ° and 168.5 ° for the second molecule. The crystal packing shows no obvious features as no π-π-stacking of the phenyl rings or hydrogen bonding is found.

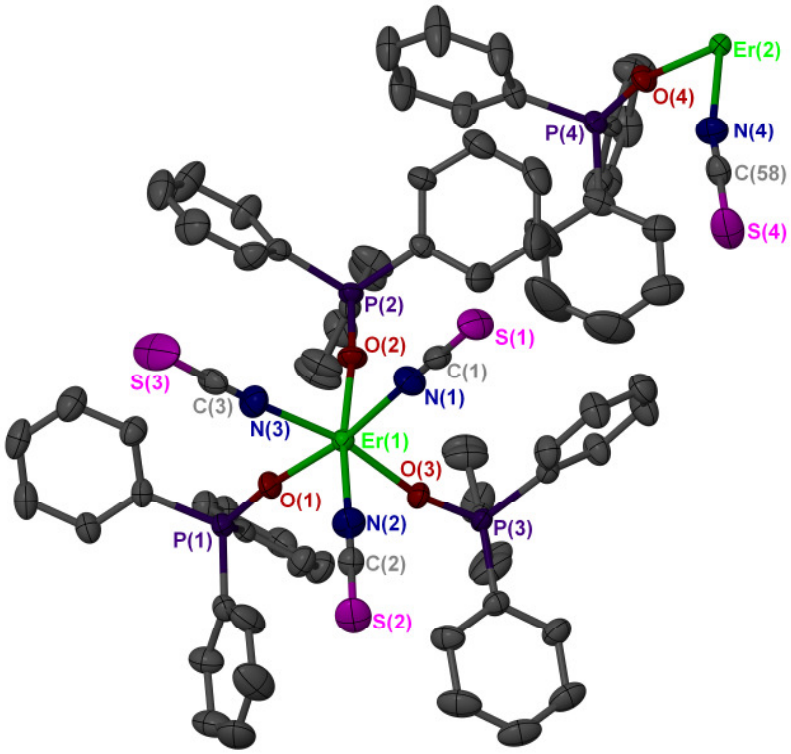

Figure 7.2: The asymmetric unit of the **Er*15** structure, showing 4/3 of the complex with hydrogens removed for clarity.

The fact that the compound exists as facial isomer suggests that the steric demands of triphenylphosphine oxide are lower than that of triphenylphosphine. This is explained by the larger distance between the bulky phenyl rings and the metal. Triphenylphosphine oxide and thiocyanate seems to be equally bulky in the first coordination sphere, as well as chloride and the tertiary phosphine oxide in $[Ln((Me_2N)_3PO)_3Cl_3]$ [137, 138], where both *fac* and *mer* isomers are found. On the other

hand Ph_3PO is more bulky than a chloride ligand as shown in $[Ln(Ph_3PO)_3Cl_3]$ (Ln = La, Ce), where the meridional structures are found [139].

The contraction of the bond length from **Sm*15** to **Lu*15** is of 0.115 Å for the Ln-N bond length and of 0.104 Å in the Ln-O distance. These contractions may be compared with a contraction of 0.097 Å [130] in the crystal radii, which lies below the two distances above. The distances in the iron complex $[Fe(Ph_3PO)_3(NCS)_3]$ are nearly identical with 2.022 Å for $Fe\text{-}N_{av.}$ and 2.024 Å for $Fe\text{-}O_{av}$ [136].

If the structures are compared with other lanthanide structures, it is shown that the average Tb-O distance of 2.260 Å in **Tb*15** compares closely with the value of 2.262 Å in the $[Tb(Ph_3PO)_4Cl_2]^+$ ion [139]. The Lu-OPh_3 distance of 2.194 Å in **Lu*15** is also comparable to similar Lu complexes (cf. 2.183 Å [140] in $[Lu(\eta^1\text{-}OTf)_2(OPPh_3)_4]$). On the other hand the average Y-O distances of 2.176 Å in the **Y*15** complex are rather shorter than the distances of 2.228 Å and 2.224 Å in the $[Y(Ph_3PO)_4Cl_2]^+$ and $[Y(Ph_3PO)_4Br_2]^+$ ions [141].

7.1.1.3. Comparison between Ln*14 and Ln*15

The complexes **Ln*14** and **Ln*15** (Sm, Gd, Eu, Tb) permit direct assessment of the effect in change of coordination number upon bond length. The decrease in Ln-N and Ln-O bond length between the seven and six- coordinate complexes lies between 0.047 Å and 0.071 Å, closely corresponding to the difference in ionic radius between seven and six coordination given by SHANNON [130].

Table 7.1: Comparison of averaged bond length between $[Ln(Ph_3PO)_x(NCS)_3]$ for Sm-Tb

		Sm	Δ (Å)	Eu	Δ (Å)	Gd	Δ (Å)	Tb	Δ (Å)
14	M-O	2.348		2.337		2.325		2.307	
15	M-O	2.298	0.050	2.282	0.055	2.269	0.056	2.260	0.047
14	M-N	2.470		2.455		2.450		2.431	
15	M-N	2.399	0.071	2.390	0.065	2.388	0.062	2.363	0.068

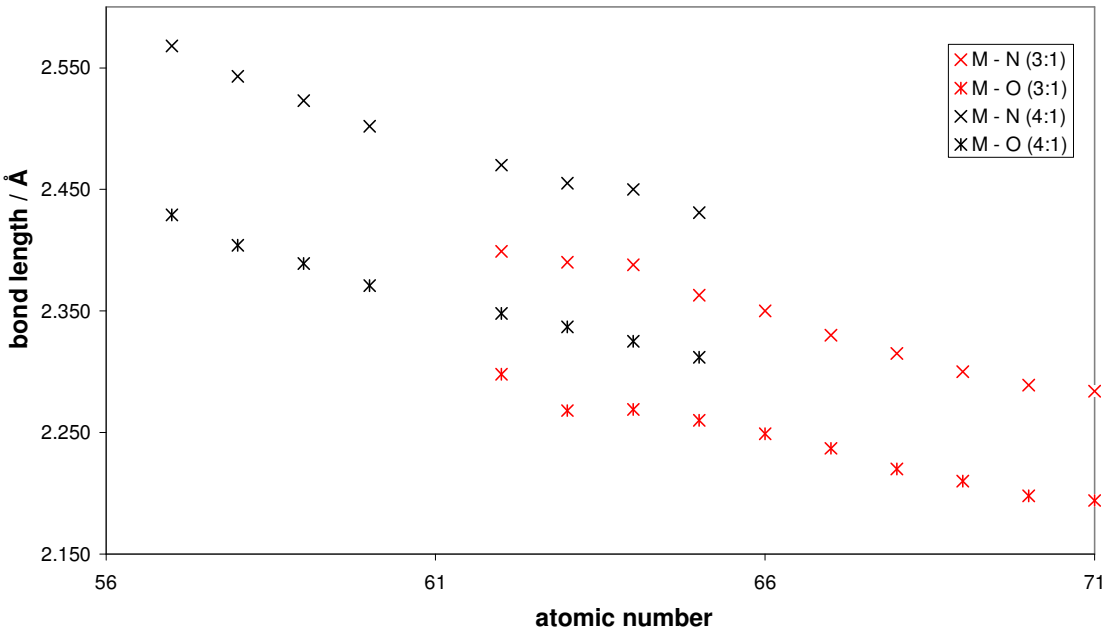

Figure 7.3: Relationship between bond lengths in complexes $Ln(Ph_3PO)_x(NCS)_3$ and the atomic number of the lanthanides.

7.1.2. Infrared Spectroscopy

The infrared spectra of the complexes were recorded and found to be generally in very good agreement with those reported by COUSINS and HART [128]. The two families of complexes can be distinguished by the spectra in the ν_{CN} region.

Table 7.2: Main infrared peaks of **Ln*14** and **Ln*15**

	Ln*14 / cm^{-1}			**Ln*15 /** cm^{-1}	
La	2069	2056	2045		
Ce	2071	2057	2047		
Pr	2072	2057	2048		
Nd	2073	2059	2049		
Sm	2076	2062	2051		2031
Eu	2077	2063	2053	2053	2029
Gd	2078	2064	2054	2061	2036
Tb	2080	2066	2056	2061	2031
Dy				2063	2037
Ho				2060	2040
Er				2067	2041
Tm				2064	2039
Yb				2070	2044
Lu				2071	2046
Y				2072	2046

The tris complexes contain two bands in the region 2000-2100 cm^{-1}, a main band at lower frequency with resolved shoulder at higher frequency as expected for a *fac*-$ML_3(NCS)_3$ system [142], whereas the tetrakis complexes give rise to three bands, a split doublet with a resolved shoulder to higher frequency, consistent with the environment of lower symmetry.

7.1.3. Triboluminescence

In order to draw conclusions regarding the activity of this lanthanide series, the compounds obtained were examined for triboluminescence. Their activity through grinding was observed with the darkness adapted eye and later on, photographs were taken to verify the visual measurements. Different experiments were performed to assign the specific mechanism for the triboluminescence of these complexes such as measuring the triboluminescence under solvent or vacuum, at higher temperature or in liquid nitrogen. One other experiment was performed as well to test the possibility of shifting the wavelength with a dye.

Table 7.3 shows that for these compounds only chiral crystals display any triboluminescence, and of these complexes only five display triboluminescence under grinding. The green triboluminescence from **Tb*15** was so strong that it was possible to see it in daylight, whereas the other ones are only visible in the dark. The complexes of samarium and europium show red, thulium blue and dysprosium white emission (Figure 7.4).

Table 7.3: Triboluminescence of $[Ln(Ph_3PO)_x(NCS)_3]$

Ln	La	Ce	Pr	Nd	Sm	Eu	Gd	Tb						
14	x	x	x	x	x	x	x	x						
Ln					Sm	Eu	Gd	Tb	Dy	Ho	Er	Tm	Yb	Lu	Y
15					✓	✓	x	✓	✓	x	x	✓	x	x	x
					red	red		green	white			blue			

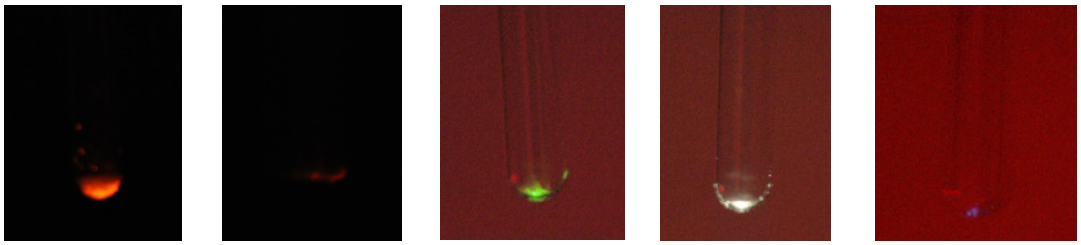

Sm Eu Tb Dy Tm

Figure 7.4: Photographs of the emission of the triboluminescent crystals.

The complex of **Tb*15** was used to investigate different experimental conditions as the emitted light was simple to observe. It was confirmed that the triboluminescence was quenched under liquid, although only a small amount of the liquid did not prevent the emission. This proves that the mechanism for these complexes is not a direct bombardment, as that would produce a photoluminescence spectrum independent of the atmosphere. The mechanism has to be excitation through an energy transfer from the surrounding gas, as the different complexes do not show the specific gas spectra. The triboluminescence is not quenched under vacuum, which suggest that gas is absorbed on the crystal surfaces. There is no thermal quenching up

to a temperature of 423 K. Even though the sample is still triboluminescent after addition of a dye, no wavelength shift could be observed. This experiment was carried out with the laser dye coumarin 343, which has its maximum emission at 490 nm. No triboluminescence was observed, when the crystal is thrown into liquid nitrogen. All the observations are displayed in Table 7.4.

Table 7.4: Triboluminescence of **Tb*15** under different conditions

H_2O	drop H_2O	DCM	drop DCM	N_2 lq	323 K	373 K	423 K	vac	dye	dye + EtOH
x	✓	x	✓	x	✓	✓	✓	✓	✓	x

7.2. Sonoluminescence Experiments

Sonoluminescence experiments were performed in teradecane, which displays a small blue emission under sonication by itself, but was used successfully in the past within the group. Figure 7.5 displays the sonoluminescence of teradecane.

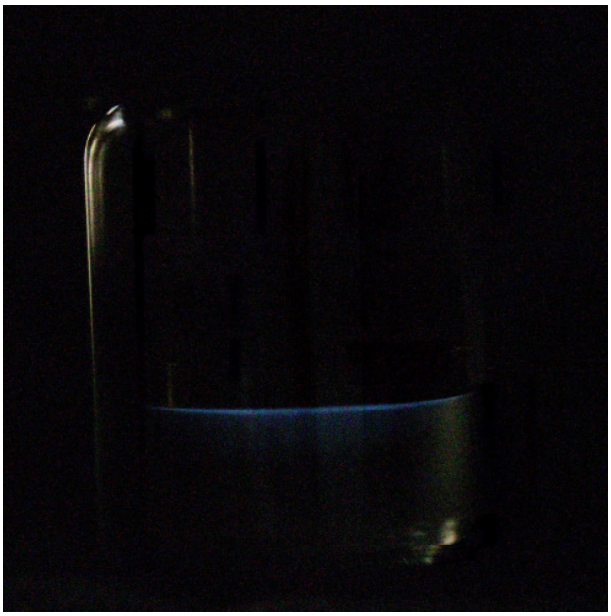

Figure 7.5: Photographs of the emission of teradecane under sonication.

No sonoluminescence was observed with our lanthanide complexes $[Ln(Ph_3PO)_3(NCS)_3]$ under constant sonication at different power settings. Nonetheless it is possible that the intensity of the emission was not high enough to observe it. Another possibility is that the emission was quenched due to the surrounding liquid, as it occurs with the triboluminescence under liquids.

It was noted that if a suspension is formed the sonoluminescence of tetradecane gets "quenched". The most likely case is that the particles absorb the emitted light.

7.3. Conclusion

A series of lanthanide complexes with a reduction of coordination number around the lanthanide is described in this chapter. Unusual here is that around the changeover point, a clear equilibrium between six- and seven- coordinate species is found in solution and that both complexes are isolable. Five complexes (**Sm*15**, **Eu*15**, **Tb*15**, **Dy*15** and **Tm*15**) display triboluminescence, whereas none shows sonoluminescence. The triboluminescence is likely to occur through excitation of the surrounding gas, as the different complexes show different spectra, but the triboluminescence is quenched under liquid.

7.4. Summary of the Crystal Data

Table 7.5: Summary of crystal data for **La*14** and **Ce*14**

Compound	**La*14**	**Ce*14**
Empirical formula	C75 H60 N3 O4 P4 S3 La	C75 H60 N3 O4 P4 S3 Ce
Formula weight	1426.23	1427.44
T/K	150	150
Wavelength / Å	0.71073	0.71073
Crystal system	monoclinic	monoclinic
Space group	*P*21/*c*	*P*21/*c*
a/Å	13.1540(1)	13.1510(1)
b/Å	23.6120(2)	23.5450(2)
c/Å	22.4610(2)	22.4670(2)
α/°	90	90
β/°	102.33(3)	102.489(1)
γ/°	90	90
V/Å^3	6815.4(1)	6792.08(10)
Size/mm	0.6, 0.4, 0.4	0.4, 0.3, 0.3
Z	4	4
D_c/g cm^{-3}	1.39	1.396
μ/mm^{-1}	0.864	0.908
$2\theta_{max}$	60.6	60.54
Reflections collected	94785	102635
Independent reflections, R_{int}	18382, 0.0437	18751, 0.0728
Reflections obs. (> 2σ)	14633	12576
T_{min}/T_{max}	0.929	0.923
Final R_1, wR_2 [I>2σ(I)]	0.0329, 0.0715	0.0426, 0.0759
Final R_1, wR_2 (all data)	0.0511, 0.0801	0.0901, 0.0907

Table 7.6: Summary of crystal data for **Pr*14** and **Nd*14**

Compound	**Pr*14**	**Nd*14**
Empirical formula	C75 H60 N3 O4 P4 S3 Pr	C75 H60 N3 O4 P4 S3 Nd
Formula weight	1428.23	1431.56
T/K	150	100
Wavelength / Å	0.71073	0.6942
Crystal system	monoclinic	monoclinic
Space group	*P*21/*c*	*P*21/*c*
a/Å	13.1347(3)	13.1148(4)
b/Å	23.4777(6)	23.3900(7)
c/Å	22.4376(7)	22.3832(6)
α/°	90	90
β/°	102.396(3)	102.65(3)
γ/°	90	90
V/Å^3	6757.8(3)	6699.4(3)
Size/mm	0.4, 0.2, 0.15	0.03, 0.02, 0.01
Z	4	4
D_c/g cm^{-3}	1.404	1.419
μ/mm^{-1}	0.96	1.016
$2\theta_{max}$	65.50	59.34
Reflections collected	81556	76486
Independent reflections, R_{int}	23095, 0.0582	20270, 0.049
Reflections obs. (> 2σ)	12830	17357
T_{min}/T_{max}	0.841	0.752391
Final R_1, wR_2 [I>2σ(I)]	0.0316, 0.0447	0.0329, 0.0777
Final R_1, wR_2 (all data)	0.0792, 0.0479	0.0397, 0.0815

Table 7.7: Summary of crystal data for **Sm*14** and **Sm*15**

Compound	**Sm*14**	**Sm*15**
Empirical formula	C75 H60 N3 O4 P4 S3 Sm	C76 H60 N4 O4 P4 S4 Sm1.33
Formula weight	1437.67	1545.86
T/K	150	150
Wavelength / Å	0.71073	0.71073
Crystal system	monoclinic	trigonal
Space group	*P*21/*c*	*R*3
a/Å	13.1360(1)	38.5767(6)
b/Å	23.3600(2)	38.5767(6)
c/Å	22.5090(2)	12.4389(2)
α/°	90	90
β/°	102.6(2)	90
γ/°	90	120
V/Å^3	6740.62(10)	16031.1(4)
Size/mm	0.5, 0.4, 0.4	0.2, 0.2, 0.1
Z	4	9
D_c/g cm^{-3}	1.417	1.441
μ/mm^{-1}	1.111	1.352
$2\theta_{max}$	54.96	62.28
Reflections collected	95107	51656
Independent reflections, R_{int}	15392, 0.0471	20080, 0.0256
Reflections obs. (> 2σ)	12727	16404
T_{min}/T_{max}	0.912	0.936
Final R_1, wR_2 [I>2σ(I)]	0.0296, 0.0637	0.025, 0.0402
Final R_1, wR_2 (all data)	0.0426, 0.0694	0.0367, 0.0416
Flack parameter		-0.016(3)

Table 7.8: Summary of crystal data for **Eu*14** and **Eu*15**

Compound	**Eu*14**	**Eu*15**
Empirical formula	C75 H60 N3 O4 P4 S3 Eu	C76 H60 N4 O4 P4 S4 Eu1.33
Formula weight	1439.28	1548.01
T/K	150	150
Wavelength / Å	0.71073	0.71073
Crystal system	monoclinic	trigonal
Space group	*P*21/*c*	*R*3
a/Å	13.1350(1)	38.5677(7)
b/Å	23.3100(3)	38.5677(7)
c/Å	22.5250(2)	12.4471(2)
α/°	90	90
β/°	102.485(1)	90
γ/°	90	120
V/Å^3	6733.54(12)	16034.2(5)
Size/mm	0.5, 0.5, 0.2	0.2, 0.2, 0.1
Z	4	9
D_c/g cm^{-3}	1.42	1.443
μ/mm^{-1}	1.172	1.427
$2\theta_{max}$	54.96	62.24
Reflections collected	42868	56628
Independent reflections, R_{int}	15348, 0.0458	19455, 0.0462
Reflections obs. (> 2σ)	12119	16631
T_{min}/T_{max}	0.912	0.829
Final R_1, wR_2 [I>2σ(I)]	0.0341, 0.0853	0.0243, 0.0434
Final R_1, wR_2 (all data)	0.0523, 0.1003	0.0346, 0.0451
Flack parameter		-0.012(3)

Table 7.9: Summary of crystal data for **Gd*14** and **Gd*15**

Compound	**Gd*14**	**Gd*15**
Empirical formula	C75 H60 N3 O4 P4 S3 Gd	C76 H60 N4 O4 P4 S4 Gd1.33
Formula weight	1444.57	1555.06
T/K	150	150
Wavelength / Å	0.6895	0.71073
Crystal system	monoclinic	trigonal
Space group	*P*21/*c*	*R*3
a/Å	13.137(5)	38.6760(9)
b/Å	23.294(5)	38.6760 (9)
c/Å	22.557(5)	12.3410(3)
α/°	90	90
β/°	102.599(5)	90
γ/°	90	120
V/Å^3	6737(3)	15986.9(7)
Size/mm	0.06, 0.05, 0.04	0.6, 0.5, 0.3
Z	4	9
D_c/g cm^{-3}	1.424	1.454
μ/mm^{-1}	1.225	1.499
$2\theta_{max}$	59.06	60.12
Reflections collected	76414	49173
Independent reflections, R_{int}	20290, 0.0803	18224, 0.0952
Reflections obs. (> 2σ)	14885	19574
T_{min}/T_{max}	0.759	0.807
Final R_1, wR_2 [I>2σ(I)]	0.048, 0.0967	0.0623, 0.1697
Final R_1, wR_2 (all data)	0.0715, 0.1095	0.1082, 0.1482
Flack parameter		-0.029(9)

Table 7.10: Summary of crystal data for **Tb*14** and **Tb*15**

Compound	**Tb*14**	**Tb*15**
Empirical formula	C75 H60 N3 O4 P4 S3 Tb	C76 H60 N4 O4 P4 S4 Tb1.33
Formula weight	1446.24	1557.24
T/K	100	100
Wavelength / Å	0.71073	0.6942
Crystal system	monoclinic	trigonal
Space group	*P*21/*c*	*R*3
a/Å	13.1001(3)	38.4516(6)
b/Å	23.2569(5)	38.4516(6)
c/Å	22.4314(5)	12.3695(4)
α/°	90	90
β/°	103.063(2)	90
γ/°	90	120
V/Å^3	6657.3(3)	15838.4(6)
Size/mm	0.3475, 0.2728, 0.2163	0.03, 0.03, 0.03
Z	4	9
D_c/g cm^{-3}	1.443	1.469
μ/mm^{-1}	1.305	1.596
$2\theta_{max}$	65.50	59.48
Reflections collected	50284	61147
Independent reflections, R_{int}	22109, 0.0359	21168, 0.0462
Reflections obs. (> 2σ)	14234	19574
T_{min}/T_{max}	0.912	0.576
Final R_1, wR_2 [I>2σ(I)]	0.0287, 0.0479	0.0372, 0.0745
Final R_1, wR_2 (all data)	0.0595, 0.0501	0.0412, 0.0769
Flack parameter		0.008(4)

Table 7.11: Summary of crystal data for **Dy*15** and **Ho*15**

Compound	**Dy*15**	**Ho*15**
Empirical formula	C76 H60 N4 O4 P4 S4 Dy1.33	C76 H60 N4 O4 P4 S4 Ho1.33
Formula weight	1561.53	1564.76
T/K	150	150
Wavelength / Å	0.71073	0.71073
Crystal system	trigonal	trigonal
Space group	*R*3	*R*3
a/Å	38.5720(6)	38.5560(3)
b/Å	38.5720(6)	38.5560(3)
c/Å	12.4070(1)	12.4000(1)
α/°	90	90
β/°	90	90
γ/°	120	120
V/Å^3	15986.1(4)	15963.8(2)
Size/mm	0.2, 0.1, 0.08	0.2, 0.2, 0.1
Z	9	9
D_c/g cm^{-3}	1.46	1.465
μ/mm^{-1}	1.653	1.738
$2\theta_{max}$	60.92	60.98
Reflections collected	83206	95049
Independent reflections, R_{int}	19143, 0.0542	20085, 0.0582
Reflections obs. (> 2σ)	14076	16018
T_{min}/T_{max}	0.939	0.824
Final R_1, wR_2 [I>2σ(I)]	0.0403, 0.0787	0.0333, 0.0676
Final R_1, wR_2 (all data)	0.077, 0.1017	0.0573, 0.086
Flack parameter	-0.022(5)	-0.014(4)

Table 7.12: Summary of crystal data for **Er*15** and **Tm*15**

Compound	**Er*15**	**Tm*15**
Empirical formula	C76 H60 N4 O4 P4 S4 Er1.33	C76 H60 N4 O4 P4 S4 Tm1.33
Formula weight	1567.86	1570.08
T/K	150	150
Wavelength / Å	0.71073	0.71073
Crystal system	trigonal	trigonal
Space group	*R*3	*R*3
a/Å	38.54(3)	38.5320(4)
b/Å	38.54(3)	38.5320(4)
c/Å	12.397(10)	12.3960(2)
α/°	90	90
β/°	90	90
γ/°	120	120
V/Å^3	15946.7(2)	15938.8(3)
Size/mm	0.5, 0.4, 0.4	0.2, 0.2, 0.16
Z	9	9
D_c/g cm^{-3}	1.469	1.472
μ/mm^{-1}	1.83	1.921
$2\theta_{max}$	60.98	60.98
Reflections collected	67407	84174
Independent reflections,	18939, 0.0461	19428, 0.0768
Reflections obs. (> 2σ)	16263	12046
T_{min}/T_{max}	0.905	0.885
Final R_1, wR_2 [I>2σ(I)]	0.0309, 0.0659	0.0469, 0.0738
Final R_1, wR_2 (all data)	0.0441, 0.0749	0.1129, 0.1072
Flack parameter	-0.033(4)	-0.025(5)

Table 7.13: Summary of crystal data for **Yb*15** and **Lu*15**

Compound	**Yb*15**	**Lu*15**
Empirical formula	C76 H60 N4 O4 P4 S4 Yb1.33	C76 H60 N4 O4 P4 S4 Lu1.33
Formula weight	1575.54	1578.11
T/K	150	150
Wavelength / Å	0.71073	0.71073
Crystal system	trigonal	trigonal
Space group	*R*3	*R*3
a/Å	38.548(3)	38.5240(3)
b/Å	38.548(3)	38.5240(3)
c/Å	12.389(10)	12.3820(1)
α/°	90	90
β/°	90	90
γ/°	120	120
V/Å^3	15943.0(2)	15914.2(2)
Size/mm	0.5, 0.5, 0.4	0.2, 0.16, 0.1
Z	9	9
D_c/g cm^{-3}	1.477	1.482
μ/mm^{-1}	2.01	2.112
$2\theta_{max}$	60.98	56
Reflections collected	60584	87469
Independent reflections, R_{int}	18292, 0.0455	16866, 0.0714
Reflections obs. (> 2σ)	15638	13447
T_{min}/T_{max}	0.856	0.725
Final R_1, wR_2 [I>2σ(I)]	0.0329, 0.0761	0.0345, 0.0708
Final R_1, wR_2 (all data)	0.047, 0.0873	0.0576, 0.0922
Flack parameter	-0.036(4)	-0.021(5)

Table 7.14: Summary of crystal data for **Y*15**

Compound	**Y*15**
Empirical formula	C76 H60 N4 O4 P4 S4 Y1.33
Formula weight	1463.94
T/K	100
Wavelength / Å	0.6942
Crystal system	trigonal
Space group	*R*3
a/Å	38.3629(16)
b/Å	38.3629(16)
c/Å	12.3474(16)
α/°	90
β/°	90
γ/°	120
V/Å^3	15737.2(16)
Size/mm	0.06, 0.04, 0.03
Z	9
D_c/g cm^{-3}	1.390
μ/mm^{-1}	1.37
$2\theta_{max}$	59.48
Reflections collected	40503
Independent reflections, R_{int}	20159, 0.0523
Reflections obs. (> 2σ)	17090
T_{min}/T_{max}	0.710
Final R_1, wR_2 [I>2σ(I)]	0.0904, 0.2408
Final R_1, wR_2 (all data)	0.1027, 0.2647
Flack parameter	0.215(8)

8. General Experimental

8.1. X-ray Diffractometers

Single crystal X-ray diffraction experiments were performed using a variety of instruments and X-ray sources. Two types of laboratory instruments were used: a Bruker Nonius Kappa CCD four circle diffractometer, with Mo-Kα radiation and an Oxford Cryosystems cryostream and an Oxford Gemini A Ultra diffractometer (either Mo-Kα or Cu-Kα radiation) equipped with a Cryojet low temperature device.

Figure 8.1: X-ray diffractometers.

Three synchrotron sources were used: the Advanced Light Source (ALS) in San Fransisco, Daresbury Synchtrotron Radiation Source (SRS) and the Diamond Light Source (DLS) in Didcot. The stations at the ALS and SRS were equipped with a Bruker APEXII CCD diffractometer. At the ALS on Station 11.3.1 the diffractometer was equipped with an Oxford Cryosystems cryostream device; it can be used for temperature studies in the range 90-500 K. On Station 9.8 in Daresbury the single-crystal X-ray data collections were carried out with either an Oxford Cryosystems cryostream cooling device (for temperature studies in the range 90-600 K) or an Oxford Cryosystems N-Helix crystal cooling device (for temperature studies in the range 30-300 K). At Diamond, a Rigaku Saturn four circle CCD diffractometer equipped with an Oxford Cryosystems Cryostream Plus (for temperature studies from

80 to 500 K) was used.

All X-ray powder data were measured on a Bruker AXS D8 Advance powder diffractometer. Copper radiation was used and the generator set at 40 kV, 40 mA. The sample can be measured in a capillary or as a flat plate sample holder from 100 K up to 723 K.

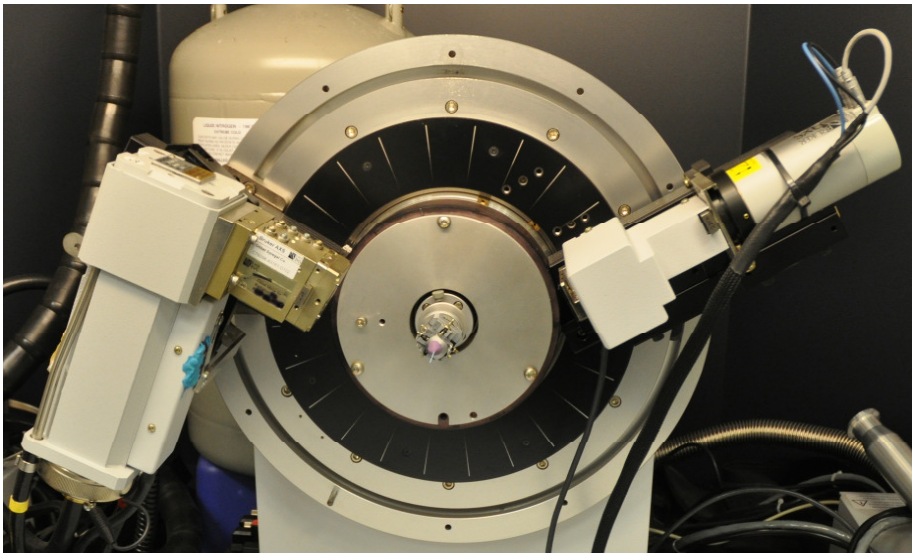

Figure 8.2: Powder diffractometer in capillary mode.

8.2. Raman Spectrometer

Raman spectra were recorded on a confocal Horiba-Jobin-Yvon LabRAM Raman Microscope using a 660 nm diode laser and a 600 lines/mm grating and a Synapse CCD detector. The spectra were recorded at laser power of ca. 10 mW. A Linkam FTIR600 variable-temperature stage with CaF_2 windows was modified with tubing to fit the Raman spectrometer and used to control the low temperatures.

Irradiation of the crystal was performed using a block of seven UV LEDs, which were placed 8 mm from the sample. The crystal was in a fixed position during irradiation.

8.3. UV-vis Spectrometer

UV-vis spectra were collected on a Perkin Elmer, Lambda 650 UV/VIS spectrometer in glass cuvettes for the solution measurements (MeOH, DCM). UV irradiation experiments with UV-vis in the solid state were carried out on sticky tape. As sticky tape is UV active as well, two reference samples were irradiated under the same conditions as the sample and the data were only used up to 240 nm for the background subtraction. The error in the data between 200-240 nm is random and can therefore not be subtracted. Another problem of using sticky tape is that the change in light source within the spectrometer results in a discontinuity of the data (which occurs at 318 nm). Additionally, the intensity is lower in the solid state, but the background is higher (Fig. 8.3).

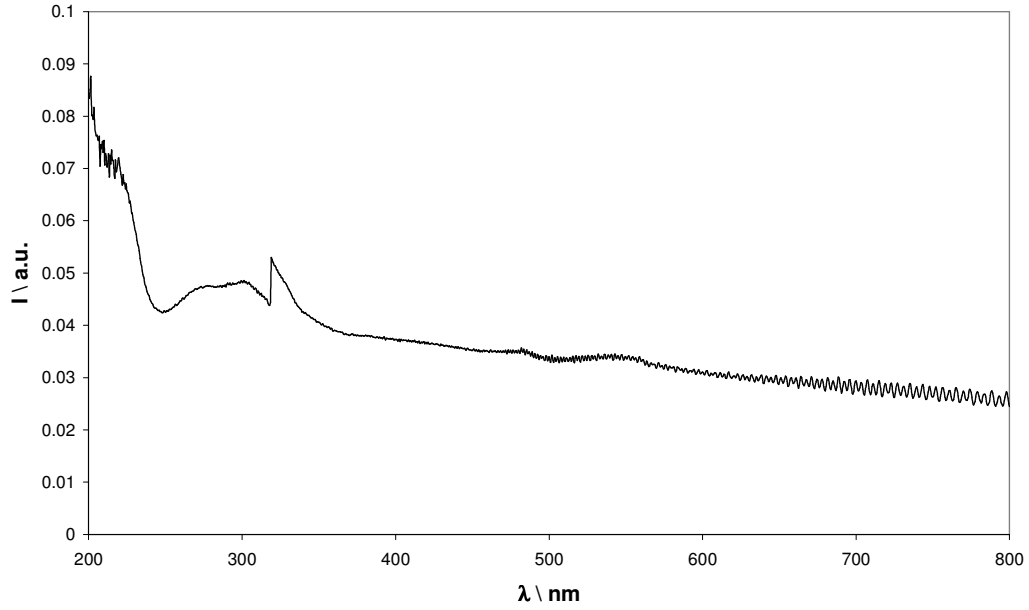

Figure 8.3: Solid state UV-vis of the complex **3b** after 30 min irradiation without any corrections.

The following procedure was used to extract the data from the solid state measurements (Fig. 8.4):

1. Background subtraction at 375 nm
2. Removing the data from 240 nm up to 200 nm
3. Removing the discontinuity by assuming that the y value of 318.5 nm equals the one from 319 nm

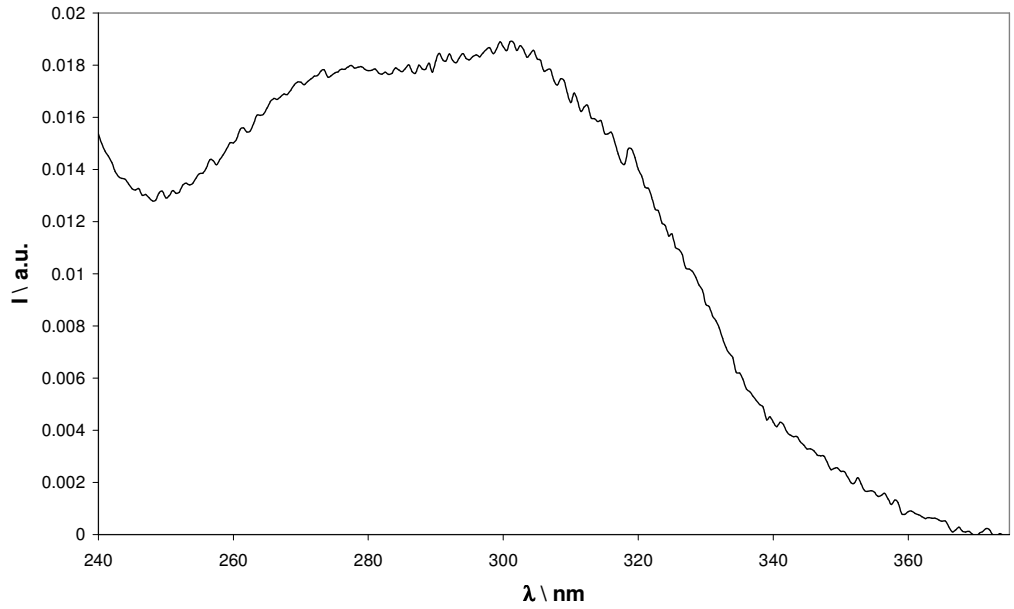

Figure 8.4: Solid state UV-vis of the complex **3b** after 30 min irradiation after corrections.

8.4. NMR

^{1}H NMR and ^{13}C NMR spectra were obtained using a Bruker Ultrashield 300 MHz (300.1 MHz for ^{1}H, 75.5 MHz for ^{13}C). All spectra were obtained in $CDCl_3$.

8.5. IR Spectrometer

IR spectra were obtained using a Perkin Elmer, Universal ATR Sampling

Accessory, Spectrum 100 FT-IR Spectrometer without additives.

8.6. MS Spectrometer

The spectra were measured with a Bruker Daltonics electrospray MicroTOF. The measurements were obtained from solutions of the samples in methanol.

8.7. Triboluminescence Measurements

The methodology of triboluminescence assessment was qualitative rather than quantitative, as the UV-vis spectrometer was not sensitive enough. A small number of crystals in a test tube were crushed with a glass rod in a dark room. At first triboluminescence was detected with a darkness adapted eye. Any observed triboluminescence was than rerecorded with a camera for scientific proof. Typically, a 5 s exposure was used for the photos, while a high F number lens (1.8) and an ISO value of 1600 assure the detection of even weak luminescence.

8.8. Sonoluminescence Measurements

100 mg of the crystalline compound and 5 ml of tetradecane in a small vial were placed in a dark box with the sonofication horn placed below the solution surface (Fig. 8.5). A photo was taken during the sonofication experiment and a second one as a background picture. The sample was sonicated for 30-120 s at different intensities (2.5-12.0 W cm^{-2}). The Generator and the horn were a Sonic Systems Sonic Processor L500-20 running at 20 kHz.

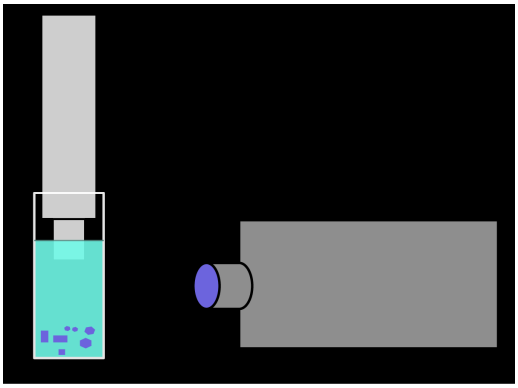

Figure 8.5: Sonoluminescent set-up in a black box, displaying the vial with the crystal to the left and the camera to the right.

8.9. Irradiation Experiments

8.9.1. Light Sources

For this project two types of light sources were used: Light emitting diodes (LEDs) and UV lamps. Different coloured LEDs were used in the range between 355 nm and 600 nm. Their specifications are described in Table 8.1.

Table 8.1: LED data

Colour	Wavelength / nm	Intensity	Voltage / V
UV	351	200 µW	4.8
UV	361	750 µW	4.8
UV	400	350 mcd	4.8
blue	470	3300 mcd	4.8
green	525	7500 mcd	4.8
yellow-orange	600	1600 mcd	4.8
white	430-730	6690 mcd	3.6

The other UV light sources used were a 100 W Blak-Ray B100 UV lamp, a 100 W Spectroline C-100PA UV lamp or an Uvitec 50/60 Hz TLC lamp. When a red laser was used, this was a HeNe laser with a wavelength of 633 nm.

8.9.2. Irradiation Experiments with the UV-lamp

As [2+2] cycloaddition reactions proceed only upon irradiation, the crystalline sample can react at every temperature. An initial single crystal structure was measured, solved and refined, and if a solid state reaction was deemed likely to occur, the crystal was irradiated. The irradiation was usually performed at room temperature; afterwards the crystal was examined for evidence of decomposition through the irradiation. If no or a limited amount of crystal decomposition occurred a second structure was measured and compared to the first one. If the crystal decomposed a powder sample was prepared, measured and irradiated. The irradiated powder was measured again and an overlay of the two powders was performed to find any differences.

8.9.3. In-situ Single Crystal Irradiation Experiments

The set-up for the excited state experiments is illustrated in Figure 8.6. The samples were cooled to temperatures between 220 K and 30 K and LEDs were used to illuminate the samples. The light source was placed within a ring (Fig. 8.6) or mounted on a rod fixed to the back of the diffractometer.

Initially, the determination of a high quality ground state structure was performed to check if the potentially excited component was absent. The crystal was then irradiated, with the time and wavelength dependent on the crystal system. During the irradiation period the crystal was continuously rotated to maximise the uniformity of radiation and data was continuously collected to observe any changes in diffraction spots. A little smearing of the spots is often a good indication of molecular rearrangement, whereas splitting indicates decomposition of the crystal has occured. A second data set was collected and after solving inspected for the metastable state. Here electron density difference maps can help identify new regions and reductions

around the linkage isomer in electron density. The partially photo-activated structure was commonly modelled as disorder within the structure; the occupancy was then used to determine the amount of conversion. In our experience, a minimum of 5 % occupancy was required to be confident in a photo-activated species. When the conversion to the excited state was substantial a parametric study was performed to examine the temperature range in which the photo-activated species exists. This was achieved by increasing or decreasing the temperature and collecting further datasets.

As shown in Figure 8.6a, the ring was placed around the cryostream with six LEDs build into it. They are connected in parallel mode and placed 8 mm away from the crystal. The beam gap was arranged in-line with the collimator. The ring does not affect the cryostream flow rate, but restrict high angles of *kappa*. *Phi*, *theta* and *omega* are able to move to their normal limitations. During collection the *theta* position was constrained, as the diffraction gap stays at the same position, nonetheless 100 % completeness was possible [143].

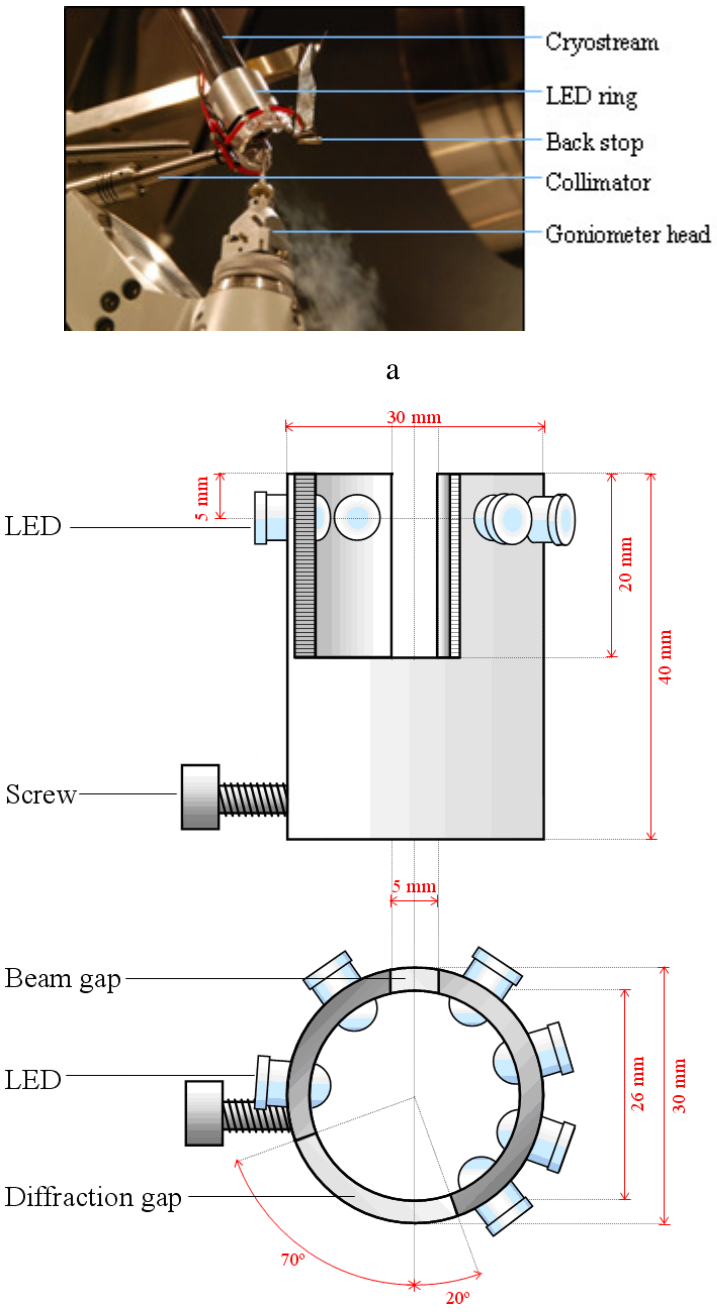

Figure 8.6: Picture of the LED ring a) on the machine b) schematic [143].

8.10. Experimental for Chapter 3 and Chapter 4

8.10.1. Synthesis of Ligands 1-5

4-picoline (2 g, 21.5 mmol) or 4-aminopyridine (2 g, 21.3 mmol) was suspended with 1 g KOH in 5 ml DMSO and heated to 150° C. An aldehyde (21.5 mmol) was added slowly and the reaction mixture was kept heated over night. After cooling down the product was extracted with water and ethylacetate.

1: 4-picoline and 2.3 g of 4-pyridine carboxaldehyde were used. The yield was 2.12 g, corresponding to 55 % of the theoretical yield.

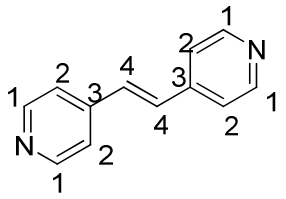

MS, ESI(+): 183.09, calc 183.09 for $C_{12}H_{10}N_2 + H$

H^1-NMR, 300 MHz, $CDCl_3$: 7.15 (s, 2H, H4), 7.35 (d, 4H, H2), 8.65 (d, 4H, H1)

C^{13}-NMR, 75 MHz, $CDCl_3$: 121.22, 130.53, 143.38, 150.42

2: 4-picoline and 2.3 g of 3-pyridine carboxaldehyde were used. The yield was 1.24 g, corresponding to 32 % of the theoretical yield.

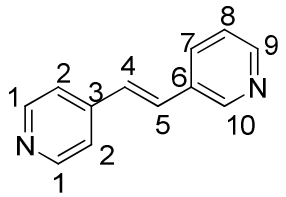

MS, ESI (+): 183.09, calc 183.09 for $C_{12}H_{10}N_2 + H$

3: 4-picoline and 2.3 g of 2-pyridine carboxaldehyde were used. The yield was 1.94 g, corresponding to 50 % of the theoretical yield.

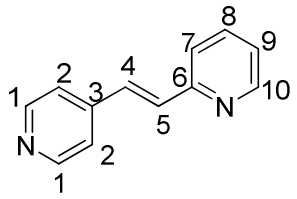

MS, ESI(+): 183.09, calc 183.09 for C_{12} H_{10} N_2 + H

H^1-NMR, 300 MHz, $CDCl_3$: 7.1-7.7 (8H), 8.55 (d, 2H, H1)

C^{13}-NMR, 75 MHz, $CDCl_3$: 121.35, 122.94, 123.04, 130.06, 132.24, 136.77, 149.94, 150.21, 154.43

4: 4-picoline and 2.3 g benzaldehyde was used. The yield was 2.36 g, corresponding to 60 % of the theoretical yield.

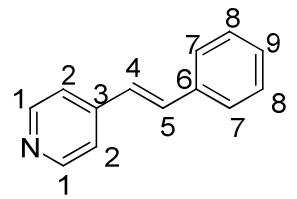

MS, ESI(+): 182.10, calc 182.10 for C_{13} H_{11} N_1 + H

H^1-NMR, 300 MHz, $CDCl_3$: 6.9-7.5 (9H), 8.5 (d, 2H, H1)

C^{13}-NMR, 75 MHz, $CDCl_3$: 121.30, 125.10, 127.32, 129.36, 130.18, 133.61, 136.50, 145.06, 150.50

X-ray, Gemini: a = 5.8173(2) Å, b = 7.5159(3) Å, c = 11.2671(4) Å, α = 90 °, β = 93.212(3) °, γ = 90 °, V = 491.85(3) $Å^3$

The structure was compared to the previously measured one from CARIATY *et al.* [144] and the data was in very good agreement.

5: 4-picoline and 3 g 4-chlorobenzaldehyde were used. The yield was 2.11 g, corresponding to 46 % of the theoretical yield.

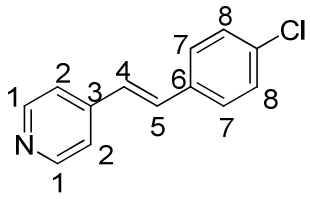

MS, ESI(+): 216.06, calc 216.06 for C_{13} H_{10} N_1 Cl_1 + H

H^1-NMR, 300 MHz, $CDCl_3$: 7.15-7.45 (8H), 8.5 (d, 2H, H1)

C^{13}-NMR, 75 MHz, $CDCl_3$: 120.93, 126.53, 128.21, 128.27, 129.10, 132.05, 134.62, 139.40, 150.01

8.10.2. Synthesis of $[M^{II}(hal)_2(L)_2(H_2O)_2]$ - complexes

Crystals of the complexes were obtained from alcohol / water mixed solvents at room temperature using the layer-separation diffusion method. The metal salt (0.05 mmol) was dissolved in water, a layer of pure alcohol was added above and finally an alcohol solution with the ligand (0.1 mmol) and the anion (0.1 mmol) was layered above (Fig. 8.7).

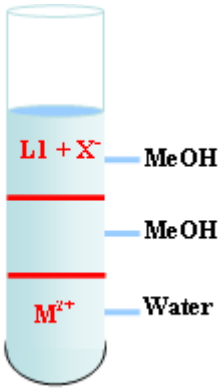

Figure 8.7: Test tube reaction scheme.

The following metal salts were used: cobalt(II) chloride hexahydrate, iron(II) sulfate heptahydrate and manganese(II) cloride, Ammonium thiocyanate and tetrabutylammonium bromide were used as anion sources.

The crystals were characterised by single crystal X-ray diffraction, powder diffraction and UV-vis measurements.

8.10.3. Synthesis of Metal - ligand - complexes

The synthesis was performed as described in 8.10.2. Additionally to the salts named there, cobalt(II) nitrate hexahydrate, tetrabutylammonium iodide and tetraethylammonium chloride were used.

The crystals were characterised mainly by single crystal X-ray diffraction, some additional powder diffraction and UV-vis measurements were performed as well.

8.10.4. Synthesis of Protonated Structures

The same layer method as for 8.10.2. was used, but 1 ml of concentrated HCl was additionally added to the water solution.

The crystals were characterised mainly by single crystal X-ray diffraction, some additional powder diffraction and UV-vis measurements were performed as well.

8.10.5. Synthesis of Structures with Other Templates

A 1:1 ratio of **7** or **8** and one of the ligands was dissolved in MeOH and crystals were obtained through slow evaporation of the solvent from the solution.

The crystals were characterised mainly by single crystal X-ray diffraction, some additional powder diffraction and UV-vis measurements were performed as well.

Table 8.2: UV-vis data in the solid state and in MeOH for the compounds of Chapter 3 and Chapter 4

compound	UV-vis solid state	UV-vis MeOH
1a	310	
1c	295	
3a	308	270, 304
3b	305	270, 304
3c	275, 310	272, 300
3d	315	
1o	298	
1q	294	
5b	315	
8*5	275, 225	

8.11. Experimental for Chapter 5

8.11.1. Synthesis of $[Ni(L)_2(NO_2)_2]$ - complexes

The complexes were synthesised following literature methods [44]. A methanolic solution (5 ml) of the diamine (2 mmol) was added to a methanolic suspension

(10 ml) of potassium hexanitronickelate(II) monohydrate (1 mmol). Crystals were obtained through slow evaporation of the solvent from the dark green solution.

The crystals were characterised by single crystal X-ray diffraction, powder diffraction, Raman and UV-vis.

Table 8.3: Raman and UV-vis data for $[Ni(L)_2(NO_2)_2]$

compound	Raman $\Delta(NO_2)$ \ cm^{-1}	UV-vis DCM \ nm
10	808	500
11		497
12	804	493
13	812	494

8.12. Experimental for Chapter 7

8.12.1. Synthesis of $[Ln(Ph_3PO)_x(NCS)_3]$ - complexes

$[Ln(Ph_3PO)_4(NCS)_3]$ **14**

The lanthanide salt (0.29 mmol), NH_4NCS (1.0 mmol) and Ph_3PO (1.33 mmol) were dissolved in warm methanol. Crystals were obtained through slow evaporation of the solvent from the solution.

$[Ln(Ph_3PO)_3(NCS)_3]$ **15**

The lanthanide salts (0.29 mmol), NH_4NCS (1.0 mmol) and Ph_3PO (1.0 mmol) were dissolved in warm methanol. Crystals were obtained through slow evaporation of the solvent from the solution.

The crystals were characterised by single crystal X-ray diffraction and IR.

Table 8.4: Main infrared peaks of **Ln*14** and **Ln*15**

	Ln*14 / cm^{-1}			**Ln*15 /** cm^{-1}	
La	2069	2056	2045		
Ce	2071	2057	2047		
Pr	2072	2057	2048		
Nd	2073	2059	2049		
Sm	2076	2062	2051		2031
Eu	2077	2063	2053	2053	2029
Gd	2078	2064	2054	2061	2036
Tb	2080	2066	2056	2061	2031
Dy				2063	2037
Ho				2060	2040
Er				2067	2041
Tm				2064	2039
Yb				2070	2044
Lu				2071	2046
Y				2072	2046

9. Literature

1	J. M. Cole, *Chem. Soc. Rev.* **2004**, *33*, 501-513.
2	J. M. Cole, *Acta Cryst.* **2008**, *A64*, 259-271.
3	J. Davaasambuu, P. Durand, S. Techert, *J. Synchrotron Rad.* **2004**, *11*, 483-489.
4	P. Coppens, I. I. Vorontsov, T. Graber, M. Gembicky, A. Y. Kovalevsky, *Acta Cryst.* **2005**, *A61*, 162-172.
5	J. Bregman, K. Osaki, G. M. J. Schmidt, F. I. Sonntag, *J. Chem. Soc.* **1964**, 2021-2030.
6	G. M. J. Schmidt, *J. Chem. Soc.* **1964**, 2014-2021.
7	M. D. Cohen, G. M. J. Schmidt, F. I. Sonntag, *J. Chem. Soc.* **1964**, 2000-2013.
8	M. D. Cohen, G. M. J. Schmidt, *J. Chem. Soc.* **1964**, 1996-2000.
9	R. B. Woodward, R. Hoffmann, *Angew. Chem. Int. Ed.* **1969**, *8, 11*, 781 –932.
10	N. Ramasubbu, K. Gnanaguru, K. Venkatesan, V. Ramamurthy, *J. Org. Chem.* **1985**, *50*, 2337-2346.
11	M. Du, C-P. Li, X-J. Zhao, *CrystEngComm* **2006**, *8*, 552-562.
12	T. J. Brett, J. M. Alexander, J. L. Clark, C. R. Ross, G. S. Harbison, J. J. Stezowski, *Chem. Commun.* **1999**, 1275-1276.
13	T. Friščić, L. R. MacGillivray, *Croat. Chem. Acta* **2006**, *79, 2*, 327-333.
14	T. Friščić, L. R. MacGillivray, *Chem. Comm.* **2005**, 5748-5750.
15	T. Friščić, D. M. Drab, L. R. MacGillivray, *Org. Lett.* **2004**, *6, 25*, 4647-4650.
16	N. Shan, W. Jones, *Tetrahedron Letters* **2003**, *44*, 3687-3689.
17	Q. Chu, D. C. Swenson, L. R. MacGillivray, *Angew. Chem. Int. Ed.* **2005**, *44*, 3569-3572.
18	N. L. Toh, M. Nagarathinam, J. J. Vittal, *Angew. Chem. Int. Ed.* **2005**, *44*, 2237-2241.
19	G. S. Papaefstathiou, I. G. Georgiev, T. Friščić, L. R. MacGillivray, *Chem. Commun.* **2005**, 3974-3976.
20	G. S. Papaefstathiou, Z. Zhong, L. Geng, L. R. MacGillivray, *J. Am. Chem. Soc.* **2004**, *126*, 9158-9159.
21	M. H. Mir, L. L. Koh, G. K. Tan, J. J. Vittal, *Angew. Chem. Int. Ed.* **2010**, *49*, 390-393.
22	A. M. P. Peedikakkal, L. L. Koh, J. J. Vittal, *Chem. Commun.* **2008**, 441-443.
23	A. M. P. Peedikakkal, J. J. Vittal, *Inorg. Chem.* **2010**, *49*, 10–12.
24	I. Turowska-Tyrk, E. Trzop, *Acta Cryst.* **2003**, *B59*, 779-786.
25	Y. Mori, K. Maeda, *J. Chem. Soc. Perkin Trans. 2* **1995**, 113-119.
26	E. Trzop, I. Turowska-Tyrk, *Acta Cryst.* **2008**, *B64*, 375-382.
27	J. H. Kim, S. M. Hubig, S. V. Lindeman, J. K. Kochi, *J. Am. Chem. Soc.* **2001**, *123*, 87 -95.

28 I. Turowska-Tyrk, J. Bąkowicz, J. R. Scheffer, *Acta Cryst.* **2007**, *B63*, 933-940.

29 M. Morimoto, S. Kobatake, M. Irie, *Photochem. Photobiol. Sci.* **2003**, *2*, 1088-1094.

30 M. Irie, *Chem. Rev. 2000*, *100*, 1685-1716.

31 A. Coleman, S. M. Draper, C. Long, M. T. Pryce, *Organometallics* **2007**, *26*, 4128-4134.

32 S-L. Zheng, M. Messerschmidt, P. Coppens, *Acta Cryst.* **2007**, *B63*, 644-649.

33 S-L. Zheng, O. Pham, C. M. L. Vande Velde, M. Gembicky, P. Coppens, *Chem. Commun.* **2008**, 2538-2540.

34 J. Narasimha Moorthy, P. Venkatakrishnan, G. Savitha, R. G. Weiss, *Photochem. Photobiol. Sci.* **2006**, *5*, 903-913.

35 J. Harada, H. Uekusa, Y. Ohashi, *J. Am. Chem. Soc.* **1999**, *121,* 5809-5810.

36 S-L. Zheng, C. M. L. Vande Velde, M. Messerschmidt, A. Volkov, M. Gembicky, P. Coppens, *Chem. Eur. J.* **2008**, *14*, 706-713.

37 J. L. Burmeister, *Coord. Chem. Rev.* **1990**, *105*, 77-133.

38 N. N. Greenwood, A. Earnshaw, *Chemistry of the Elements* **1984**, *1 ed., Pergamon Press,* 344.

39 D. Schaniel, T. Woike, L. Kushch, E. Yagubskii, *Chemical Physiks* **2007**, *340*, 211-216.

40 I. Grenthe, E. Nordin, *Inorg. Chem.* **1979**, *18, 7*, 1869-1874.

41 N. N. Greenwood, A. Earnshaw, *Chemistry of the Elements* **1984**, *1 ed., Pergamon Press,* 340.

42 A. Y. Kovalevsky, K. A. Bagley, P. Coppens, *J. Am. Chem. Soc.* **2002**, *124*, 9241-9248.

43 M. K. Smith, J. A. Gibson, C. G. Young, J. A. Broomhead, P. C. Junk, F. R. Keene, *Eur. J. Inorg. Chem.* **2000**, 1365-1370.

44 D. Das, I. R. Laskar, A. Ghosh, A. Mondal, K. Okamoto, N. R. Chaudhuri, *J. Chem. Soc., Dalton Trans.* **1998**, 3987-3990.

45 I. R. Laskar, D. Das, G. Mostafa, T-H. Lu, T-C. Keng, J-C. Wang, N. R. Chaudhuri, A. Ghosh, *New J. Chem.* **2001**, *25*, 764-768.

46 H. E. Toma, E. Giesbrecht, R. L. Espinoza Rojas, *Can. J. Chem.* **1983**, *61*, 2520-2525.

47 S. M. Jørgensen, *Z. Anorg. Chem.* **1894**, *5*, 147-196.

48 M. Ruedlinger, J. Schefer, T. Vogt, T. Woike, S. Haussuehl, H. Zoellner, *Physica* **1992**, *B180 & 181*, 293-298.

49 A. Werner, *Ber.* **1907**, *40*, 765-772.

50 M. Kubota, S. Ohba, *Acta Cryst.* **1992**, *B48*, 627-632.

51 J. L. Burmeister, *Coord. Chem. Rev.* **1968,** *3,* 225-245.

52 M. R. Warren, S. K. Brayshaw, A. L. Johnson, S. Schiffers, P. R. Raithby, T. L. Easun, M. W. George, J. E. Warren, S. J. Teat, *Angew. Chem. Int. Ed.* **2009**, *48*, 5711 –5714.

53 D. V. Fomichev, T. R. Furlani, P. Coppens, *Inorg. Chem.* **1998**, *37*, 1519-1526.

54 D. A. Johnson, V. C. Dew, *Inorg. Chem.* **1979**, *18*, 3273-3274.

55 A. Y. Kovalevsky, K. A. Bagley, J. M. Cole, P. Coppens, *Inorg. Chem.* **2003**, *42*, 140-147.

56 K. F. Bowes, J. M. Cole, S. L. G. Husheer, P. R. Raithby, T. L. Savarese, H. A. Sparkes, S. J. Teat, J. E. Warren, *Chem. Commun.* **2006**, 2448-2450.

57 M. A. Halcrow, *Coord. Chem. Rev.* **2009**, *253*, 2493-2514.

58 A. Hauser, *Chem. Phys. Lett.* **1986**, *124*, *6*, 543-548.

59 M. Marchivie, P. Guionneau, J. A. K. Howard, G. Chastanet, J-F. Létard, A. E. Goeta, D. Chasseau, *J. Am. Chem. Soc.* **2002**, *124, 2*, 194-195.

60 C. D. Kim, S. Pillet, G. Wu, W. K. Fullagar, P. Coppens, *Acta Cryst.* **2002**, *A58*, 133-137.

61 N. Yasuda, M. Kanazawa, H. Uekusa, Y. Ohashi, *Chem. Lett.* **2002**, 1132-1133.

62 P. Coppens, O. Gerlits, I. I. Vorontsov, A. Y. Kovalesky, Y. Chen, T. Graber, M. Gembicky, I. V. Novozhilova, *Chem. Commun.* **2004**, 2144-2145.

63 I. I. Vorontsov, T. Graber, A. Y. Kovalevsky, I. V. Novozhilova, M. Gembicky, Y-S. Chen, P. Coppens, *J. Am. Chem. Soc.* **2009**, *131, 18*, 6566–6573.

64 J. Davaasumbuu, P. Durand, S. Techert, *J. Synchrotron Rad.* **2004**, *11*, 483-489.

65 S. Techert, K. A. Zachariasse, *J. Am. Chem. Soc.* **2004**, *126*, 5593-5600.

66 G. Busse, T. Tschentscher, A. Plech, M. Wulff, B. Frederichs, S. Techert, *Faraday Discuss.* **2002**, *122*, 105-117.

67 W. C. Roentgen, *Nature* **1896**, *53*, 274-276.

68 P. Luger, *Modern X-ray analysis on single crystals*, de Gruyter **1980**, 149-150.

69 *X-ray structure analysis*, 11th BCA/CCG Intensive teaching School **2007**, *17*.

70 W. Clegg, A. J. Blake, R. O. Gould, P. Main, *Crystal Structure Analysis Principles and Practice*, Oxford Science Publications **2001**, 6-7.

71 M. de Graef, M. E. McHenry, *Structure of materials*, Cambridge University Press **2008**, 97-100.

72 C. Giacovazzo, H. L. Monaco, D. Viterbo, F. Scordari, G. Gilli, G. Zanotti, M. Catti, *Fundamentals of Crystallography*, Oxford Science Publications **1992**, 18-22.

73 G. E. Herberich, U. Englert, *Script der Vorlesung Struktur und Symmetrie*, **2005**, *2*.

74 *International Tables for Crystallography, Vol. A,* Springer **2005**, *5*.

75 W. Clegg, A. J. Blake, R. O. Gould, P. Main, *Crystal Structure Analysis Principles and Practice*, Oxford Science Publications **2001**, 31-34.

76 *X-ray structure analysis*, 11th BCA/CCG Intensive teaching School **2007**, B1-2.

77 *X-ray structure analysis*, 11th BCA/CCG Intensive teaching School **2007**, *8*.

78 A. L. Patterson, *Phys. Rev.***1934**, *46*, 372–376.
79 W. Clegg, A. J. Blake, R. O. Gould, P. Main, *Crystal Structure Analysis Principles and Practice*, Oxford Science Publications **2001**, *9*.
80 W. Clegg, *J. Chem. Soc. Dalton Trans.* **2000**, 3223-3232.
81 P. R. Raithby, *Crystallography Reviews* **2007**, *13, 2*, 121-142.
82 http://www-ssrl.slac.stanford.edu/
83 http://www.diamond.ac.uk/AboutDiamond/Diamondstep-by-step/HowDoesItWork.htm/
84 I. R. Laskar, D. Das, W.-T. Wong, N. R. Chaudhuri, *Transition Metal Chemistry* **2001**, *26*, 594-597.
85 Y. Hill, A. Briceño, *Chem. Commun.* **2007**, 3930-3932.
86 C. Roux, J. Zarembowitch, B. Gallois, M. Bolte, *New J. Chem*. **1992**, *16*, 671.
87 S. Nakashima, A. Yamamoto, Y. Asada, N. Koga, T. Okuda, *Inorg. Chim. Acta* **2005**, 358, 257-264.
88 Y. Hill, A. Briceño, *Chem. Commun.* **2007**, 3930-3932.
89 H. Miura, S. Takahashi, H. Kasai, S. Okada, K. Yase, H. Oikawa, H. Nakanishi, *Crystal Growth & Design* **2010***, 10*, 510–517.
90 G. De Munno, F. Cipriani, D. Armentano, M. Julve, J. A. Real, *New J. Chem.* **2001**, *25*, 1031-1036.
91 S. H. Park, K. M. Kim, S. Lee, O-S. Jung, *Bull. Korean Chem. Soc.* **1998**, *19*, 79-82.
92 http://www.ccdc.cam.ac.uk/products/csd/
93 G. Yang, Q. Zhang, X.-P. Zhang, Y. Zhu, S. W. Ng, *J. Chem. Res.* **2007**, 384-386.
94 M. A. Porai-Koshits, G. N. Tishchenko, *Kristallografiya* **1960**, *4*, 239.
95 R. Micu-Semeniuc, E. Hila, G. Dobos-Roman, L. Ghergari, *Rev. Roum. Chim.* **1983**, *28*, 471.
96 J. Y. Lee, S. Y. Lee, W. Sim, K-M. Park, J. Kim, S. S. Lee, *J. Am. Chem. Soc.* **2008**, *130, 22*, 6902-6903.
97 G. G. Shipley, S. C. Wallwork, *Acta Cryst.* **1967,** *22*, 593-601.
98 K. Prout, J. Fail, R. M. Jones, R. E. Warner, J. C. Emmett, *J. Chem. Soc. Perkin Trans. II* **1988,** 265-284.
99 S. K. Brayshaw, T. L. Easun, M. W. George, A. M. E. Griffin, A. L. Johnson, P. R. Raithby, T. L. Savarese, S. Schiffers, J. E. Warren, M. R. Warren, S. J. Teat, *Inorg. Chem.* **2010**, *in press*.
100 L. J. Farrugia, *J. Appl. Cryst.* 1999, 32, 837-838.
101 T. Chattopadhyay, M. Ghosh, A. Majee, M. Nethaji, D. Das, *Polyhedron* **2005**, *24*, 1677-1681.
102 A. Y. Kovalesky, G. King, K. A. Bagley, P. Coppens, *Chem. Eur. J.* **2005**, *11*, 7254-7264.
103 E. Boldyreva, J. Kivikoski, J. A. K. Howard, *Acta Cryst.* **1997**, *B53*, 405-414.
104 E. Boldyreva, J. Kivikoski, J. A. K. Howard, *Acta Cryst.* **1997**, *B53*, 394-404.
105 A. J. Walton, *Advances in Physics* **1977**, *26*, *6*, 887-948.

106 L. M. Sweeting, A. L. Rheingold, *J. Am. Chem. Soc.* **1987**, *109*, 2652-2658.
107 L. M. Sweeting, *Chem. Mater.* **2001**, *13*, 854-870.
108 J. T. Dickinson, L. B. Brix, L. C. Jensen, *J. Phys. Chem.* **1984**, *88*, 1698-1701.
109 C. R. Hurt, N. McAvoy, S. Bjorklund, N. Filipescu, *Nature* **1966**, *212*, 179-180.
110 I. Sage, R. Badcock, L. Humberstone, N. Geddes, M. Kemp, G. Bourhill, *Smart Mater. Struct* **1999**, *8*, 504-510.
111 L. M. Sweeting, A. L. Rheingold, J. M. Gingerich, A. W. Rutter, R. A. Spence, C. D. Cox, T. J. Kim, *Chem. Mater.* **1997**, *9*, 1103-1115.
112 A. L. Rheingold, W. King, *Inorg. Chem.* **1989**, *28*, 1715-1719.
113 J. I. Zink, G. E. Hardy, J. E. Sutton, *J. Phys. Chem.* **1976**, 248-249.
114 J. I. Zink, W. Klimt, *J. Am. Chem. Soc.* **1974**, 4690-4692.
115 J. P. Duignan, I. D. H. Oswald, I. C. Sage, L. M. Sweeting, K. Tanaka, T. Ishihara, K. Hirao, G. Bourhill, *J. Lumin.* **2002**, *97*, 115-126.
116 M. P. Brenner, S. Hilgenfeld, D. Lohse, *Rev. Mod. Phys.* **2002**, *74*, 425-484.
117 A. N. Magunov, *Instruments and experimental techniques* **2009**, *52, 4*, 451-472.
118 G. L. Sharipov, *Jept Letters* **2007**, *85, 9*, 458-460.
119 G. L. Sharipov, R. K. Gainetdinov, A. M. Abdrakhmanov, *Russ. Chem. Bull. Int. Ed.* **2008**, *57, 9*, 1827-1830.
120 N. C. Eddingsaas, K. S. Sulick, *Nature* **2006**, *444*, 9.
121 N. C. Eddingsaas, K. S. Sulick, *J. Am. Chem. Soc.* **2007**, *129,* 6718–6719.
122 *Comprehensive Inorganic Chemistry*, Pergamon Press **1973**, *1, 4*.
123 S. Cotton, *Lanthanide and Actinide Chemistry*. John Wiley & Sons Ltd. **2007**, *2*.
124 S. A. Cotton, *C. R. Chimie* **2005**, *8*, 129-145.
125 G. R. Willey, T. J. Woodman, M. G. B. Drew, *Polyhedron* **1997**, *16, 19*, 3385-3393.
126 L. I. Semenova, A. H. White, *Aust. J. Chem.* **1999**, *52*, 507-517.
127 A. Lossin, G. Meyer, *Z. anorg. allg. Chem.* **1993**, *619*, 1609-1615.
128 D. R. Cousin, F. A. Hart, *J. Inorg. Nucl. Chem.* **1968**, *30*, 3009-3015.
129 R. P. Feazell, J. B. Gary, J. A. Kautz, K. K. Klausmeyer, C. W. Wong, M. Zancanella, *Acta Cryst.* **2004**, *E60*, m532-m534.
130 R. D. Shannon, *Acta Cryst.* **1976**, *A32*, 751-767.
131 S.-H. Lin, Z.-C. Dong, J.-S. Huang, Q.-E. Zhang, J.-X. Lu, *Acta Cryst.* **1991**, *C47*, 426-427.
132 M. C. Gallazzi, F. Bianchi, L. Depero, M. Zocchi, *Polymer* **1998**, *29*, 1516-1521.
133 K. Izod, S. T. Liddle, W. Clegg, *Inorg. Chem.* **2004**, *43*, 214-218.
134 D. Barr, A. T. Brooker, M. J. Doyle, S. R. Drake, P. R. Raithby, R. Snaith, D. S. Wright, *Angew. Chem. Int. Ed.* **1990**, *29, 3*, 285-287.
135 J. Fawcett, A. W. G. Platt, D. R. Russell, *Polyhedron* **2002**, *21,* 287-293.

136 Z. Olejnik, T. Lis, *Acta Cryst.* **1995***, C51*, 2246-2249.

137 L. J. Radonovich, M. D. Glick, *J. Inorg. Nucl. Chem.* **1973**, *35*, 2745-2752.

138 S. Petriček, A. Demšar, L. Golič, J. Košmrlj, *Polyhedron* **2000**, *19*, 199-204.

139 M. J. Glazier, W. Levason, M. L. Matthews, P. L. Thornton, M. Webster, *Inorg. Chim. Acta* **2004**, *357*, 1083-1091.

140 J. Fawcett, A. W. G. Platt, D. R. Russell, *Polyhedron* **2002**, *21*, 287-293.

141 N. J. Hill, W. Levason, M. C. Popham, G. Reid, M. Webster, *Polyhedron* **2002**, *21*, 445-455.

142 D. M. Adams, *Metal-Ligand and Related Vibrations*, Edward Arnold, London **1967**, 101-102.

143 S. K. Brayshaw, J. W. Knight, P. R. Raithby, T. L. Savarese, S. Schiffers, S. J. Teat, J. E. Warren, M. R. Warren, *J. Appl. Cryst.* **2010**, *43*, 337-340.

144 E. Cariati, D. Roberto, R. Ugo, V. I. Srdanov, S. Galli, P. Macchic, A. Sironi, *New J. Chem* **2002**, *26*, 13-15.